Holly Pacey and the Half-Spin Particles: Searching for new physics with leptons at the ATLAS experiment

Holly Pacey

of

King's College,
University of Cambridge

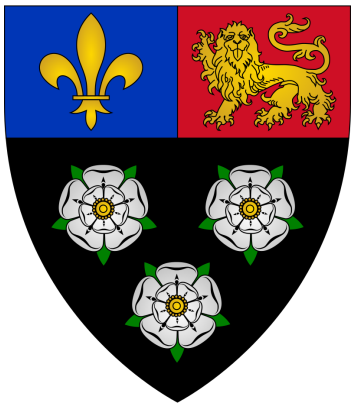

This thesis is submitted for the degree of Doctor of Philosophy.

June 2020

Declaration

This thesis is the result of my own work and includes nothing which is the outcome of work done in collaboration except as declared in the Preface and specified in the text. It is not substantially the same as any that I have submitted, or, is being concurrently submitted for a degree or diploma or other qualification at the University of Cambridge or any other University or similar institution except as declared in the Preface and specified in the text. I further state that no substantial part of my thesis has already been submitted, or, is being concurrently submitted for any such degree, diploma or other qualification at the University of Cambridge or any other University or similar institution except as declared in the Preface and specified in the text. It does not exceed the prescribed word limit for the relevant Degree Committee.

Holly Pacey

Holly Pacey and the Half-Spin Particles: Searching for new physics with leptons at the ATLAS experiment

Holly Pacey

Abstract

Whilst the Large Hadron Collider (LHC) has spent just over a decade pushing experimental boundaries in energy and intensity of proton-proton collisions, it has yet to discover new physics beyond the Standard Model. The Standard Model remains one of the most robustly tested theories of all time, despite evidence that it is incomplete, such as its inability to account for dark matter or the weakness of gravity. It is thus highly motivated that new particles should appear in proton-proton collisions at the ATLAS detector, around the TeV scale. This thesis contains three searches for such new particles which represent substantial improvements to constraints on possible new physics beyond the Standard Model. They demonstrate that data remains consistent with the Standard Model in collision events with two leptons in the final state.

The first two searches seek electroweak supersymmetry, using $80.5\,\text{fb}^{-1}$ and the full $139.5\,\text{fb}^{-1}$ of the ATLAS Run 2 dataset, respectively. The first search placed the first ATLAS Run 2 limits on chargino pair production decaying via W-bosons, excluding chargino masses up to 410 GeV for a massless neutralino. This was surpassed by the second search, resulting in world-leading exclusion limits on this process, up to 420 GeV, as well as excluding direct slepton production with slepton masses up to 700 GeV and chargino pair production decaying via sleptons or sneutrinos with chargino masses up to 1 TeV.

The third search uses an innovative technique to pursue signs of lepton charge-flavour asymmetry in the full Run 2 ATLAS dataset. Whilst it can be shown that the ratio of $e^+\mu^-$ to $e^-\mu^+$ events within Standard Model proton-proton collisions should not exceed one, this need not be the case for collision processes beyond the Standard Model. This search measures the ratio in data to be 0.988 ± 0.005 and 0.987 ± 0.005 in two regions

of phase space (one with missing transverse momentum and one with a hard jet in the final state, respectively), as well as providing measurements binned in different variables. Furthermore, the search places the first direct exclusion limits at the LHC for single-production of a smuon within an R-parity violating supersymmetry model with the λ'_{231} coupling switched on, excluding left-handed smuons up to 1.2 TeV for neutralino masses below the top quark mass and λ'_{231} couplings up to one. It also interprets results in a scalar leptoquark model, placing the first LHC limits on a singly-produced leptoquark decaying to an $e\mu$ final state, excluding masses up to 2.2 TeV for leptoquark couplings λ_{eu} and $\lambda_{\mu c}$ up to a value of one.

Acknowledgements

PhDs are difficult and stressful, particularly when they finish during a global pandemic. Whilst the past 3.5 years have occasionally driven me to tears from manic deadlines and statistics code which refused to cooperate, I have been driven to laughter and fits of the giggles by my colleagues much more often. These years have been the best of my life so far, partially because I'm still convinced that high energy physics is really cool, but mainly due to the wonderful people I have befriended along the way.

Firstly I'd like to thank my supervisor Chris Lester. Thank you for moulding me into a scientist, for giving me the space to grow as an independent researcher but always being there to teach me when I needed it, for making it possible for me to go to a ridiculous number of conferences, and of course for providing the world's best anecdotes. If I am anywhere near as creative a scientist and full of endless ideas and enthusiasm as you are when I 'grow up', it will be an honour.

Secondly, I would like to thank Sarah Williams, who has grown from being an incredibly helpful second supervisor and invaluable mentor to a kind and generous friend. Thank you for all your advice and support on not just literally all my research but the large volume of job applications and thesis drafts I've made you read too. Thank you for teaching me almost as much about wine as you have about physics, and for being excellent company to travel the world with.

The rest of the Cambridge ATLAS group also deserves my gratitude for constantly making me feel supported and valued. I would like to thank Will Fawcett for being a brilliant person to work with. Thank you for making me slightly less terrible at coding, for filling our office with so much laughter and for proof-reading this thesis. I'm sorry about all the bugs. I'd also like to thank Tina Potter for supporting me over the years. You are a great role model and such a badass. Additionally, thank you Andy Parker for your valuable insight and wisdom on our Networks project, and for your career support. Furthermore, my thanks go to Will Buttinger for saving the emu analysis statistics code.

Way outside of Cambridge, it's been a pleasure to work with the hilarious and very wise Martin White. I am very grateful that you came up with the idea for our Networks project, which though it did not make it into this thesis, was a very fun challenge that

took up a large portion of my PhD. Thank you for inspiring me to have more whacky ideas, and for all your support with my efforts to get a JRF.

Of course working inside a collaboration as big as ATLAS, there are many people I have worked with who have taught me a lot of physics, and provided excellent company at conferences. First of all I'd like to thank Zach Marshall, for (almost) always knowing the answers to my questions, for all the career support, and for being in a contagiously good mood all the time. Secondly, I'd like to thank Max Swiatlowski for being so approachable to work with and for all the valuable advice. The rest of the ATLAS JetEtMiss group comprises the best karaoke talent in high energy physics, who have an immensely good capacity for tolerating my many and terrible puns. My particular thanks also go to Doug Schaefer, Emma Tolley and Marco Valente for training me in the art of studying missing transverse momentum.

A vast portion of my PhD has been spent working in the ATLAS supersymmetry group. It has been a pleasure to work on two papers with colleagues in Lecce, Milan and Oslo, especially Margherita Primavera, Sonia Carrà, Francesco Gravili and Alessandro Mirto.

Whilst at CERN during my second year, I am incredibly grateful for the company of my friends; especially Tom Powell (another contender for the funniest person alive) and Matt Anthony. I am also incredibly grateful for the support of my other friends throughout my PhD, including Bill Balunas, Joonatan Laulainen, Will Collins, Graham Kimbell, Tom Gillam and Shane Mahen among others.

It was a privilege to share my office with Dan Noel, and one of my best friends Rupert Tombs. Thank you for being a kind and thoughtful friend, a wonderfully unique person, and for helping me so much with the statistics section of this thesis (and for proofreading the rest). Thank you for supplying the office with penguins and colluding in the secret sofa project.

Vanessa Marton, Suzanne Marton, Elizabeth Cotton, Alice Robbins and Lucy Robbins have now been my close friends for 18 years; and have spent the whole time inspiring me. I would not be who I am today without having grown up with you. In fact I probably wouldn't have even gone into physics without watching that documentary about Schrödinger's cat with you. So thank you for that, and for your limitless friendship.

Penultimately, I could never have gotten through my undergraduate degree or PhD without Alex Mason. Though we were at times separated by multiple continents, 8 hour

time differences and the X5 bus journey, you were always there for me. I can never be grateful enough for your support.

Finally, I am most grateful to my family, I am eternally thankful for your efforts to understand supersymmetry and your unconditional love and support. To my Grandma Irene, thank you for always being so excited by my achievements, it's a pleasure to make you proud. Thank you for all the places you have taken me, and the things you have taught me. Finally, and most of all, thank you to my parents, who raised me to follow my dreams and work hard at the things I'm passionate about. Thank you for never ceasing to inspire me, support me, teach me or feed me tapas. I doubtless could not have reached this point without you.

Preface

This thesis contains my contribution so far to the pursuit of understanding the ingredients of the universe. The Standard Model of particle physics does a phenomenal job of describing high energy particle collisions, but does not paint a full picture. No account is given for the identity of dark matter, and no explanation is provided of why gravity is so much weaker than the other forces of nature, to give two examples. There are endless ideas to be found suggesting what additional particles can be added to the Standard Model to complete the picture, and a primary goal within the high energy physics community is to try to find evidence for them being produced within high energy particle collisions. The author worked on this goal as part of the ATLAS collaboration, and this thesis describes three searches for different new-physics processes within proton-proton collision data recorded by the ATLAS detector between 2015 and 2018.

As presented in Chapter 1, this thesis first focuses on one of the most popular 'beyond the Standard Model' theories: supersymmetry. After summarising the Standard Model, superysmmetry will be motivated, primarily as a solution to the problem of why gravity is so weak. Before embarking on a description of the searches for new physics, Chapter 2 of the thesis is devoted to a description of the ATLAS detector. Part of this Chapter summarises work done by the author to quantify uncertainties on the inference of undetectable particles through the measurement of missing transverse momentum. These uncertainties are used by many other searches and measurements throughout ATLAS. Following this, the third Chapter provides an overview of the data analysis concepts common to all three searches, introduces useful kinematic variables, and explains the statistical concepts used to obtain concrete results from the searches.

Two of the searches described in this thesis — in Chapters 4 and 5 — seek a variant of supersymmetry that also provides a dark matter candidate. The first used the 2015–2017 dataset to set world-leading exclusion limits on the pair production of charginos decaying via W bosons. The author designed this search, and played a leading role in a small team of ATLAS colleagues to perform it, resulting in a conference paper [1] presented at the SUSY18 conference in June 2018. The author was also the leading analyser on the second search, working with other ATLAS colleages to extend the analysis's reach using the 2018 dataset to place the current (at time of submission) world-leading limits

on the same model. In addition, it provided world-leading re-interpretations for models of direct slepton pair production and chargino pair production decaying via sleptons or sneutrinos. This second result was the first search for electroweak supersymmetry published using the full Run 2 ATLAS or CMS datasets; it was published [2], and presented at the SUSY19 conference in May 2019.

The third search in this thesis, found in Chapter 6, takes a different approach: it is primarily a measurement of the ratio of $e^+\mu^-$ to $e^-\mu^+$ events in data. This ratio is expected to be less than or equal to one for the Standard Model, but can be greater than one for new-physics models such as R-parity violating supersymmetry or scalar leptoquarks. A measurement of the ratio in full Run 2 ATLAS data provides a largely model-independent search for new physics, and is the first measurement of this ratio at the Large Hadron Collider (LHC). This ratio measurement is performed in two regions of phase space, in bins of a variety of kinematic variables. In addition, the measurement relies less on Monte Carlo simulations of events, which are normally required to test a given hypothesis, and are limited by statistical and modelling uncertainties. As well as the model-independent measurement, the first LHC exclusion limits are placed on specific single-production processes for the R-parity violation supersymetry and scalar leptoquark scenarios motivated in the first Chapter. This search targets publication in 2020; the unblinded results and preliminary statistical interpretations are included in the thesis. The author was the 'Analysis Contact' for this search and was heavily involved in most aspects, working again with other colleagues in ATLAS. The search is based upon the initial ideas of the author's supervisor (Dr Chris Lester) and a previous student (Dr Ben Brunt), which are presented in Reference [3] and the student's doctoral thesis [4].

Contents

Chapter 1

Theoretical background: Life, the universe and everything

1.1 Introduction

One of the many great things to happen in science in the 20^{th} century was the construction of the Standard Model (SM) of particle physics. This elegant theory emerged from a plethora of experimental observations combined with quantum mechanics and special relativity. It describes the fundamental ingredients, called particles, that exist in the universe and how they behave and interact. Along with successfully explaining things we see in the world every day, like atoms and electromagnetism, the Standard Model has done brilliantly at describing most experimental data physicists have gathered. However, there are some exceptions to this that — along with unanswered theoretical questions — motivate new extensions to the theory.

One popular type of extension, or 'beyond the SM' (BSM) theory, is Supersymmetry (SUSY), which can solve some of the theoretical and experimental problems with the SM. Along with searches for evidence of SUSY, this thesis also considers another type of BSM theory which has recently increased in popularity: leptoquarks.

This Chapter begins with a brief overview of the Standard Model and its problems. This is followed by a discussion of how SUSY or leptoquarks could help solve them.

1.2 The Standard Model

Fundamentally, the SM is a gauge field theory describing the electroweak and strong forces of nature. It is built from three symmetry groups: $SU(3)_C \times SU(2)_L \times U(1)_Y$. $SU(3)_C$ describes the strong interaction (QCD) and $SU(2)_L \times U(1)_Y$ describes the electroweak interaction. At energies below 246 GeV, the electroweak force breaks down into the weak interaction and $U(1)_Q$ electromagnetism (QED). This breaking occurs due to the Higgs mechanism, which ascribes masses to certain particles. Particle interactions are allowed if they conserve the symmetries in the model — i.e. if the symmetry's conserved charge[1] remains constant before and after the interaction.

All 'particles' in the SM are indivisible quanta constituting fundamental ingredients of the universe. The SM particles can be split into two categories depending on their spin. Particles with half-integer spin are known as fermions[2]. Fermions constitute 'matter' and interact with each other through the 'force carrying' gauge bosons — particles with integer spin. Fermions also have anti-matter partners, which have the same mass but opposite electric charges to their particle counterpart. In the SM, there is a further divide within the fermions into leptons and quarks. Quarks are the only fermions which carry a colour charge, thus they interact through the strong force. Leptons are colourless so do not feel the strong force. They are split into those with electric charge and those without, called neutrinos (which are approximately massless in the SM). It is not known why, but there exist three 'generations' of fermions; there are three sets of fermions each with heavier masses than the last. In each of these generations there are two types of quark, differing by their electric charges and masses. A Table of the fermions is shown in Table 1.1. All fermions interact through the weak force and all but the neutrinos interact via electromagnetism since they possess an electric charge.

The SM gauge bosons arise from the symmetries defined by the gauge groups. QCD predicts 8 massless and coloured gauge bosons called gluons. These interact with quarks and other gluons whilst preserving the three $SU(3)_C$ 'colour' charges — red, green and blue. One phenomenon resulting from the ability of gluons to 'self-interact' with other gluons is the 'quark confinement hypothesis', which states that the only stable and observable states allowed are colour singlets. This leads to quarks and gluons being unobservable on their own, instead forming bound states called hadrons. In ATLAS, when quarks and gluons are produced in collisions, this phenomenon leads to a complex

[1] Using Noether's theorem [5], for any continuous symmetry there is an associated conserved charge.
[2] As the thesis title suggests, electrons and muons are half-spin particles

Fermion	Generation		
	1	2	3
Leptons	e	μ	τ
	ν_e	ν_μ	ν_τ
Quarks	u	c	t
	d	s	b

Table 1.1: SM fermions.

shower of hadrons hitting the detectors, which are called 'jets'. Another unique property of QCD is its interaction strength, which has asymptotic freedom at low energies. This means that the force cannot be described perturbativity at low energies, for example when describing the internal structure of the proton (a type of hadron). Regarding the LHC, which collides beams of protons, this means that numerical approximations must be used for the interactions between quarks and gluons still bound within the proton. Quantitatively these are described by parton density functions (PDFs) and they provide a source of theoretical uncertainty to all ATLAS results.

To discuss the electroweak interaction it is helpful to consider splitting fermions into their left- and right-handed chiral parts. Chirality arises when considering representations of the Lorentz group. It is observed that the $SU(2)_L$ weak interaction only couples to left-handed particles. Before electroweak symmetry breaking, there are three massless W bosons (W^1, W^2, W^3) corresponding to $SU(2)_L$ and one massless B boson corresponding to $U(1)_Y$. After the Higgs mechanism spontaneously breaks this symmetry we are left with $U(1)_Q$, where $Q = Y/2 + I_3$ is the electric charge. The neutral B and W^3 bosons mix to give the photon (γ) and the neutral Z^0 boson (responsible for neutral-current weak interactions). This mixing is parametrised by the weak mixing angle (θ_W). The remaining W^1 and W^2 bosons mix to give charge conjugate states W^+ and W^- which mediate the charge-current weak interaction, and also interact through electromagnetism. Since it includes a contribution from the $U(1)_Y$ B boson, Z^0 interacts with all fermions, but more strongly with left-handed ones. Photons only interact with the charged fermions, but do so equally strongly for their left- and right-handed chiral parts. Since they are formed entirely from $SU(2)_L$ bosons, $W^\pm$ only interact with the left-handed components of fermions. The electroweak bosons can also interact with each other, provided quantum numbers are conserved, for example W bosons can interact with photons.

A Table of the quantum numbers for the SM fermions is given in Table 1.2, where the $SU(2)_L$ chiral representation for fermions is used. This convention puts the left-handed components into a doublet and leaves the right-handed component as a singlet. $SU(2)_L$ singlets don't interact in $SU(2)_L$.

Fermion		Y	I	I_3	Q
Leptons	e_R^-	-2	0	0	-1
	$\begin{pmatrix}\nu_e\\ e^-\end{pmatrix}_L$	-1	$\frac{1}{2}$	$\frac{1}{2}$ $-\frac{1}{2}$	0 -1
Quarks	u_R	$\frac{4}{3}$	0	0	$\frac{2}{3}$
	d_R	$-\frac{2}{3}$	0	0	$-\frac{1}{3}$
	$\begin{pmatrix}u\\ d\end{pmatrix}_L$	$\frac{1}{3}$	$\frac{1}{2}$	$\frac{1}{2}$ $-\frac{1}{2}$	$\frac{2}{3}$ $-\frac{1}{3}$

Table 1.2: SM fermion electroweak quantum numbers.

An unexpected property of the SM is that the quark mass eigenstates don't match the quark weak interaction eigenstates. This leads to the introduction of the Cabibbo–Kobayashi–Maskawa (CKM) matrix [6, 7], which relates these two eigenstate bases, and leads to the mixing between quark generations in the $W^{\pm}$ interaction. The values in this matrix are not predicted by the SM and must be experimentally determined.

The final piece of the SM is the Higgs boson. It is a complex scalar (spin-0) field which was introduced to facilitate electroweak symmetry breaking. In the $SU(2)$ representation, the Higgs field is a complex doublet ($Y = 1$) with four real degrees of freedom. During electroweak symmetry breaking one degree of freedom obtains a non-zero vacuum expectation value (VEV)[3] and the other three lead to the W and Z boson masses. These masses are all determined by the VEV, and are thus related to each other. The Higgs field also gives the charged fermions mass through Yukawa couplings. The charged fermion masses are not predicted by the SM so are experimentally determined, along with the value of the VEV. The Higgs boson itself is an excitation of the Higgs field about its VEV; it also gets given a mass. Since the Higgs boson has a mass, it can

[3]VEVs are the minimum energy of the potential of the field. They are obtained by having a negative square mass term.

undergo self-interactions.

The neutral fermions are not given a mass through the Higgs mechanism. Though they have been observed to possess non-zero (but very small) masses in neutrino oscillation experiments [8], though the mechanism through which they obtain them is unknown. Like the quark sector, neutrinos have eigenstates that differ from their weak interaction eigenstates, with a relationship determined by the Pontecorvo-Maki-Nakagawa-Sakata (PMNS) matrix [9].

Overall the SM has twenty-three free parameters that must be experimentally determined. These are: the nine charged fermion masses, the Higgs VEV and mass, θ_W, three gauge couplings, four parameters that define the CKM matrix and the four parameters defining the PMNS matrix.

1.3 Problems with the Standard Model

There are several problems with the SM, some of which are detailed in this section. First of all, cosmological observations indicate that there must be vast amounts of an additional source of mass in the universe beyond ordinary matter. This additional source of mass can only interact weakly (if at all) via the SM forces but does feel gravity. This 'dark matter' must be non-relativistic so as to sit in the predicted parts of galaxies (the halos), where observed dynamics don't agree with predictions based on the amount of visible matter alone. There are no SM particles which have the properties that dark matter needs.

Secondly, why is the electroweak scale of $\sim 100\,\text{GeV}$ significantly smaller than the Planck scale ($10^{19}\,\text{GeV}$) associated with quantum gravitational effects becoming significant? Quantitatively one considers the 'technical' hierarchy problem [10]. The experimentally measured mass of the Higgs boson will be different to the 'bare' mass appearing in the SM Lagrangian because of contributions from loop diagrams, as in Figure 1.1. To calculate the contribution of the Higgs mass coming from these loops requires fixing divergent integrals of the propagators over loop momenta with a cut-off scale Λ. This Λ is the scale at which the theory becomes insufficient — where new physics appears! The mass corrections from fermions and bosons become:

$$\delta m_{h,f}^2(\mu) \propto -g_f^2 \left[\Lambda^2 + m_f^2 \ln\left(\frac{m_f}{\Lambda}\right)\right], \quad \delta m_{h,b}^2(\mu) \propto g_b^2 \left[\Lambda^2 + m_b^2 \ln\left(\frac{m_b}{\Lambda}\right)\right], \tag{1.1}$$

where the subscripts f or b indicate bosons or fermions, respectively. If new physics is assumed to appear at the Planck scale, where an explanation for gravity should enter a complete model of particle physics, then the Higgs mass should have a measured value $\gg 125\,\text{GeV}$. To get to the 125 GeV measured at the LHC [11, 12], the bare Higgs mass ($m_{h,0}$) would need to lie around the planck scale also, requiring cancellation or 'fine-tuning' of over 30 orders of magnitude between $m_{h,0}^2$ and δm_h^2.

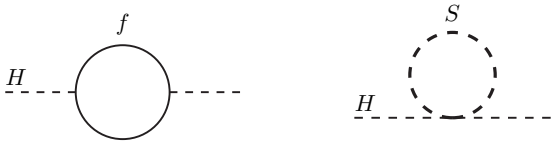

Figure 1.1: Loop corrections to the Higgs boson mass [13].

Thirdly, the SM fails to account for the existence of gravity at all, regardless of its relative weakness. Thus there is no unification of quantum field theory and general relativity. Ideally, the fundamental theory of nature should incorporate both of these ideas. For example, one might expect gravity to have an associated gauge boson mediator, much like the other forces of nature.

Furthermore, neutrinos have been shown experimentally to have a non-zero mass. The SM cannot explain this as it does not contain a right-handed neutrino. It can simply be extended to include them, but the unusually small size of their masses is not explained.

Since the electromagnetic and weak forces unite, it would follow that the electroweak force and strong force should also unite into one unified gauge group at a high energy. This 'grand unification' implies that the SM $SU(3)_C \times SU(2)_L \times U(1)_Y$ is a subgroup of a higher dimensional gauge group, for example $SO(10)$. This class of theory is called a grand unified theory (GUT). Having a GUT would be elegant, potentially lead to a mechanism for neutrino masses and lead to a reduction in the number of free parameters as some become related to reduce to a single gauge coupling. It is useful to look at the gauge couplings as a function of energy (figure 1.2). In the SM, it is clear that the three couplings will not meet at a single point without some additional mechanism to change their dependence on energy.

The final problem with the SM considered in this section is that it does not address why the universe is seemingly filled almost entirely with matter as opposed to a mixture of matter and anti-matter. According to the SM, almost equal amounts of matter and

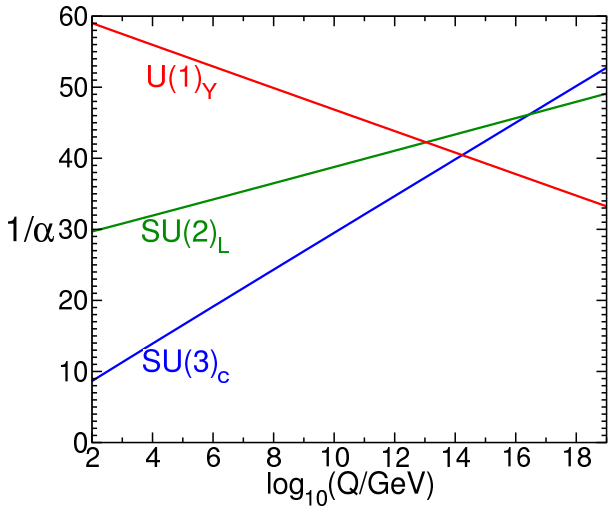

Figure 1.2: SM running couplings as a function of energy [14].

anti-matter are expected to have been created at the beginning of the universe. Where did this anti-matter go? There must be some BSM mechanism which treats matter and anti-matter differently in order to explain the universe's preference for matter. Within the SM itself, there are some mechanisms which prefer matter over anti-matter found in the quark sector. However, these don't cause enough of an imbalance to explain the observed lack of anti-matter in the universe.

1.4 Supersymmetry

> "It is a mistake to think you can solve any major problems just with potatoes"
> — Douglas Adams

SUSY theories are a popular class of BSM theories which can often provide a dark matter candidate [15, 16] and solve the technical hierarchy problem [17–20] if it is broken at the TeV scale [21–26]. The solution to the technical hierarchy problem would provide an explanation for the relative weakness of gravity. It also allows grand unification to occur, and is required for some theories of quantum gravity such as string theory [27].

Essentially, SUSY is a new symmetry based on spin. It relates fermions and bosons by creating a fermion (boson) superpartner particle for each SM boson (fermion). These 'sparticles' have the same quantum numbers (such as electric charge and colour) as

their particle counterparts but have spin differing by one half. A Table of the particles, sparticles and their spins present for the simplest realisation of SUSY is given in Table 1.3. SUSY is invoked before electroweak symmetry breaking occurs so the electroweak superpartners are those of W^1, W^2, W^3 and B rather than $W^\pm, Z^0$ and γ.

SM		SUSY	
Particle	Spin	Sparticle	Spin
gluon	1	gluino	1/2
W^1, W^2, W^3, B	1	wino/bino	1/2
Higgs	0	Higgsino	1/2
lepton	1/2	slepton	0
quarks	1/2	squarks	0
neutrinos	1/2	sneutrinos	0

Table 1.3: SM and SUSY particles.

In order to give all of the sparticles masses, the theory requires two Higgs doublets. After electroweak symmetry breaking this leads to 5 Higgs bosons. The combination of the neutral parts of the two doublets gives the observed SM Higgs boson and another heavier scalar. The SUSY partners of the two Higgs doublets are called Higgsinos. SUSY mass matrices can mix sparticles with the same quantum numbers. This leads to 'charginos' ($\tilde{\chi}^\pm$) which are a mixture of the charged winos and Higgsinos; and 'neutralinos' ($\tilde{\chi}^0$) which are a mixture of neutral bino and Higgsinos. In practice, the production of these mixed chargino or neutralino states are what is searched for at the LHC.

SUSY can solve the technical gauge hierarchy problem as a result of the fermionic and bosonic corrections to the Higgs mass having different signs. If the particles and their sparticles have the same masses then once loop corrections are added for the additional sparticles, all of the loops will cancel leaving the measured Higgs mass equal to the bare Higgs mass. However, since no SUSY particles have been observed, they must be heavier than the SM particles. This means SUSY is a broken symmetry, requiring some additional new physics to break it. Enough cancellation can occur to adequately solve the technical gauge hierarchy problem provided that $|M^2_{\text{fermion}} - M^2_{\text{boson}}| \lesssim 1\ \text{TeV}^2$ for the case of the top/stop and the Higgs/Higgsinos [28]. If this criterion is met then SUSY is 'natural'. The mass differences for the other particles are less important since their Yukawa couplings are smaller so they make a smaller correction to the Higgs mass. It is worth noting that even more 'un-natural' SUSY will still provide some reduction in the

amount of required fine-tuning.

Another consequence of SUSY is the ability to affect the running of the SM force couplings. This allows the possibility of a unification of all of the SM forces at some high energy. This implies that SUSY can provide a basis for a GUT, which was proposed in the previous section, and is desirable as an elegant way to better connect the laws of physics.

An important quantity related to SUSY is R-parity [29]. This is defined in equation 1.2, where s is spin, B is baryon number and L is lepton number. Given that proton decay hasn't been observed and no B or L number violation occurs in the SM, it is sensible to suppose that baryon and lepton number violating interactions are suppressed by new physics and thus that R-parity is conserved. If R-parity was not conserved, the potential for proton decay could still be avoided by only permitting the violation of B or L number, not both. SM particles have R-parity of $+1$ and SUSY particles have R-parity of -1. Thus, in R-parity conserving theories, SUSY particles must always be produced in pairs. This implies that the lightest SUSY particle is stable, and is referred to as the LSP. The LSP can be massive, and doesn't undergo any SM interactions; it is a natural candidate for dark matter.

$$R = (-1)^{2s+3B+L} \tag{1.2}$$

In the electroweak SUSY searches in this thesis, R-parity conservation is assumed. Here the lightest neutralino is taken to be the LSP and is thus a stable dark matter candidate. In the charge-flavour asymmetry search presented in this thesis an R-parity violating (RPV) model is considered instead. Whilst R-parity conservation is initially a sensible assumption, R-parity violating models still provide a potential solution to the technical gauge hierarchy problem. Additionally, a lack of observation of R-parity conserving SUSY suggests that experimentalists should 'cast their net wider' and consider other possibilities.

The simplest SUSY extension to the SM is the Minimal Supersymmetric SM (MSSM). This is an R-parity conserving model. The MSSM must incorporate SUSY breaking but the mechanism for this is unknown, so soft[4] SUSY breaking operators are explicitly added resulting in 105 free parameters. This is a huge amount of phase space to search through experimentally, so the number of free parameters can be reduced by choosing

[4]Here, soft means that the operators results in TeV scale sparticles

a SUSY breaking mechanism. The mechanism determines many properties of SUSY, such as the identity of the LSP (usually a neutralino), sparticle masses and which decay chains are more likely. Overall, whilst eventually the identity of the mechanism should be sought if signs of SUSY are found, it is more practical to first try to make general experimental statements.

There are traditionally two ways to consider SUSY without specifying a particular SUSY model. The most prevalent approach taken by ATLAS is the construction of simplified models. In this case, a small number of parameters are chosen to investigate, which allows a certain SUSY process to be 'switched on' at ATLAS. In this thesis, certain electroweak SUSY process branching fractions are set to be one, and two sparticle masses are set to be free parameters. The 'search' will scan over possible values of these two sparticle masses, individually looking for signs of them within the ATLAS data. All other SUSY parameters are set to have values which will have no visible effects at the LHC. For example, masses of the other sparticles are assumed to be too heavy to be produced at LHC proton-proton collision energies.

Simplified models are a pragmatic way to produce a fairly realistic SUSY model and be able to search over a 2-D plane of SUSY parameter space. Historically, they have been a very sensible way to look for the most obvious ways that a natural SUSY model would appear at the LHC. They provide a realistic final state to drive analysis strategy, and results from these searches are crucial to guide the direction of future searches. Computationally, producing simulated events from multiple simplified models which target various planes of parameter space whilst being well-sampled, is greatly easier than trying to simulate events from a more complete model over the enormous 105 dimensional complete SUSY phase space.

On the other hand, the specific possibilities of sparticle decay from simplified models don't necessarily correspond to what SUSY model parameters ATLAS is able to exclude at 95% confidence level. If results are re-interpreted in some more complete model such as the MSSM, the specific processes searched for often become rarer, and therefore not as strongly excluded by data. It is important to emphasise that this does not invalidate the results of simplified-model-based searches, which stand alone as well as being available for re-interpretation in a variety of BSM models, but means one must be careful when making statements interpreting the results. Optimistically, this implies that SUSY has actually not been ruled out as strongly as many physicists consider. Pessimistically, it also suggests that alternative paradigms for ATLAS SUSY searches could be more useful in the future. In the author's opinion, the ideal approach that should be taken in the

next few years is to focus on broader, more model independent searches aiming to find disagreement with the SM. In addition to the charge-flavour asymmetry search in this thesis which pursues this approach, the author's work beyond this thesis considers this endeavour.

One alternative to simplified models is to introduce the pMSSM (phenomenological MSSM) which makes some experimentally and theoretically motivated assumptions on the free parameters without specifying a breaking mechanism. This leaves only 19 new free parameters. Whilst the searches in this thesis do not directly consider the pMSSM, it is likely that the result obtained in Chapter 5 will be re-interpreted in the context of the pMSSM in combination with many other ATLAS full Run 2 electroweak SUSY results.

1.5 Leptoquarks

An alternative type of BSM model considered in this thesis is 'leptoquarks' [30]. Looking at the Standard Model, one cannot help but see similarities between leptons and quarks. Both have 3 generations of progressively larger mass, and both have two distinct types within each generation which differ in electric charge. It seems reasonable to suppose that there is some deeper connection between leptons and quarks which are responsible for these unexplained similarities. Leptoquarks are one possible way to establish such a connection.

The general idea of this model is to introduce a new heavy boson which permits the direct interaction of quarks and leptons: and is thus called a leptoquark. If quarks and leptons are allowed to interact directly then one can begin to consider unifying them at some high energy as part of a GUT. Critically, leptoquarks allow for the violation of lepton flavour universality, a rule which has been frequently experimentally observed but does not appear to derive from any fundamental symmetry in particle theory. Recent results, such as that from the LHCb experiment described in Reference [31], show signs that lepton flavour universality may not always be obeyed. Thus there is motivation to search for this class of BSM model [32, 33].

In different specific models, leptoquarks can either be scalar (spin-0) or vector (spin-1), and can have different electric charges. In addition to these properties, and the leptoquark's mass, free parameters for a leptoquark model are found in the couplings to

leptons and quarks. These couplings are governed by two coupling matrices, to right and left handed fermions, which can potentially also allow for couplings between generations. These couplings will be limited by the choice of the leptoquark's electric charge, since SM symmetries should still be conserved in these interactions.

In leptoquark searches within ATLAS, generally a specific choice of model (spin and charge) is made. A limited number of couplings are set as non-zero. In analogy with the simplified models discussed in section 1.4, these leptoquark models allow searches to scan over possible values of the leptoquark mass and the one or two non-zero couplings.

Leptoquark models are not necessarily distinct from other BSM models, which may include a heavy boson permitting the direct interaction of quarks and leptons but not name such a boson as a leptoquark. For example, the R-parity violating SUSY model considered in Chapter 6 involves a smuon which directly interacts with a muon and a top quark. This smuon is thus, technically a leptoquark.

Chapter 2

The ATLAS experiment

2.1 The LHC: One ring to rule them all

The Large Hadron Collider (LHC) is the world's largest machine, spanning a perimeter of 27 km across the Swiss-French border and situated on average 100 m underground. An aerial photograph of the area inhabited by the LHC, the world's largest and highest energy particle accelerator, is shown in Figure 2.1. Whilst it is capable of accelerating and colliding heavy ions such as lead nuclei, and does so during part of the data-taking period, the LHC is primarily a proton accelerator. Protons produced from ionised hydrogen gas enter the linear accelerator LINAC2, and are passed through three stages of acceleration in circular accelerators as shown in Figure 2.2, before being accelerated through the LHC — a two-ring synchrotron — from an energy of 450 GeV up to an energy of 6.5 TeV per beam. These protons are accelerated in beams with up to 2544 bunches per 25 ns interval; each bunch contains around 10^{11} protons. Proton bunches are grouped into so-called trains, with gaps in-between corresponding to how quickly the magnets which kick bunches of protons into the SPS and LHC ramp up and down. Excepting for stone marten related interference, these 6.5 TeV proton bunches are steered and focussed by dipole and quadrupole magnets into four interaction points around the LHC ring, each encompassed by one of four detectors: ATLAS, ALICE [34], CMS [35] and LHCb [36]. This thesis focusses on the proton-proton physics program at the ATLAS detector.

The intensity of the colliding proton beams is proportional to the rate of expected

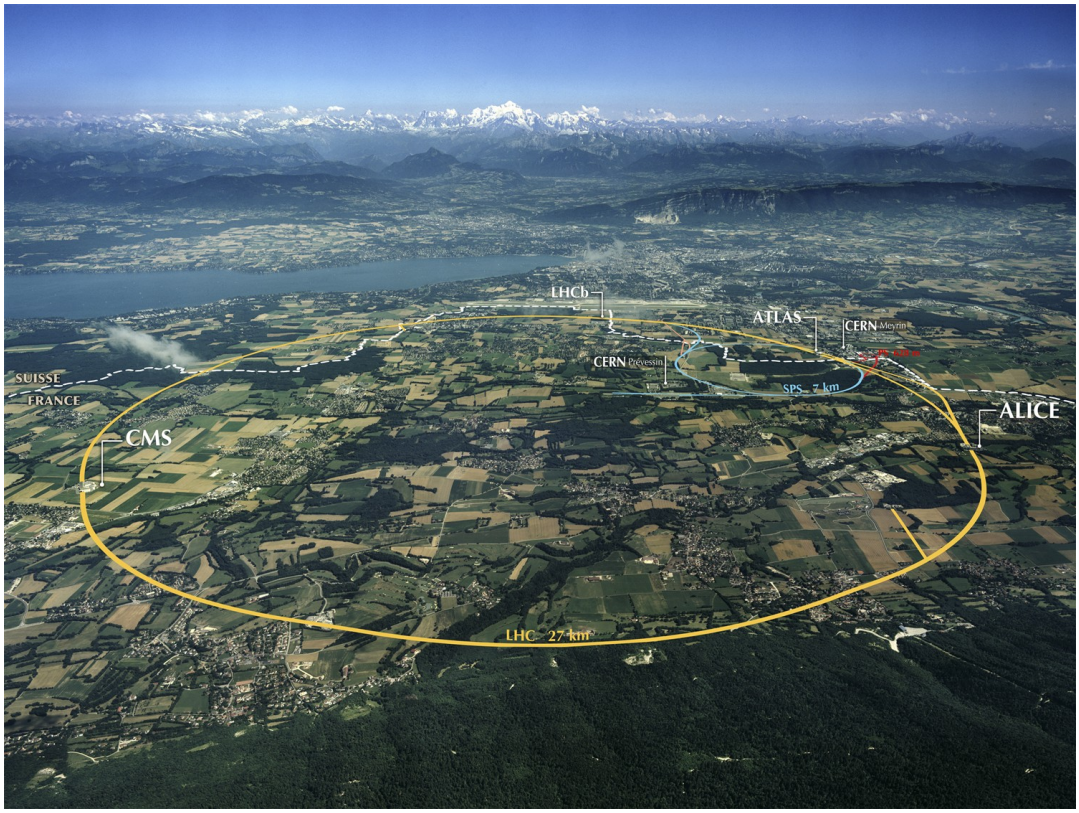

Figure 2.1: An aerial photograph of the area enclosed by the LHC (superimposed in yellow), taken from Reference [37]. The dashed-white line indicates the Swiss-French border, whilst the blue line indicates the acceleration stage preceding the LHC — the Super-Proton-Synchroton (SPS).

interactions (dN/dt); it is quantified by the instantaneous luminosity $\mathcal{L}_{inst}$:

$$\frac{dN}{dt} = \sigma \mathcal{L}_{inst}, \tag{2.1}$$

where σ is the process cross section. In this thesis, the integrated luminosity is more commonly referred to, which is calculated as the integral of the instantaneous luminosity over time: $L = \int \mathcal{L}_{inst}\, dt$. This value is interpreted as a measure of the quantity of data recorded since it is proportional to the number of events available for physics analysis. This thesis analyses proton-proton collision data recorded in ATLAS's 'Run 2' data-taking period, from 2015 to 2018. These collisions occurred with a centre of mass energy of $\sqrt{s} = 13\,\text{TeV}$, and a bunch spacing of 25 ns. The integrated luminosity of data in this period is shown in Figure 2.3a. Overall, $139.5\,\text{fb}^{-1}$ data was produced for analysis in this thesis, with an uncertainty of 1.7% [39].

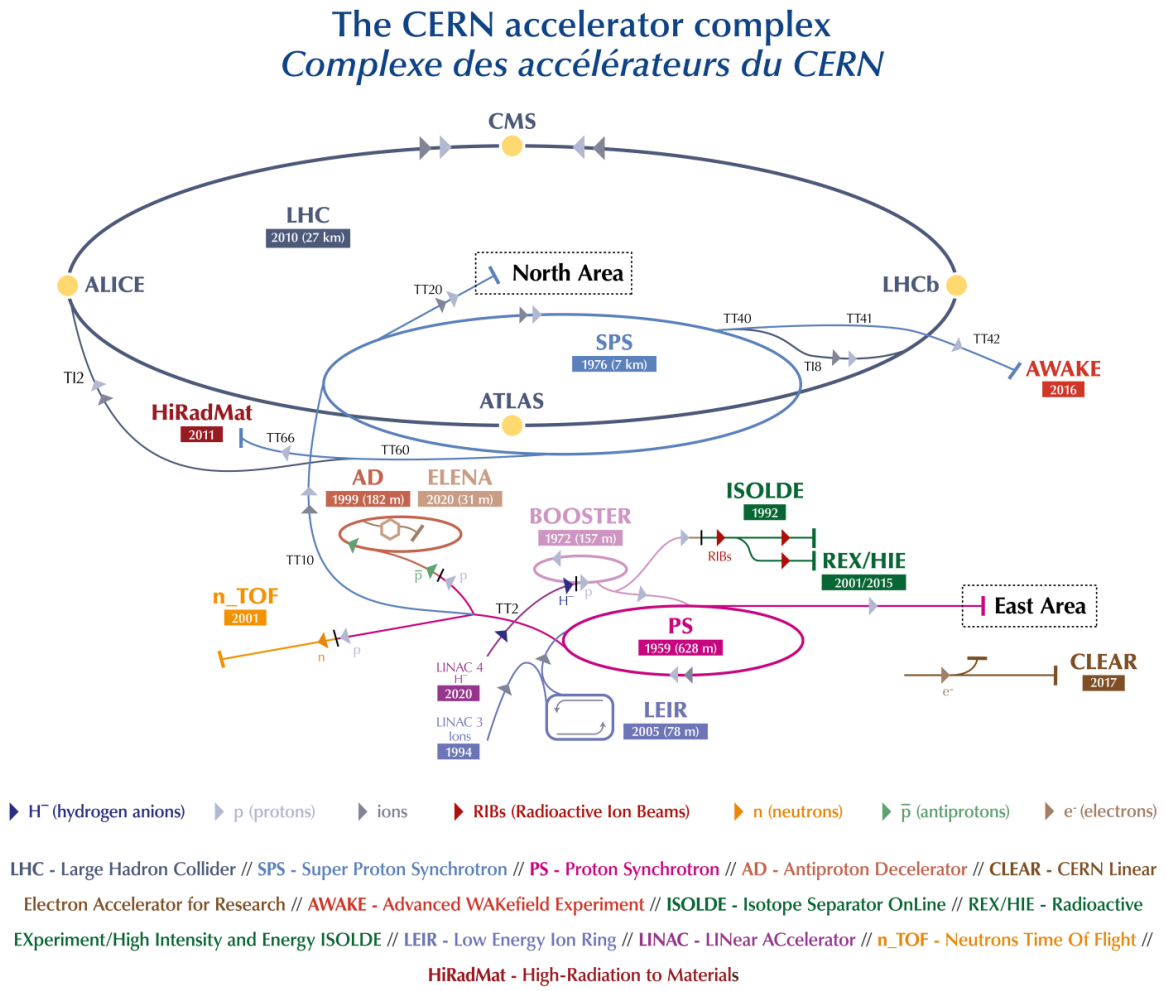

Figure 2.2: A schematic of the various stages of the LHC accelerator chain. For proton-proton collisions, protons are accelerated first by the LINAC2 linear accelerator, and then pass through the BOOSTER, PS (Proton Synchrotron) and SPS (Super Proton Synchroton) before finally arriving at the LHC [38].

The high luminosity of the LHC does however come with a drawback in the form of 'pile-up'. Pile-up appears in two categories: firstly *in-time pile-up* arises from multiple proton-proton collisions occurring in the same bunch and is parametrised by the number of reconstructed 'primary' vertices N_{PV}. Secondly, *out-of-time pile-up* occurs when events are incorrectly identified with those coming from a different bunch due to the rate of detector readout being lower than the rate of bunch crossings. Both categories of pile-up can also be parametrised by the mean number of interactions per bunch crossing $\langle\mu\rangle$. *Out-of-time pile-up* is at a minimum at the beginning of each bunch train and

increases throughout the train. Distributions of the mean number of interactions per bunch crossing are shown for the whole of Run 2, as well as for each year individually, in Figure 2.3b. Pile-up causes an additional background to appear in analyses, with stochastic kinematics and generally lower momentum than the corresponding 'hard-scatter' interactions that analyses are interested in.

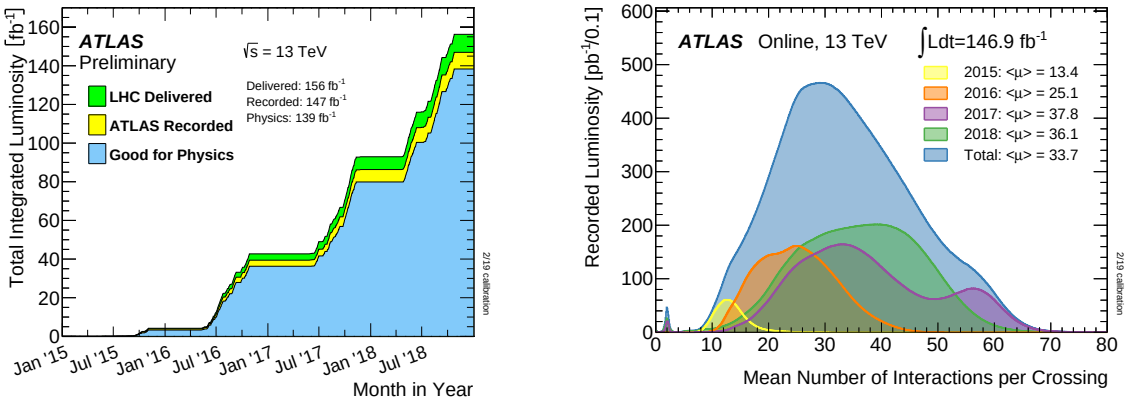

(a) Luminosity collected by ATLAS (b) Pile-up distributions

Figure 2.3: Shown are: (a) the total integrated luminosity delivered by the LHC during 2015-2018 data-taking, or 'Run 2' (green), recorded by ATLAS (yellow), and usable for physics analysis (blue); (b) the luminosity-weighted distributions of mean number of interactions per bunch crossing for each year of Run 2 data taking as well as the total distribution for Run 2. Reproduced from [40].

2.2 The ATLAS detector

2.2.1 Introduction

The ATLAS detector [41] is a general particle detector which covers nearly 4π in solid angle through its forward-backward symmetric cylindrical geometry. It sits at one of the four points of the LHC where two proton beams collide. This point is surrounded by the inner detector (ID), followed by the calorimeter system and finally the muon spectrometer. The overall detector layout is shown in Figure 2.4.

ATLAS adopts a right-handed coordinate system where the origin is defined as the proton interaction point. The x axis of this system is directed towards the LHC's centre, and the y axis points upwards. The system uses cylindrical coordinates (r, ϕ), where $r =$

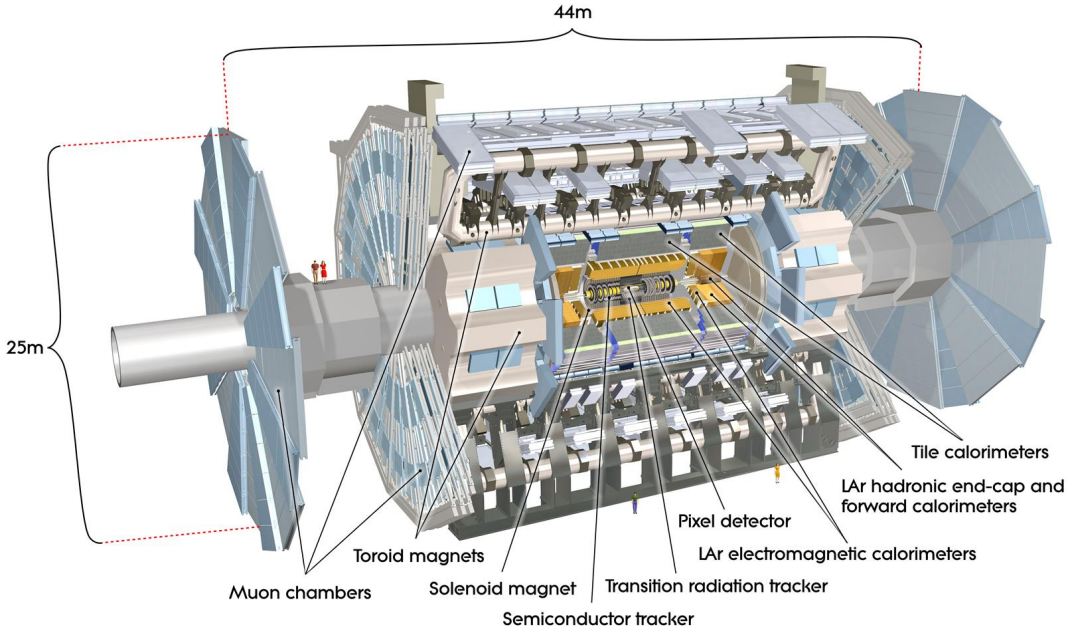

Figure 2.4: Cut-away view of the ATLAS detector. The detector has a height of 25 m and a length of 44 m. It weighs approximately 7000 tonnes [41].

x. Additional useful variables include the rapidity y given by $y = \frac{1}{2}\ln\left((E + p_z)/(E - p_z)\right)$. More commonly referred to is the pseudorapidity, η, defined by $\eta = \ln(\cot(\theta/2))$, where θ is the polar angle from the beam axis (z), which coincides with the rapidity in the case of a massless particle. In hadronic collisions, the hard collisions under study are between partons within each hadron which carry some portion of the hadron's momentum. The resulting longitudinal boost of the underlying partonic interaction is undetermined, motivating the use of variables such as the rapidity, since rapidity differences between two objects are Lorentz invariant under boosts along the z axis. Finally, angular distances are measured using $\Delta R = \sqrt{(\Delta\eta)^2 + (\Delta\phi)^2}$.

The ATLAS experiment was designed to probe a broad range of physics, from the detection and measurement of the Higgs boson to the search for new physics. As such, robust triggering, identification and particle reconstruction are required — all with non-negligible radiation conditions. The heavy states, such as the Higgs boson, expected to be produced within ATLAS, tend to have lower values of $|\eta|$ than from other Standard Model processes that are less interesting to study. As such, ATLAS was chosen to be hermetic in ϕ and has a good coverage up to $|\eta| = 4.9$.

As well as ATLAS itself, it is worth pointing out the existence of LUCID (LUminosity

measurement using Cherenkov Integrating Detector). This was upgraded to become LUCID2 in 2019 [42]. This detector is in two parts, lying $\pm 17\,\text{m}$ from the interaction point, and is designed to detect inelastic proton scattering to allow the measurement of ATLAS's instantaneous luminosity and its corresponding uncertainty. The method for the luminosity calculation used in the search described in Chapter 4 [43], considers calibrations of the luminosity scale using x-y beam-separation scans performed in August 2015, May 2016 and July 2017. The method used for the calculation used in the searches described in Chapters 5 and 6 is described in Reference [39], obtained using the LUCID-2 detector [42].

2.2.2 The inner detector

The ID precisely tracks charged particles, capable of ionising, with $|\eta| < 2.5$. It allows the measurement of the location of multiple interaction vertices, in addition to measuring the direction, transverse momentum and electric charge of these particles. A schematic of the barrel section of the ID is shown in Figure 2.5.

The ID consists of a silicon pixel detector, a silicon microstrip detector (SCT) and a transition radiation tracker (TRT) for $|\eta| < 2.0$. This composition of detector systems was chosen in order to satisfy several driving factors. Firstly, the total amount of material used to build the detector must be as small as possible to limit the probability of multiple scattering. Secondly, a large amount of radiation hardness is required in order for many years of LHC beam operation to be supported. Thirdly, at small radii, a high granularity of tracking is needed in order to correctly resolve multiple overlapping interactions.

These three systems are surrounded by a 2 Tesla axial magnetic field created by a superconducting solenoid, which bends differently charged particles in different directions allowing their charge to be determined. The magnetic bending of charged particles is also crucial to the determination of their momenta.

Overall the ID can reconstruct the transverse component of a particle track's momentum to a resolution of

$$\frac{\sigma(p_{\text{T}})}{p_{\text{T}}} = 0.05\% \frac{p_{\text{T}}}{\text{GeV}} \oplus 1\%. \tag{2.2}$$

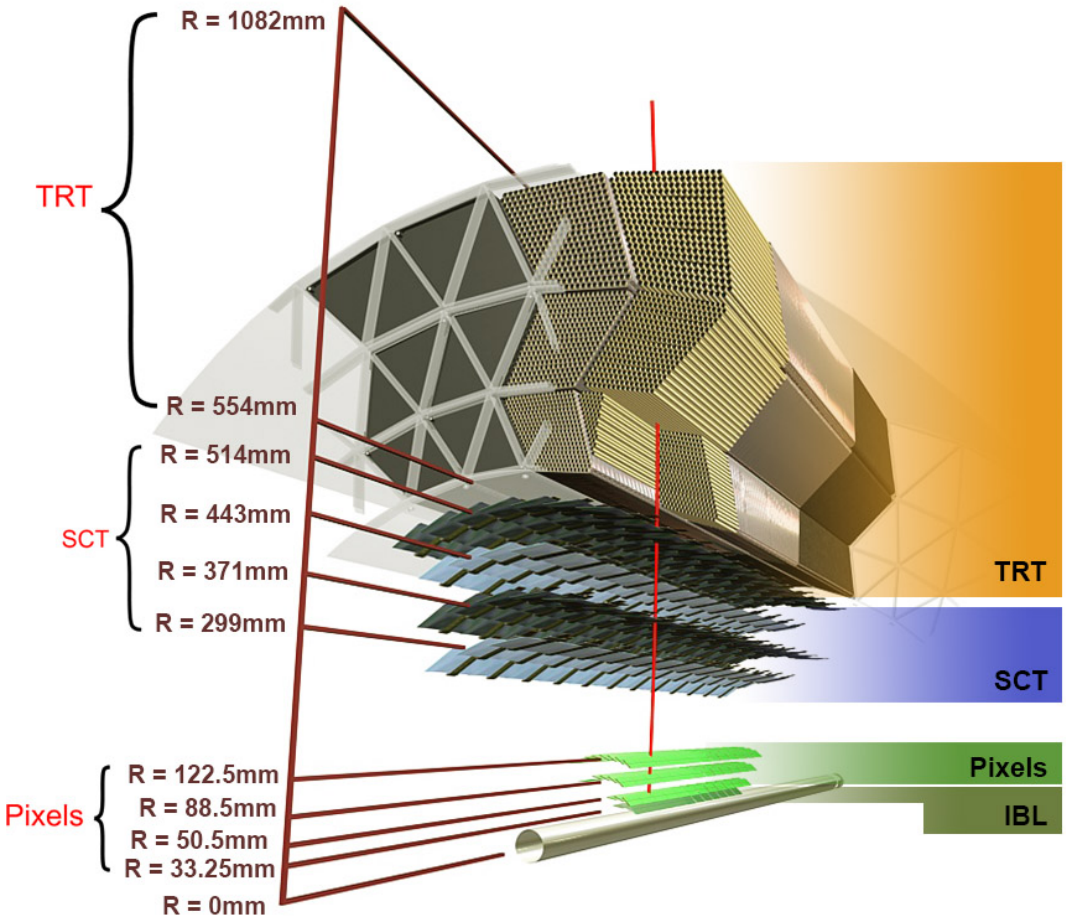

Figure 2.5: Cut-away view of the ATLAS inner detector barrel section [44].

The silicon pixel detector

The innermost detector region is filled with silicon pixels in the form of reverse-biased diodes. When a charged particle passes through a pixel, electron-hole pairs are created, charge is collected on the silicon surface, and a binary "hit" or "no-hit" decision is read out.

These pixels, each usually of dimension $50 \times 400\,\mu m^2$, are arranged in four cylindrical barrel layers, with three layers of discs situated at each end. The three barrel layers range in radius from 5 cm to 12 cm. This set-up provides adequate resolution to resolve many interaction vertices. Furthermore, they are able to resist high levels of radiation.

In 2013–2014, an insertable B-Layer was installed [45]. This additional layer of pixels at 3.3 mm radius, a slightly smaller radii to the original three pixel layers, allows

much higher resolution hits at small radii — improving tracking performance. After the addition of this layer, the intrinsic resolution in the barrel region is 10 µm in $R\phi$ and 115 µm along z [41].

The semiconductor tracker

Radially beyond the pixel detector lies the SCT. Since the coverage area here is larger, continuing to use silicon pixels would be overly expensive and have an impractically high read-out bandwidth. However, a good measurement of the bending plane of the axial field needs to be maintained. Here this requirement is met at the expense of z direction information, by using pixel layers in the form of 6 or 12 cm long strips. These are pitched at 80 µm and arranged into four cylindrical barrel layers at radii 30–51 cm. Additionally there are nine discs on each end.

Within each module lies a pair of sensors, mounted at a 40 mrad stereo angle to allow for some sensitivity along the strip's length. The SCT's resultant resolution is 17 µm in $R\phi$ and 580 µm in z for the barrel layers [41].

The transition radiation tracker

Following the SCT radially outwards, the TRT is met next. This extends the ID's tracking capabilities out to 1 m, within an acceptance of $|\eta| < 2$.

The TRT is built using polyamide straw tubes, each of 4 mm in diameter and filled with a mixture of oxygen, xenon, argon and carbon dioxide gasses. The straw is held at a 1.6 kV potential difference from its central wire. Within these tubes, a charged particle will ionise the gas mixture, resulting in a charge collected by this potential difference. The straws provide no position measurement along their length.

Straws up to 144 cm long, running parallel to z and with a gap at $z = 0$, lie in the barrel region. In the end-cap region, 37 cm long straws are positioned radially about the beam axis. Drift time information is also included in the tracking measurements, which allows an overall resolution of 130 µm in the $R\phi$ direction [41].

Between the straw detectors, abrupt variations of the medium's refractive index are caused by a system of polypropylene fibres and foils. Particles traversing this space can therefore emit transition radiation — with different properties depending on the traversing particles. This provides some particle identification, for example distinguish-

ing electrons from pions.

2.2.3 The calorimeters

The purpose of the ATLAS calorimeter system is to measure the energies of charged and neutral particles. 'Sampling' calorimeters are used, where the active medium and dense passive medium are produced from different materials. Particles incident on the dense, passive 'absorber' material layers shower to produce a cascade of other particles such as electrons and photons. These particles then ionise the 'active' material. The resulting electrons are drawn into anodes in-between the layers of absorber, and the charge produced is read out as signal. The magnitude of the signal coming from a particle shower is proportional to the energy of the original incident particles. The calorimeters are segmented in the transverse direction to allow the determination of the energy deposit's position. The calorimeters are segmented in the z-direction to provide measurements of the shower shape, which is used to aid particle identification.

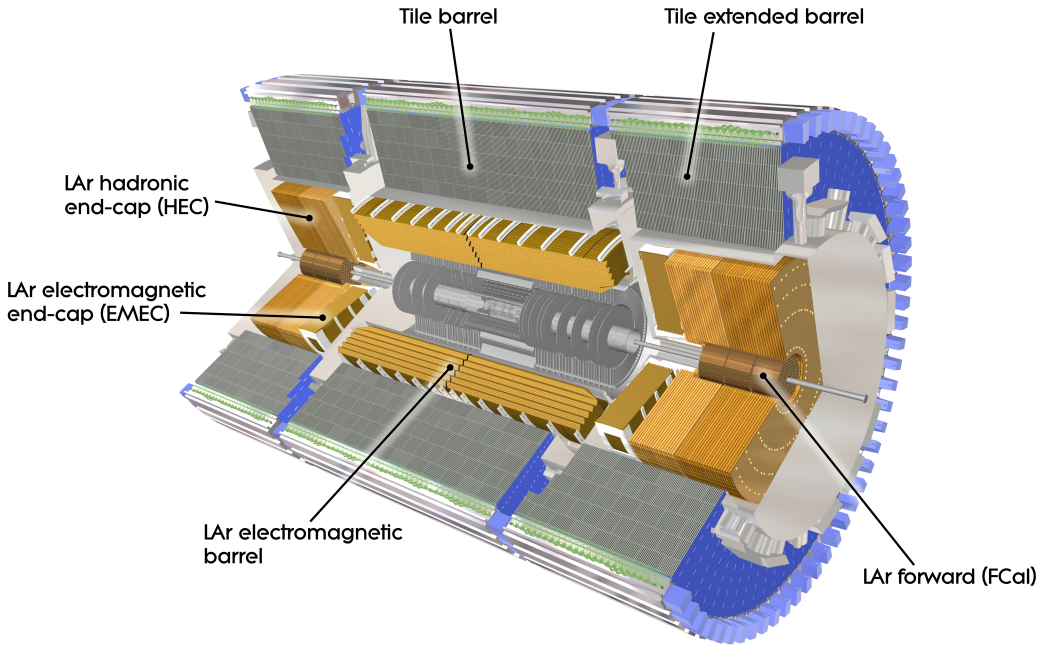

Figure 2.6: Cut-away view of the ATLAS calorimeter system [41].

A schematic of the ATLAS calorimeter system is shown in Figure 2.6. This consists of two separate systems. As one moves radially outwards, the first calorimeter system

encountered is the liquid argon (LAr) electromagnetic (EM) calorimeter system, just outside of the solenoid magnet. Beyond this lie the hadronic calorimeters, which make use of a range of technologies. In total, the calorimeter system effectively contains the entirety of ATLAS's particle showers, with very low leakage into the muon spectrometer outside.

The liquid argon EM calorimeter

The liquid argon calorimeters use lead absorber and a liquid argon active medium. They are divided into a barrel section covering $|\eta| < 1.5$, and end-caps allowing coverage of $1.4 < |\eta| < 3.2$. The barrel section is once again divided into three main layers. Discrimination between electron- and photon-initiated showers is provided by longitudinal shower development information from these three layers.

The innermost layer is divided into 4 mm strips in η, a granularity fine enough to distinguish between photons and electrons coming from neutral and charged pions. Since pions are the most commonly produced particles at the LHC, this discrimination power is of particular importance. The middle and outermost layers have 'towers' of dimension 0.025×0.025 and 0.05×0.025 in $\eta - \phi$, respectively. This granularity is ideal for distinguishing neutral signatures.

The EM calorimeter's energy resolution is approximately described as

$$\frac{\sigma_E}{E} = \frac{a}{E} \oplus \frac{b}{\sqrt{E}} \oplus c. \tag{2.3}$$

The first term on the right-hand side of this equation describes electronics noise and the energy deposits of many soft particles produced in pile-up interactions. A value of $a \approx 0.4\,\text{GeV}$ [46] well fits this combined effect. The second term that arises is stochastic, and is caused by poisson fluctuations in shower development. This term is small for homogenous calorimeters but for sampling calorimeters takes into account fluctuation in sampling. A value of $b \sim 10\% \sqrt{\text{GeV}}$ is appropriate here [41], which dominates the resolution at low energies. The third term is most significant at high energy. The constant $c \sim 0.7\%$ arises from levels of uniformity in detector construction [41].

The hadronic calorimeters

Radially beyond the EM calorimeters, one next meets the hadronic calorimeter system. Over a wide range of pseudorapidity, multiple technologies are used to achieve good energy resolution in different radiation conditions.

In the most central region, for $|\eta| < 1.7$, the tile calorimeter is found. This is used to measure the energies of hadrons, using a series of interleaved layers of steel absorbers and plastic scintillator sheets. Photons produced from the interactions of charged particles in the scintillator tiles are collected by wavelength-shifting optical fibres and transmitted into signals by photomultiplier tubes. There are again three layers in the most central region, in the form of cylinders around the LAr calorimeter. There is a central three-layer cylinder up to $|\eta| = 1.0$ and an extended barrel covering $1.0 < |\eta| < 1.7$. For the first two layers, these barrels are each segmented into towers of size 0.1×0.1 in $\eta - \phi$; for the outermost 0.2×0.1.

For $1.5 < |\eta| < 3.2$, end-cap hadronic calorimeters (HEC) are designed using copper absorbers with a liquid argon active medium. In this more forward region, the calorimeter is closer to the high-radiation environment of the beam-pipe, and thus the more radiation-hard LAr calorimeters are a more appropriate choice of technology than a tile calorimeter. For these end-caps, the tower dimensions are 0.1×0.1 up to $|\eta| = 2.5$, and dimension 0.2×0.2 beyond.

The energy resolution for the tile calorimeter and HEC can also be parametrised using equation 2.3. In this case, the parameters best describing each term are $0.5\,\text{GeV} < a < 1.5\,\text{GeV}$ (depending on $|\eta|$), $b \approx 60\% \sqrt{\text{GeV}}$ and $c \approx 3\%$ [41].

For $3.1 < |\eta| < 4.9$, a separate LAr calorimeter is found (the FCal), this time using dense tungsten as the absorber material. Other than contributing to measurements of the missing transverse momentum, the FCal is not used to detect the objects used in this thesis and will thus not be described in more detail.

2.2.4 The muon spectrometer

Since muons typically pass through the ID and calorimeters, a 'muon spectrometer' is designed to detect them. This is the outermost layer of the ATLAS detector and consists of a magnet system, precise gas tracking chambers and a fast trigger system. Toroidal magnets of average strength 0.5 Tesla and 1 Tesla are situated in the barrel and end-cap

regions, respectively [47].

Precision tracking chambers

The curvature of muon tracks in the magnet system allows the measurement of muon momentum. Precise measurement of the curvature in the $R-z$ bending plane is provided by two sub-detector systems.

Monitored drift tubes (MDTs) filled with argon and carbon dioxide gasses provide most of the tracking. In the barrel region, three concentric layers of MDTs are placed at radii of 5 m, 7.5 m and 10 m. These are divided into sixteen overlapping sections in the azimuthal direction. At $z = 0$, some tracking coverage is lost due to a gap in the detector where cabling is passed into the inner subsystems. In the end-cap region, four 'wheels' of MDT are situated perpendicular to the beam axis, 7.4 m to 21.5 m from the interaction point in the z-direction.

In the region of the detector expected to have the highest traffic of muons, from $2.0 < |\eta| < 2.7$, better timing and flux requirements are needed, thus the MDTs are joined by cathode strip chambers (CSCs). Whilst MDTs have a timing resolution (maximal drift time) of 700 ns, the CSCs have a much shorter drift time of 40 ns. These are multiwire proportional chambers, placed in orthogonal orientations, where the cathodes are split into smaller strips to localise ionisation. The combination of orthogonal position information allows hit coordinates to be determined.

Overall, the combination of the MDT and CSC tracking systems reach a resolution of 35-49 µm per chamber in the $R-z$ bending place. This corresponds to roughly a 10% accuracy of momentum measurement up to a few TeV [41].

Fast trigger chambers

To achieve an adequate read-out rate for triggering within the 25 ns spacing of proton bunches, separate sub-detectors must be used. Within the barrel region, resistive plate chambers (RPCs) are used. Each of these chambers consists of a pair of parallel resistive plates, 2 mm apart, held at a potential differences of 4.9 kV/mm. When ionising particles pass between these plates, avalanches form leading to detection. The RPC system has a rapid response time of 1.5 ns.

In the end-cap region, thin gap chambers (TGCs) extend up to $|\eta| = 2.4$. These are

multiwire proportion chambers where the separation between adjacent wires is greater than the distance from the wire to the cathode. As the magnetic field in the forward region is weaker, the smaller pitch provided by TGCs is required for sufficient pattern recognition and measurement of muon momentum. The TGC system has a response time of 4 ns [41].

2.2.5 The ATLAS trigger system

Within detector bandwidth constraints, it is impossible to read-out and retain every proton-proton collision event in ATLAS as they occur at a rate of 40 MHz. ATLAS selects the most interesting events using a two level trigger system [48]. The first-level trigger uses detector information from the calorimeters and muon spectrometer. It is implemented in hardware, and reduces the event rate to about 85 kHz. The second-level is software based and can run offline, reducing the event rate to about 1 kHz.

Events used in the analyses described in this thesis are required to pass a di-lepton or mixed-lepton trigger selection. The selection of lepton (e/μ) $p_{\mathrm{T}} > 25\,\mathrm{GeV}$ ensures that all trigger efficiencies are constant and above threshold.

2.3 Object reconstruction

The many detector systems described in this Chapter all work towards one goal: to identify and reconstruct all interacting, stable particles produced in proton-proton collisions. This is necessary for ATLAS to work as a general particle detector, capable of sensitivity to a wide range of Standard Model — and hopefully beyond the Standard Model — processes. Once reconstruction is complete, particles ready for use in physics analysis are referred to as 'Physics Objects' in ATLAS jargon. This section provides an overview of the reconstruction methods for the physics objects focused on in this thesis. Details about the specific requirements made for objects used in this thesis' analyses can be found in Sections 4.3 and 6.5.

Before this overview, it is worth defining what is meant practically by an 'event'. Theoretically, an event refers to a single proton-proton collision. However in practice, since there are many proton-proton collisions per bunch crossing and the detector suffers the curse of pile-up, care must be taken to associate different physics objects to different

events. Charged particles emerging from collisions points with $p_{\mathrm{T}} > 0.5\,\mathrm{GeV}$ are reconstructed as tracks in the ID. The trajectories of these tracks will point towards some given origin; if two or more particles point towards a single origin then an interaction vertex can be defined. The primary vertex (PV) of a bunch crossing can then be defined as the vertex with the largest $\sum p_{\mathrm{T}}^2$ of tracks associated to it. The event is then defined by all of the reconstructed objects associated to the PV.

2.3.1 Electrons

Electrons are identified through a combination of information from the EM Calorimeters and ID. Firstly, an ID track is required. Where this track's trajectory meets the calorimeter, a nearby calorimeter cluster should be found. These calorimeter clusters (variable-sized 'superclusters') are formed from deposits of energy ('showers') [49].

To fully reconstruct an electron, more stringent requirements are made on the cluster and track properties. A likelihood-based discriminating variable is built based on the shower shape and degree of leakage into the hadronic calorimeters. This allows the definition of multiple levels of electron purity, commonly referred to as 'working points' [50].

An additional method of discriminating between electrons coming from the hard interaction and secondary decays or pile-up is isolation. These also suppress contributions from conversions, jets wrongly identified as electrons, or electrons originating from decays of heavy-flavour hadrons. Isolation working points are defined using transverse momentum dependent requirements on the ratio of the electron's energy or momentum to the rest of the energy or momentum in a surrounding region. This region is defined as a cone surrounding the electron, where the energy and momentum are calculated by summing contributions from topological clusters and tracks, respectively.

2.3.2 Hadronic jets

When quarks or gluons are produced in collision events, due to the properties of the strong force, they do not remain as stable isolated particles. Instead, they undergo a process called hadronisation where a shower of composite particles called hadrons are produced. In ATLAS jargon these showers of particles are called 'jets' and are primarily detected in the hadronic calorimeters. Two different jet reconstruction algorithms are

used in this thesis: 'EMTopo' jets and Particle Flow, or 'PFlow', jets [51]. Initially, ATLAS used EMTopo jets as default, and this algorithm is used for the electroweak supersymmetry searches described in this thesis. However, in the higher pile-up conditions present in later years of data-taking, PFlow performs better and has become the ATLAS default in 2019. The PFlow algorithm is used in the charge flavour asymmetry search described in Chapter 6.

To identify one jet from the shower of energy deposits it creates using the EMTopo algorithm, groups of neighbouring cells which meet a required signal to noise ratio form topological clusters [52]. These clusters are then combined using the anti-k_{T} algorithm [53] using a radius parameter of 0.4.

The PFlow algorithm [51] differs by also making use of tracking information. In cases where the tracker is expected to perform better than the calorimeters, hadronic showers are first identified from the tracks. One example is when jet constituents, predominantly charged pions, have transverse momentum below $\sim 20\,\mathrm{GeV}$, in which case the tracker provides a better momentum measurement than the calorimeters. The calorimeter deposits which match these tracks are removed to avoid double counting, and then the final jet is built from the remaining clusters and tracks, still using the anti-k_{T} algorithm with a radius parameter of 0.4.

Firstly, charged particle tracks are matched to the PV with a requirement of $|z_0 \sin(\theta)| < 2.0\,\mathrm{mm}$, where z_0 is the longitudinal impact parameter. Secondly, calorimeter energy clusters are included, which have survived an energy subtraction algorithm to remove the energy deposits from the particles that are included instead as tracks.

The energy and resolution of jets must be calibrated. One example reason for this is the fact that any electrically neutral components of the hadronic shower will not be detected by the calorimeter. The reconstructed jets are calibrated by the jet energy scale (JES) derived from 13 TeV data and simulation [54].

In the electroweak supersymmetry searches described in this thesis, the ability to distinguish hadronic jets produced from b quarks is used. b quarks have a longer lifetime than other quarks so decay a few hundred µm from the primary vertex, where the proton-proton interaction occurs. The ID tracking systems have sufficient resolution to distinguish jets initiated at this distance from the primary vertex with a reasonable success rate [55]. The MV2C10 boosted decision tree algorithm [56] identifies these "b-tagged jets" or "b-jets" through the use of quantities such as the impact parameters of associated tracks and positions of any good reconstructed secondary vertices. A selection

that provides 85% efficiency for tagging b-jets in simulated $t\bar{t}$ events is used.

To ensure good jet quality after reconstruction, jets which are likely to have originated from pile-up are identified and removed by the 'Jet Vertex Tagger' [57]. This is applied to jets with $|\eta| < 2.4$, and $p_{\mathrm{T}} < 60\,\mathrm{GeV}$ for the analyses in Chapters 4 and 5. This reduces the contribution of jets from pile-up to 1%, with an efficiency for pure hard scatter jets of 92%. For the analysis in Chapter 6 this is loosened to $p_{\mathrm{T}} < 120\,\mathrm{GeV}$. A similar 'forward Jet Vertex Tagger' is used to identify and remove pile-up jets in the forward region of the detector ($|\eta|$ >2.5) [58].

Finally, events containing a jet that does not pass jet quality requirements [59, 60] are vetoed in order to remove events impacted by detector noise and non-collision backgrounds.

2.3.3 Muons

The muons used in this thesis are reconstructed using combined information from the ID and muon spectrometer. Whilst this means they must all fall within the ID acceptance region of $|\eta| < 2.5$, it provides a more precise measurement of their momentum and robust identification than exclusively using muon spectrometer information.

As with electrons, multiple working points of muon reconstruction purity are defined to suppress backgrounds from hadronic decays whilst reliably measuring prompt muons. These use various requirements on the number of MDT layers the muon hits, in addition to assessing the consistency of the ID tracks and hits in the Muon Spectrometer [61].

Furthermore, isolation working points can be defined for muons [62]. These follow the same approach and motivation as described for electrons.

2.3.4 Event Cleaning

To avoid any double counting of objects in analyses, an overlap removal procedure is applied to the preliminarily (so-called 'Baseline') objects found. Objects surviving this overlap-removal are then subject to more stringent requirements for further use in analysis. The overlap removal employs the following steps:

- jets within $\Delta R = \sqrt{\Delta y^2 + \Delta\phi^2} < 0.2$ of an electron are removed;

- jets with fewer than three tracks which lie within $\Delta R < 0.4$ around a muon are removed;
- electrons and muons within $\Delta R < 0.4$ to the remaining jets are discarded, in order to reject leptons from b- or c-hadron decays;
- electron candidates are rejected if they share a track with a muon.

Good quality data is ensured through the use of a good run list (GRL) selection. Runs are excluded from the GRL if data-taking is compromised, for example by an intolerable problem with a particular sub-detector. Events can also be rejected for other reasons, for example if they contain a muon which might have a cosmic origin. Such muons are defined to be those having a track with longitudinal impact parameter greater than 1.0 mm or a transverse impact parameter greater than 0.2 mm. Events are rejected if they are are thought to contain LAr or Tile calorimeter noise bursts or data corruption. After a 'timing, trigger and control' restart incomplete events can be produced (i.e. events which fail to record information from one or more parts of the detector). Such events are checked for and removed. Events are rejected if they contain a jet that shows evidence of having come from detector noise or non-collision backgrounds (for example from cosmic ray muons being mis-reconstructed as jets).

As introduced in Section 2.1, pile-up plays an important role in data, and can be quantified by the average number of interactions per bunch crossing, $\langle\mu\rangle$. The yearly average level of this is $\langle\mu\rangle = 14$ in 2015, $\langle\mu\rangle = 25$ in 2016, $\langle\mu\rangle = 38$ in 2017 and $\langle\mu\rangle = 36$ in 2018. The Monte Carlo samples are re-weighted to match the pile-up distribution in data.

2.3.5 Missing Transverse Momentum

One of ATLAS's main aims, which is explored in this thesis, is to discover the production of weakly-interacting, stable, massive new particles. Unfortunately, ATLAS cannot directly detect these. Nor is it capable of directly detecting neutrinos, which do not interact with any of the detector materials and escape ATLAS as invisible particles. However, in proton-proton collisions momentum is conserved. Whilst the initial net momentum of the partons in the z direction is unknown, it can be assumed that there is no initial transverse momentum. Due to ATLAS's hermetic design, the final transverse momentum of detectable particles can be measured. Since the sum of of transverse mo-

menta of the detectable and invisible final state particles should equal zero, the sum of the transverse momenta of the invisible particles can be inferred.

This quantity is called the missing transverse momentum ($p_{\mathrm{T}}^{\mathrm{miss}}$) [63], and is defined as the magnitude of the missing transverse momentum vector, the negative vector sum of the objects in the event:

$$\mathbf{p}_{\mathrm{T}}^{\mathrm{miss}} = -\sum_{\text{visible}} \mathbf{p}_{\mathrm{T}} = \sum_{\text{invisible}} \mathbf{p}_{\mathrm{T}}. \tag{2.4}$$

To calculate this quantity in practice, we consider a vector sum including each of the reconstructed physics objects in the event as so:

$$\mathbf{p}_{\mathrm{T}}^{\mathrm{miss}} = -\sum \mathbf{p}_{\mathrm{T},\mu} - \sum \mathbf{p}_{\mathrm{T},e} - \sum \mathbf{p}_{\mathrm{T},\gamma} - \sum \mathbf{p}_{\mathrm{T,jets}} - \mathbf{p}_{\mathrm{T}}^{\mathrm{soft}}. \tag{2.5}$$

The use of separate terms here allows the calculation to benefit from the better momentum resolution of photons and electrons relative to jets. To avoid any double counting of tracks or calorimeter deposits, these terms are added in the order given in the equation, and once added the tracks or cluster energy is removed from the remaining physics objects. This vector sum of hard, reconstructed physics objects is called the hard term, with magnitude $p_{\mathrm{T}}^{\mathrm{hard}}$. Finally, a so-called 'soft term' ($p_{\mathrm{T}}^{\mathrm{soft}}$) is constructed from any remaining tracks, and jets with $p_{\mathrm{T}} < 20\,\mathrm{GeV}$ that are not associated to any physics object. This is technically referred to as the track soft term, in contrast to the calorimeter soft term which was used in the first run of ATLAS data taking and used leftover calorimeter deposits, rather than tracks. The track soft term has a better resolution in the higher pile-up conditions of Run 2, since only tracks associated to the primary vertex are added. This reduces the contamination from pile-up entering the calculation. The benefits to this pile-up-resistance outweigh the downside that the track soft term cannot count the electrically neutral component that leaves calorimeter deposits but not tracks.

It is important to note that $p_{\mathrm{T}}^{\mathrm{miss}}$ unfortunately does not always exclusively arise from the production of an invisible stable particle. Since it is calculated from physics objects, any mis-measurement in these can result in an imperfect balance between the momenta, resulting in the appearance of so-called fake $p_{\mathrm{T}}^{\mathrm{miss}}$. Tracks incorrectly associated to the event which are actually from pile-up will be included in the soft term. Again this can upset the momentum balance of the event and lead to fake $p_{\mathrm{T}}^{\mathrm{miss}}$.

One key aspect of using missing transverse momentum in analysis is the construction of uncertainties on the calculation of the soft term. The author calculated all values of the soft term systematic uncertainties used in this thesis, as discussed in Section 2.4.

Finally, it should be noted that there are different $p_{\mathrm{T}}^{\mathrm{miss}}$ 'working points'. These include different levels of stringency in the jet definition to reduce pile-up dependency by different amounts. As the level of stringency increases, the efficiency of the jet selection is reduced so there is a compromise to be made. In most cases it is sufficient to use the default `Tight` working point, which requires jets with $|\eta| > 2.4$ to have $p_{\mathrm{T}} > 30\,\mathrm{GeV}$ to enter the jet term. Jets that fail this selection can enter the soft term. This working point is used for all the analyses in this thesis.

2.4 Improvements to the missing transverse momentum uncertainty calculation for the full Run 2 dataset

As introduced in Section 2.3.5, $p_{\mathrm{T}}^{\mathrm{miss}}$ is an important quantity for ATLAS physics analysis. Ensuring that uncertainties in the $p_{\mathrm{T}}^{\mathrm{miss}}$ calculation are accurately measured and propagated into analysis results is, thus, also important. As $p_{\mathrm{T}}^{\mathrm{miss}}$ is a topological quantity constructed for each event, its uncertainty is computed using the systematic uncertainties associated to each object entering the construction. For the hard component of $p_{\mathrm{T}}^{\mathrm{miss}}$ coming from reconstructed physics objects such as electrons and jets, the uncertainties are calculated for the reconstruction of those objects separately and propagated to the $p_{\mathrm{T}}^{\mathrm{miss}}$ during its reconstruction. For the soft term, on the other hand, separate uncertainties must be calculated. For most Run 2ATLAS physics analyses involving $p_{\mathrm{T}}^{\mathrm{miss}}$ published since 2017, the soft term uncertainties were produced by the author.

The soft term uncertainty is assumed to be dominated by how well it is modelled by Monte Carlo simulation. To understand the uncertainty, one would ideally like to access a source of events with no intrinsic $p_{\mathrm{T}}^{\mathrm{miss}}$. The closest example available are $Z \to ee$ events. Here, the soft and hard term vectors should theoretically perfectly balance to ensure that $\mathbf{p}_{\mathrm{T}}^{\mathrm{miss}} = -\mathbf{p}_{\mathrm{T}}^{\mathrm{soft}} - \mathbf{p}_{\mathrm{T}}^{\mathrm{hard}} = 0$ if the soft term is perfectly reconstructed. In practise detector resolution effects will spoil this balance, as well as the fact that any neutral component to the soft term is missed, and so one may end up reconstructing a non-zero value of $p_{\mathrm{T}}^{\mathrm{miss}}$: fake $p_{\mathrm{T}}^{\mathrm{miss}}$.

The uncertainty in the soft term reconstruction can be calculated by considering

how well this expectation of perfect balance is met. Quantitatively, one can consider the projection of the soft term onto the hard term. This leads to three variables that are used to study the soft term modelling, which can be defined with the help of Figure 2.7. The three variables comprise the soft term systematic uncertainties. These are:

- the parallel scale (Δ_L) — defined as the mean of the parallel projection of $p_{\mathrm{T}}^{\mathrm{soft}}$ along $p_{\mathrm{T}}^{\mathrm{hard}}$, $\langle p_{\parallel}^{\mathrm{soft}} \rangle$;
- the parallel resolution ($\sigma_{\parallel}$) — defined as the root-mean-square of $p_{\parallel}^{\mathrm{soft}}$;
- and the perpendicular resolution ($\sigma_{\perp}$) — defined as the root-mean-square of the perpendicular projection of $p_{\mathrm{T}}^{\mathrm{soft}}$ along $p_{\mathrm{T}}^{\mathrm{hard}}$, $p_{\perp}^{\mathrm{soft}}$.

The perpendicular scale was found to be consistent with zero in both Monte Carlo and data in Reference [64], so is not of interest.

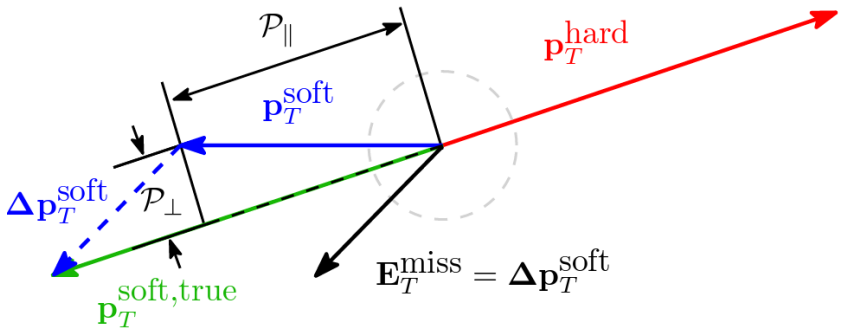

Figure 2.7: $p_{\mathrm{T}}^{\mathrm{soft}}$ projections along $p_{\mathrm{T}}^{\mathrm{hard}}$ [65].

The values of these variables are calculated by computing the maximal disagreement between the data and different Monte Carlo generators, in different bins of $p_{\mathrm{T}}^{\mathrm{hard}}$. Two different event topologies are also considered. Firstly the so-called jet inclusive topology, where $Z \to ee$ events are selected by requiring two electrons with an invariant mass of 66.2 – 116.2 GeV. Here no additional requirements are placed on the multiplicity of hard jets (those of $p_{\mathrm{T}} > 20$ GeV) in the event. Secondly, the so-called jet veto topology is considered, where the same requirements are made as before, with the addition of requiring that no hard jets are present in the event. The finer details of the soft term uncertainty calculation vary between the two iterations described in the remainder of this section.

2.4.1 Partial Run 2 uncertainties

The author's ATLAS qualification task included calculating values of the track soft term uncertainties using the 2015–2016 dataset and corresponding Monte Carlo simulation. These uncertainties were used for the analyses described in this thesis, among many others. To get a full picture of how the soft term modelling changes throughout the $p_{\mathrm{T}}^{\mathrm{hard}}$ distribution, whilst avoiding becoming limited by statistical uncertainties, fine bins of $p_{\mathrm{T}}^{\mathrm{hard}}$ increasing in width up to 50 GeV are used. Above this, one bin is used to capture the high $p_{\mathrm{T}}^{\mathrm{hard}}$ behaviour of the remainder of the distribution.

Separate soft term uncertainties are calculated for EMTopo and PFlow jets. Since the jet definition used determines what jets are used to build the $p_{\mathrm{T}}^{\mathrm{miss}}$, the $p_{\mathrm{T}}^{\mathrm{miss}}$ can change between jet definitions too. The uncertainties are calculated using the `Tight` $p_{\mathrm{T}}^{\mathrm{miss}}$ working point. The uncertainties are calculated by considering the maximal difference between the data and the difference Monte Carlo generators, and taking the maximum of these between both the jet inclusive and jet veto topologies. The uncertainty values are shown for EMTopo in Table 2.1.

$p_{\mathrm{T}}^{\mathrm{hard}}$ bin [GeV]	$\sigma_{\parallel}$ [GeV]	$\sigma_{\perp}$ [GeV]	Δ_{L} [GeV]
0.0–2.5	1.71	1.61	0.09
2.5–5.0	1.86	1.85	0.03
5.0–10.0	1.93	1.99	0.23
10.0–15.0	1.81	1.96	0.40
15.0–20.0	1.68	1.96	0.49
20.0–25.0	1.82	2.09	0.51
25.0–30.0	2.19	2.21	0.57
30.0–35.0	2.23	2.25	0.70
35.0–40.0	2.43	2.44	0.88
40.0–50.0	2.67	2.60	1.07
50.0–200.0	3.82	3.21	1.22

Table 2.1: Partial Run 2 soft term uncertainty values for EMTopo jets.

Similar values of the soft term uncertainties for PFlow are shown in Table 2.2. For the three variables, the uncertainties increase slightly with $p_{\mathrm{T}}^{\mathrm{hard}}$. Below ~ 20 GeV, the uncertainties are dominated by the jet veto topology where the Z is directly balancing the soft term; all jets with a p_{T} below 20 GeV enter the soft term. Above this, the jet inclusive

selection starts to dominate, where the soft term consists mainly of diffuse radiation which hasn't formed jets. Here the soft term in the jet veto topology consists mainly of hard jets which have been vetoed by the Jet Vertex Tagger. The PFlow jet reconstruction algorithm applies more vertexing constraints than in EMTopo jets, leading to a general reduction in the p_{T} of reconstructed jets. This means the events tend to have a lower value of $p_{\mathrm{T}}^{\mathrm{hard}}$ and thus the higher $p_{\mathrm{T}}^{\mathrm{hard}}$ bins have more statistical uncertainty, leading to larger uncertainties. For EMTopo jets, the perpendicular resolution dominates the uncertainty for the bulk of the $p_{\mathrm{T}}^{\mathrm{hard}}$ distribution, whilst the parallel resolution dominates for high and low values of $p_{\mathrm{T}}^{\mathrm{hard}}$. For PFlow jets, The parallel resolution dominates the uncertainty.

$p_{\mathrm{T}}^{\mathrm{hard}}$ bin [GeV]	$\sigma_{\parallel}$ [GeV]	$\sigma_{\perp}$ [GeV]	Δ_{L} [GeV]
0.0–2.5	1.90	1.80	0.10
2.5–5.0	1.88	1.85	0.10
5.0–10.0	1.93	1.95	0.21
10.0–15.0	1.92	1.89	0.30
15.0–20.0	1.88	1.83	0.55
20.0–25.0	2.09	2.09	0.75
25.0–30.0	2.48	2.06	0.84
30.0–35.0	2.70	2.15	0.81
35.0–40.0	2.49	2.41	0.96
40.0–200.0	4.21	2.95	1.78

Table 2.2: Partial Run 2 soft term uncertainty values for PFlow jets.

Once the soft term uncertainty values were calculated, they were validated to check they cover the discrepancies between Monte Carlo and Data in different cases. First of all, it was confirmed that the values cover discrepancies for when $Z \to \mu\mu$ simulations are used and a $Z \to \mu\mu$ event selection applied. Next, the effectiveness of the values on the 2017 dataset and corresponding Monte Carlo was checked. Figure 2.8 shows the three variables as functions of the bins of $p_{\mathrm{T}}^{\mathrm{hard}}$ used for the calculations. The 2017 data and corresponding Monte Carlo are shown for the $Z \to ee$ selection, in the jet inclusive topology, and using EMTopo jets. The 2015–2016 uncertainty values are overlaid as a shaded band, and indeed cover the discrepancies. The discrepancies were also confirmed to be covered for the jet veto case, and for PFlow jets. It was later confirmed by a colleague that the uncertainties are also adequately satisfactory for the 2018 dataset,

and for the other $p_{\mathrm{T}}^{\mathrm{miss}}$ working points.

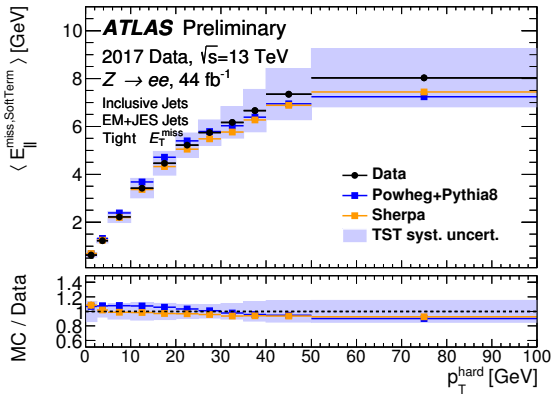

(a) Δ_L

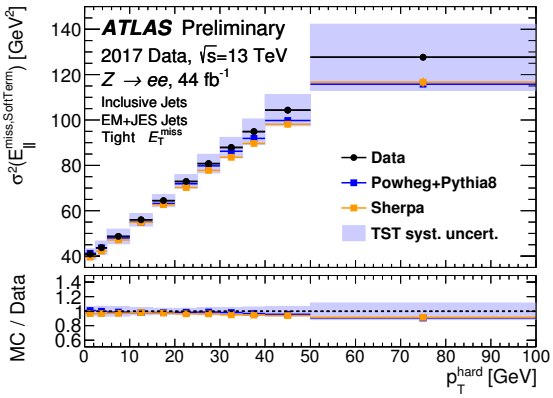

(b) $\sigma_{\parallel}$

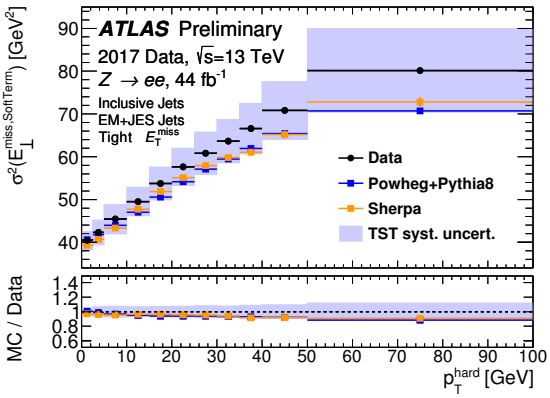

(c) $\sigma_{\perp}$

Figure 2.8: Distributions of the three variables used to calculate soft term uncertainties. Distributions of 2017 data and $Z \to ee$ Monte Carlo samples are shown with a $Z \to ee$ event selection applied. 2015–2016 uncertainties are shown as a shaded band about the data. The distributions are binned in $p_{\mathrm{T}}^{\mathrm{hard}}$.

2.4.2 Full Run 2 uncertainties

Once the full Run 2 data-taking was complete, and various developments had been made to physics object reconstruction and cleaning, it became appropriate to produce a new set of soft term systematics using the full dataset. The increased size of the dataset implies a reduction in the statistical uncertainty of the Monte Carlo, meaning one would expect the size of the soft term uncertainties to be reduced. It also allows a finer binning of $p_{\mathrm{T}}^{\mathrm{hard}}$ to be considered. To avoid any effects from statistical uncertainties

and to improve the data–Monte Carlo agreement, this time Monte Carlo simulations of diboson and $t\bar{t}$ events were added to the various $Z \to ee$ simulations. These events can pass the $Z \to ee$ selection in data, but both include neutrinos in their final state so generally possess some amount of real $p_{\mathrm{T}}^{\mathrm{miss}}$. At the point in the $p_{\mathrm{T}}^{\mathrm{hard}}$ distributions in which these additional processes dominate, the initial assumption of the $p_{\mathrm{T}}^{\mathrm{soft}}$-$p_{\mathrm{T}}^{\mathrm{hard}}$ balance the calculation relies on breaks down. This occurs at around 100 GeV, where the $Z \to ee$ events would require the Z boson to be increasingly off-shell. As a result, the measurement of the soft term uncertainty stops at $p_{\mathrm{T}}^{\mathrm{hard}} = 100\,\mathrm{GeV}$, and the value obtained in the final bin up to 100 GeV is used for any event with a higher $p_{\mathrm{T}}^{\mathrm{hard}}$.

Up to a $p_{\mathrm{T}}^{\mathrm{hard}}$ of 60 GeV, both the jet inclusive and jet veto topologies are considered. Above this, events are more likely to contain hard enough jets for the Jet Vertex Tagger to not be applied, since it is only considered for jets with $p_{\mathrm{T}} < 60\,\mathrm{GeV}$. For lower values of $p_{\mathrm{T}}^{\mathrm{hard}}$ the jet veto topology will primarily consist of events with one hard jet which was cut by the Jet Vertex Tagger, and thus enters the soft term. For higher values of $p_{\mathrm{T}}^{\mathrm{hard}}$ the soft term will be a conflation of multiple effects, including events with two jets which were vetoed by the Jet Vertex Tagger, or events with a large jet p_{T} mis-measurement. The jet veto topology then becomes a less well-defined probe of the behaviour of the soft term, and thus is not used to calculate the soft term uncertainty values.

Again the uncertainty values are calculated using the `Tight` $p_{\mathrm{T}}^{\mathrm{miss}}$ working point and separate values are considered for EMTopo and PFlow jets. The values of the soft term uncertainties calculated for EMTopo and PFlow, respectively, are given in Tables 2.3 and 2.4. As expected, the uncertainties are generally smaller than for the partial Run 2 case. The same trend of increasing uncertainties with $p_{\mathrm{T}}^{\mathrm{hard}}$ is observed, and the jet inclusive topology still dominates the uncertainty values above around $p_{\mathrm{T}}^{\mathrm{hard}} = 20\,\mathrm{GeV}$. Unlike the partial Run 2 results, the PFlow uncertainties are smaller than EMTopo. The increased dataset has reduced the impact of the relatively lower $p_{\mathrm{T}}^{\mathrm{hard}}$ tail size. For both jet collections, the perpendicular resolution dominates the uncertainties for the bulk of the $p_{\mathrm{T}}^{\mathrm{hard}}$ distribution and the parallel resolution dominates at low and high values.

Figure 2.9 shows the three variables for the jet inclusive and jet veto topologies, in the same bins of $p_{\mathrm{T}}^{\mathrm{hard}}$ used for the uncertainty calculation. The distributions are given for data and the different Monte Carlo generators, with the uncertainty values illustrated as a shaded band centred on the data. The uncertainty values cover all of the differences between the data and Monte Carlo. Similar plots are shown in Figure 2.10.

$p_{\mathrm{T}}^{\mathrm{hard}}$ bin [GeV]	$\sigma_{\parallel}$ [GeV]	$\sigma_{\perp}$ [GeV]	Δ_{L} [GeV]
0.0–2.5	1.19	1.14	0.06
2.5–5.0	1.32	1.34	0.12
5.0–10.0	1.40	1.47	0.25
10.0–15.0	1.48	1.76	0.40
15.0–20.0	1.46	1.95	0.51
20.0–25.0	1.46	2.10	0.55
25.0–30.0	1.44	2.19	0.55
30.0–35.0	1.47	2.27	0.52
35.0–40.0	1.75	2.42	0.59
40.0–50.0	2.11	2.55	0.81
50.0–60.0	2.59	2.81	1.34
60.0–70.0	3.51	3.05	1.97
70.0–80.0	4.60	3.30	2.19
80.0–90.0	5.21	3.10	2.29
90.0–100.0	5.55	3.15	2.04

Table 2.3: Full Run 2 soft term uncertainty values for EMTopo jets.

$p_{\mathrm{T}}^{\mathrm{hard}}$ bin [GeV]	$\sigma_{\parallel}$ [GeV]	$\sigma_{\perp}$ [GeV]	Δ_{L} [GeV]
0.0–2.5	1.21	1.18	0.05
2.5–5.0	1.19	1.25	0.12
5.0–10.0	1.23	1.38	0.26
10.0–15.0	1.25	1.58	0.41
15.0–20.0	1.31	1.79	0.50
20.0–25.0	1.23	1.89	0.53
25.0–30.0	1.30	1.94	0.51
30.0–35.0	1.47	2.00	0.47
35.0–40.0	1.70	2.20	0.54
40.0–50.0	1.78	2.32	0.71
50.0–60.0	2.28	2.73	1.10
60.0–70.0	2.66	2.56	1.48
70.0–80.0	2.97	2.61	1.77
80.0–90.0	4.06	2.56	1.80
90.0–100.0	4.55	2.86	1.73

Table 2.4: Full Run 2 soft term uncertainty values for PFlow jets.

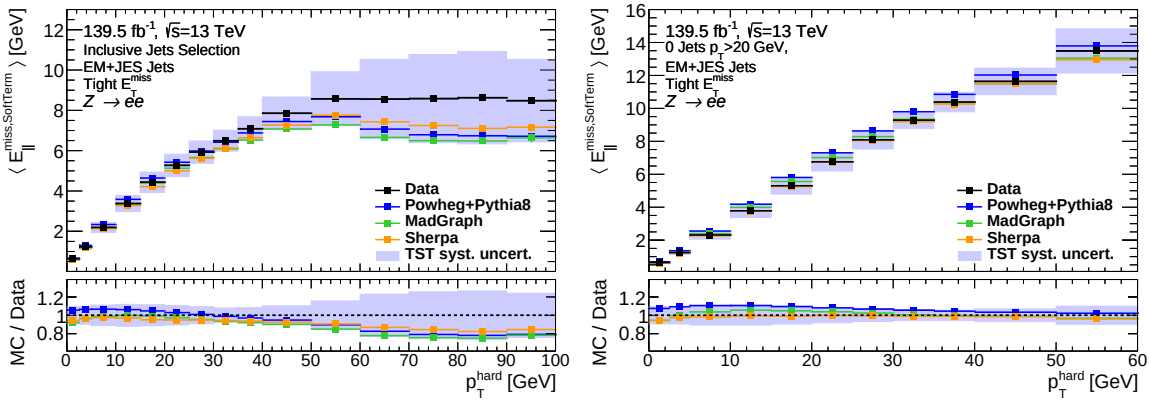

(a) jet inclusive Δ_L

(b) jet veto Δ_L

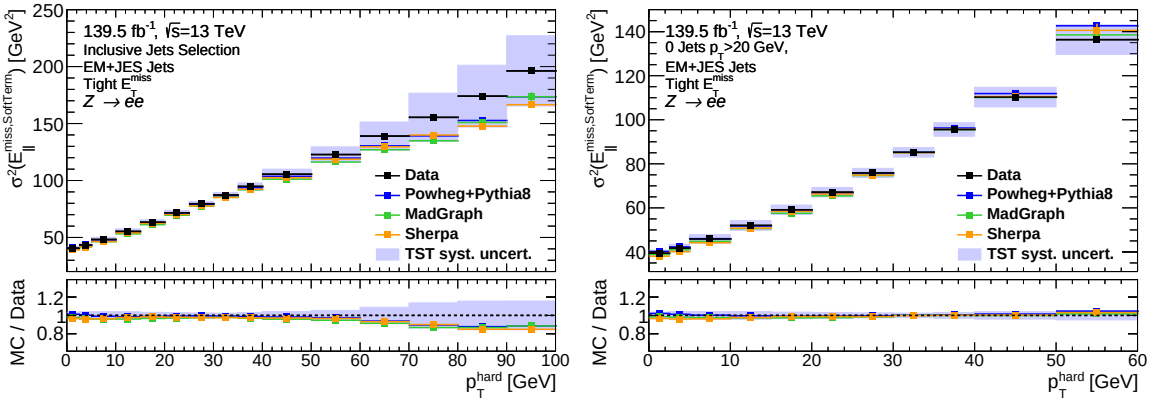

(c) jet inclusive $\sigma_{\parallel}$

(d) jet veto $\sigma_{\parallel}$

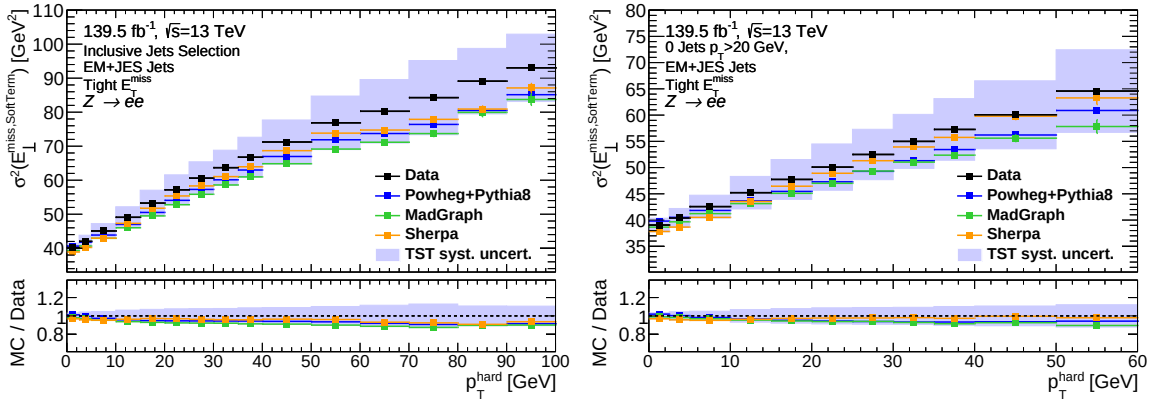

(e) jet inclusive $\sigma_{\perp}$

(f) jet veto $\sigma_{\perp}$

Figure 2.9: Distributions of the three variables used to calculate soft term uncertainties. Distributions of full Run 2 data and $Z \to ee$ Monte Carlo samples are shown with a $Z \to ee$ event selection applied using EMTopo jets. Full Run 2 uncertainties are shown as a shaded band about the data. The distributions are binned in $p_{\mathrm{T}}^{\mathrm{hard}}$.

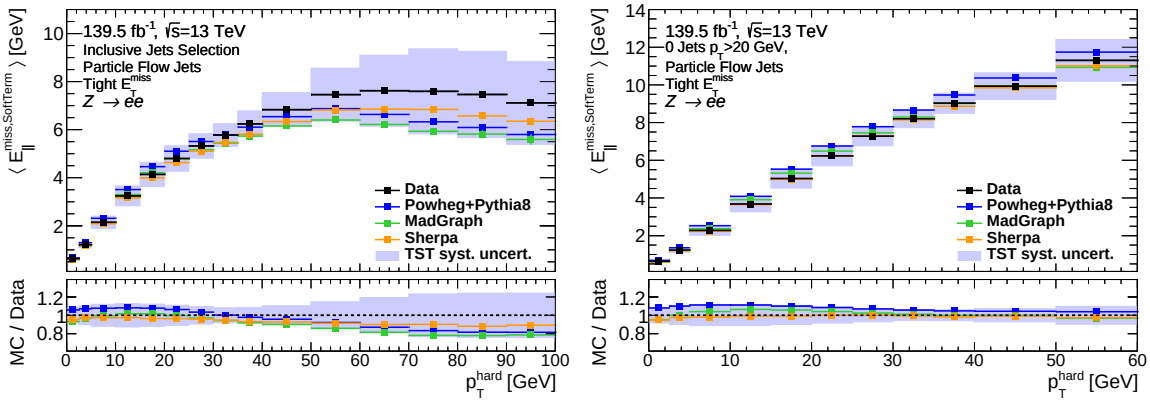

(a) jet inclusive Δ_L

(b) jet veto Δ_L

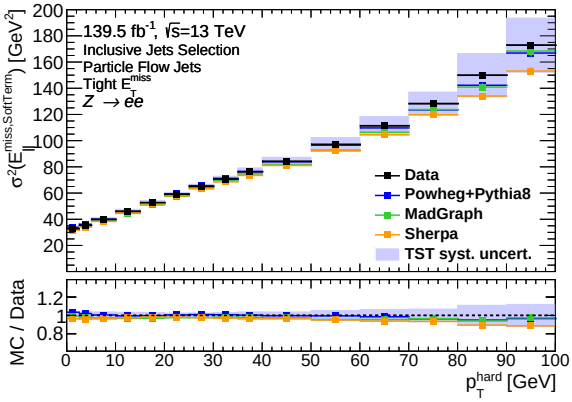

(c) jet inclusive $\sigma_{\parallel}$

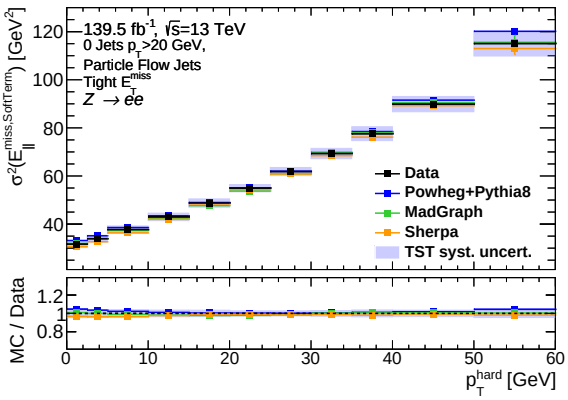

(d) jet veto $\sigma_{\parallel}$

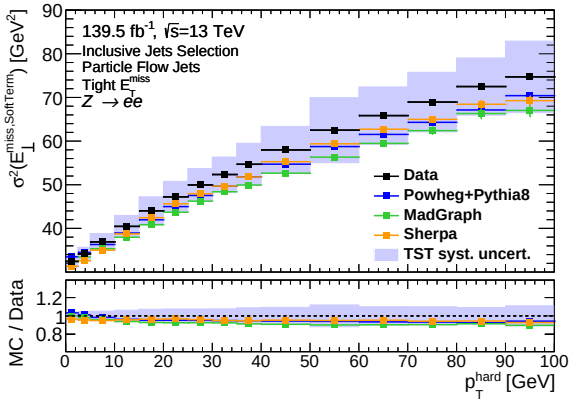

(e) jet inclusive $\sigma_{\perp}$

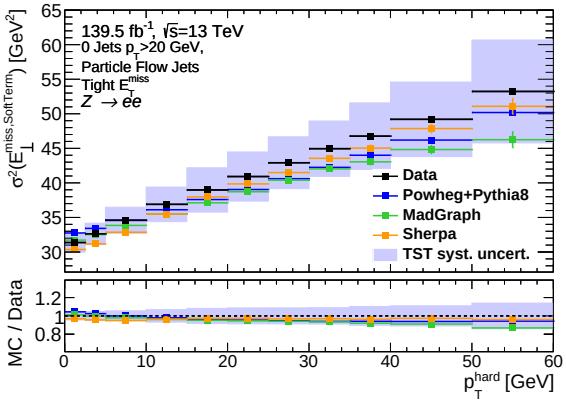

(f) jet veto $\sigma_{\perp}$

Figure 2.10: Distributions of the three variables used to calculate soft term uncertainties. Distributions of full Run 2 data and $Z \to ee$ Monte Carlo samples are shown with a $Z \to ee$ event selection applied using PFlow jets. Full Run 2 uncertainties are shown as a shaded band about the data. The distributions are binned in $p_{\mathrm{T}}^{\mathrm{hard}}$.

Chapter 3

Physics analysis in ATLAS: How to search for undiscovered, invisible hay in a haystack

3.1 Introduction

In this Chapter, fundamental concepts of how one can search for new physics using the ATLAS proton-proton collision data are presented. To begin, an introduction to where in the data one performs searches for new physics is given. This is followed with a summary of common selections made of the data in all of the searches performed in this thesis. After this, the most useful kinematic variables used in this thesis to discriminate between BSM and SM physics processes are described. To end, a detailed discussion of the statistical methods used to extract meaningful statements about BSM physics from the data is given.

3.2 Analysis Strategy

3.2.1 Defining signal, control and validation regions

A fundamental part of analysis searching for a specific signal is finding the subsets of the data where there the signal being searched for is most likely to be found. These

subsets, or 'signal regions' of the data are where the statistical analysis is performed and results are obtained. Considering 'data' as a list of events, each with the reconstructed particles produced and their properties, this corresponds to optimising which particles and properties are expected in the signal events. Moreover, to produce the best signal to background ratio, those properties which best distinguish the signal (BSM) and background (Standard Model) processes must be found. In practice, a signal region is defined by a set of kinematic requirements which are placed on the data.

In addition to signal regions, other regions of the data are often used to produce a robust estimate of the Standard Model background expectation. The easiest way to estimate this expectation is to directly use Monte Carlo simulation. These simulation samples are processed through a simulation of the ATLAS detector [66] based on GEANT4 [67] or a fast simulation using a parametrisation of the ATLAS calorimeter response and GEANT4 for the other detector components. The Monte Carlo samples are reconstructed with the same algorithms that are used for data. Differences between the data and the simulation can come from the lepton reconstruction efficiency, energy scale and energy resolution, b-tagging efficiency, the electron charge identification tool and trigger modelling. These are corrected for in the simulation by the application of correction factors derived in data. Monte Carlo samples are also weighted to match the measured luminosity in data.

However, simulation can not be assumed to always perfectly model the data, since it is limited — for example — by the level of accuracy in models for QCD, which governs the proton-proton interaction. Alternatively, one could take the shapes of kinematic distributions in the simulation to be sufficiently accurate, but use information about the Standard Model backgrounds taken from the data to improve its normalisation in the phase space near signal regions. This data-driven approach scales the Monte Carlo predictions for a given type of Standard Model background to better match the data prediction. Calculating the appropriate scaling requires a sample of data events expected to be maximally enriched in the specific background type. These events are found in 'control regions' which are designed to be pure in the desired background type (indicated from Monte Carlo) and low in expected contamination from any BSM events. The background under study can be scaled to make the total expected SM background yield in the control region match the observed data yield.

To ensure that the scaling obtained from the control region produces a good estimate, it is validated in an aptly named validation region. Here, 'good' means that the estimate can be reliably assumed to provide an accurate reflection of the background yield in the

data in the signal regions. One can also check whether the shapes of important kinematic distributions show good agreement between the data and SM background estimation. Validation regions are designed to again be pure in the background under study, and low in expected BSM events. They tend to be kinematically closer to the signal regions, so that one could expect the relative data yields of each background in the signal region to be similar to the validation region. If the background estimate is good, then the scaled Monte Carlo background should lead to a good agreement between the total SM background estimate and the data yield in the validation region. More importantly, it should result in an accurate estimate of the SM in the signal regions.

3.2.2 Useful variables

Missing transverse momentum, $p_{\mathrm{T}}^{\mathrm{miss}}$

The definition of missing transverse momentum is discussed in detail in Section 2.3.5. Both the R-parity conserving and R-parity violating SUSY scenarios considered in this thesis have a stable lightest supersymmetric particle (LSP) which is stable on detector scales. Thus, regions of high $p_{\mathrm{T}}^{\mathrm{miss}}$ are promising grounds for a search. Missing transverse momentum is constructed from the Baseline objects described in Sections 4.3 and 6.5.

Transverse mass

In events where a particle decays into two other visible particles, one can calculate the mass of the decaying particle using the momenta and energy of the two final state particles. However in the case where one of the decay products is invisible, $p_{\mathrm{T}}^{\mathrm{miss}}$ must be used as a proxy for the momentum of the particle. Given the undetermined boost along the beam-line in this case, transverse mass, m_{T} is instead considered. One can define m_{T} as the non-negative solution of:

$$m_{\mathrm{T}}^2 = E_{\mathrm{T}}^2 - |\overrightarrow{p_{\mathrm{T}}}|^2 \tag{3.1}$$

where $(E_{\mathrm{T}}, \overrightarrow{p_{\mathrm{T}}}) = (e_1, \overrightarrow{p}_1) + (e_2, \overrightarrow{p}_2)$, and $e_i = \sqrt{m_i^2 + |\overrightarrow{p}_i|^2}$.

As electron, muon and neutrino masses are small in comparison to the magnitudes of the momenta involved, they are treated as massless, and the transverse mass is ap-

proximated by the expression:

$$m_{\mathrm{T}} \approx \sqrt{2|p_1||p_2| - 2\vec{p_1}.\vec{p_2}} = \sqrt{2p_{\mathrm{T}}^{\ell}p_{\mathrm{T}}^{\mathrm{miss}}\left(1-\cos\Delta\phi\right)} \tag{3.2}$$

where $\Delta\phi$ is the azimuthal angle between the two final state particles. The distribution of m_{T} should have a kinematic endpoint at the mass of the decaying object.

Stransverse mass

The "Stransverse mass" variable, m_{T2} [68, 69], is defined in equation 3.3. It can in principle be calculated using any two visible objects and the missing transverse momentum but for all the analyses in this thesis the two visible objects are taken to be the two leading (highest p_{T}) leptons. Here $\vec{p}_T^{\ell 1}$ and $\vec{p}_T^{\ell 2}$ are the transverse momentum vectors of the two leptons, $\vec{q}_T$ is a transverse vector that minimizes the larger of $m_{\mathrm{T}}(\vec{p}_T^{\ell 1}, \vec{q}_T)$ and $m_{\mathrm{T}}(\vec{p}_T^{\ell 2}, \vec{p}_{\mathrm{T}}^{\mathrm{miss}} - \vec{q}_T)$. In m_{T}, m_p and m_q are assumed to be zero.

$$m_{\mathrm{T2}}(\vec{p}_{\mathrm{T}}^{\ell 1}, \vec{p}_{\mathrm{T}}^{\ell 2}) = \min_{\vec{q}_{\mathrm{T}}}\left[\max\left(m_{\mathrm{T}}(\vec{p}_{\mathrm{T}}^{\ell 1}, \vec{q}_{\mathrm{T}}), m_{\mathrm{T}}(\vec{p}_{\mathrm{T}}^{\ell 2}, \vec{p}_{\mathrm{T}}^{\mathrm{miss}} - \vec{q}_{\mathrm{T}})\right)\right] \tag{3.3}$$

This stransverse mass is designed to place a lower bound on the mass of a pair produced, semi-invisibly decaying particle. Therefore, it is expected to have a kinematic endpoint at the mass of said particle. For SM events, the distribution should start to tail off around the W mass, whereas for the SUSY models considered it should not do so until the generally much higher sparticle mass.[1]

Object based missing transverse momentum significance

Associated to the $p_{\mathrm{T}}^{\mathrm{miss}}$ value is the object based $p_{\mathrm{T}}^{\mathrm{miss}}$ Significance value ($\mathcal{S}$). Here 'objects' include the baseline leptons and jets used in the $p_{\mathrm{T}}^{\mathrm{miss}}$ calculation. The $p_{\mathrm{T}}^{\mathrm{miss}}$ significance gives a measure of how 'real' the $p_{\mathrm{T}}^{\mathrm{miss}}$ in an event is, as opposed to 'fake' $p_{\mathrm{T}}^{\mathrm{miss}}$ coming from object mis-measurement. Larger values indicate the event has a larger amount of 'real' $p_{\mathrm{T}}^{\mathrm{miss}}$. This variable is defined as:

$$\mathcal{S}^2 = \frac{|p_{\mathrm{T}}^{\mathrm{miss}}|^2}{\sigma_{\mathrm{L}}^2(1-\rho_{\mathrm{LT}}^2)}, \tag{3.4}$$

[1] Within this thesis, m_{T2} is calculated using the bisection-based algorithm described in Reference [70].

where σ_{L}^2 is the momentum resolution of objects in the direction longitudinal to the $p_{\mathrm{T}}^{\mathrm{miss}}$ and ρ_{LT}^2 is the correlation factor for object measurements longitudinal and transverse to the $p_{\mathrm{T}}^{\mathrm{miss}}$. Further details can be found in reference [71].

Since all of the SUSY scenarios considered in this thesis should have a large amount of real $p_{\mathrm{T}}^{\mathrm{miss}}$, they should also have a high values of $p_{\mathrm{T}}^{\mathrm{miss}}$ Significance. On the contrary, for the leptoquark scenario considered, a very small amount of real $p_{\mathrm{T}}^{\mathrm{miss}}$ is expected in the signal. In this case, low values of $p_{\mathrm{T}}^{\mathrm{miss}}$ Significance are expected.

3.3 Statistics

In this thesis, searches are made for new physics beyond the Standard Model. In a model-independent way this takes the form of seeking out data which look sufficiently different to the Standard Model expectation by looking for an excess of events over the Standard Model prediction in given regions of data. Alternatively, specific BSM theories are tested, where one additionally seeks observations of data which look sufficiently similar to those expected in the theory being probed, such that the event yield in a given region matches that expected from the BSM theory.

But what does 'sufficiently' mean? When testing a hypothesis, either the SM or a BSM theory, a quantitative measure of how significantly the data agrees or disagrees with it is required. Once one has this, one can then decide whether the agreement or disagreement is sufficient to claim a discovery or exclude the theory based on some value of the measure.

This section, describes the statistical methods used in this thesis. First, a discussion of the likelihood is presented, followed by an introduction to test statistics. After this, a description of the frequentist hypothesis testing used in Chapter 6 is given. Finally, a summary of the $\mathrm{CL_s}$ prescription used in Chapters 4, 5 and 6 is presented.

3.3.1 Likelihoods

To quantify the relationship between a given model and observed data, a good place to begin is the probability density function (PDF): $f(x)$ [72]. This should not be confused with the parton density function from Chapter 1. If the outcome of an experiment is a single continuous random variable x, then $f(x)dx$ is defined as the probability to observe

a value within the infinitesimal range $[x, x + dx]$. The PDF is normalised so that the total probability is equal to one over the entire space of possible values for x, S,

$$\int_S f(x)\, dx = 1. \tag{3.5}$$

In the case where x is discrete, one can consider the probability to observe a value x_i to be $f(x_i) = f_i$, and the PDF is instead normalised such that

$$\sum_{i=1}^{N} f_i = 1. \tag{3.6}$$

It is generally the case that the form of the PDF constraining the likely values of the data will depend on how the data is hypothesised to have been generated. It could also depend on the value of some other parameters, relating to uncertainty of the experiment used to obtain the data. This dependence can be formulated by including them into the PDF equation thus: $f(x; \boldsymbol{\theta}, \mu)$. This is defined as the probability of obtaining a data point within in infinitesimal range $[x, x+dx]$, under the assumption of a given hypothesis $H(\mu)$ which depends on some parameter μ, and some parameters $\boldsymbol{\theta}$ which represent, for example, systematic uncertainties in the experiment.

The parameters $\boldsymbol{\theta}$, each written as θ_j, are named nuisance parameters. Like the data x, these are random variables. It is assumed that their true values are unknown, but information about their likely true value is encoded through their own PDFs. Generally, these PDFs obey a Gaussian distribution about nominal values $\hat{\theta}_j$ estimated by the experimenters, $\text{Gauss}_j(\hat{\theta}_j, \theta_j, \sigma_j)$[2]. The determination of $\hat{\theta}_j$ is called an auxiliary measurement. σ_j represents the uncertainty on these nominal values. It is also usually assumed that the random variables x and $\boldsymbol{\theta}$ are independent, and thus their joint PDF is the product of their individual PDFs.

Often, one will obtain a set of multiple data points each corresponding to an independent observation. In this case the data is represented as a vector $\mathbf{x}$ where each element of the vector, x_i, is an observation; in this thesis an observation is the number of proton collision events entering a given signal region, or bin of a signal region. Proton collision data entering a signal region can be treated as a Poisson counting experiment, so provided the signal regions are independent $f(\mathbf{x}; \boldsymbol{\theta}, \mu)$ can be taken as a product of Poisson distributions for each signal region.

[2]Though sometimes log-normal distributions are used instead of Gaussians.

One can now construct the joint PDF for the entire observed dataset and nominal parameter values under a given hypothesis and parameters. The probability that x_i lies within $[x_i, x + dx_i]$ for all i, and θ_j lies within $[\theta_j, \theta_j + d\theta_j]$ for all j, can be written as:

$$\prod_{i=1}^{X} f(x_i; \boldsymbol{\theta}, \mu) dx_i \prod_{j=1}^{T} \text{Gauss}_j(\hat{\theta}_j, \theta_j) d\theta_j, \tag{3.7}$$

for a set of X data points in $\mathbf{x}$, and taking the length of $\boldsymbol{\theta}$ to be T.

Once the experiment has been performed, the data $\mathbf{x}$ and the nominal values $\hat{\boldsymbol{\theta}}$ are fixed. The dx_i and $d\theta_i$ can be put to the side and one can define the likelihood $\mathcal{L}$ as the joint PDF for the dataset under a given hypothesis and parameters:

$$\mathcal{L}(\boldsymbol{\theta}, \mu) = \prod_{i=1}^{X} f(x_i; \boldsymbol{\theta}, \mu) \prod_{j=1}^{T} \text{Gauss}_j(\hat{\theta}_j, \theta_j). \tag{3.8}$$

The likelihood is a function of the parameter defining the hypothesis and the parameters defining the uncertainty in the data.

One example of μ used in this thesis is signal strength parameter, μ_{sig}. This parameter is a multiplicative constant associated with the expected signal yield from a given BSM model, S, such that the expected event yield in a signal region N is defined by $N = B + \mu_{\text{sig}} S$, where B is the number of expected SM background events. In this case, μ_{sig} is a variable defined within some reasonable range, for example $\mu_{\text{sig}} \geq 0$[3]. Rather than constraining the variable with a Gaussian PDF, it is either left to float as a free parameter, or set to a specific value to calculate the likelihood for a specific hypothesis. Here $\mu_{\text{sig}} = 0$ would correspond to the SM hypothesis, and $\mu_{\text{sig}} = 1$ would correspond to whatever model was used to generate S. Other values would correspond to a similar BSM model with an increased or decreased signal production cross section.

Often, as will be described later, the purpose of the likelihood function is to obtain the value of the parameter μ which best describes the data, in order to determine which hypothesis the data is most likely to have been generated from. For this reason, it is called the parameter of interest (POI).

If the hypothesis and parameters chosen were in fact true, one would expect the probability of the data observed to be high. Taking this further, one would also expect

[3]This assumes that the signal can only provide an increase in the event yield, and so cannot be used to consider destructive interference.

that the highest probability of the observed data given a hypothesis and parameters would occur for the true hypothesis and true parameter values. This motivates the maximum likelihood approach for parameter estimation. To find which parameters are most consistent with the data, the parameters which maximise the likelihood function are sought.

Assuming the likelihood is a differentiable function of the parameters, it is maximised by solving:

$$\frac{\partial \mathcal{L}}{\partial \theta_i} = 0, i = 1, ..., T. \tag{3.9}$$

The solutions to theses equations are denoted with hats, $\hat{\boldsymbol{\theta}}$. This optimisation of the values of the nuisance parameters is called profiling. It is standard in practice to instead consider the negative logarithm of the likelihood, since it converts the product of PDFs into a sum. This sum is generally easier to calculate derivatives for when performing the likelihood maximisation. All of the statistical tests used in this thesis include the idea of maximising a likelihood to uncover parameter values and hypotheses most consistent with data.

3.3.2 Test statistics

When attempting to establish how well the observed data agrees with a hypothesis, and furthermore to compare which of two hypotheses is more consistent with the data, it is useful to define a test statistic. A test statistic is a function of the data and the hypothesis, which returns a single number. The values this number can take, have an order corresponding to increasing consistency between the hypothesis and the data. This ordering allows direct comparisons to be made between different hypotheses. Technically, since the likelihood itself has the property of increasing values implying a stronger consistency, it qualifies as a test statistic. However it is not necessarily the most useful, and on its own can only consider one hypothesis at a time.

To compare which of two hypotheses is most likely to have been true when generating the observed dataset, it can be shown that the most powerful test statistic is given by the likelihood ratio:

$$\Lambda = \frac{\mathcal{L}(\boldsymbol{\theta}, \mu)}{\mathcal{L}(\boldsymbol{\theta}, \mu')}, \tag{3.10}$$

where μ is the parameter defining the first hypothesis H, and μ' is that defining the second hypothesis H'. The previous statement is called the Neymann-Pearson Lemma [73]. If both hypotheses are equally consistent with the data, this ratio will have a value of one. If H is more consistent than H' then the ratio will increase above one; if H' is more consistent, it will decrease below one. As with the likelihood itself, the standard approach is to consider the logarithm of the likelihood ratio which changes this division into a subtraction.

It is also possible to use likelihood ratios with only one well-defined hypothesis under test. Rather than the alternative hypothesis $H'(\mu')$, a generic alternative can be introduced without yet choosing a value for μ'. The global maximum likelihood value can be calculated, simultaneously choosing the values of μ' and $\boldsymbol{\theta}$ which are the most consistent with the data. This maximum is written as $\mathcal{L}(\hat{\boldsymbol{\theta}}, \hat{\mu})$. This maximum indicates the hypothesis most consistent with the data when the parameters $\boldsymbol{\theta}$ can also be chosen to be most consistent: $\boldsymbol{\theta} = \hat{\boldsymbol{\theta}}$. Building on this, the likelihood for the null hypothesis — the hypothesis under test — can now be considered. The maximum likelihood for $H(\mu)$ is calculated choosing parameters $\boldsymbol{\theta} = \hat{\hat{\boldsymbol{\theta}}}$, and written as $\mathcal{L}(\hat{\hat{\boldsymbol{\theta}}}, \mu)$. The ratio

$$q_{\boldsymbol{\mu}} = \begin{cases} -2\ln\left(\frac{\mathcal{L}(\hat{\hat{\boldsymbol{\theta}}},\mu)}{\mathcal{L}(\hat{\boldsymbol{\theta}},\hat{\mu})}\right) & \text{if } \mu \geq \hat{\mu} \geq 0, \\ 0 & \text{otherwise} \end{cases} \tag{3.11}$$

is called the one-sided profile log likelihood ratio, and allows a comparison to be made between the hypothesis $H(\mu)$ under test and that which maximises the global likelihood. As the hypothesis becomes more consistent with the data, q_μ approaches 0. As it becomes less consistent, q_μ approaches infinity. Whilst a growing value of the numerator alone indicates the same trend, the ratio provides an effective scaling to the maximum possible value, so the interpretation is more meaningful.

q_μ is also defined to only allow for positive values of μ. In new physics searches this is appropriate, and means that new physics hypotheses predicting a negative number of events have no probability of consistency with the dataset, since they are considered non-physical. All of the hypothesis tests in this thesis rely on q_μ as a test statistic.

For example, in the ratio measurement described in Section 6.9 the goal is to find the value of a ratio $r = \mu$ which is most likely to have generated the data. At this value, q_r will equal 0, so it is sufficient to calculate the denominator. This is done numerically in the RooStats package [74] using MINUIT, where the initial parameter values corre-

spond to the SM hypothesis. Since the data have statistical fluctuations, $\mathcal{L}(\hat{\hat{\boldsymbol{\theta}}}, r)$ and q_r might change value in a repeat of the experiment. Therefore it is also necessary to find the uncertainty on R, which is done by considering a likelihood confidence interval. As considered in more detail in the next Section, the likelihood can be approximated as a Gaussian distribution. Thus the uncertainty on q_r desired is that which corresponds to a $\pm 1\sigma$ change in the likelihood. It can be shown that the values of R corresponding to $\pm 1\sigma$ occur when $q_r = 1$. This convenient value is the motivation for the factor of two included in the definition of the one-sided profile log likelihood ratio.

3.3.3 Frequentist hypothesis testing

Instead of trying to find the value of μ most consistent with the data, one may instead test the consistency of a specific value — equivalent to testing a specific hypothesis. As mentioned previously, the key consideration here is deciding how consistent the hypothesis must be with the data to conclude that it is true beyond reasonable doubt, or conversely that the hypothesis is inconsistent enough to be declared false and excluded. In practice, a test statistic that can be interpreted as a well-defined probability is desired. This requires further development beyond the one-sided profile log likelihood ratio, q_μ.

As introduced in the previous Section, the data is subject to statistical fluctuation which propagates through to the observed value: $q_{\mu,obs}$. One can consider $q_{\mu,obs}$ itself follow some probability distribution $f(q_\mu|\mu)$.

At this point, the concept of a p-value can be introduced. The p-value for a given hypothesis is the probability of obtaining data with equal or lesser compatibility than that which is observed, assuming the hypothesis did, in fact, generate the data. This can be written as:

$$p_\mu = \int_{q_\mu,obs}^{\infty} f(q_\mu|\mu)\, dq_\mu, \tag{3.12}$$

where smaller values of p imply a stronger disagreement between the data and the hypothesis $H(\mu)$. If $f(q_\mu|\mu)$ were a Gaussian, then one could use this test-statistic to quantify the level of disagreement between the data and the hypothesis by considering how many standard deviations away from the expected value $q_{\mu,obs}$ is. This is properly quantified by defining the significance Z, which counts the number of standard

deviations:

$$p = 1 - \Phi(Z), \tag{3.13}$$

$$Z = \Phi^{-1}(1 - p). \tag{3.14}$$

Here Φ is the cumulative distribution for a Gaussian. In this case, the test-statistic p provides a sufficiently well defined measure of the consistency between the data and hypothesis. This allows conclusions to be drawn at a particular level of confidence, aptly called a confidence level. To exclude a hypothesis in high energy physics, it is standard to require a significance of 3, corresponding to a p-value of 1.35×10^{-5}. To confidently reject the hypothesis under test and claim discovery of an alternative hypothesis, it is required to have a significance of 5, corresponding to a p-value of 2.87×10^{-7}.

But can it be assumed that $f(q_\mu|\mu)$ is Gaussian? It is not commonly possible to analytically calculate the form of $f(q_\mu|\mu)$, so it must be approximated numerically using ensembles of simulated data. Monte Carlo simulation is used to generate samples under the hypothesis $H(\mu)$. Within this thesis, the computationally easier of two common approaches is taken: the asymptotic approach. The expected yields in all of the signal regions are large enough to render this approach valid. The asymptotic approach, derived in Reference [75], proposes that for a sufficiently large number of samples (signal region yield) N, in a measurement n, the one-sided profile log likelihood ratio can be approximated as:

$$q_\mu(n) \sim \left(\frac{\mu - \hat{\mu}}{\sigma}^2\right) + \mathcal{O}\left(\frac{1}{\sqrt{N}}\right). \tag{3.15}$$

where $\hat{\mu}$ is the estimator for the parameter of interest μ. In this approximation, the ensemble of simulated data is replaced by the so-called Asimov dataset [75]. This dataset is built from the Monte Carlo prediction, taking it to be the true value of the parameter of interest, and thus the value of the estimator $\hat{\mu}$. Here the standard deviation is also calculated using the value of the test statistic under the Asimov dataset, q_A, thus:

$$\sigma^2 \approx \frac{(\mu - \hat{\mu})^2}{q_A}. \tag{3.16}$$

3.3.4 Modified frequentist testing

Given two alternative hypotheses, how can one decide which one is more consistent with the data? What is the best way to decide if one of them can be excluded or confirmed to have been discovered? One approach could be to calculate the p-values for both hypotheses, and see which provides the largest inconsistency. But what if the data is simply not sensitive enough to make a conclusion about a given hypothesis? A fundamental property of confidence levels is the possibility of a false positive — that is, the result that a hypothesis is excluded when in reality, it is true. This could occur, for example, by a statistical downward fluctuation in the Monte Carlo SM background expectation, making any observed excess in the data appear larger.

A standard approach within ATLAS to avoid false positives of 'new physics' is to normalise the p-value of the 'new physics' hypothesis, p_1, (where $\mu = 1$) using the p-value of the SM hypothesis, p_0, (where $\mu = 0$). It is expected that for the case of a false positive, the data should be more consistent with the Standard Model. This normalisation leads to a new test statistic: the $\mathrm{CL_s}$ value, defined as

$$\mathrm{CL_s} = \frac{p_1}{1 - p_0}. \tag{3.17}$$

When $\mathrm{CL_s} < 0.05$, the hypothesis associated with p_1 is said to be excluded at a 95% confidence level. More detailed discussions of the $\mathrm{CL_s}$ value can be found in Reference [76].

In addition to the observed $\mathrm{CL_s}$ value which can be computed from the observed dataset, an expected value can be calculated assuming that the data is consistent with the SM hypothesis. This assumption is implemented by using Monte Carlo simulations of the SM background hypothesis to construct an Asimov dataset. The expected $\mathrm{CL_s}$ value is very useful to optimise a search, as it indicates whether there is enough sensitivity in a given region of data to be able to exclude or discover a hypothesis, before unblinding the data to see what it contains.

In the case that no discovery is made, the $\mathrm{CL_s}$ approach can also be used to place an upper limit on what new physics can be excluded in a given test. Instead of choosing the numerator to be p_1, a range of values of μ can be scanned over, and the value corresponding to $\mathrm{CL_s} = 0.05$ found. Values of μ larger than this limit represent hypotheses which can be excluded, whereas smaller values represent rarer new physics processes

which cannot be ruled out by the experiment. In practice, this upper limit is computed as the upper limit on a new physics process production cross section that is still possible in nature. This limit is often referred to as a 'model-independent' limit.

CL_s values are used to calculate the observed exclusion limits for the supersymmetry models considered in Chapters 4 and 5. They are also used to calculate exclusion limits for the R-parity violating supersymmetry and leptoquark models considered in Chapter 6. In both of these cases, limits are calculated for a set of multiple variations of the BSM model. Two free parameters in the model, either the masses of new particles or their coupling strength, are varied to produce a two-dimensional grid upon which the observed and expected 95% confidence level exclusion limits can be overlaid as contours. Each point in the grid corresponds to testing a different hypothesis where the POI $\mu = 1$, but the signal region yield S multiplying it, changes. This change is due to the BSM model's free parameter choices affecting the signal production cross section.

For the fits in this thesis (where fit refers to the calculation of the profile-likelihood test statistic, et cetera), an added layer of complexity comes from combining multiple signal regions, or bins. These signal regions are all orthogonal; they each include an entirely different subset of the data. This means the the observed yields in each are independent variables and thus the PDFs for each signal region can be combined through multiplication.

The benefit of this approach over having one larger signal region is the signal to background discrimination can be enhanced. For example, if a hypothesis is disfavoured with insufficient significance to be excluded or discovered in each region, when the combined likelihood is calculated it will be reduced in comparison to the global maximum likelihood. This will in turn increase the value of the test statistic q_μ. It is possible for this increase to alter the CL_s value sufficiently to then be able to expect to exclude or discover the hypothesis overall.

Another benefit to this approach comes from considering the 2-dimensional grid of hypotheses being considered. Different hypotheses in the grid may show more sensitivity in different signal regions, and one would like to be sensitive to as much of the grid as possible. Being able to put all of the signal regions together into the same statistical fit of the data is an easy way to ensure the best significance across the entire grid.

In Chapters 4 and 5 the situation is even more complex. The expected Standard Model background yields used to build the Asimov datasets are not taken directly from Monte Carlo. Instead, as introduced in Section 3.2, a data-driven approach is adopted.

The dominant Standard Model backgrounds are estimate by scaling the Monte Carlo prediction in control regions which are orthogonal to the signal regions. This scaling is included in the fit using scale factors μ_B for some Standard Model background process B.

Going back to the example of a POI in Section 3.3.1, and just considering one type of scaled-background (B) as an example, the total number of events expected for hypothesis $H(\mu)$ is $N = \mu_B B + \mu_{sig} S + B'$. Here B' represents some other kind of background which is taken straight from Monte Carlo. For the signal regions, this expression for N is indeed the case. For well-designed control regions, where negligible signal is expected, the total expected number of events can instead be written as: $N = \mu_B B + B'$. The scale factor μ_B is included as a nuisance parameter, which is free to float within some sensible range, for example it must be positive. Provided that the control region is well-designed — that is to say adequately pure in background B — then the fit should constrain the value of μ_B to make the expected background B match that produced in the data.

It is important to note that the constraint of the scale factors is done in the control and signal regions. However, because the control regions are purer and have more events than the signal regions, they have more power to constrain the scale factors than the signal regions. If multiple backgrounds are being constrained, they are constrained simultaneously in all regions, so that contamination from the other backgrounds in each control region is treated correctly. It is also the case that the simultaneous fitting of all the regions to profile the other nuisance parameters ensures that correlations between the parameters in each region are also treated correctly.

Chapter 4

A new search for electroweak supersymmetry in 2-lepton final states using the Run-2 dataset

4.1 Introduction

This Chapter describes the first search for chargino pair production with W-boson mediated decays at $\sqrt{s} = 13\,\text{TeV}$ with the ATLAS detector. This analysis uses $80.5\,\text{fb}^{-1}$ of integrated luminosity of data from LHC pp collisions collected in 2015–2017, corresponding to integrated luminosities of $36.2\ \text{fb}^{-1}$ in 2015–2016 and $44.3\ \text{fb}^{-1}$ in 2017, with an uncertainty of 2%. The results were made public [1] and presented at the SUSY18 conference on the 24^{th} June 2018.

The author produced the first definitions of optimised signal, control and validation regions, along with results showing the expected sensitivity, using 2015-2016 data. After moving to a newer release of ATLAS analysis software and adding 2017 data, other analysers took over the Standard Model background estimation and performed the background-only fit (including following optimisation suggestions made by the author). The author continued the final optimisation of the signal regions as well as producing the model-dependent and model-independent limits. The author also produced most of the plots for both the internal documentation and public note. Unless otherwise stated the author produced all plots shown in this Chapter. Other analysers calculated the experimental and theoretical systematic uncertainties, however the author contributed

to understanding the systematic uncertainties and provided studies recommending moving to the Tight $p_{\mathrm{T}}^{\mathrm{miss}}$ reconstruction working point and the tighter 85% efficiency b-jet tagger working point.

An introduction to supersymmetry was given in Section 1.4. If gluino and squark masses were much heavier than low-mass electroweakinos, then SUSY production at the LHC would be dominated by direct electroweak production. The latest ATLAS limits on squark and gluino production [77] extend well beyond the TeV scale, thus making electroweak production of sparticles a promising and important probe to search for SUSY at the LHC.

This analysis targets the direct production of oppositely charged charginos ($\tilde{\chi}_1^+\tilde{\chi}_1^-$), where each chargino decays to the neutralino ($\tilde{\chi}_1^0$, considered as the LSP) and a W-boson. A diagram illustrating this process is shown in Figure 4.1. Only the leptonic decay mode of the W-boson is considered, so the events are characterised by the presence of two isolated leptons (e and/or μ) with opposite charge, and significant $p_{\mathrm{T}}^{\mathrm{miss}}$, expected from neutrinos and neutralinos in the final state. A simplified model [78] is considered for the signal, assuming a branching ratio of 100% for the decay under study. The charginos are considered to be wino-like and the neutralinos bino-like. In the simplified models the masses of the relevant sparticles, in this case $\tilde{\chi}_1^{\pm}$ and $\tilde{\chi}_1^0$, are the only free parameters. This is because all other sparticle masses are set to be too high for viable LHC production. The cross section for chargino pair production is assumed to correspond to a wino-like state. The lightest neutralino is considered bino-like.

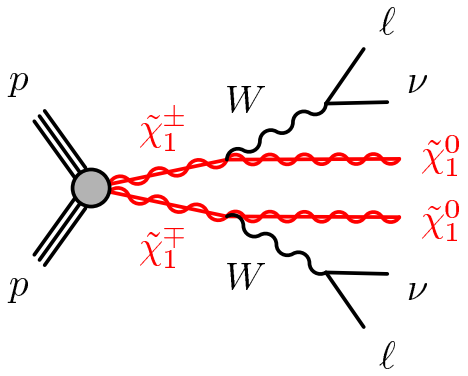

Figure 4.1: Diagram of the supersymmetric model considered in this analysis: $\tilde{\chi}_1^+\tilde{\chi}_1^-$ production with W-boson-mediated decays. Reproduced from Reference [1].

Due to significant background contributions from SM WW production and the low

expected signal cross section (58.6 ± 4.7 fb for a chargino mass of 400 GeV), the analysis of this channel is challenging. This search targets high chargino masses in areas of the parameter space previously not excluded by the corresponding ATLAS Run-1 search [79] and by a recent CMS search at 13 TeV [80] in the same channel.

It is also important to consider model-independent limits: to make general statements about BSM process which could have occurred in the signal regions without limitations coming from simplified models. Limits are placed on the possible number of BSM events and visible cross sections which could have occurred without the result being inconsistent with the SM only hypothesis given the data and expected background yields.

The Chapter continues in Section 4.2 with a summary of the data and Monte Carlo samples used, followed by a description of the object selection in Section 4.3. In Section 4.4 the signal region optimisation is presented and the background estimation strategy is described in Section 4.5. The systematic uncertainties included in the analysis are described in Section 4.6. Finally, the results and conclusions are presented in Sections 4.7 and 4.8 respectively.

4.2 Data and Monte Carlo samples

Events used in this analysis are required to pass triggers and various cleaning selections, as described in Section 2.3.4.

The dominant SM background processes are those producing a final state with two leptons and missing transverse momentum:

- Pair production of electroweak bosons ("diboson"): WW, WZ or ZZ,
- $t\bar{t}$ production, where the top quarks subsequently decay leptonically to produce e and/or μ,
- and single top quark production in association with a W boson, where both decay leptonically.

These backgrounds are estimated using a data-driven approach. Sub-dominant backgrounds estimated directly from Monte Carlo include:

- $t\bar{t}$ production in association with one or two electroweak bosons ($t\bar{t}V$),

- single top production in association with a Z boson (Zt),
- Z or γ production in association with jets, with the boson decaying to two leptons ($Z/\gamma + \text{jets}$),
- production of three electroweak bosons (VVV),
- and Higgs boson production.

The background denoted as "Other" in the plots and Tables in this Chapter includes the non-dominant background sources for this analysis, i.e. $Z + \text{jets}$, $t\bar{t}V$, Higgs, VVV and Drell-Yan events. Finally there is also the 'fake or non-prompt leptons' (FNP) background, which consists of events which have been falsely reconstructed in ATLAS as having two leptons in the final state. The most probable cause of this is $W + \text{jets}$ production, where the W decays to a muon but the jet is falsely reconstructed as an electron. However, many other sources of fake leptons also contribute to the background, such as conversions and other instances of light jets faking electrons, for example in QCD multijets events. The FNP background is estimated using a data-driven approach which will be discussed more in Section 4.5.

To model the SUSY signal and the Standard Model background, Monte Carlo simulations of events are used. The configurations of all SM background simulated samples used are listed in Table 4.1 which is taken from the conference paper [1]. This includes the relevant parton distribution function (PDF) set, the configuration of underlying-event and hadronisation parameters, and the cross section calculation order in α_S that is used to normalise the sample's event yields.

The SUSY signal samples are generated as described in Table 4.1. Jet-parton matching has been performed following the CKKW-L prescription [81], with a matching scale set to one quarter of the mass of the pair-produced $\tilde{\chi}_1^{\pm}$. Signal cross sections are calculated at NLO, with soft gluon emission effects added at next-to-leading-logarithm (NLL) accuracy [82–86]. The nominal cross section and its uncertainty are taken from an envelope of cross section predictions using different PDF sets and factorisation and renormalisation scales, as described in Reference [87].

Minimum-bias interactions were generated and overlaid on top of the hard-scattering process to simulate the effect of multiple pp interactions occurring during the same (in-time) or a nearby (out-of-time) bunch-crossing. These were produced using Pythia version 8.186 with the A2 tune [88] and the MSTW2008LO PDF [89] set. The MC

samples are re-weighted so that the distribution of the average number of interactions per bunch-crossing matches the observed distribution in the data.

Physics process	Generator	Parton shower	Cross section	Tune	PDF set
$t\bar{t}$	POWHEG-BOX [90, 91]	PYTHIA [8.186] [92]	NNLO+NNLL	Perugia2012 [93]	CT10[94]
$t\bar{t}+V(V=W,Z)$	MADGRAPH5_AMC@NLO [95]	PYTHIA [8.186]	NLO	A14 [96]	NNPDF 2.3 LO [97]
$t\bar{t}+WW$	MADGRAPH5_AMC@NLO	PYTHIA [8.186]	LO	A14	NNPDF 2.3 LO
$tZ, t\bar{t}t\bar{t}, t\bar{t}t$	MADGRAPH5_AMC@NLO	PYTHIA [8.186]	NLO	A14	NNPDF 2.3 LO
single top	POWHEG-BOX	PYTHIA [6.428] [98]	Approx. NNLO	Perugia2012	CT10
$Z/\gamma^*(\to ll)+$jets	SHERPA 2.2.1 [99]	SHERPA 2.2.1	NNLO	SHERPA default	NNPDF 3.0 NNLO [100]
WW, WZ, ZZ	POWHEG-BOX	PYTHIA [8.210]	NLO	AZNLO [101]	CTEQ6L1 [102]
$VVV(V=W,Z)$	SHERPA 2.2.2	SHERPA 2.2.2	NLO	SHERPA default	NNPDF 3.0 NNLO
Higgs	PYTHIA [8.186]	PYTHIA [8.186]	NLO	A14	NNPDF 2.3 LO
SUSY signal	MADGRAPH5_AMC@NLO	PYTHIA [8.186]	LO	A14	NNPDF 2.3 LO

Table 4.1: Simulated background event samples used in this analysis with the corresponding matrix element and parton shower generators, cross section order in α_S used to normalise the event yield, underlying-event tune and PDF set.

4.3 Object selection

The leptons selected in this analysis are categorised as Baseline or Signal according to kinematic and quality selections. The baseline objects are used for the calculation of the missing transverse momentum, to resolve any cases where objects may be double counted, and in the estimation of the FNP lepton background. More stringent requirements are then added to select the Signal leptons which are used for the signal and control regions in the analysis.

Baseline electrons are required to pass `loose` likelihood-based identification [50], to have $p_{\mathrm{T}} > 10\,\mathrm{GeV}$ and have $|\eta| < 2.47$. They are also required to be within $|z_0 \sin\theta| = 0.5\,\mathrm{mm}$ of the primary vertex, where z_0 is the longitudinal impact parameter with respect to the primary vertex.

Signal electrons are required to satisfy a tighter `medium` identification requirement [103]. As motivated in Section 2.3.1, an isolation working point is applied. The `GradientLoose` working point is used, as defined in Reference [104], which correctly reconstructs prompt-

electron candidates with 95% efficiency at $p_{\mathrm{T}} = 25\,\mathrm{GeV}$ and 99% efficiency at $p_{\mathrm{T}} = 60\,\mathrm{GeV}$, in $Z \to ee$ events. Finally, the Signal electron's associated track must have a significance of the transverse impact parameter (d_0) with respect to the reconstructed primary vertex, $|\,d_0|\,/\sigma(d_0) < 5$.

Baseline muon candidates are reconstructed in the region $|\eta| < 2.7$ using muon spectrometer tracks matching inner detector tracks. They must have $p_{\mathrm{T}} > 10\,\mathrm{GeV}$, be within $|z_0 \sin\theta| = 0.5\,\mathrm{mm}$ of the primary vertex and satisfy the `medium` identification requirements defined in Reference [61]. With the same motivation as for electrons, Signal muons are required to be isolated: the `GradientLoose` [61] isolation working point is used to obtain 95% efficiency at $p_{\mathrm{T}} = 25\,\mathrm{GeV}$ for $Z \to \mu\mu$ events. Finally, the track associated with the Signal muon must have a significance of the transverse impact parameter with respect to the reconstructed primary vertex of $|\,d_0|\,/\sigma(d_0) < 3$.

Jets are reconstructed from topological clusters as described in Section 2.3.2. Only jet candidates with $p_{\mathrm{T}} > 20\,\mathrm{GeV}$ and $|\eta| < 2.4$ are selected as jets in the analysis, although jets with $|\eta| < 4.5$ are included in the estimate of the missing transverse momentum.

As described in Section 2.3.2, the JVT and jet cleaning cuts are applied. b-jets are tagged using the procedure described in Section 2.3. The overlap removeal procedure defined in Section 2.3.4 is applied.

4.4 Summary of the signal regions

This analysis uses two separate sets of signal regions for the two types of result. Specially optimised binned signal regions are used to maximise sensitivity for the SUSY process considered, and as no sign of SUSY was found in the data, they are used to produce exclusion limits. Unbinned signal regions, which are less well-specifically optimised to gain sensitivity over the signal mass grid, are used to produce model-independent limits of possible BSM events. All events selected must pass a set of preselection cuts to select the correct signature and exclude regions of phase-space where things like reconstruction and trigger efficiencies are inadequate. Events are required to contain exactly two oppositely charged leptons with $p_{\mathrm{T}} > 20\,\mathrm{GeV}$ which pass the Signal selections defined in the previous Section. To avoid low mass resonances and regions low in expected signal, the leptons' invariant mass ($m_{\ell\ell}$) must be greater than 25 GeV. Since no b-jets are expected in the signal events, events containing reconstructed b-tagged jets are vetoed. This helps

to reduce the SM backgrounds from processes including top quarks.

When constructing signal regions the events are first separated into same flavour (ee or $\mu\mu$) and different flavour ($e\mu$) channels, because the dominating backgrounds for each channel are different. In the different flavour (DF) channel the dominant background is coming from WW whereas in the same flavour channel there is more ZZ and WZ.

The additional requirements used to optimise the signal regions are shown in Figures 4.2 and 4.3 for the different flavour and same flavour regions, respectively. The Monte Carlo SM background and signals at some benchmark points are shown along with the binomial significance (Z_n) values for each cut point. The binomial significance [105] approximates the $\mathrm{CL_s}$ value, and measures sensitivity to a given signal hypothesis to a given statistical significance. $Z_n > 1.64$ corresponds to adequate sensitivity for exclusion at 3σ, whilst $Z_n > 3.0$ corresponds to that for discovery of the signal hypothesis at 5σ. A 25% uncertainty is used in the Z_n calculation, in accordance with studies performed with the 2015 + 2016 datasets, where the Z_n value was used for initial signal region optimisation.

One downside of Z_n is that it can favour low signal yields, which could lead to statistical uncertainties becoming too dominant. Unlike the $\mathrm{CL_s}$ values, Z_n also doesn't consider the improvement that can be gained from combining different signal region bins, which may each be more sensitive to a different region of signal mass space and can exploit shape information available in the binned variable.

After adding in the 2017 data, re-optimisation was performed by considering the full $\mathrm{CL_s}$ calculation using multi-binned signal regions at three benchmark signal points for the progression of cuts. The benchmark points considered were $(M_{\tilde{\chi}_1^\pm}, M_{\tilde{\chi}_1^0}) = (250, 1)$, $(300, 50)$, $(300, 100)$ GeV in order to cover the region of expected sensitivity. The $\mathrm{CL_s}$ values were calculated with the HistFitter statistics framework [106] and only statistical errors were considered. Once the optimum cut points for each variable were chosen, the dominant systematic uncertainties were added to check that a reasonable amount of sensitivity remained across the whole signal grid. The motivations for each variable cut are described in the following paragraphs.

The primary discriminating variable in this search is the stransverse mass 'm_{T2}', as introduced in Section 3.2.2. For the main SM diboson background m_{T2} ideally has a kinematic endpoint at the W-boson mass, whilst for the signal process the endpoint should go up to the (generally higher) chargino mass. The m_{T2} calculation assumes that the mass of the invisible particles is zero, which is approximately correct for the

background, but not for the signal in the case of a heavy neutralino, so the endpoint in practice is less well-defined. The distributions will have a more smeared tail however, due to the finite momentum resolution and other imperfections of the detector. Thus, for all of the signal regions $m_{\mathrm{T2}} > 100\,\mathrm{GeV}$, as shown in Figures 4.3a and 4.2a.

The signal process contains no jets in the final state from the decay products, so a clear way to cut out background events such as top and Z+jets would be to add a veto cutting out central ($|\eta| < 2.4$) light (non b-tagged) jets with $p_{\mathrm{T}} > 20\,\mathrm{GeV}$ (defined as 'n_{CLJ}'). However in order to increase the number of signal events, the process where an ISR (initial state radiation) jet is produced along with the chargino pair can be considered. In this scenario the chargino pair system is boosted to a higher $p_{\mathrm{T}}^{\mathrm{miss}}$ and m_{T2} regime which can counteract the increased levels of SM background processes containing jets, however it does have a lower production cross section. For this reason separate

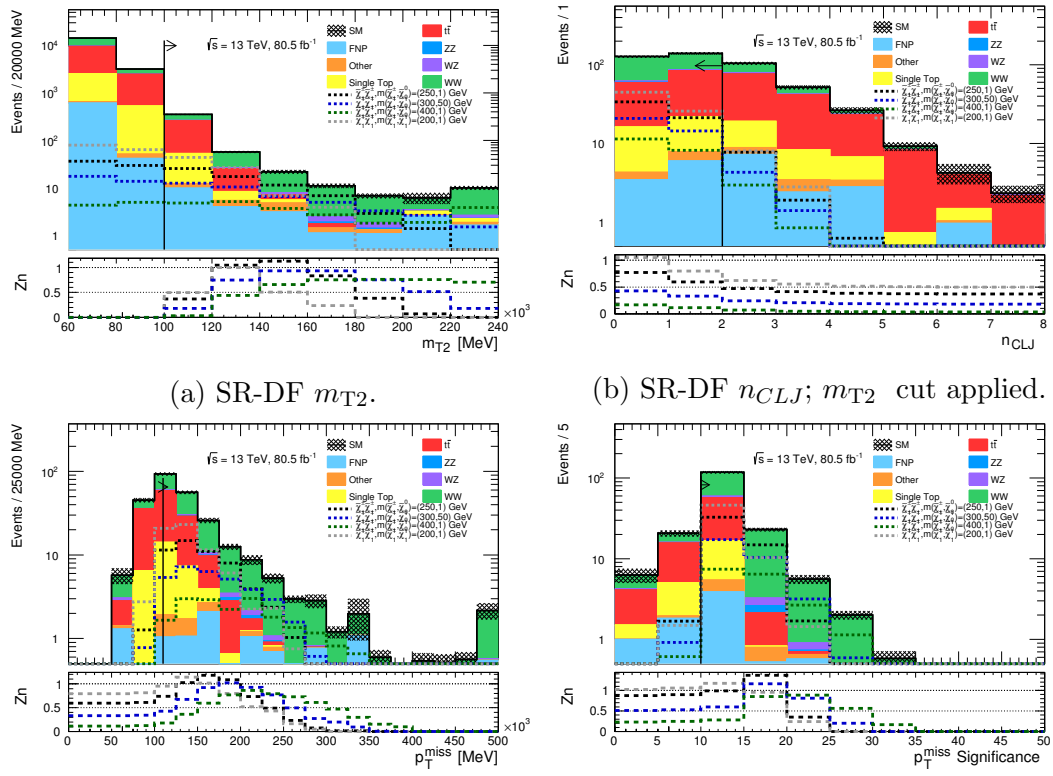

(a) SR-DF m_{T2}.

(b) SR-DF n_{CLJ}; m_{T2} cut applied.

(c) SR-DF $p_{\mathrm{T}}^{\mathrm{miss}}$; m_{T2} and n_{CLJ} cuts applied.

(d) SR-DF $p_{\mathrm{T}}^{\mathrm{miss}}$ Significance; m_{T2} , n_{CLJ} and $p_{\mathrm{T}}^{\mathrm{miss}}$ cuts applied.

Figure 4.2: Kinematic distributions of Monte Carlo (without any normalisation factors applied) and Z_n values in different flavour regions with cuts sequentially applied, including the preselection cuts for all distributions. The errors shown are statistical only. The final bin includes overflow.

signal regions with $n_{CLJ} = 0$ and $n_{CLJ} = 1$ are used. This choice showed better overall sensitivity than having one region with $n_{CLJ} \leq 1$, as shown in Figures 4.3b and 4.2b.

The two neutralinos (and two neutrinos) produced in the signal process are undetectable in ATLAS and instead are expected to provide a large amount of missing transverse momentum. This should generally be higher than the amount of missing transverse momentum produced in the main diboson background, thus constituting a discriminating variable. All of the signal regions require $p_{\mathrm{T}}^{\mathrm{miss}} > 110\,\mathrm{GeV}$ as shown in Figures 4.3c and 4.2c.

The final cut comes from the object based $p_{\mathrm{T}}^{\mathrm{miss}}$ Significance variable, described in Section 3.2. In the signal process high values of real $p_{\mathrm{T}}^{\mathrm{miss}}$ is expected, so higher values of $p_{\mathrm{T}}^{\mathrm{miss}}$ are also expected. Whilst the top and Z + jets backgrounds may also have high

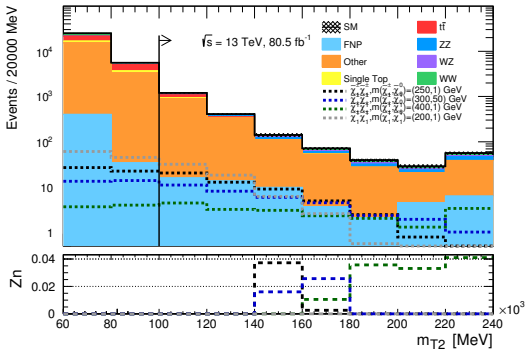

(a) SR-SF m_{T2}.

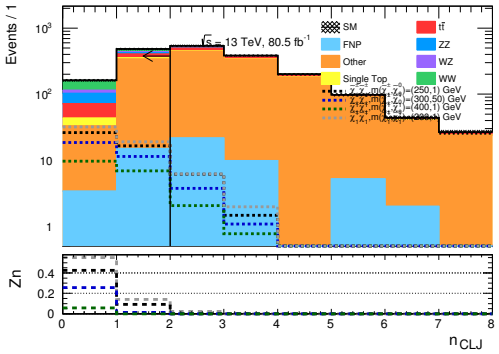

(b) SR-SF n_{CLJ}; m_{T2} cut applied.

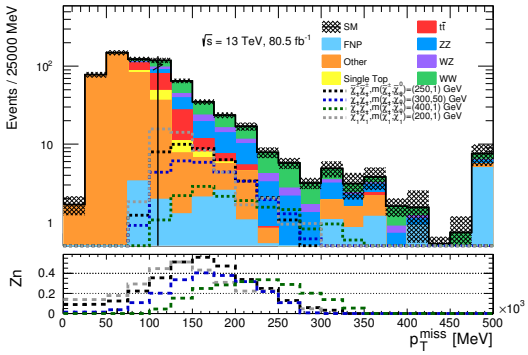

(c) SR-SF $p_{\mathrm{T}}^{\mathrm{miss}}$; m_{T2} and n_{CLJ} cuts applied.

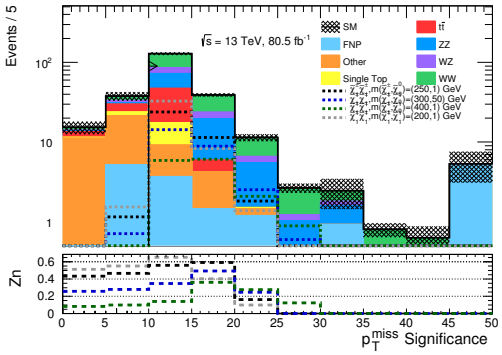

(d) SR-SF $p_{\mathrm{T}}^{\mathrm{miss}}$ Significance; m_{T2} , n_{CLJ} and $p_{\mathrm{T}}^{\mathrm{miss}}$ cuts applied.

Figure 4.3: Kinematic distributions of Monte Carlo (without any normalisation factors applied) and Z_n values in same flavour regions with cuts sequentially applied, including the preselection cuts and a Z mass veto for all distributions. The errors shown are statistical only. The final bin includes overflow.

$p_{\mathrm{T}}^{\mathrm{miss}}$ coming from the neutrinos in their final states, the jets in the processes provide more scope for object mis-reconstruction leading to more 'fake' $p_{\mathrm{T}}^{\mathrm{miss}}$. In particular, the Z + jets events tend to have low values of $p_{\mathrm{T}}^{\mathrm{miss}}$ Significance. For all signal regions, $p_{\mathrm{T}}^{\mathrm{miss}}$ Significance greater than 10 is required, as shown in Figures 4.3d and 4.2d.

In addition to these cuts, the signal regions are further split into different bins of m_{T2}. For the regions used for calculating exclusion limits, orthogonal regions of m_{T2} are considered which will each be more sensitive to different regions of sparticle mass space and allow any discrimination information from the shape of the m_{T2} distribution to improve the results. All of the regions are statistically combined to give the final exclusion contours, considering all combinations of flavour channels, n_{CLJ} and m_{T2} range. The m_{T2} bins were optimised by looking at the expected $\mathrm{CL_s}$ values across the entire signal grid — with only statistical systematics applied. Initially evenly sized bins were used, to study upper limits and widths. In Figure 4.4 some examples of the tested binning configurations are shown. These are defined in Table 4.2.

To avoid low yields in the high m_{T2} region the upper bins are combined to reduce the statistical uncertainty. In the low m_{T2} region the yields are much higher so finer bins are used. The final m_{T2} binning is shown in Figure 4.4d. It should be emphasised the use of m_{T2} binning was key in achieving good sensitivity across the signal grid.

Label	m_{T2} GeV $\in$
A	> 100
B	$[100, 140), [140, 180), [180, 220), > 220$
C	$[100, 120), [120, 140), [140, 160), [160, 180), [180, 200), [200, 220), > 220$
Final	$[100, 105), [105, 110), [110, 120), [120, 140), [140, 160), [160, 180), [180, 220), > 220$

Table 4.2: The definitions of the tested binning strategies illustrated in Figure 4.4.

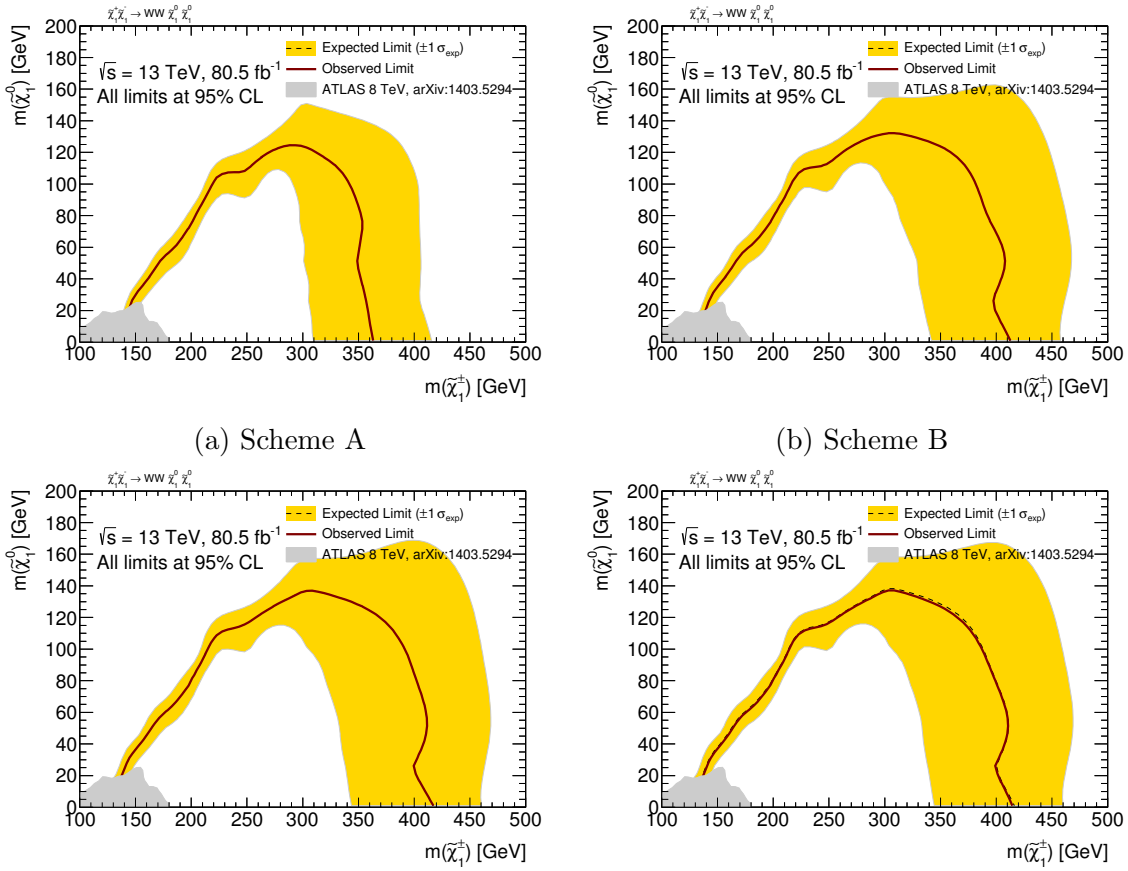

(a) Scheme A

(b) Scheme B

(c) Scheme C

(d) Final binning scheme

Figure 4.4: Example exclusion plots showing the improvement as the m_{T2} binning procedure is optimised. Plots contain statistical uncertainties only. Both the signal and control regions are blinded.

For the model-independent limits fewer m_{T2} regions are considered, and they are made wider to be sensitive to a larger variety of potential BSM models which could have hard upper limits or longer tails. The m_{T2} bins for these regions were chosen by other analysers, based on the Binned SRs.

The final signal regions for the analysis are described in Table 4.3.

Signal region (SR)	SR-DF-0J	SR-DF-1J	SR-SF-0J	SR-SF-1J
n_{CLJ}	$= 0$	$= 1$	$= 0$	$= 1$
$\lvert m_{\ell\ell} - m_Z \rvert$ [GeV]	–		>30	
$p_{\mathrm{T}}^{\mathrm{miss}}$[GeV]	>110			
$p_{\mathrm{T}}^{\mathrm{miss}}$ Significance	>10			
Binned SRs				
m_{T2} [GeV]	$\in$ [100,105)			
	$\in$ [105,110)			
	$\in$[110,120)			
	$\in$[120,140)			
	$\in$[140,160)			
	$\in$[160,180)			
	$\in$[180,220)			
	$\in [220, \infty)$			
Unbinned SRs for model-independent limits				
m_{T2} [GeV]	$\in [100, \infty)$			
	$\in [160, \infty)$			
	$\in [100, 120)$			
	$\in [120, 160)$			

Table 4.3: The definitions of the binned and inclusive signal regions. Relevant kinematic variables are defined in the text. The bins labelled "DF"or "SF" refer to signal regions with different-flavour or same-flavour lepton pair combinations, respectively [1].

4.5 Outline of background estimation techniques

In order to provide an accurate estimation of the dominant SM backgrounds in the analysis, a data driven method is used. Three control regions are defined for the main background processes: WW (CR-WW), WZ and ZZ (CR-VZ), and $t\bar{t}$ and single top (CR-top). The concept of control regions was introduced in Section 3.1.

The author provided initial designs for the three control regions and collaborated with other analysers to produce the final definitions after the signal regions were finalised. The final control region definitions can be seen in Table 4.4. The purities achieved for these regions are: 95.7% for CR-VZ, 63.9% for CR-WW and 92.0% for CR-top. The low purity in CR-WW is due to $t\bar{t}$ contamination, caused by the similar m_{T2} and $p_{\mathrm{T}}^{\mathrm{miss}}$ distributions to WW. Reducing this contamination is the cause of the tight m_{T2} requirement in CR-WW: as one moves to lower values of m_{T2} the WW purity increases, though further away from the signal regions. Whilst this requirement may seem very severe, there are still over a thousand events in the region. The low m_{T2} region is chosen to maximise the purity, whilst not moving too far away from the signal region. Since the $t\bar{t}$ background is normalised simultaneously, the contamination is not a great concern.

Distributions of m_{T2} in the CR-VZ and CR-top are shown alongside the $p_{\mathrm{T}}^{\mathrm{miss}}$ distribution for CR-WW in Figure 4.5. Some data–MC disagreement can be seen in the tail of the $p_{\mathrm{T}}^{\mathrm{miss}}$ distribution in CR-WW, after the dominant backgrounds have been scaled. This suggests mis-modelling in the shape of the $p_{\mathrm{T}}^{\mathrm{miss}}$ distribution at low m_{T2} in the diboson or $t\bar{t}$ MC, which cannot be improved with one SF throughout the distribution. However, since the same disagreement is not seen later in the validation regions (Figures 4.7c and 4.7d), which are kinematically closer to the signal regions, the mis-modelling does not present a problem. To check that the expected signal yields are low in the control regions, plots are made showing the signal yield as a percentage of the total expected Standard Model background yield in Figure 4.6. It can be seen that the contamination is indeed low across the signal grid.

The sub-dominant backgrounds listed in Section 4.2 are taken straight from Monte Carlo. Finally, the fake and non-prompt lepton background also introduced earlier is estimated using a data-driven approach called the matrix method [107]. This approach is more appropriate than using Monte Carlo, since the processes of mis-reconstruction which lead to the FNP background occur at such a low rate that very large samples would be required to get an adequately reliable prediction. Since the occurrence of the

Region	CR-VZ	CR-WW	CR-top
Lepton flavour	SF	DF	DF
$n_{b\text{-tagged jets}}$	$= 0$	$= 0$	$= 1$
n_{CLJ}	$= 0$	$= 0$	$= 0$
m_{T2} [GeV]	> 120	$\in [60,65)$	> 100
$p_{\mathrm{T}}^{\mathrm{miss}}$ [GeV]	> 110	> 60	> 110
$p_{\mathrm{T}}^{\mathrm{miss}}$ Significance	> 10	> 5	> 5
$\lvert m_{\ell\ell} - m_Z \rvert$ [GeV]	< 30	–	–

Table 4.4: Control region definitions for extracting normalisation factors for the dominant background processes. "DF" or "SF" refer to regions with different-flavour or same-flavour lepton pair combinations, respectively [1].

FNP background is also primarily due to detector effects, it would be heavily reliant on the accuracy of the simulation of the detector.

The matrix method uses regions of the data with less stringent lepton reconstruction requirements, in addition to regions orthogonal to the signal regions which maintain the same Signal lepton reconstruction requirements. The relative yields of these so called 'loose' and 'tight' leptons are studied to produce efficiencies for real and fake leptons entering the signal regions. The yields of 'loose' or 'tight' leptons, and real or fake leptons, are related using a matrix built from these efficiencies, assuming Gaussian statistics. This matrix is inverted to obtain a prediction for the rate at which events with one or two fake leptons enter the signal regions. Since the author was not involved in the implementation of the FNP background estimate, further details are not provided here, but can be found in Reference [1].

In order to validate the scale factors extracted from the control regions, the agreement of data and the Standard Model background is studied in validation regions. These regions should be kinematically close to the signal regions to ensure the correct region of phase space is being validated, have a high purity in the desired process and have a low signal contamination. Separate validation regions are designed for WW, $WZ + ZZ$ and top processes. For the WW process, separate validation regions with $n_{CLJ} = 0$or1 are used to check both the result in a higher purity region and the extrapolation into the $n_{CLJ} = 1$ signal regions. For top processes, separate validation regions are used which have different m_{T2} ranges in order to check both the top modelling in a higher purity region closer to CR-WW and the extrapolation into the higher m_{T2} range used in the

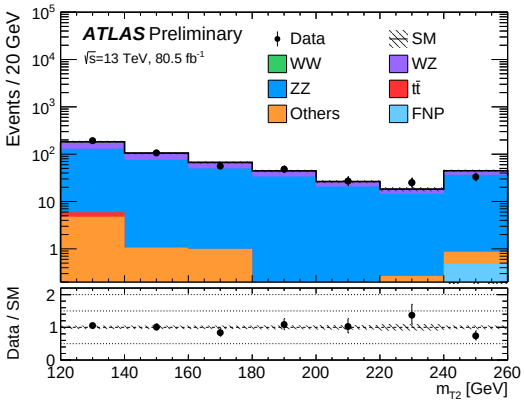

(a) m_{T2}, CR-VZ

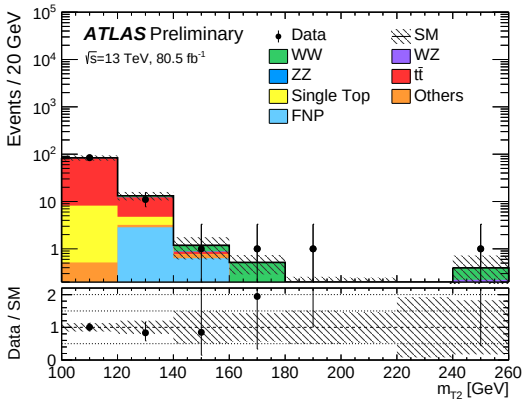

(b) m_{T2}, CR-top

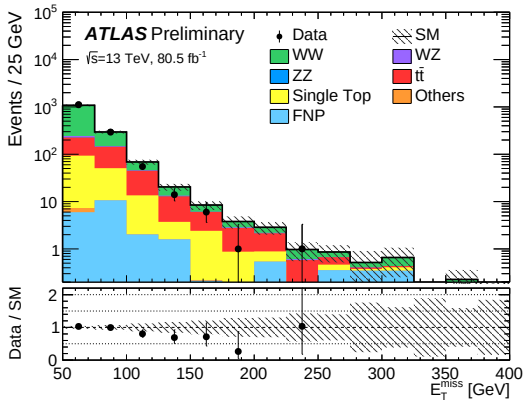

(c) $p_{\mathrm{T}}^{\mathrm{miss}}$, CR-WW

Figure 4.5: Example kinematic distributions of m_{T2} in the control regions, for data and the estimated SM backgrounds. The normalisation factors extracted from the corresponding CRs are used to rescale the $t\bar{t}$, single top, WW, WZ and ZZ backgrounds. Negligible background contributions are not included in the legends. The uncertainty band includes all systematic and statistical sources and the final bin in each histogram includes the overflow.

signal regions.

Some examples of kinematic distributions in the validation regions are shown in Figure 4.7. As with the control regions, the signal contamination is studied in plots showing the expected signal percentage yield in Figure 4.8.

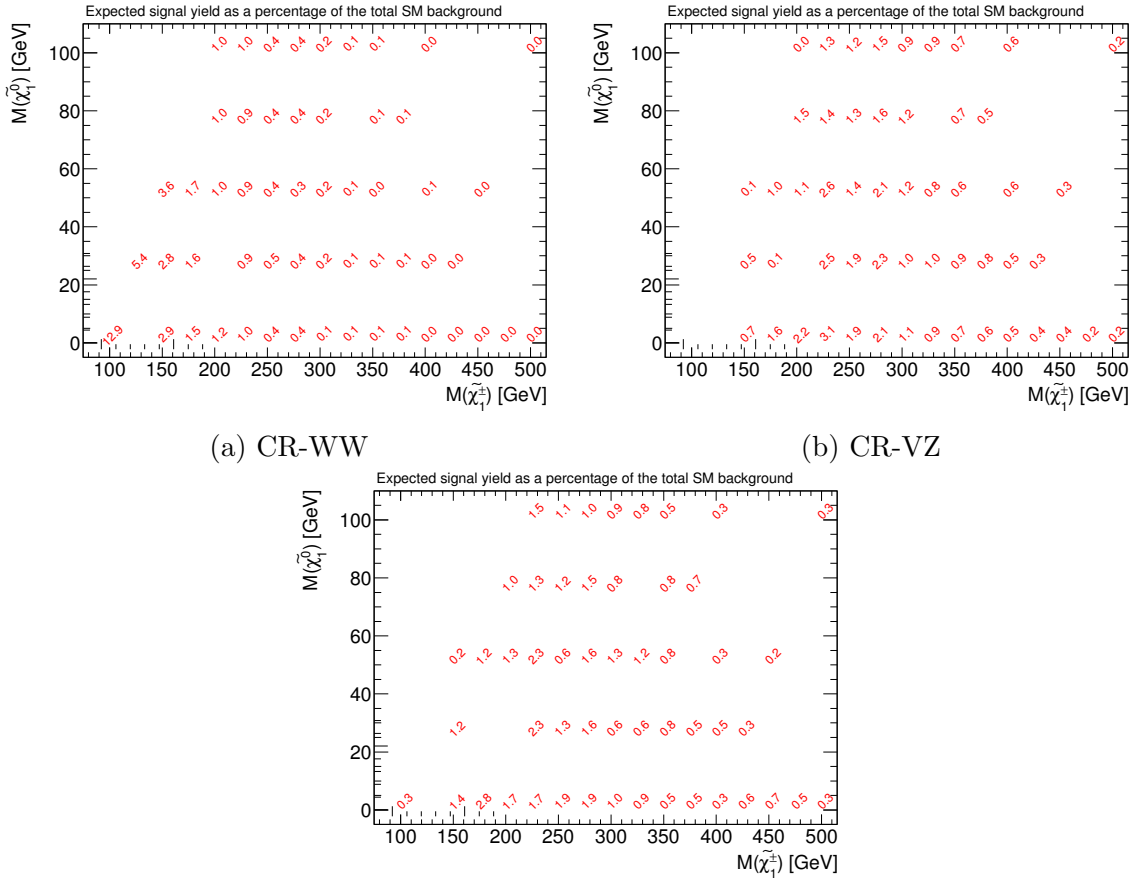

(a) CR-WW

(b) CR-VZ

(c) CR-top

Figure 4.6: Plots of the CR signal contamination over the whole grid. Plots show the signal yield as a percentage of the total expected background yield at each mass point.

Region	VR-WW-0J	VR-WW-1J	VR-VZ	VR-top-low	VR-top-high
Lepton flavour	DF	DF	SF	DF	DF
$n_{b\text{-tagged jets}}$	$= 0$	$= 0$	$= 0$	$= 1$	$= 1$
n_{CLJ}	$= 0$	$= 1$	$= 0$	$= 0$	$= 1$
m_{T2} [GeV]	$\in$ [65,100)	$\in$[65,100]	$\in$[100,120)	$\in$[80,100)	> 100
$p_{\mathrm{T}}^{\mathrm{miss}}$ [GeV]	> 60	> 60	> 110	> 110	> 110
$p_{\mathrm{T}}^{\mathrm{miss}}$ Significance	> 5	> 5	> 10	> 5	> 5
$\lvert m_{\ell\ell} - m_Z \rvert$ [GeV]	–	–	< 30	–	–

Table 4.5: Validation region definitions used to study the modelling of the SM backgrounds. "DF" or "SF" refer to regions with different-flavour or same-flavour lepton pair combinations, respectively [1].

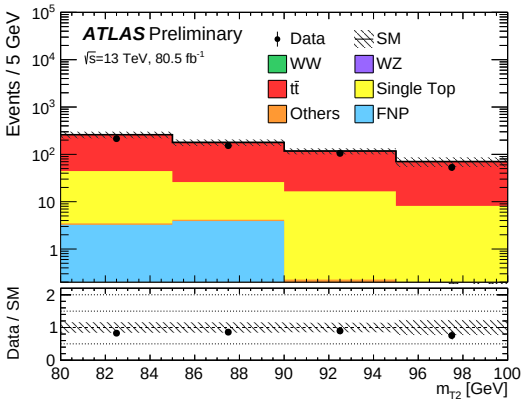

(a) m_{T2}, VR-top-low

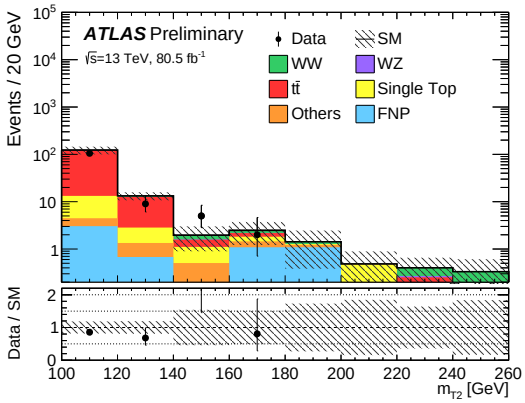

(b) m_{T2}, VR-top-high

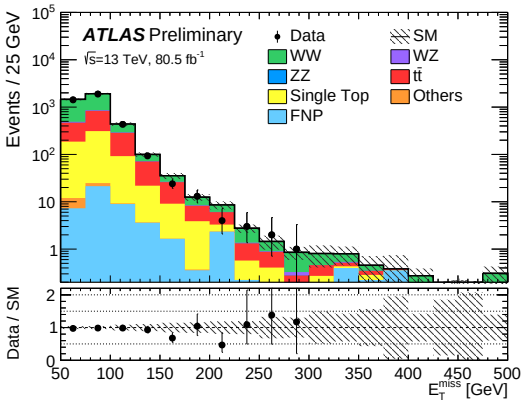

(c) $p_{\mathrm{T}}^{\mathrm{miss}}$, VR-WW-0J

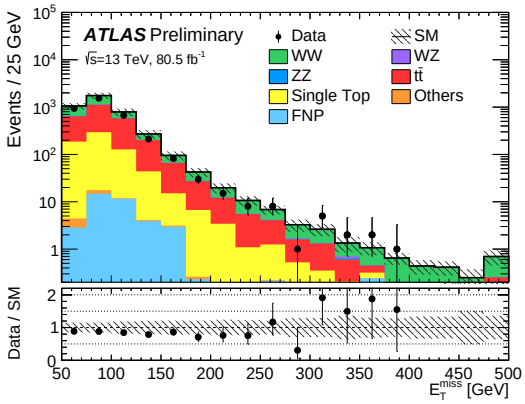

(d) $p_{\mathrm{T}}^{\mathrm{miss}}$, VR-WW-1J

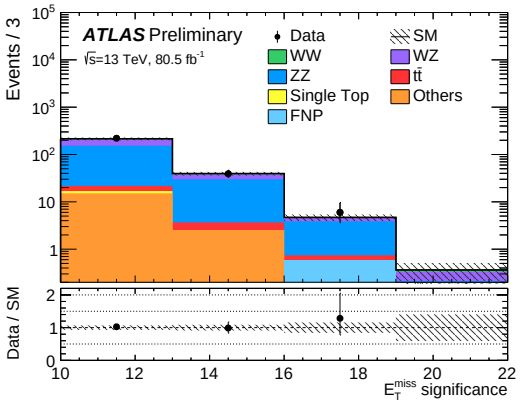

(e) $p_{\mathrm{T}}^{\mathrm{miss}}$ Significance, VR-VZ

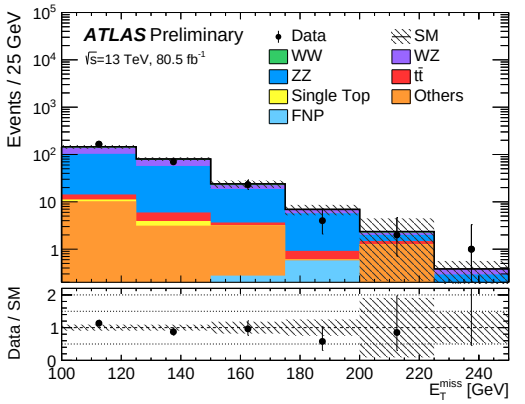

(f) $p_{\mathrm{T}}^{\mathrm{miss}}$, VR-VZ

Figure 4.7: Example kinematic distributions in the validation regions, for data and the estimated SM backgrounds. The normalisation factors extracted from the corresponding CRs are used to rescale the $t\bar{t}$, single top, WW, WZ and ZZ backgrounds. Negligible background contributions are not included in the legends. The uncertainty band includes all systematic and statistical sources and the last bin includes the overflow.

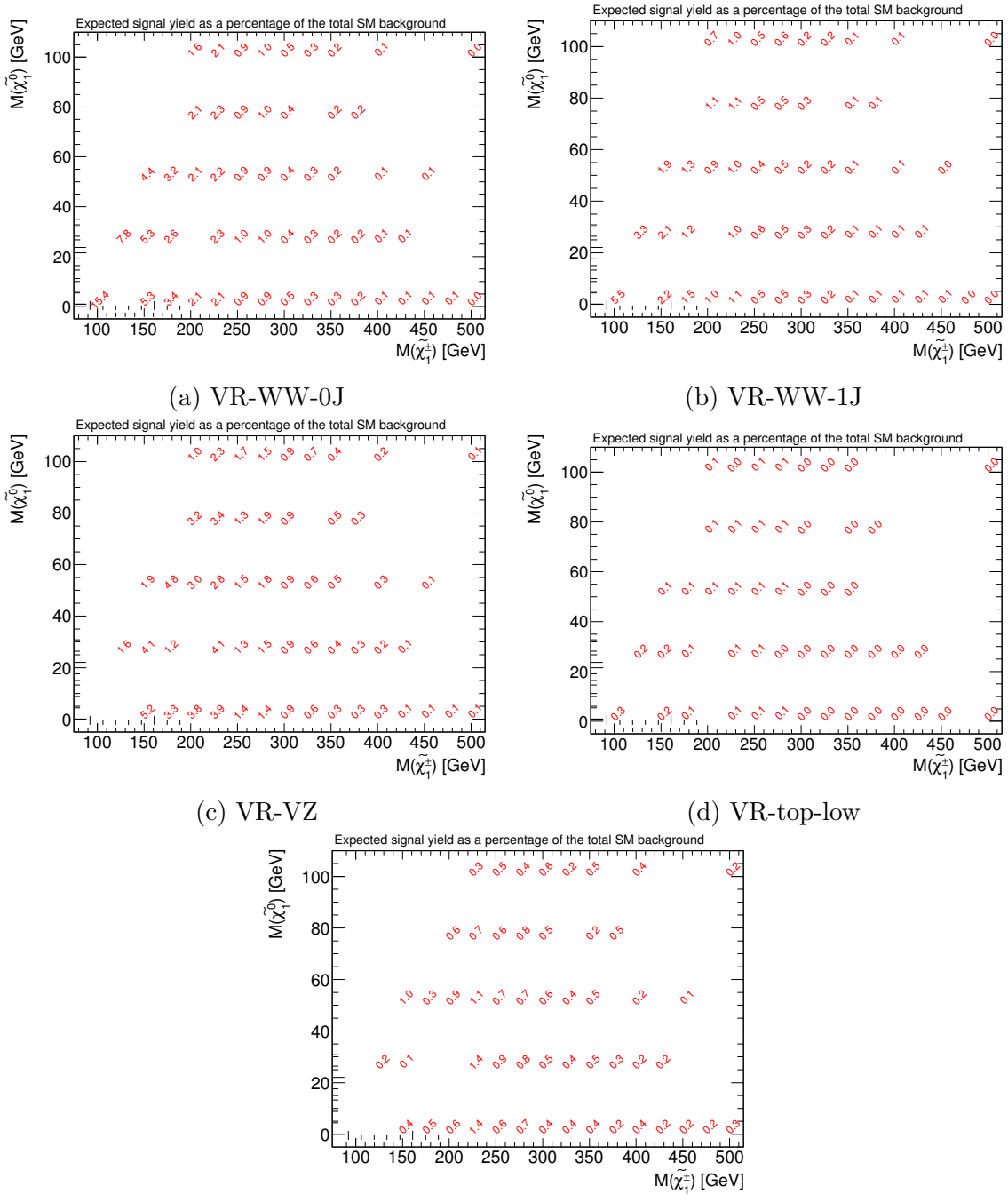

(a) VR-WW-0J

(b) VR-WW-1J

(c) VR-VZ

(d) VR-top-low

(e) VR-top-high

Figure 4.8: Plots of the VR signal contamination over the whole grid. Plots show the signal yield as a percentage of the total expected background yield at each mass point.

4.6 Systematic uncertainties

The profile likelihood fit described in Section 4.7 includes all relevant sources of systematic uncertainties affecting the background estimates and signal predictions, along with statistical uncertainties. The dominant uncertainties come from the jet energy scale (JES) and resolution (JER), the efficiency of b-jet identification and the theoretical uncertainties in the Monte Carlo. A non-negligible contribution also comes from the pile-up re-weighting procedure, where uncertainties account for mis-modelling of the minimum bias overlay used in MC pile-up simulation.

The jet energy scale and jet energy resolution uncertainties are derived using a combination of data and MC, by measuring the balance between a jet and a reference object in di-jet, Z+jets and γ+jets events. They are calculated as a function of the jet p_{T}, η, pile-up conditions and flavour composition of the jet samples [108, 109].

Another uncertainty comes from the $p_{\mathrm{T}}^{\mathrm{miss}}$ soft term's resolution and scale, as discussed in detail in Section 2.4. Uncertainties on the scale factors applied to the MC samples to account for differences between data and simulation in the b-jet identification efficiency are also included. The remaining experimental systematic uncertainties, such as those in the lepton reconstruction efficiency, lepton energy scale and lepton energy resolution and differences of the trigger efficiencies in data and simulation, are included and were found to be negligible. The uncertainty on the luminosity measurement introduced in Section 2.2 is also considered, for the combined 2015–2017 dataset this amounts to 2%.

Several sources of theoretical uncertainty on the modelling of the dominant MC backgrounds are considered. Uncertainties in the MC modelling of diboson events are estimated by varying the PDF sets as well as the renormalisation, factorisation and merging scales used to generate the samples. For $t\bar{t}$ production, uncertainties from the parton shower simulation are accounted for by comparing samples with Powheg interfaced to either Pythia or Herwig++. Another source of uncertainty comes from the modelling of initial and final state radiation (ISR/FSR) where Powheg+Pythia8 is compared to samples with a varied 'hdamp' parameter, as well as considering varied renormalisation and factorisation scales and varying the showering. Finally, for single top Wt production an uncertainty is associated to the treatment of the interference between the Wt and $t\bar{t}$ samples. This compares the nominal sample generated using the diagram removal method to a sample generated using the diagram subtraction method [110].

For the matrix method estimate of the FNP background, systematic uncertainties

Region	SR-DF-0J	SR-DF-1J	SR-SF-0J	SR-SF-1J
m_{T2} [GeV]	$\in[100,\infty)$	$\in[100,\infty)$	$\in[100,\infty)$	$\in[100,\infty)$
Total background expectation	101	83	120	113
MC statistical uncertainties	4%	5%	4%	5%
WW normalisation	6%	5%	4%	3%
VZ normalisation	$< 1\%$	$< 1\%$	2%	2%
$t\bar{t}$ normalisation	4%	6%	2%	4%
Diboson theoretical uncertainties	3%	10%	5%	4%
Top theoretical uncertainties	9%	8%	2%	5%
$p_{\mathrm{T}}^{\mathrm{miss}}$modelling	2%	2%	2%	2%
JES	1%	8%	1%	5%
JER	1%	4%	1%	3%
Pile-up re-weighting	1%	1%	1%	2%
b-tagging	$< 1\%$	6%	$< 1\%$	4%
Lepton modelling	1%	$< 1\%$	$< 1\%$	1%
FNP	$< 1\%$	$< 1\%$	$< 1\%$	$< 1\%$
Total systematic uncertainties	11.8%	17.7%	7.4%	11.0%

Table 4.6: Breakdown of the dominant systematic uncertainties on background estimates in the unbinned SRs requiring $m_{\mathrm{T2}} > 100\,\mathrm{GeV}$. Note that the individual uncertainties can be correlated, and do not necessarily add up quadratically to the total background uncertainty. The percentages show the size of the uncertainty relative to the total expected background. "Top theoretical uncertainties" refers to $t\bar{t}$ theoretical uncertainties and the uncertainty associated to Wt–$t\bar{t}$ interference added quadratically [1].

are assigned to account for possible differences in FNP lepton composition between the regions used to derive the FNP yields and the ones defined to validate the method itself.

A summary of the impact of the systematic uncertainties on the unbinned SRs with $m_{\mathrm{T2}} > 100\,\mathrm{GeV}$, after performing the profile likelihood fit, is shown in Table 4.6. For the binned SRs defined in Table 4.3, the uncertainties associated with limited MC statistics are higher, ranging between 6-20%.

4.7 Results and statistical interpretation

The results of the analysis are statistically interpreted using the HistFitter framework [106]. Initially a background-only fit is performed. This is a simultaneous likelihood fit to the data in the control regions, where likelihood is a product of the Poisson probability density functions describing the data in each region and Gaussian constraints of the nuisance parameters associated with the systematic uncertainties. When the systematic uncertainties are correlated across samples, the fit uses the same nuisance parameter for the different samples. For the background only fit, the background scale factors are included as nuisance parameters. These are measured to be: $\mu_{WW} = 1.36 \pm 0.11$, $\mu_{VZ} = 1.26 \pm 0.06$ and $\mu_{top} = 1.07 \pm 0.17$.

Region	CR-VZ	CR-WW	CR-top
Observed events	487	1480	99
Fitted backgrounds	486 ± 22	1480 ± 40	99 ± 10
Fitted WW	11.3 ± 1.6	1020 ± 80	3.5 ± 1.9
Fitted WZ	114 ± 6	21.6 ± 1.8	0.23 ± 0.09
Fitted ZZ	353 ± 17	0.8 ± 0.1	–
Fitted $t\bar{t}$	$1.2^{+1.3}_{-1.2}$	270 ± 50	81 ± 9
Fitted single top	–	144 ± 23	9.2 ± 1.8
FNP	–	22.0 ± 2.5	3.34 ± 0.32
Other backgrounds	7.4 ± 3.4	1.4 ± 1.1	1.28 ± 0.15
MC exp. WW	8.5	762	2.6
MC exp. WZ	92	17.2	0.18
MC exp. ZZ	282	0.65	–
MC exp. $t\bar{t}$	1.1	256	76
MC exp. single top	–	134	8.6

Table 4.7: Observed events and predicted background yields from the fit for the CRs. For backgrounds whose normalisation is extracted by the fit, the yield expected from the MC before the fit is also reported. The background denoted as "Other" in the Table includes the non-dominant background sources for this analysis, i.e. Z+jets, $t\bar{t}$+V, Higgs and Drell-Yan events [1].

The results of the fit across the control, validation and signal regions are shown in Tables 4.7, 4.8 and 4.9 – 4.12 respectively, which are taken from the analysis conference paper. Good agreement between the observed data yields and fitted Standard Model

Region	VR-WW-0J	VR-WW-1J	VR-VZ	VR-top-low	VR-top-high
Observed events	3873	3509	265	526	121
Fitted background	3970 ± 170	4000 ± 700	260 ± 21	620 ± 100	143 ± 29
Fitted WW	2210 ± 190	1360 ± 150	11.0 ± 1.3	6 ± 5	$2.9^{+3.0}_{-2.9}$
Fitted WZ	49 ± 4	36 ± 4	61 ± 5	0.17 ± 0.13	$0.18^{+0.22}_{-0.18}$
Fitted ZZ	2.97 ± 0.28	1.28 ± 0.21	161 ± 14	–	–
Fitted $t\bar{t}$	1076 ± 200	2000 ± 600	6 ± 4	520 ± 90	118 ± 26
Fitted single top	570 ± 100	640 ± 160	1.7 ± 1.3	87 ± 13	11.5 ± 2.9
FNP	47 ± 6	36 ± 6	–	6.9 ± 0.7	5.8 ± 0.5
Other backgrounds	9 ± 3	5 ± 2	17.7 ± 6.6	–	3.4 ± 0.4
MC exp. WW	1660	1020	8.2	4.5	2.2
MC exp. WZ	39	28	48	0.13	0.14
MC exp. ZZ	2.35	1.01	128	–	–
MC exp. $t\bar{t}$	1000	1800	6	490	110
MC exp. single top	540	600	1.6	81	10.8

Table 4.8: Observed events and predicted background yields from the fit for the VRs. For backgrounds whose normalisation is extracted by the fit, the yield expected from the MC before the fit is also reported. The background denoted as "Other" includes the non-dominant background sources for this analysis, i.e. Z+jets, $t\bar{t}$+V, Higgs and Drell-Yan events. A "–" symbol indicates that the background contribution is negligible [1].

backgrounds is observed for the control and validation regions. For the binned signal regions, no significant deviation between observed data yield and Standard Model background is observed in any bin. The largest excess occurs in the $m_{\mathrm{T2}} = [110, 120]\,\mathrm{GeV}$ bin of SR-SF-0J, but is only 1.95σ. This can also be seen in Figure 4.9, which shows the m_{T2} distributions of the four signal regions.

To obtain exclusion limits for the $\tilde{\chi}_1^{\pm}$ and $\tilde{\chi}_1^0$ masses in this simplified model, the $\mathrm{CL_s}$ prescription is used, as introduced in Section 3.3. The exclusion fit is performed in a similar manner to the background-only fit described above, with the addition of the data in the binned signal regions. The resulting exclusion plot is shown in Figure 4.10. The yellow band on the expected limit includes all systematic uncertainties. The theory error band on the observed contour considers the error on the signal cross section calculation. At 95% confidence level, $\tilde{\chi}_1^{\pm}$ masses up to 410 GeV are excluded for a massless $\tilde{\chi}_1^0$. For high mass-differences, the observed limit is stronger than the expected limit. This suggests that a deficit in the data was observed relative to the SM background estimate

SR-DF-0J m_{T2} bin	[100, 105]	[105, 110]	[110, 120]	[120, 140]	[140, 160]	[160, 180]	[180, 220]	> 220
Observed events	13	17	21	12	8	7	5	3
Fitted backgrounds	17.00 ± 4.00	16.24 ± 3.28	20.39 ± 3.04	22.15 ± 2.76	9.43 ± 1.20	5.80 ± 0.86	5.44 ± 0.98	5.01 ± 0.66
Fitted WW	7.39 ± 1.32	8.95 ± 1.26	14.21 ± 1.73	16.98 ± 2.17	8.77 ± 1.09	5.37 ± 0.81	4.71 ± 0.88	4.85 ± 0.64
Fitted WZ	0.31 ± 0.12	0.21 ± 0.14	0.46 ± 0.24	0.37 ± 0.09	0.21 ± 0.04	0.17 ± 0.04	0.15 ± 0.04	0.15 ± 0.02
Fitted ZZ	0.10 ± 0.05	0.05 ± 0.04	0.10 ± 0.05	0.19 ± 0.03	0.05 ± 0.01	0.07 ± 0.01	0.10 ± 0.04	0.00 ± 0.00
Fitted $t\bar{t}$	6.92 ± 3.24	4.85 ± 2.38	4.49 ± 2.49	2.69 ± 1.33	$0.31^{+0.33}_{-0.31}$	0.00 ± 0.00	0.00 ± 0.00	0.00 ± 0.00
Fitted single top	1.83 ± 1.11	1.97 ± 1.24	0.86 ± 0.46	0.00 ± 0.00	0.00 ± 0.00	0.00 ± 0.00	0.00 ± 0.00	0.00 ± 0.00
FNP leptons	0.44 ± 0.06	0.00 ± 0.20	0.00 ± 0.41	1.66 ± 0.17	0.08 ± 0.04	0.17 ± 0.05	0.46 ± 0.12	0.00 ± 0.05
Other backgrounds	0.02 ± 0.01	0.20 ± 0.16	0.25 ± 0.04	0.26 ± 0.06	$0.02^{+0.03}_{-0.02}$	0.03 ± 0.01	0.03 ± 0.01	0.00 ± 0.00
Simulated WW	5.44 ± 0.80	6.59 ± 0.75	10.46 ± 0.93	12.50 ± 1.24	6.45 ± 0.63	3.95 ± 0.51	3.47 ± 0.58	3.57 ± 0.37
Simulated WZ	0.25 ± 0.10	0.16 ± 0.11	0.36 ± 0.19	0.29 ± 0.07	0.16 ± 0.03	0.14 ± 0.04	0.12 ± 0.03	0.12 ± 0.02
Simulated ZZ	0.08 ± 0.04	0.04 ± 0.03	0.08 ± 0.04	0.15 ± 0.02	0.04 ± 0.01	0.06 ± 0.01	0.08 ± 0.03	0.00 ± 0.00
Simulated $t\bar{t}$	6.46 ± 3.00	4.52 ± 2.16	4.20 ± 2.19	2.51 ± 1.20	$0.29^{+0.32}_{-0.29}$	0.00 ± 0.00	0.00 ± 0.00	0.00 ± 0.00
Simulated singletop	1.71 ± 1.06	1.85 ± 1.15	0.80 ± 0.42	0.00 ± 0.00	0.00 ± 0.00	0.00 ± 0.00	0.00 ± 0.00	0.00 ± 0.00

Table 4.9: Background-only fit results for SR-DF-0J. All the experimental and theory uncertainties are included. Table taken from the analysis conference paper [1].

SR-DF-1J m_{T2} bin	[100, 105]	[105, 110]	[110, 120]	[120, 140]	[140, 160]	[160, 180]	[180, 220]	> 220
Observed events	16	12	13	20	6	5	2	2
Fitted backgrounds	22.34 ± 5.20	12.60 ± 3.04	15.40 ± 4.29	15.00 ± 3.14	6.28 ± 1.28	3.73 ± 0.88	4.84 ± 1.08	3.96 ± 0.97
Fitted WW	6.14 ± 1.69	4.97 ± 1.39	8.59 ± 2.19	10.18 ± 2.45	5.08 ± 1.21	3.35 ± 0.83	3.87 ± 1.00	2.65 ± 0.78
Fitted WZ	0.27 ± 0.11	0.31 ± 0.19	0.18 ± 0.15	0.27 ± 0.09	0.29 ± 0.12	0.16 ± 0.15	0.23 ± 0.07	0.10 ± 0.06
Fitted ZZ	0.06 ± 0.06	$0.06^{+0.07}_{-0.06}$	$0.02^{+0.04}_{-0.02}$	0.10 ± 0.07	0.08 ± 0.04	0.12 ± 0.03	0.18 ± 0.06	0.00 ± 0.00
Fitted $t\bar{t}$	11.21 ± 3.94	4.63 ± 1.72	5.18 ± 2.44	3.41 ± 1.48	0.35 ± 0.29	0.00 ± 0.00	0.00 ± 0.00	0.00 ± 0.00
Fitted singletop	3.31 ± 2.05	1.89 ± 1.34	1.29 ± 1.16	0.77 ± 0.45	0.00 ± 0.00	0.00 ± 0.00	0.00 ± 0.00	0.00 ± 0.00
FNP leptons	1.30 ± 0.14	0.70 ± 0.09	0.00 ± 0.28	0.00 ± 0.36	0.00 ± 0.11	0.00 ± 0.12	0.54 ± 0.08	1.16 ± 0.25
Other backgrounds	0.05 ± 0.02	0.04 ± 0.02	0.12 ± 0.05	0.27 ± 0.06	0.47 ± 0.07	0.09 ± 0.03	0.03 ± 0.01	0.04 ± 0.02
Simulated WW	4.52 ± 1.18	3.66 ± 0.98	6.33 ± 1.53	7.49 ± 1.70	3.74 ± 0.87	2.47 ± 0.59	2.85 ± 0.71	1.95 ± 0.56
Simulated WZ	0.22 ± 0.09	0.24 ± 0.15	0.15 ± 0.12	0.21 ± 0.07	0.23 ± 0.09	0.13 ± 0.12	0.18 ± 0.06	0.08 ± 0.05
Simulated ZZ	0.05 ± 0.05	$0.05^{+0.05}_{-0.05}$	$0.01^{+0.03}_{-0.01}$	0.08 ± 0.05	0.06 ± 0.03	0.09 ± 0.03	0.14 ± 0.05	0.00 ± 0.00
Simulated $t\bar{t}$	10.56 ± 3.41	4.36 ± 1.52	4.88 ± 2.17	3.21 ± 1.38	0.33 ± 0.26	0.00 ± 0.00	0.00 ± 0.00	0.00 ± 0.00
Simulated singletop	3.09 ± 1.80	1.77 ± 1.27	1.21 ± 1.10	0.72 ± 0.40	0.00 ± 0.00	0.00 ± 0.00	0.00 ± 0.00	0.00 ± 0.00

Table 4.10: Background-only fit results for SR-DF-1J. All the experimental and theory uncertainties are included. Table taken from the analysis conference paper [1].

SR-SF-0J m_{T2} bin	[100, 105]	[105, 110]	[110, 120]	[120, 140]	[140, 160]	[160, 180]	[180, 220]	> 220
Observed events	13	19	34	25	11	12	7	13
Fitted backgrounds	15.65 ± 2.48	13.10 ± 2.16	23.87 ± 2.21	26.86 ± 2.42	15.53 ± 1.48	8.52 ± 0.95	10.75 ± 1.61	8.28 ± 0.90
Fitted WW	5.57 ± 1.01	4.96 ± 0.90	10.59 ± 1.62	13.25 ± 1.93	7.15 ± 1.07	3.82 ± 0.71	4.65 ± 0.91	3.62 ± 0.62
Fitted WZ	0.55 ± 0.12	0.92 ± 0.12	2.29 ± 0.28	2.89 ± 0.25	1.73 ± 0.17	1.11 ± 0.17	0.92 ± 0.14	0.69 ± 0.07
Fitted ZZ	2.08 ± 0.30	2.30 ± 0.37	5.85 ± 0.56	7.77 ± 0.63	5.51 ± 0.54	3.56 ± 0.35	4.06 ± 0.61	3.95 ± 0.42
Fitted $t\bar{t}$	3.74 ± 1.09	3.83 ± 1.19	4.47 ± 1.12	1.25 ± 0.63	$0.33^{+0.39}_{-0.33}$	$0.02^{+0.04}_{-0.02}$	0.00 ± 0.00	0.00 ± 0.00
Fitted singletop	1.89 ± 1.30	1.09 ± 0.67	$0.66^{+0.71}_{-0.66}$	0.00 ± 0.00	0.00 ± 0.00	0.00 ± 0.00	0.00 ± 0.00	0.00 ± 0.00
FNP leptons	0.96 ± 0.11	0.00 ± 0.26	0.00 ± 0.36	1.26 ± 0.11	0.24 ± 0.02	0.00 ± 0.18	1.05 ± 0.16	0.00 ± 0.24
Other backgrounds	0.86 ± 0.45	0.00 ± 0.00	0.00 ± 0.00	0.44 ± 0.19	0.57 ± 0.07	0.00 ± 0.00	0.06 ± 0.04	$0.01^{+0.14}_{-0.01}$
Simulated WW	4.10 ± 0.63	3.65 ± 0.57	7.80 ± 0.96	9.75 ± 1.15	5.26 ± 0.65	2.81 ± 0.45	3.42 ± 0.60	2.66 ± 0.39
Simulated WZ	0.44 ± 0.10	0.72 ± 0.09	1.81 ± 0.20	2.29 ± 0.17	1.37 ± 0.12	0.88 ± 0.13	0.73 ± 0.11	0.54 ± 0.05
Simulated ZZ	1.64 ± 0.22	1.82 ± 0.28	4.63 ± 0.39	6.14 ± 0.39	4.36 ± 0.37	2.82 ± 0.24	3.21 ± 0.46	3.12 ± 0.28
Simulated $t\bar{t}$	3.51 ± 0.97	3.60 ± 1.12	4.19 ± 0.87	1.17 ± 0.55	$0.31^{+0.36}_{-0.31}$	$0.02^{+0.04}_{-0.02}$	0.00 ± 0.00	0.00 ± 0.00
Simulated singletop	1.77 ± 1.28	1.02 ± 0.65	$0.61^{+0.65}_{-0.61}$	0.00 ± 0.00	0.00 ± 0.00	0.00 ± 0.00	0.00 ± 0.00	0.00 ± 0.24

Table 4.11: Background-only fit results for SR-SF-0J. All the experimental and theory uncertainties are included. Table taken from the analysis conference paper [1].

SR-SF-1J m_{T2} bin	[100, 105]	[105, 110]	[110, 120]	[120, 140]	[140, 160]	[160, 180]	[180, 220]	> 220
Observed events	16	14	26	16	19	7	7	10
Fitted backgrounds	21.90 ± 5.86	14.21 ± 3.32	15.90 ± 3.23	19.27 ± 2.54	14.21 ± 2.29	7.01 ± 0.89	8.93 ± 1.62	13.55 ± 2.88
Fitted WW	5.24 ± 0.98	4.04 ± 1.10	5.45 ± 0.89	8.42 ± 1.43	4.30 ± 0.82	2.79 ± 0.45	3.33 ± 0.66	2.58 ± 0.66
Fitted WZ	0.80 ± 0.19	0.99 ± 0.22	1.49 ± 0.29	2.72 ± 0.48	1.87 ± 0.37	1.50 ± 0.24	1.53 ± 0.31	1.35 ± 0.32
Fitted ZZ	1.29 ± 0.31	1.88 ± 0.44	2.27 ± 0.63	4.32 ± 0.79	3.95 ± 0.77	2.43 ± 0.35	2.83 ± 0.69	2.89 ± 0.69
Fitted $t\bar{t}$	9.37 ± 3.83	4.40 ± 1.84	4.72 ± 1.86	0.97 ± 0.93	0.00 ± 0.00	$0.14^{+0.17}_{-0.14}$	0.00 ± 0.00	0.00 ± 0.00
Fitted singletop	3.08 ± 2.45	0.72 ± 0.58	0.96 ± 0.76	0.58 ± 0.41	0.00 ± 0.00	0.00 ± 0.00	0.00 ± 0.00	0.00 ± 0.00
FNP leptons	1.24 ± 0.13	1.22 ± 0.18	0.00 ± 0.23	1.00 ± 0.13	3.04 ± 0.48	0.14 ± 0.03	1.25 ± 0.21	3.16 ± 0.66
Other backgrounds	0.88 ± 0.60	$0.95^{+1.03}_{-0.95}$	$1.00^{+1.72}_{-1.00}$	1.26 ± 0.74	1.06 ± 0.45	0.00 ± 0.00	0.00 ± 0.00	3.57 ± 0.95
Simulated WW	3.86 ± 0.64	2.98 ± 0.75	4.01 ± 0.54	6.20 ± 0.92	3.16 ± 0.54	2.06 ± 0.28	2.45 ± 0.44	1.90 ± 0.45
Simulated WZ	0.64 ± 0.15	0.78 ± 0.17	1.18 ± 0.23	2.15 ± 0.37	1.48 ± 0.28	1.19 ± 0.18	1.21 ± 0.24	1.07 ± 0.25
Simulated ZZ	1.02 ± 0.24	1.48 ± 0.34	1.79 ± 0.49	3.41 ± 0.60	3.12 ± 0.58	1.92 ± 0.26	2.23 ± 0.53	2.28 ± 0.54
Simulated $t\bar{t}$	8.76 ± 3.44	4.11 ± 1.63	4.42 ± 1.62	0.91 ± 0.85	0.00 ± 0.00	$0.14^{+0.16}_{-0.14}$	0.00 ± 0.00	0.00 ± 0.00
Simulated singletop	2.89 ± 2.31	0.68 ± 0.51	0.89 ± 0.74	0.54 ± 0.38	0.00 ± 0.00	0.00 ± 0.00	0.00 ± 0.00	0.00 ± 0.00

Table 4.12: Background-only fit results for SR-SF-1J. All the experimental and theory uncertainties are included. Table taken from the analysis conference paper [1].

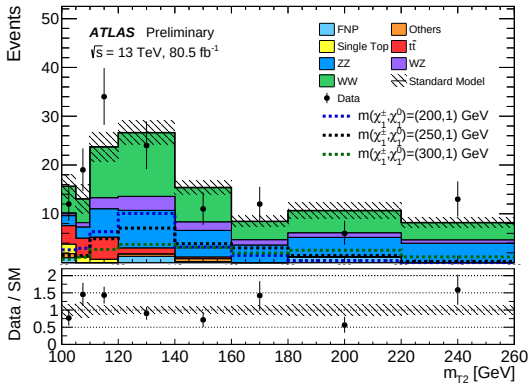

(a) SR-SF-0

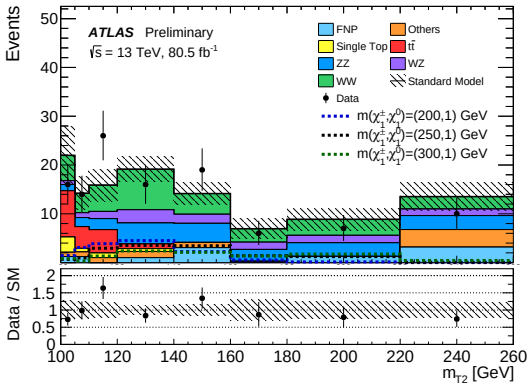

(b) SR-SF-1

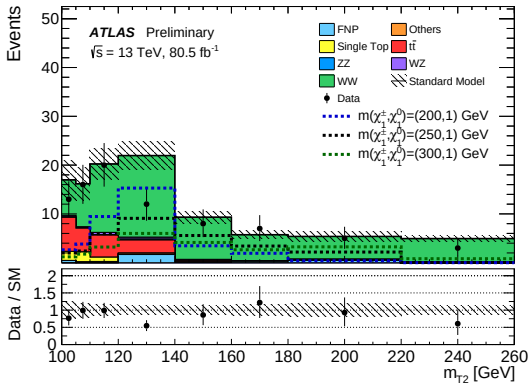

(c) SR-DF-0

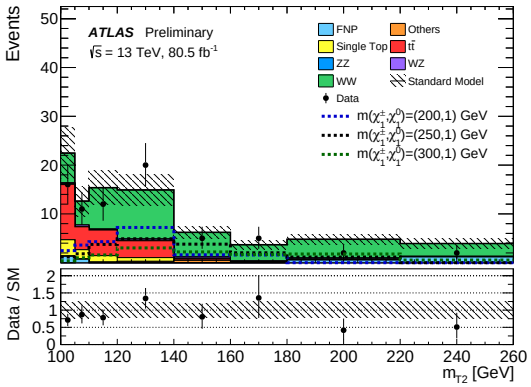

(d) SR-DF-1

Figure 4.9: Distributions of m_{T2} in the signal regions, for data and the estimated SM backgrounds. The normalisation factors extracted from the corresponding CRs are used to rescale the $t\bar{t}$, Wt, WW, WZ and ZZ backgrounds. Negligible backgrounds are not included in the legends. The uncertainty band includes all systematic and statistical sources and the last bin includes the overflow. Distributions for three benchmark signal points are overlaid for comparison [1].

in bins particularly sensitive to this region of mass space. Indeed the data observation does lie below the expected yield in the high m_{T2} bins of the SRs, in particular in SR-DF-1, the final two m_{T2} bins both have a deficit of $\sim 2\sigma$.

This exclusion limit is significantly larger than the Run 1 result. Some improvement can be expected from the increased collision centre of mass energy from 7 TeV to 13 TeV, along with the increased size of the dataset. The Run 1 result additionally lacked the increased sensitivity resulting from binning in m_{T2}, using $p_{\mathrm{T}}^{\mathrm{miss}}$ Significance, and adding in the 1-jet channels. A comparison can also be drawn with the most recent result for this process from CMS. The CMS result [111] only uses the 2015–2016 dataset, and does

not make use of $p_{\mathrm{T}}^{\mathrm{miss}}$ Significance, however it produces a set of signal regions binned in m_{T2} and $p_{\mathrm{T}}^{\mathrm{miss}}$ and exploits the possibility of an ISR jet. Chargino masses of 170–200 GeV were excluded for a neutralino mass of 1 GeV, substantially weaker limits than have been placed by the analysis in this Chapter. A discussion of this analysis's place in the wider context of ATLAS searches for electroweak supersymmetry is left to Section 5.6 using the results of the full Run 2 analysis.

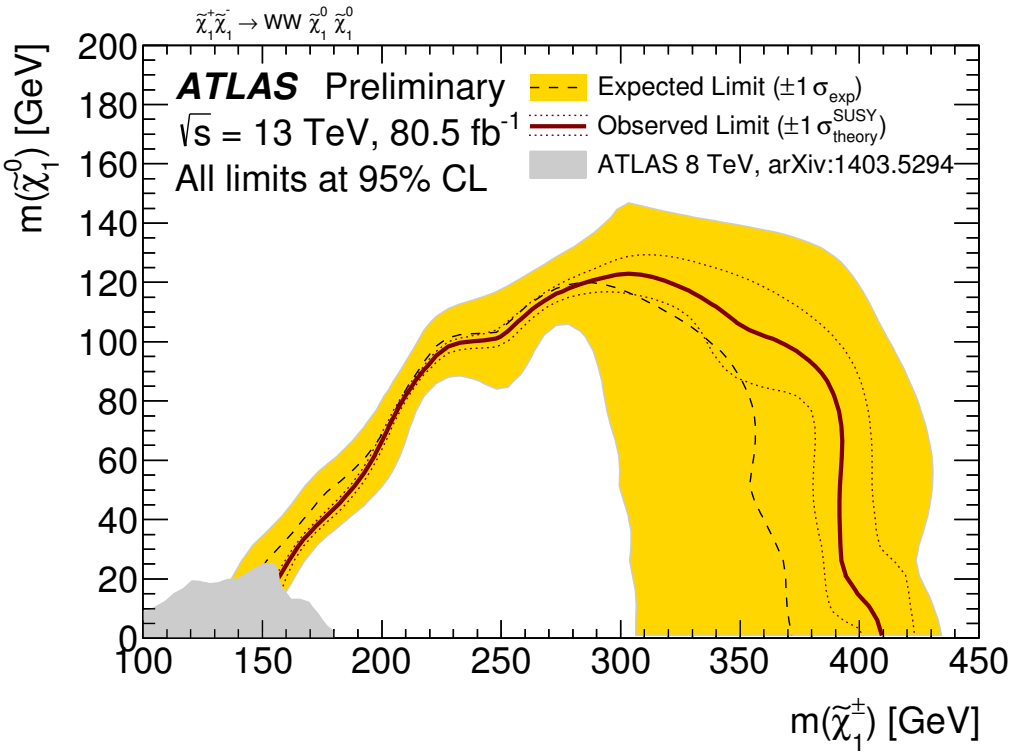

Figure 4.10: Observed and expected exclusion limits on SUSY simplified models for chargino-pair production with W-boson mediated decays. The observed (solid thick line) and expected (thin dashed line) exclusion contours are indicated. The upper shaded band corresponds to the $\pm 1\sigma$ variations in the expected limit, including all uncertainties except theoretical uncertainties in the signal cross section. The dotted lines around the observed limit illustrate the change in the observed limit as the nominal signal cross section is scaled up and down by the theoretical uncertainty. All limits are computed at 95% confidence level. The observed limits obtained from ATLAS in Run-1 are also shown [79].

Model-independent limits for possible BSM physics processes are also considered. The upper limit of the visible signal cross section $\sigma_{\mathrm{obs}}^{0.95}$ (defined as cross section times efficiency) is set for each of the unbinned signal regions. These are calculated by performing separate model-independent fits for each signal region which take the observed

data as a constraint and add a 'signal yield' contribution to the total background, as a free parameter. The model-independent fit results are presented in Table 4.13, where the observed ($S^{0.95}_{\text{obs}}$) and expected ($S^{0.95}_{\text{exp}}$) BSM process yields at 95% CL are shown in addition to the $\sigma^{0.95}_{\text{obs}}$ limits. Furthermore the p_0 values are shown. These measure the probability of the Standard Model background to fluctuate up to at least the observed data yield. Here a value of $p_0 < 0.05$ indicates a rejection of the SM-only hypothesis.

4.8 Conclusions

This Chapter presented the first search in ATLAS Run 2 for the electroweak pair production of charginos decaying via W-bosons into final states with exactly two oppositely charged leptons and $p_{\text{T}}^{\text{miss}}$. This analysis used the $80.5\,\text{fb}^{-1}$ of pp collision data collected by the ATLAS detector between 2015 and 2017. No significant excess above the SM was observed so exclusion limits were placed on the chargino and neutralino masses. At 95% CL, chargino masses up to 410 GeV were excluded for a massless neutralino. This result greatly improves on the corresponding Run 1 result [79]. The results also provide better exclusion than the first Run 2 CMS result, using 2015-2016 data [80].

Region	SR-SF-0J $[100, \infty]$	SR-SF-0J $[160, \infty]$	SR-SF-0J $[100, 120]$	SR-SF-0J $[120, 160]$
Observed events	131	31	65	35
Fitted background	119.67 ± 9.0	27.1 ± 2.7	50.9 ± 5.7	42.3 ± 3.4
Fitted WW	53.2 ± 7.7	12.0 ± 2.0	21.0 ± 3.3	20.3 ± 2.9
Fitted WZ	11.09 ± 0.74	2.72 ± 0.26	3.75 ± 0.44	4.62 ± 0.35
Fitted ZZ	35.1 ± 2.4	11.6 ± 1.0	10.2 ± 1.0	13.28 ± 0.95
Fitted $t\bar{t}$	13.9 ± 3.2	$0.02^{+0.04}_{-0.02}$	12.3 ± 2.9	1.61 ± 0.66
Fitted single top	3.7 ± 2.2	–	3.7 ± 2.2	$0.00^{+0.15}_{-0.00}$
FNP	2.03 ± 0.21	0.82 ± 0.11	$0.00^{+0.01}_{-0.00}$	1.51 ± 0.12
Other backgrounds	$0.6^{+1.7}_{-0.6}$	$0.00^{+0.30}_{-0.00}$	$0.00^{+1.5}_{-0.00}$	1.02 ± 0.19
$S^{0.95}_{\text{obs}}$	42.0	16.4	34.2	11.5
$S^{0.95}_{\text{exp}}$	$31.1^{+12.5}_{-8.1}$	$14.7^{+4.0}_{-5.4}$	$22.0^{+6.6}_{-8.0}$	$15.8^{+5.8}_{-4.1}$
$\sigma^{0.95}_{\text{obs}}$ [fb]	0.52	0.21	0.43	0.14
p_0	0.17	0.23	0.05	0.50

Region	SR-SF-1J $[100, \infty]$	SR-SF-1J $[160, \infty]$	SR-SF-1J $[100, 120]$	SR-SF-1J $[120, 160]$
Observed events	114	23	56	35
Fitted background	114 ± 13	29 ± 5	51.7 ± 10.0	33 ± 4
Fitted WW	36 ± 5	8.6 ± 1.7	14.6 ± 2.4	12.6 ± 1.9
Fitted WZ	12.2 ± 1.7	4.38 ± 0.80	3.28 ± 0.47	4.59 ± 0.75
Fitted ZZ	21.8 ± 3.0	8.1 ± 1.5	5.43 ± 0.95	8.3 ± 1.3
Fitted $t\bar{t}$	20.0 ± 7.5	$0.15^{+0.17}_{-0.15}$	19 ± 7	0.99 ± 0.95
Fitted single top	5.4 ± 3.5	–	4.9 ± 3.2	0.59 ± 0.41
FNP	10.44 ± 0.83	4.58 ± 0.68	1.79 ± 0.16	4.07 ± 0.45
Other backgrounds	8.0 ± 2.7	2.8 ± 1.5	2.9 ± 1.8	2.34 ± 0.89
$S^{0.95}_{\text{obs}}$	32.3	11.6	29.0	18.4
$S^{0.95}_{\text{exp}}$	$30.9^{+13.2}_{-7.4}$	$14.1^{+5.9}_{-3.2}$	$27.5^{+9.1}_{-8.3}$	$17.2^{+3.5}_{-6.9}$
$\sigma^{0.95}_{\text{obs}}$ [fb]	0.40	0.15	0.36	0.23
p_0	0.47	0.50	0.35	0.39

Region	SR-DF-0J $[100, \infty]$	SR-DF-0J $[160, \infty]$	SR-DF-0J $[100, 120]$	SR-DF-0J $[120, 160]$
Observed events	84	15	49	20
Fitted background	100.8 ± 11.9	16.1 ± 2.0	53.4 ± 9.0	31.5 ± 3.5
Fitted WW	70.7 ± 7.5	14.8 ± 1.9	30.3 ± 3.5	25.6 ± 3.0
Fitted WZ	2.02 ± 0.25	0.47 ± 0.07	0.98 ± 0.21	0.58 ± 0.10
Fitted ZZ	0.66 ± 0.08	0.17 ± 0.04	$0.25^{+0.25}_{-0.25}$	0.23 ± 0.04
Fitted $t\bar{t}$	19.6 ± 9.3	–	16.6 ± 7.9	3.1 ± 1.5
Fitted single top	4.8 ± 2.6	–	4.8 ± 2.6	$0.00^{+0.14}_{-0.00}$
FNP	2.19 ± 0.33	0.53 ± 0.15	$0.00^{+0.05}_{-0.00}$	1.75 ± 0.17
Other backgrounds	0.81 ± 0.18	0.05 ± 0.01	0.47 ± 0.17	0.28 ± 0.07
$S^{0.95}_{\text{obs}}$	23.1	9.2	20.9	7.4
$S^{0.95}_{\text{exp}}$	$33.1^{+11.1}_{-8.7}$	$9.7^{+4.0}_{-2.8}$	$23.4^{+9.1}_{-6.4}$	$13.6^{+5.1}_{-3.7}$
$\sigma^{0.95}_{\text{obs}}$ [fb]	0.29	0.12	0.26	0.09
p_0	0.50	0.48	0.50	0.50

Region	SR-DF-1J $[100, \infty]$	SR-DF-1J $[160, \infty]$	SR-DF-1J $[100, 120]$	SR-DF-1J $[120, 160]$
Observed events	73	9	39	25
Fitted background	83.5 ± 14.6	12.2 ± 2.5	50.6 ± 10.7	21.2 ± 4.0
Fitted WW	45 ± 10	9.8 ± 2.3	19.6 ± 4.8	15.2 ± 3.5
Fitted WZ	1.83 ± 0.45	0.50 ± 0.15	0.77 ± 0.24	0.56 ± 0.17
Fitted ZZ	0.60 ± 0.15	0.29 ± 0.09	0.14 ± 0.04	0.17 ± 0.05
Fitted $t\bar{t}$	25.2 ± 8.4	–	21.4 ± 7.3	3.8 ± 1.6
Fitted single top	7.4 ± 4.1	–	6.6 ± 3.7	0.78 ± 0.46
FNP	2.77 ± 0.27	1.48 ± 0.20	1.90 ± 0.16	$0.00^{+0.01}_{-0.00}$
Other backgrounds	1.11 ± 0.18	0.15 ± 0.04	0.21 ± 0.07	0.75 ± 0.10
$S^{0.95}_{\text{obs}}$	24.0	6.8	17.8	14.4
$S^{0.95}_{\text{exp}}$	$29.2^{+11.5}_{-8.0}$	$8.4^{+4.2}_{-2.6}$	$25.8^{+9.3}_{-8.3}$	$13.4^{+4.3}_{-2.1}$
$\sigma^{0.95}_{\text{obs}}$ [fb]	0.30	0.09	0.22	0.18
p_0	0.50	0.50	0.50	0.23

Table 4.13: Observed events and predicted background yields from the fit for the unbinned SRs. The model independent upper limits on the observed and expected number of BSM events $S^{0.95}_{\text{obs/exp}}$ and the effective BSM cross section $\sigma^{0.95}_{\text{obs}}$ are also reported. The last row reports the p_0-value of the SM-only hypothesis. For SRs where the data yield is smaller than expected, the p-value is truncated at 0.50. A "–" symbol indicates that the background contribution is negligible [1].

Chapter 5

Extending the search for electroweak supersymmetry with the full Run-2 dataset

5.1 Introduction

This Chapter describes a follow-up search for chargino pair production with W-boson mediated decays with the ATLAS detector, which included several improvements. Firstly, 59.9 fb^{-1} data collected in 2018, with an uncertainty of 2%, was added to the search, giving a total luminosity of 139.5 fb^{-1} of data from LHC pp collisions collected in 2015-2018, at $\sqrt{s} = 13\,\text{TeV}$. Secondly, the scope of the resulting publication accepted by EPJC [2] was expanded to include interpretations for additional simplified SUSY models involving slepton production. The results were made public [112] and presented at the SUSY19 conference on the 20^{th} May 2019.

This search was based on the analysis described in Chapter 4, re-optimised for the full Run 2 dataset. As is shown in Figure 2.3b, the 2018 dataset has a higher average level of pile-up. This is due to the increase in the proton-proton collision rate, and leads to a larger amount of contamination in each event coming from objects or detector hits that actually belong to adjacent events. The increased pile-up means that updating the analysis with the additional dataset is not as straightforward as simply adding in the new events.

The author performed a re-optimisation of the signal region binning in order to

exploit the additional event statistics whilst avoiding mis-modelling coming from higher pile-up. Other analysers re-optimised the data-driven background estimate, whilst the author maintained their implementation in HistFitter.

The author performed the full statistical analysis of the data to produce model-dependent limits for the three SUSY processes, in addition to model-independent upper limits on possible new-physics process cross sections. The author also produced most of the plots for both the internal documentation, public note and submitted paper. Unless otherwise stated the author produced all plots shown in this Chapter. Other analysers calculated the experimental and theoretical systematic uncertainties. The author ran the background only fits which calculated the yields and uncertainty values shown in all Tables in this Chapter.

This analysis primarily targets the same direct production of $\tilde{\chi}_1^+\tilde{\chi}_1^-$, where each decays to the $\tilde{\chi}_1^0$ and a real W-boson. Two additional processes involving sleptons, the superpartners of leptons, are targeted. First, direct pair production of sleptons ($\tilde{\ell}$) is considered, where each slepton decays to a lepton and a neutralino. Only selectron and smuon modes are considered in the model, so the final state will either contain two oppositely charged electrons or two oppositely charged muons. The free parameters of interest in this model are the masses of the slepton and neutralino, which define the two-dimensional grid on which exclusion limits are placed. All other sparticle masses are defined to be too heavy for LHC production, and couplings are set to zero.

Secondly, direct pair production of $\tilde{\chi}_1^+\tilde{\chi}_1^-$ with each decaying into either a lepton-sneutrino pair ($\ell\tilde{\nu}$) or a slepton-neutrino pair ($\tilde{\ell}\nu$), is considered. Each of these two choices has a 50% branching ratio. Each slepton decays to a lepton and neutralino; each sneutrino decays to a neutrino and neutralino. In this case all three generations of slepton and lepton are considered, and the slepton and sneutrino masses are chosen to be midway between the chargino and neutralino masses. Each of the three generations has an equal branching ratio. In the case where taus are produced, they are considered only if they decay leptonically into elecrons or muons. Apart from the masses of the chargino and neutralino, all other masses in the model are constrained to be out of reach of the LHC and all other couplings are set to zero. Schematic diagrams for these processes are shown in Figure 5.1.

The data and MC samples used in this analysis are largely the same as in the previous Chapter, along with the object selections. For details on these, please refer to the paper corresponding to this analysis, found in Ref. [2]. This Chapter will focus on the updates

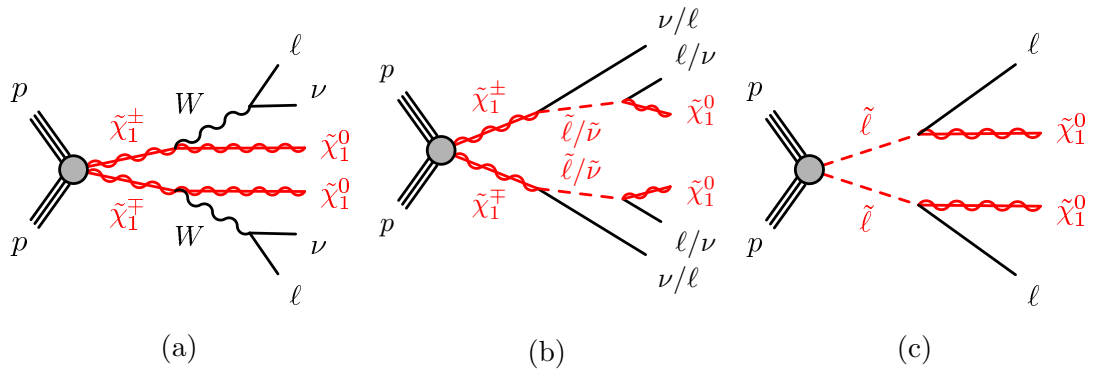

Figure 5.1: Diagrams of the supersymmetric models considered in this chapter: (a) $\tilde{\chi}_1^+\tilde{\chi}_1^-$ production with W-boson-mediated decays, (b) $\tilde{\chi}_1^+\tilde{\chi}_1^-$ production with slepton/sneutrino-mediated-decays and (c) slepton pair production. Diagrams taken from the analysis paper [2].

and improvements to the analysis relative to Chapter 4.

This Chapter begins in Section 5.2, where the signal region optimisation is presented. The background estimation strategy is described in Section 5.3. The systematic uncertainties included in the analysis are described in Section 5.4. Finally, the results and conclusions are presented in Sections 5.5 and 5.6 respectively.

5.2 Updates to the signal regions

This analysis uses signal regions for exclusion limits and model-independent limits based on those used in Section 4.4. Except for where specifically mentioned below, the definitions for these regions are the same, along with the justifications for the choices made. These signal regions are optimised for sensitivity to the electroweak supersymmetry process where charginos are pair-produced and decay to neutralinos via a SM W-boson. Since the final state for the other two supersymmetry processes considered is very similar — consisting of two oppositely-charged hard leptons and a large amount of $p_{\mathrm{T}}^{\mathrm{miss}}$ — the same regions are used to place exclusion limits on these two processes also.

In order to remain kinematically close to the re-optimised control and validation regions used for the data-driven SM background estimation, a cut on the lepton invariant mass $m_{\ell\ell}$is placed at $m_{\ell\ell} > 100\,\mathrm{GeV}$ in all signal regions. For the case of SF leptons, a Z mass veto is also applied, so the final $m_{\ell\ell}$ cut is $m_{\ell\ell} > 121.2\,\mathrm{GeV}$. With the addition of the 2018 dataset, the signal region event yields are higher. This allowed the author

to re-optimise the m_{T2} binning used for the exclusion fit signal regions.

Optimisation was performed using a similar strategy to Section 4.4.The final binning strategy chosen is shown in Table 5.1, where it can also be seen that other cuts remain unchanged from the previous analysis iteration. This Table also shows the unchanged 'Unbinned' signal regions used to place model-independent limits.

Signal region (SR)	SR-DF-0J	SR-DF-1J	SR-SF-0J	SR-SF-1J
$n_{\text{non-}b\text{-tagged jets}}$	$= 0$	$= 1$	$= 0$	$= 1$
$m_{\ell_1\ell_2}$ [GeV]	>100		>121.2	
$p_{\mathrm{T}}^{\mathrm{miss}}$[GeV]	>110			
$p_{\mathrm{T}}^{\mathrm{miss}}$significance	>10			
$n_{b\text{-tagged jets}}$	$= 0$			
Binned SRs				
m_{T2} [GeV]	$\in[100,105)$			
	$\in[105,110)$			
	$\in[110,120)$			
	$\in[120,140)$			
	$\in[140,160)$			
	$\in[160,180)$			
	$\in[180,220)$			
	$\in[220,260)$			
	$\in[260,\infty)$			
Unbinned SRs for model-independent limits				
m_{T2} [GeV]	$\in[100,\infty)$			
	$\in[160,\infty)$			
	$\in[100,120)$			
	$\in[120,160)$			

Table 5.1: The definitions of the binned and inclusive signal regions. Relevant kinematic variables are defined in the text. The bins labelled 'DF' or 'SF' refer to signal regions with different lepton flavour or same lepton flavour pair combinations, respectively, and the '0J' and '1J' labels refer to the multiplicity of non-b-tagged jets. Table taken from the analysis paper [2].

5.3 Outline of background estimation techniques

This analysis uses a data-driven background estimation based on that used in Section 4.5. Except for where specifically mentioned below, the definitions for these regions are the same, along with the justifications for the choices made. The control and validation regions used were re-optimised for the full Run 2 dataset. These re-optimisations do not reflect inadequacies with the previous approach, but ensure reasonable purities and low signal contamination is present with the addition of 2018 data; and remain in regions where the updated MC samples show good modelling.

Definitions of the three control regions used are found in Table 5.2. Plots showing examples of kinematic distributions in the control regions are shown in Figure 5.2. Here it can be seen that the tightened constraint on $p_{\mathrm{T}}^{\mathrm{miss}}$ in CR-WW has removed the region of phase space where mis-modelling seen in the previous Chapter. Corresponding plots showing the contamination from the signal process with charginos decaying via W-bosons as a percentage of the total background yield, are displayed in Figure 5.3

As in the previous analysis, the sub-dominant backgrounds are estimated directly from Monte Carlo. The FNP background is estimated using the matrix method, as described in the paper [2].

Region	CR-WW	CR-VZ	CR-top
Lepton flavour	DF	SF	DF
$n_{b\text{-tagged jets}}$	$= 0$	$= 0$	$= 1$
$n_{\text{non-}b\text{-tagged jets}}$	$= 0$	$= 0$	$= 0$
m_{T2} [GeV]	$\in$ [60,65]	> 120	> 80
$p_{\mathrm{T}}^{\mathrm{miss}}$ [GeV]	$\in$ [60,100]	> 110	> 110
$p_{\mathrm{T}}^{\mathrm{miss}}$significance	$\in$ [5,10]	> 10	> 10
$m_{\ell_1\ell_2}$ [GeV]	> 100	$\in$ [61.2,121.2]	> 100

Table 5.2: Control region definitions for extracting normalisation factors for the dominant background processes. 'DF' or 'SF' refer to signal regions with different lepton flavour or same lepton flavour pair combinations, respectively. Table taken from the analysis paper [2].

Definitions of the validation regions used in the analysis can be found in Table 5.3. In addition to the five VRs used in Section 4.5, an additional region named 'VR-top-WW' is used to validate the modelling of the top background in a region kinematically close to CR-WW. Plots showing examples of kinematic distributions in the control regions are

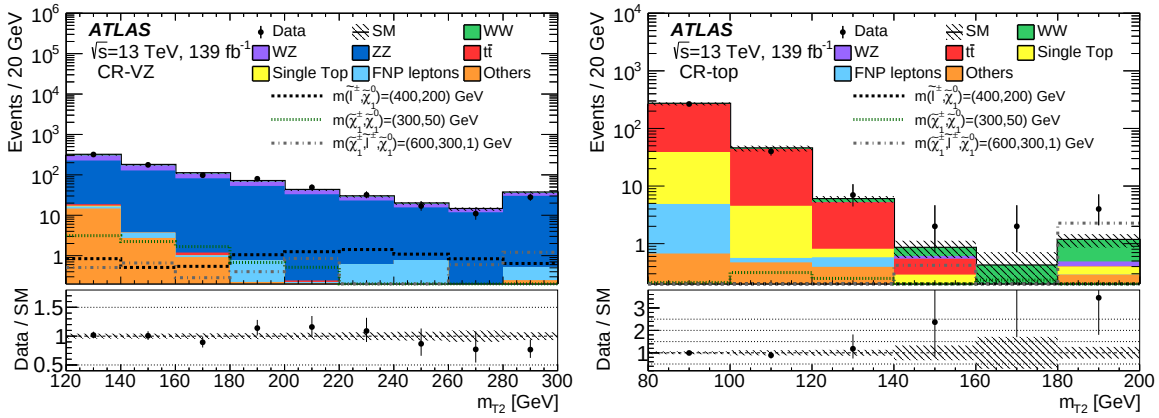

(a) m_{T2}, CR-VZ

(b) m_{T2}, CR-top

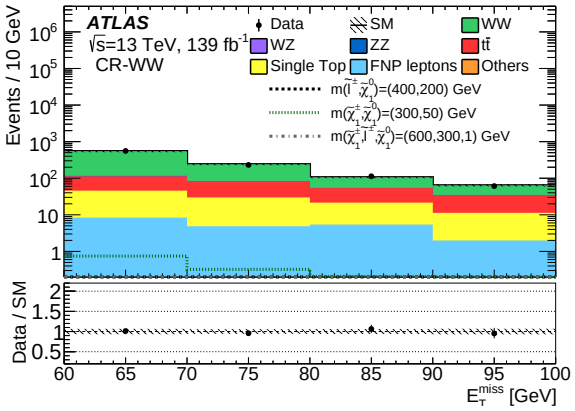

(c) $p_{\mathrm{T}}^{\mathrm{miss}}$, CR-WW

Figure 5.2: Example kinematic distributions in the control regions, for data and the estimated SM backgrounds. The normalisation factors extracted from the corresponding CRs are used to rescale the $t\bar{t}$, single top, WW, WZ and ZZ backgrounds. Negligible background contributions are not included in the legends. The uncertainty band includes all systematic and statistical sources and the final bin in each histogram includes the overflow. Distributions for three benchmark signal points are overlaid for comparison.

shown in Figure 5.4. Corresponding plots, showing the contamination from the signal process with charginos decaying via W-bosons as percentage of the total background yield, are displayed in Figure 5.5.

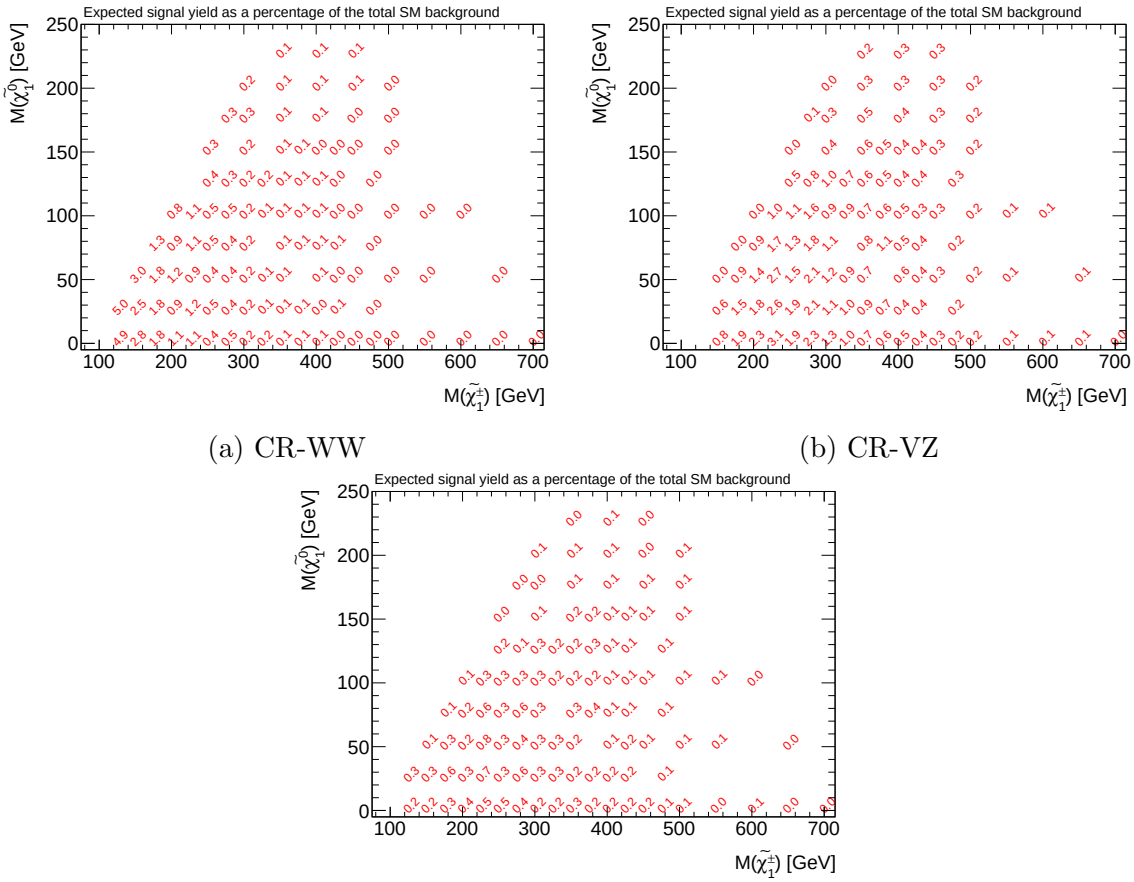

(a) CR-WW

(b) CR-VZ

(c) CR-top

Figure 5.3: Plots of the CR signal contamination over the whole grid. Plots show the signal yield as a percentage of the total expected background yield at each mass point.

Region	VR-WW-0J	VR-WW-1J	VR-VZ	VR-top-low	VR-top-high	VR-top-WW
Lepton flavour	DF	DF	SF	DF	DF	DF
$n_{b\text{-taggedjets}}$	$= 0$	$= 0$	$= 0$	$= 1$	$= 1$	$= 1$
$n_{\text{non-}b\text{-taggedjets}}$	$= 0$	$= 1$	$= 0$	$= 0$	$= 1$	$= 1$
m_{T2}[GeV]	$\in$[65,100]	$\in$[65,100]	$\in$[100,120]	$\in$[80,100]	> 100	$\in$[60,65]
$p_{\text{T}}^{\text{miss}}$[GeV]	> 60	> 60	> 110	> 110	> 110	$\in$[60,100]
$p_{\text{T}}^{\text{miss}}$ Significance	> 5	> 5	> 10	$\in$[5,10]	> 10	$\in$[5,10]
$m_{\ell_1\ell_2}$[GeV]	> 100	> 100	$\in$[61.2,121.2]	> 100	> 100	> 100

Table 5.3: Validation region definitions used to study the modelling of the SM backgrounds. 'DF' or 'SF' refer to regions with different lepton flavour or same lepton flavour pair combinations, respectively. Table taken from the analysis paper [2].

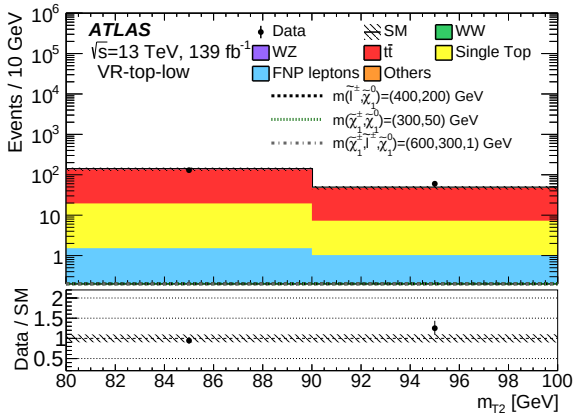

(a) m_{T2}, VR-top-low

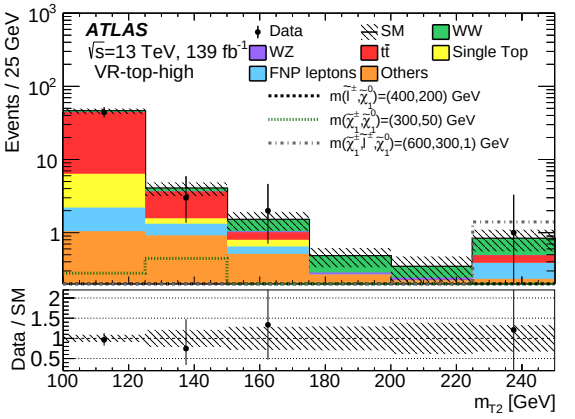

(b) m_{T2}, VR-top-high

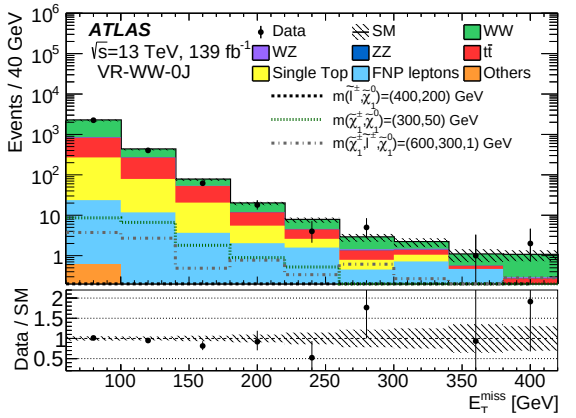

(c) $p_{\mathrm{T}}^{\mathrm{miss}}$, VR-WW-0J

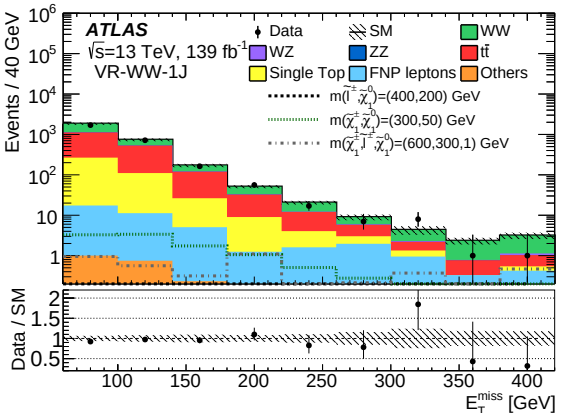

(d) $p_{\mathrm{T}}^{\mathrm{miss}}$, VR-WW-1J

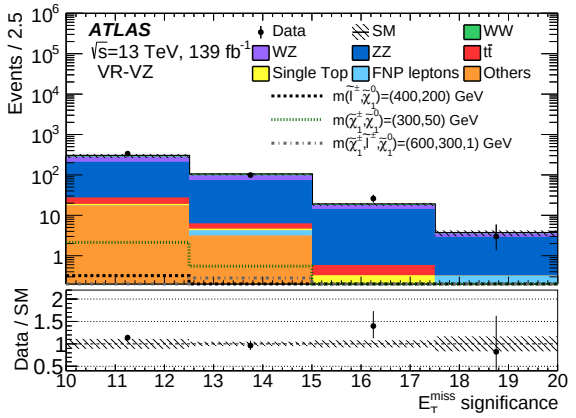

(e) $p_{\mathrm{T}}^{\mathrm{miss}}$, VR-VZ

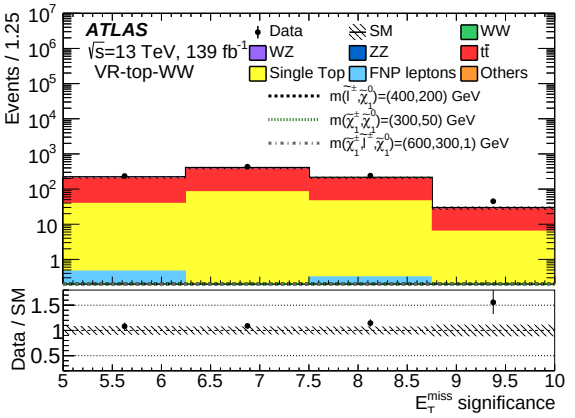

(f) $p_{\mathrm{T}}^{\mathrm{miss}}$ Significance, VR-top-WW

Figure 5.4: Example kinematic distributions in the validation regions, for data and the estimated SM backgrounds. The normalisation factors extracted from the corresponding CRs are used to rescale the $t\bar{t}$, single-top-quark, WW, WZ and ZZ backgrounds. Negligible background contributions are not included in the legends. The uncertainty band includes systematic and statistical errors from all sources and the last bin includes the overflow. Distributions for three benchmark signal points are overlaid for comparison.

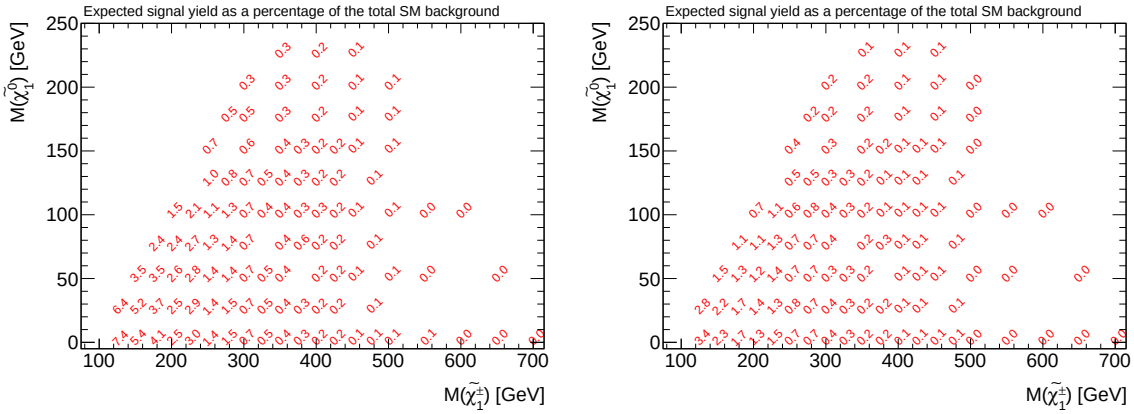

(a) VR-WW-0

(b) VR-WW-1

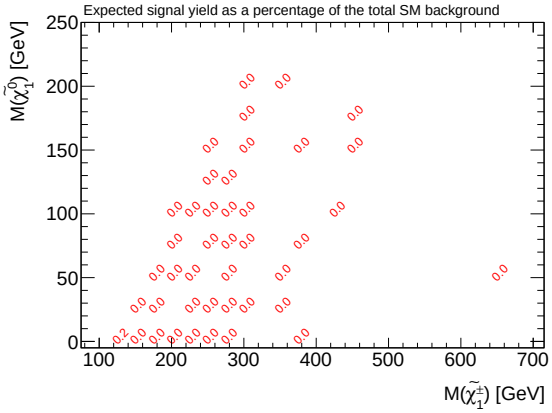

(c) VR-top-WW

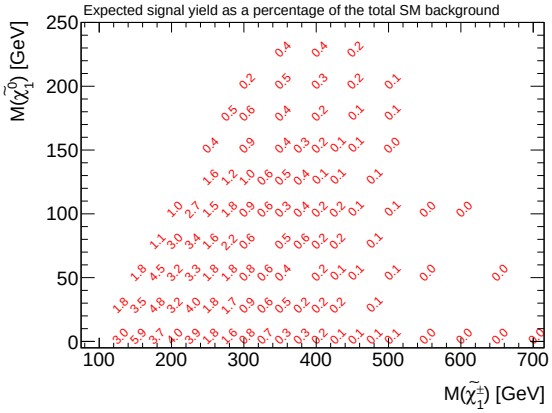

(d) VR-VZ

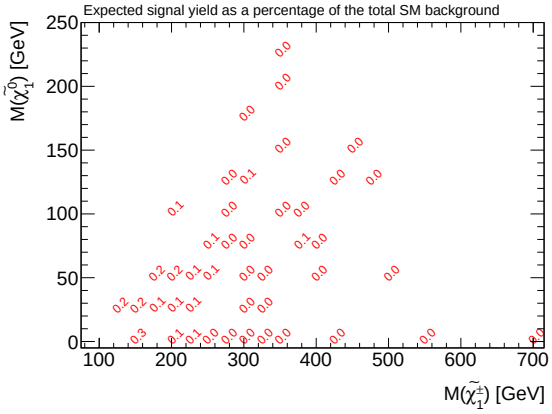

(e) VR-top-L

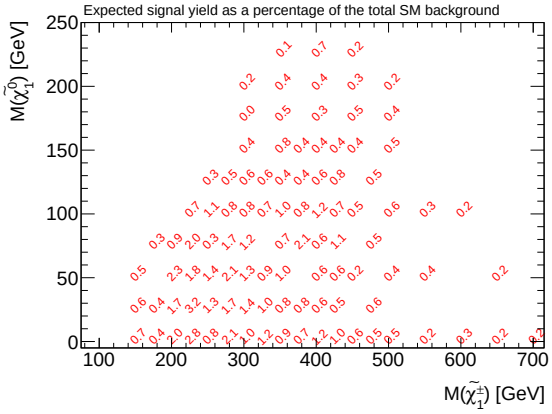

(f) VR-top-H

Figure 5.5: Plots of the VR signal contamination over the whole grid. Plots show the signal yield as a percentage of the total expected background yield at each mass point.

5.4 Systematic uncertainties

Unless otherwise stated, it can be assumed that the systematic uncertainties are included in the profile likelihood fits, and were calculated in the same way as in the previous analysis, as described in Section 4.6. As in Chapter 4, the dominant source of systematic uncertainty comes from theoretical uncertainties in the MC modelling and the dominant experimental uncertainties come from the JES and JER. The procedure to calculate JES and JER uncertainties has been updated since performing the analysis in Chapter 4, and is described in [54].

After performing the profile likelihood fit, summary of the impact of the systematic uncertainties on the unbinned SRs with $m_{\mathrm{T2}} > 100\,\mathrm{GeV}$, is shown in Table 5.4. For the binned SRs defined in Table 5.1, the uncertainties associated with limited MC statistics are higher, ranging between 6-20%. Relative to the previous analysis, the total systematic uncertainties remain fairly similar, and uncertainties related to leptons, the FNP background estimate and pile-up re-weighting continue to be small. As expected from the increased dataset size, the MC statistical uncertainties in these unbinned regions have decreased. The $t\bar{t}$ normalisation uncertainty has reduced quite substantially relative to the previous analysis, which makes sense since the number of events in CR-top has increased substantially.

Uncertainty on the 2015–2018 dataset luminosity is also considered, as introduced in Section 2.2. The uncertainty value is 1.7% [39].

5.5 Results and statistical interpretation

Initially a background-only fit is performed, as described in Section 4.7. The estimated normalisation factors for the dominant backgrounds obtained in this fit are are $\mu_{WW} = 1.25 \pm 0.11$, $\mu_{VZ} = 1.18 \pm 0.05$ and $\mu_{top} = 0.82 \pm 0.06$. The results of the fit across the control, validation and signal regions are shown in Appendix A. Good agreement between the observed data yields and fitted Standard Model backgrounds is observed for the control and validation regions. For the binned signal regions, no significant deviation between observed data yield and Standard Model background is observed in any bin. This can be seen in Figure 5.6, which shows the m_{T2} distributions in the signal regions.

Region	SR-DF-0J	SR-DF-1J	SR-SF-0J	SR-SF-1J
m_{T2} [GeV]	$\in[100,\infty)$	$\in[100,\infty)$	$\in[100,\infty)$	$\in[100,\infty)$
Total background expectation	96	75	144	124
MC statistical uncertainties	3%	3%	2%	3%
WW normalisation	7%	6%	4%	3%
VZ normalisation	$< 1\%$	$< 1\%$	1%	1%
$t\bar{t}$ normalisation	1%	2%	$< 1\%$	1%
Diboson theoretical uncertainties	7%	7%	4%	3%
Top theoretical uncertainties	7%	8%	3%	6%
$p_{\mathrm{T}}^{\mathrm{miss}}$ modelling	1%	1%	$< 1\%$	2%
JES	2%	3%	2%	2%
JER	1%	2%	1%	2%
Pile-up reweighting	$< 1\%$	1%	$< 1\%$	$< 1\%$
b-tagging	$< 1\%$	2%	$< 1\%$	1%
Lepton modelling	1%	1%	1%	3%
FNP leptons	1%	1%	1%	1%
Total systematic uncertainties	15%	12%	8%	10%

Table 5.4: Summary of the dominant systematic uncertainties in the background estimates in the unbinned SRs requiring $m_{\mathrm{T2}} > 100\,\mathrm{GeV}$ after performing the profile likelihood fit. The individual uncertainties can be correlated, and do not necessarily add in quadrature to the total background uncertainty. The percentages show the size of the uncertainty relative to the total expected background. 'Top theoretical uncertainties' refers to $t\bar{t}$ theoretical uncertainties and the uncertainty associated with Wt–$t\bar{t}$ interference added in quadrature.

To obtain exclusion limits for the $\tilde{\chi}_1^{\pm}$, $\tilde{\ell}$ and $\tilde{\chi}_1^0$ masses in the three considered simplified model processes, the $\mathrm{CL_s}$ prescription is used, as in the previous Chapter. For the case of direct slepton production, only the same-flavour signal regions are added to the fit, since the signal exclusively produces same-flavour lepton pairs in the final state. The resulting exclusion plots are shown in Figures 5.7–5.9. The yellow bands on the expected limits include all systematic uncertainties. The theory error bands on the observed contours considers the error on the signal cross section calculation.

For the case of chargino pair production with W-boson-mediated decays, $\tilde{\chi}_1^{\pm}$ masses up to 420 GeV are excluded for a massless $\tilde{\chi}_1^0$ at 95% confidence level. Relative to the search in the previous Chapter, the full run-two result has a small improvement in

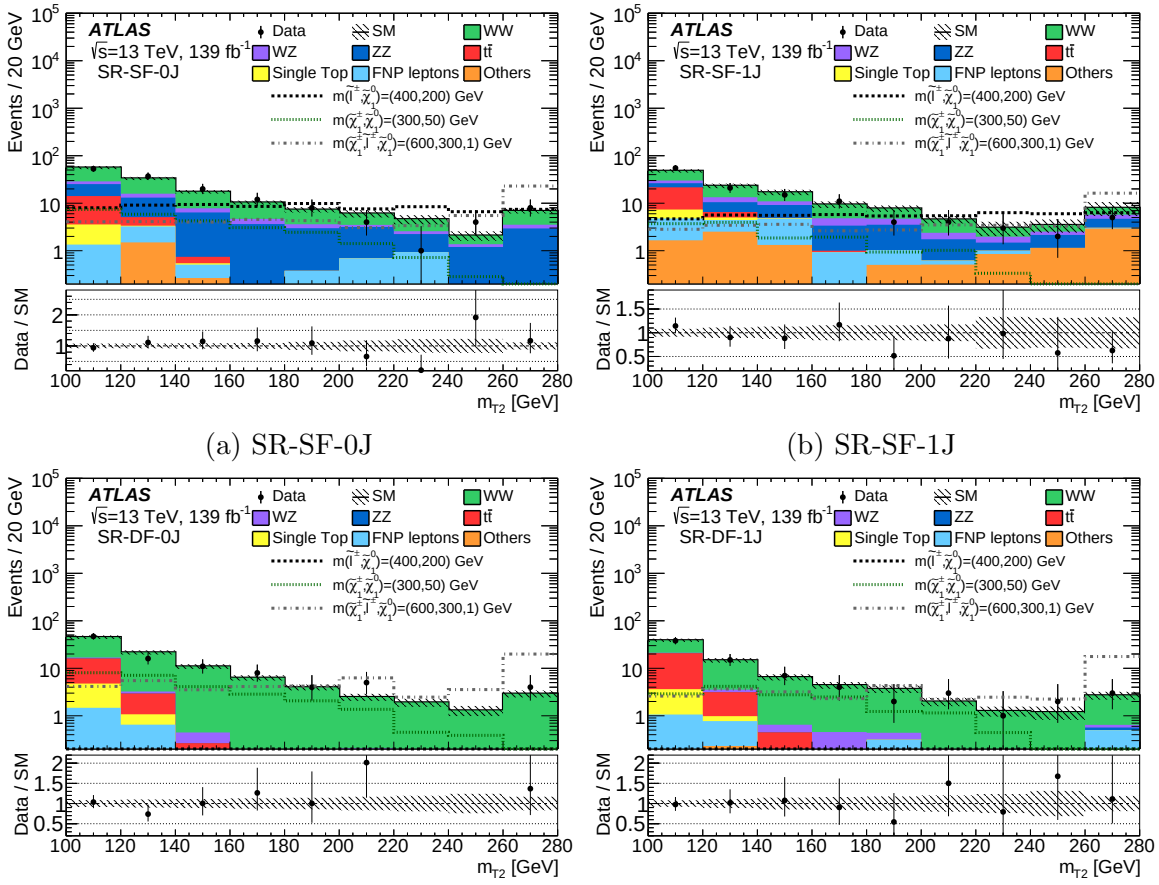

(a) SR-SF-0J (b) SR-SF-1J

(c) SR-DF-0J (d) SR-DF-1J

Figure 5.6: Distributions of m_{T2} in the signal regions, for data and the estimated SM backgrounds. The normalisation factors extracted from the corresponding CRs are used to rescale the $t\bar{t}$, single-top-quark, WW, WZ and ZZ backgrounds. Negligible background contributions are not included in the legends. The uncertainty band includes systematic and statistical errors from all sources and the last bin includes the overflow. Distributions for three benchmark signal points are overlaid for comparison.

exclusion sensitivity throughout the sparticle mass space. Increased sensitivity to higher mass splittings is expected from the additional data allowing the signal regions to probe further into the tails of m_{T2}. However, the dominant uncertainties in this analysis are systematic not statistical, so an increase in dataset statistics of around $2\times$ would not be expected to allow for a significant improvement in reach. Furthermore, the signal production cross section rapidly drops as the chargino mass increases, reaching below $20\mathrm{fb}^{-1}$ above chargino masses of 500 GeV, so it is expected that the increase in luminosity between the two searches is insufficient to improve the sensitivity significantly. In the case of direct chargino pair production with decays via sleptons or sneutrinos with a

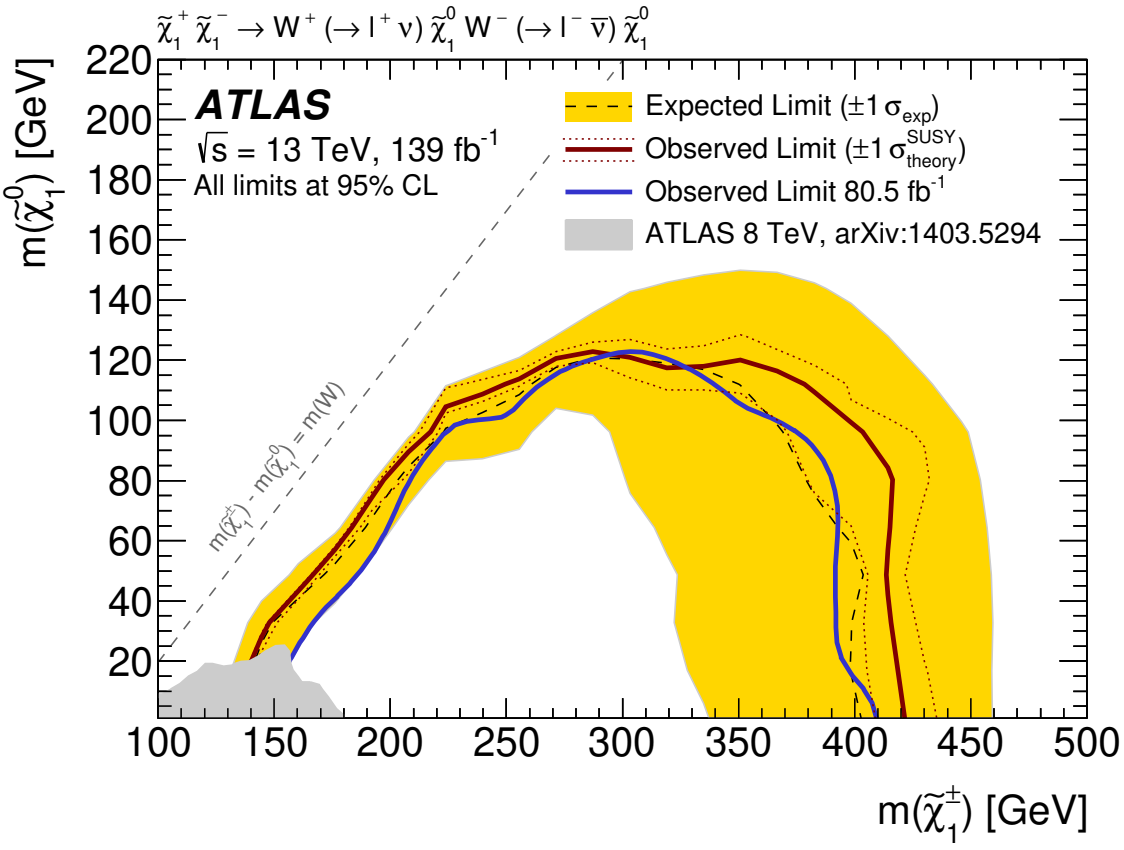

Figure 5.7: Observed and expected exclusion limits on SUSY simplified models for $\tilde{\chi}_1^+\tilde{\chi}_1^-$ production with W-boson-mediated decays. The observed (solid thick line) and expected (thin dashed line) exclusion contours are indicated. The upper shaded band corresponds to the $\pm 1\sigma$ variations in the expected limit, including all uncertainties except theoretical uncertainties in the signal cross section. The dotted lines around the observed limit illustrate the change in the observed limit as the nominal signal cross section is scaled up and down by the theoretical uncertainty. All limits are computed at 95% CL. The observed limit obtained in Chapter 4 is shown in blue. The observed limits obtained by ATLAS in the Run-1 search is also shown in the lower shaded area [79].

massless $\tilde{\chi}_1^0$, $\tilde{\chi}_1^\pm$ masses up to 1 TeV are excluded at 95% CL. Finally, for the case of direct slepton pair production with a massless $\tilde{\chi}_1^0$, slepton masses up to 700 GeV are excluded at 95% CL.

It is interesting to illustrate the differing sensitivities of the direct slepton production model and the chargino pair production model decaying via sleptons. The direct slepton model can be considered as a subset of the other, and its exclusion contour overlaid if a chargino, of the appropriate mass for the model, is introduced. This contour is shown in blue in Figure 5.8, and demonstrates that probing both processes is useful as they have

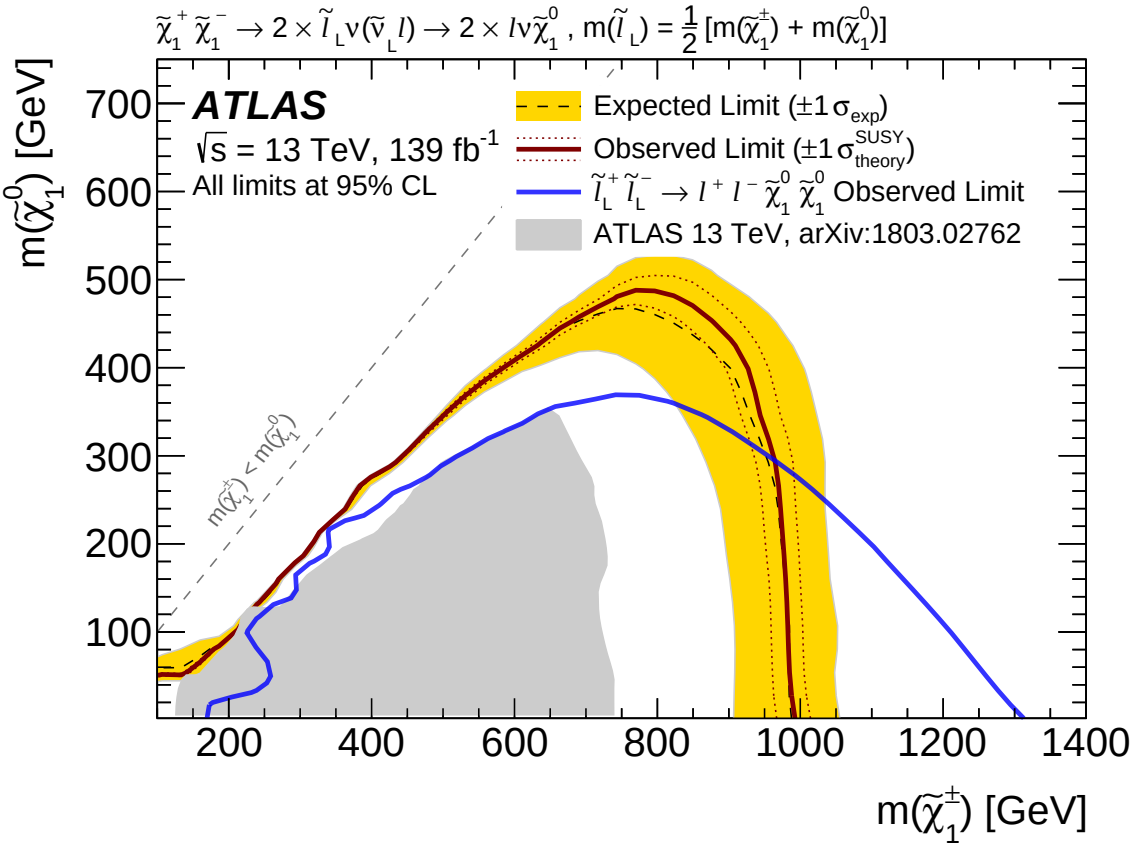

Figure 5.8: Observed and expected exclusion limits on SUSY simplified models for $\tilde{\chi}_1^+\tilde{\chi}_1^-$ production with $\tilde{\ell}/\tilde{\nu}$-mediated decays. All three slepton flavours ($\tilde{e}$, $\tilde{\mu}$, $\tilde{\tau}$) are considered. The observed (solid thick line) and expected (thin dashed line) exclusion contours are indicated. The upper shaded band corresponds to the $\pm1\sigma$ variations in the expected limit, including all uncertainties except theoretical uncertainties in the signal cross section. The dotted lines around the observed limit illustrate the change in the observed limit as the nominal signal cross section is scaled up and down by the theoretical uncertainty. The blue line corresponds to the observed limit for $\tilde{\ell}_L$ projected into this model for the chosen slepton mass hypothesis where the slepton mass lies midway between the mass of the chargino and neutralino. All limits are computed at 95% CL. The observed limits obtained by ATLAS in a previous search is also shown in the lower shaded area [113].

sensitivity to different regions of SUSY phase space.

For direct slepton production, exclusion limits are also set for selectrons and smuons separately by including only the di-electron and di-muon SF SRs in the likelihood fit, respectively. These are shown in Figure 5.10 for single slepton species $\tilde{e}_R$, $\tilde{\mu}_R$, $\tilde{e}_L$, $\tilde{\mu}_L$ along with combined limits for mass-degenerate $\tilde{e}_{L,R}$ and $\tilde{\mu}_{L,R}$. These results significantly extend the previous exclusion limits [79, 80, 113–117] for the same scenarios. It should

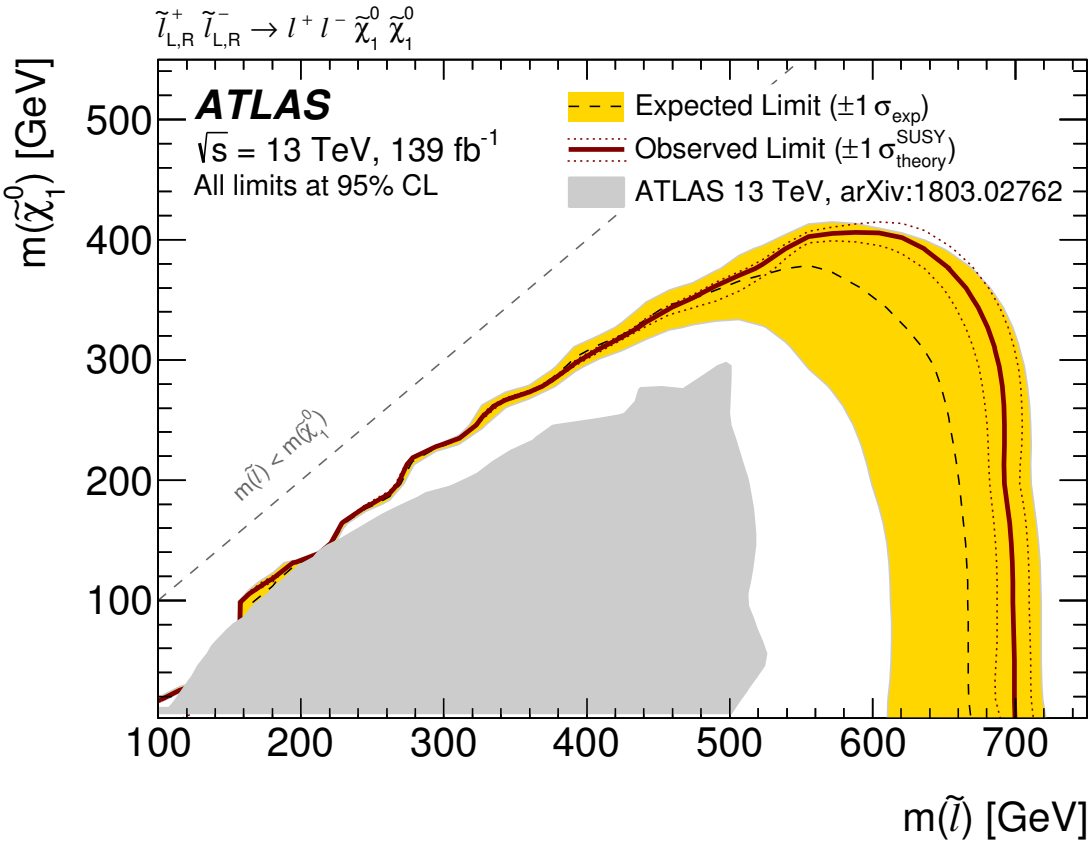

Figure 5.9: Observed and expected exclusion limits on SUSY simplified models for $\tilde{\ell}\tilde{\ell}$ production. Only $\tilde{e}$ and $\tilde{\mu}$ are considered. The observed (solid thick line) and expected (thin dashed line) exclusion contours are indicated. The upper shaded band corresponds to the $\pm 1\sigma$ variations in the expected limit, including all uncertainties except theoretical uncertainties in the signal cross section. The dotted lines around the observed limit illustrate the change in the observed limit as the nominal signal cross section is scaled up and down by the theoretical uncertainty. All limits are computed at 95% CL. The observed limits obtained by ATLAS in a previous search is also shown in the lower shaded area [113].

be noted that where a slepton of particular handedness is mentioned, it refers to the handedness of the lepton of which the slepton is a superpartner. Since sleptons are bosons, they do not have a handedness themselves.

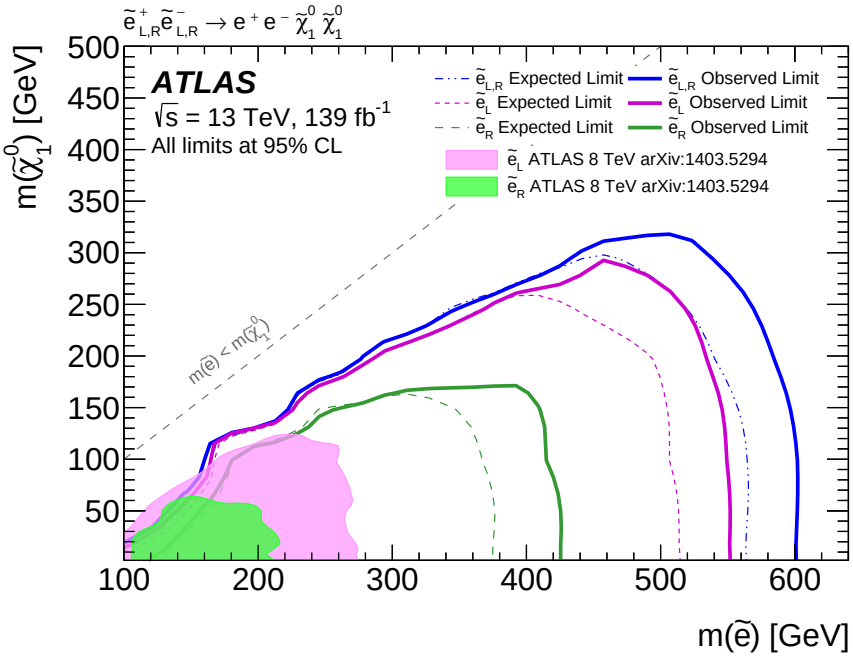

(a) $\tilde{e}\tilde{e}$ production

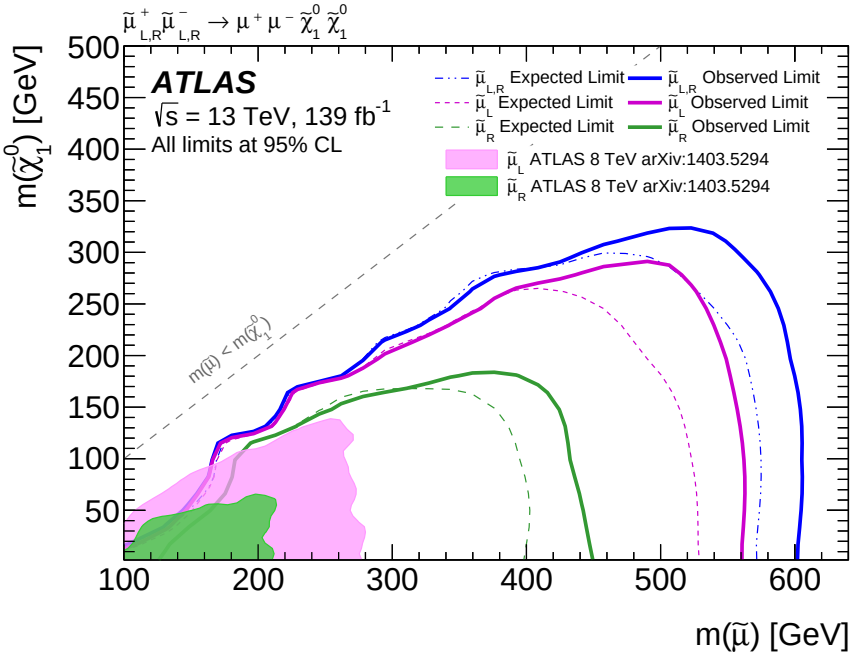

(b) $\tilde{\mu}\tilde{\mu}$ production

Figure 5.10: Observed and expected exclusion limits on SUSY simplified models for (a) direct selectron production and (b) direct smuon production. In Figure (a) the observed (solid thick lines) and expected (dashed lines) exclusion contours are indicated for combined $\tilde{e}_{\mathrm{L,R}}$ and for $\tilde{e}_{\mathrm{L}}$ and $\tilde{e}_{\mathrm{R}}$. In Figure (b) the observed (solid thick lines) and expected (dashed lines) exclusion contours are indicated for combined $\tilde{\mu}_{\mathrm{L,R}}$ and for $\tilde{\mu}_{\mathrm{L}}$ and $\tilde{\mu}_{\mathrm{R}}$. All limits are computed at 95% CL. The observed limits obtained by ATLAS in previous searches are also shown in the shaded areas [113].

Model-independent limits for possible BSM physics processes are also considered, in the same way as the previous Chapter. The model-independent fit results are presented in Tables 5.5 and 5.6, where the observed ($S^{0.95}_{\text{obs}}$) and expected ($S^{0.95}_{\text{exp}}$) BSM process yields are 95% CL are shown in addition to the $\sigma^{0.95}_{\text{obs}}$ limits. Furthermore the p_0 values are shown.

Region	SR-DF-0J	SR-DF-0J	SR-DF-0J	SR-DF-0J
m_{T2} [GeV]	$\in[100,\infty)$	$\in[160,\infty)$	$\in[100,120)$	$\in[120,160)$
Observed events	95	21	47	27
Fitted backgrounds	96 ± 15	18.8 ± 2.4	45 ± 9	33 ± 5
Fitted WW	76 ± 10	18.2 ± 2.4	29 ± 4	29 ± 4
Fitted WZ	1.53 ± 0.17	0.40 ± 0.07	0.66 ± 0.11	0.47 ± 0.07
Fitted ZZ	$0.00^{+0.19}_{-0.00}$	0.14 ± 0.03	$0.06^{+0.23}_{-0.06}$	< 0.04
Fitted $t\bar{t}$	13 ± 7	–	11 ± 6	2.1 ± 1.2
Fitted single top	3.7 ± 2.0	–	3.3 ± 1.8	0.42 ± 0.25
Other backgrounds	0.24 ± 0.08	0.07 ± 0.02	0.08 ± 0.02	0.09 ± 0.05
FNP leptons	1.8 ± 0.6	–	1.4 ± 0.4	0.47 ± 0.17
$S^{0.95}_{\text{obs}}$	34.1	12.7	23.8	11.8
$S^{0.95}_{\text{exp}}$	$35.2^{+13.9}_{-10.0}$	$11.0^{+4.9}_{-3.2}$	$22.8^{+9.1}_{-6.5}$	$15.1^{+6.3}_{-4.5}$
$\sigma^{0,95}_{\text{obs}}$ [fb]	0.24	0.09	0.17	0.08
p_0	0.50	0.33	0.44	0.50

Region	SR-DF-1J	SR-DF-1J	SR-DF-1J	SR-DF-1J
m_{T2} [GeV]	$\in[100,\infty)$	$\in[160,\infty)$	$\in[100,120)$	$\in[120,160)$
Observed events	75	15	38	22
Fitted backgrounds	75 ± 9	15.1 ± 2.7	39 ± 6	21.3 ± 2.8
Fitted WW	48 ± 8	13.4 ± 2.6	17.7 ± 2.6	17.1 ± 2.8
Fitted WZ	1.54 ± 0.21	0.53 ± 0.12	0.43 ± 0.09	0.59 ± 0.11
Fitted ZZ	0.08 ± 0.01	$0.07^{+0.24}_{-0.07}$	< 0.04	0.01 ± 0.00
Fitted $t\bar{t}$	20 ± 7	0.09 ± 0.03	17 ± 6	2.4 ± 0.9
Fitted single top	2.8 ± 1.4	–	2.6 ± 1.3	0.21 ± 0.13
Other backgrounds	0.80 ± 0.13	0.25 ± 0.05	0.19 ± 0.10	0.34 ± 0.04
FNP leptons	2.2 ± 0.6	0.71 ± 0.16	0.87 ± 0.29	0.59 ± 0.16
$S^{0.95}_{\text{obs}}$	25.1	10.2	16.8	12.3
$S^{0.95}_{\text{exp}}$	$25.3^{+10.3}_{-7.2}$	$10.3^{+4.6}_{-3.0}$	$17.6^{+7.3}_{-5.1}$	$11.9^{+5.2}_{-3.3}$
$\sigma^{0,95}_{\text{obs}}$ [fb]	0.18	0.07	0.12	0.09
p_0	0.50	0.50	0.50	0.45

Table 5.5: Observed event yields and predicted background yields from the fit for the DF unbinned SRs. The model-independent upper limits at 95% CL on the observed and expected numbers of beyond-the-SM events $S^{0.95}_{\text{obs/exp}}$ and on the effective beyond-the-SM cross section $\sigma^{0.95}_{\text{obs}}$ are also shown. The $\pm 1\sigma$ variations on $S^{0.95}_{\text{exp}}$ are also provided. The last row shows the p_0-value of the SM-only hypothesis. For SRs where the data yield is smaller than expected, the p_0-value is capped at 0.50.

Region	SR-SF-0J	SR-SF-0J	SR-SF-0J	SR-SF-0J
m_{T2} [GeV]	$\in[100,\infty)$	$\in[160,\infty)$	$\in[100,120)$	$\in[120,160)$
Observed events	147	37	53	57
Fitted backgrounds	144 ± 12	37.3 ± 3.0	56 ± 6	51 ± 5
Fitted WW	73 ± 8	18.1 ± 2.1	27.6 ± 3.0	27 ± 4
Fitted WZ	10.8 ± 0.8	3.08 ± 0.27	3.55 ± 0.29	4.2 ± 0.5
Fitted ZZ	38.6 ± 2.6	13.8 ± 1.0	11.1 ± 0.8	13.7 ± 1.5
Fitted $t\bar{t}$	13 ± 4	–	11 ± 4	1.9 ± 0.7
Fitted single top	2.4 ± 1.4	–	2.2 ± 1.3	0.15 ± 0.09
Other backgrounds	2.1 ± 1.5	$0.10^{+0.33}_{-0.10}$	$0.2^{+1.4}_{-0.2}$	1.76 ± 0.30
FNP leptons	5.4 ± 1.4	2.2 ± 0.4	1.1 ± 0.6	2.0 ± 0.5
$S^{0.95}_{\mathrm{obs}}$	35.5	14.3	17.8	23.5
$S^{0.95}_{\mathrm{exp}}$	$33.6^{+13.6}_{-9.3}$	$14.5^{+6.3}_{-4.2}$	$20.0^{+8.1}_{-5.6}$	$18.7^{+7.8}_{-5.3}$
$\sigma^{0.95}_{\mathrm{obs}}$ [fb]	0.25	0.10	0.13	0.17
p_0	0.44	0.50	0.50	0.25

Region	SR-SF-1J	SR-SF-1J	SR-SF-1J	SR-SF-1J
m_{T2} [GeV]	$\in[100,\infty)$	$\in[160,\infty)$	$\in[100,120)$	$\in[120,160)$
Observed events	120	29	55	36
Fitted backgrounds	124 ± 12	36 ± 5	48 ± 8	40 ± 4
Fitted WW	48 ± 6	14.1 ± 2.1	18.1 ± 2.4	16.0 ± 2.2
Fitted WZ	13.4 ± 1.1	5.2 ± 0.6	3.62 ± 0.33	4.7 ± 0.5
Fitted ZZ	22.2 ± 1.8	9.1 ± 1.1	4.8 ± 0.5	8.2 ± 0.9
Fitted $t\bar{t}$	16 ± 8	$0.07^{+0.10}_{-0.07}$	14 ± 7	1.6 ± 0.8
Fitted single top	3.3 ± 1.7	–	2.6 ± 1.4	0.7 ± 0.4
Other backgrounds	11.1 ± 4.0	5.6 ± 2.1	$1.7^{+2.4}_{-1.7}$	3.8 ± 1.3
FNP leptons	10.3 ± 1.5	1.80 ± 0.34	3.1 ± 0.6	5.3 ± 0.7
$S^{0.95}_{\mathrm{obs}}$	30.6	11.2	27.3	12.6
$S^{0.95}_{\mathrm{exp}}$	$33.5^{+13.3}_{-9.3}$	$15.3^{+6.5}_{-4.5}$	$21.9^{+9.0}_{-6.2}$	$15.5^{+6.5}_{-4.2}$
$\sigma^{0.95}_{\mathrm{obs}}$ [fb]	0.22	0.08	0.19	0.09
p_0	0.50	0.50	0.26	0.50

Table 5.6: Observed event yields and predicted background yields from the fit for the SF unbinned SRs. The model-independent upper limits at 95% CL on the observed and expected numbers of beyond-the-SM events $S^{0.95}_{\mathrm{obs/exp}}$ and on the effective beyond-the-SM cross section $\sigma^{0.95}_{\mathrm{obs}}$ are also shown. The $\pm 1\sigma$ variations on $S^{0.95}_{\mathrm{exp}}$ are also provided. The last row shows the p_0-value of the SM-only hypothesis. For SRs where the data yield is smaller than expected, the p_0-value is capped at 0.50.

5.6 Conclusions and outlook

This chapter presented a search for three possible electroweak supersymmetry simplified model processes. This search was based on a previous search, detailed in Chapter 4, which targeted the electroweak pair production of charginos decaying via W-bosons into final states with exactly two oppositely charged leptons and $p_{\mathrm{T}}^{\mathrm{miss}}$. This analysis extends the previous search through the addition of the 2018 ATLAS dataset, leading to a total luminosity of $139.5\,\mathrm{fb}^{-1}$ of data. It also adds interpretations for direct slepton production, and chargino pair production decaying via sleptons or sneutrinos.

No significant excess above the SM was observed so exclusion limits were placed on the chargino, slepton and neutralino masses. At 95% CL masses up to 420 GeV are excluded for a massless neutralino, for the production of chargino pairs assuming W-boson-mediated decay, and up to 1 TeV for slepton-pair-mediated decays. For direct slepton-pair production, slepton masses up to 700 GeV are excluded at 95% CL assuming two generations of mass-degenerate sleptons. These results significantly extend the previous exclusion limits for the same scenarios, including the limits presented in Chapter 4.

There have been several other searches for electroweak supersymmetry, which have produced exclusion limits for the same sparticles using different processes, at ATLAS using the Run 2 dataset. It is interesting to consider how these different exclusion limits compare and complement each other. Summary plots for these searches for the slepton mass–lightest neutralino mass plane is shown in Figure 5.11a. It is clear that the complementary design of the 'compressed' analysis, which targeted scenarios with low mass difference and this thesis' analysis, which targeted larger mass differences, has successfully resulted in sensitivity to different areas of the plane. There is an obvious gap between the two searches, where the mass difference is around the W-boson mass. Within this region, the m_{T2} endpoint for the signal becomes incredibly similar to the dominant WW SM background, rendering the variable much less powerful at discriminating the signal and background. Since this analysis relies on m_{T2}, it is not designed to provide any sensitivity to these models. Similarly, the compressed analysis targets very low lepton p_{T}, and thus relies on high values of $p_{\mathrm{T}}^{\mathrm{miss}}$ for background discrimination and to trigger on. These reduce its effectiveness as the mass difference increases and the leptons become typically higher in p_{T}.

A similar plot in the lightest chargino mass–lightest neutralino mass plane is shown in Figure 5.11b, where for all the simplified models considered, the second lightest neutralino ($\tilde{\chi}_2^0$) is set to have the same mass as the lightest chargino ($\tilde{\chi}_1^{\pm}$) as a result of it being assumed to be a wino. The small size of the contour for the WW process relative to the others clearly demonstrates the challenging nature of this production channel, as it has a much larger and more kinematically similar background than the others. Again the searches so far have been highly effective at targeting regions with a high mass difference. However, there is a lack of exclusion in the smaller mass difference region.

The author is involved in ongoing efforts searching for direct slepton production, and for chargino pair production decaying via W bosons, which aims to gain sensitivity to these low mass difference gaps. A different analysis strategy is being developed, based

on using machine learning to classify signal and background events, instead of the m_{T2} based cut-and-count approach used in this thesis. Alternative triggering options being studied could potentially be useful in this case too — for example using single-lepton triggers instead of two-lepton triggers can allow the second lepton to become lower in p_{T} without having a low trigger efficiency.

As established in Section 5.4, the dominant uncertainties in these searches come from the modelling of the diboson and top MC backgrounds. To maximise the sensitivity of future searches, it is important to try to reduce the impact of these uncertainties. One approach being taken to achieve this is to design estimates of the Standard Model background which are less dependent on MC. For the direct slepton search, the flavour symmetric nature of the signal process — that it the only produces final states with two same-flavour leptons — can be exploited. The dominant SM backgrounds, including diboson and top, are equally likely to produce final states with either ee, $\mu\mu$, or $e\mu$ lepton pairs, to leading order. This allows the creation of a diboson and top background estimate which is based on extrapolating the data yield in a different-flavour control region to the same-flavour signal region, using correction factors to account for the differences in properties like muon and electron reconstruction. These correction factors are also primarily calculated using data. This 'flavour-symmetry' approach was previously used in ATLAS searches for strong supersymmetry in two lepton final states, as described in References [119, 120]. The author produced the first studies illustrating the viability of this approach in searches for direct slepton production, and its implementation in the future search has been continued by other analysers.

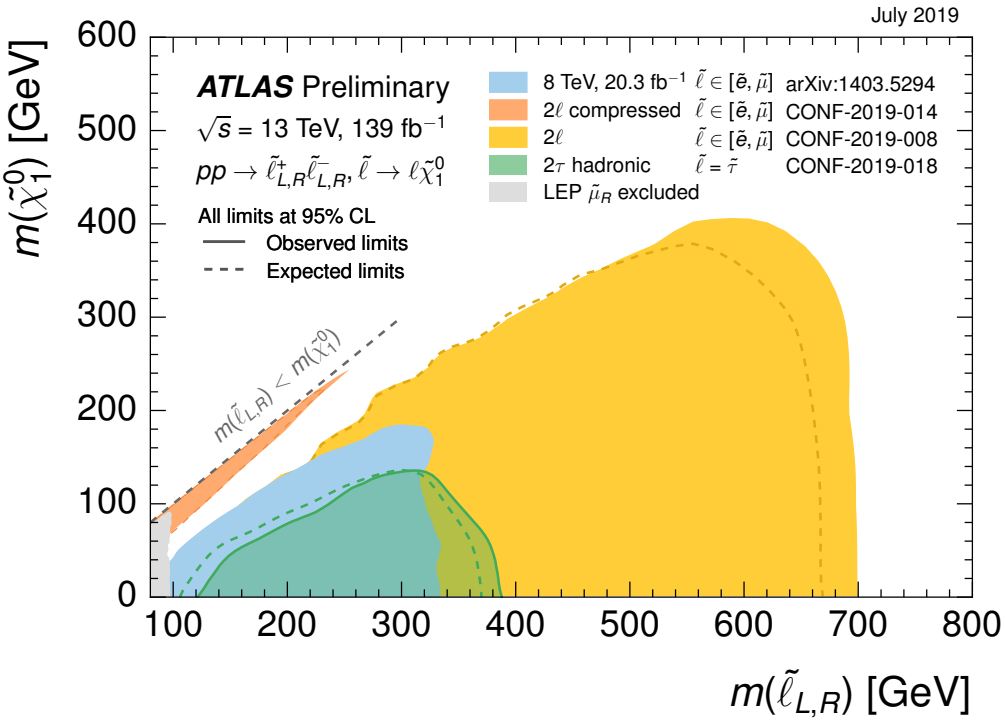

(a)

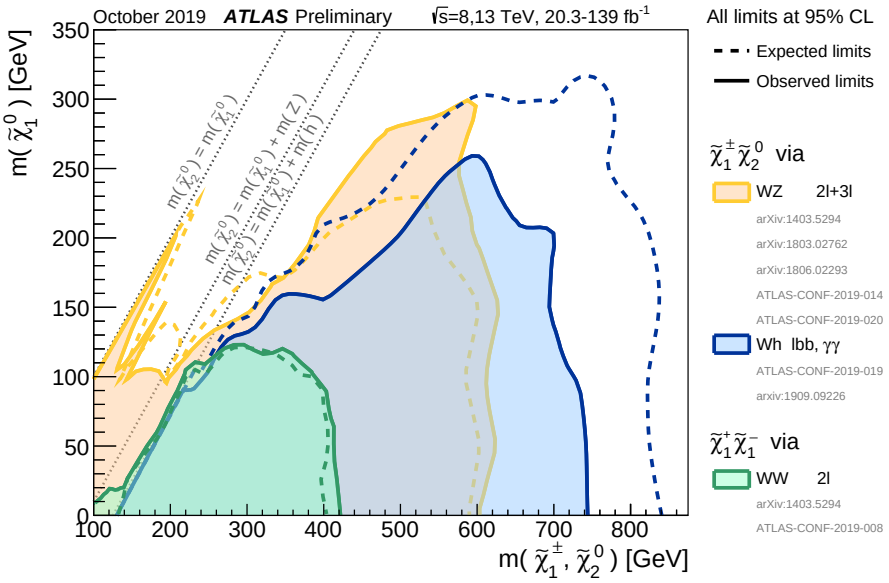

(b)

Figure 5.11: Summary plots of exclusion of electroweak supersymmetry production from ATLAS Run 2 searches [118]. The first Figure shows the slepton–lightest neutralino plane; the second shows the lightest chargino–lightest neutralino plane. For all simplified models considered in these searches, the lightest chargino is considered to have the same mass as the second lightest neutralino.

Chapter 6

A search for new physics with charge flavour asymmetry

6.1 Introduction

This Chapter presents a novel search for new physics hiding within charge-flavour asymmetry in ATLAS data. The primary goal of the analysis is the measurement of the ratio r of $e^+\mu^-$ to $e^-\mu^+$ events in the $139.5\,\text{fb}^{-1}$ of proton-proton collisions comprising the ATLAS full Run 2 dataset. Within the SM, this ratio is expected to be consistent with, or slightly below, one; however for some BSM models this ratio would increase above one. The main measurement in this Chapter is, thus, a model-independent search for deviations from the SM.

Whilst many ATLAS new-physics searches have improved their sensitivity through a rapidly increasing dataset volume, they also rely on making comparisons between observed event yields and predictions from Monte Carlo simulation. As the dataset volume grows, maintaining a data-equivalent number of simulated events becomes more and more challenging. Given these factors, searches which can test expected symmetries of the Standard Model without requiring simulation are desirable. Since there have yet to be any signs of what new physics will look like, searches for new physics which are not limited to probing a specific model are more desirable still. This analysis' r measurement meets these desires.

A secondary goal of the analysis is to place the first direct LHC constraints on two example BSM model processes, which predict a ratio greater than one as a result of

proton PDF asymmetry favouring the $e^+\mu^-$ final state. The first process comes from an RPV-SUSY model, where a single smuon is produced and decays into a leptonically decaying top quark and a muon. The second process comes from a scalar leptoquark model, where an electron and a single leptoquark are produced, and the leptoquark decays into a charm quark and a muon.

The Standard Model charged leptons are taken to differ only in their masses. In particular, electrons and muons both have small masses relative to typical collision energy scales, resulting in a high amount of universality between them. As far as is known, this is not the result of a fundamental symmetry, making this apparent property an interesting topic of study. Further interest has been cast in this direction by recent results from the LHCb experiment [31]. Testing the difference between lepton flavours is non-trivial, owing to potential biases from the ATLAS detector and to situations where the e/μ mass difference becomes significant, such as pion decay. Charge asymmetry, meanwhile, is a feature of pp collisions at the LHC that has been previously measured, for example in W + jets events [121]. Combining the properties of lepton charge and flavour into one measurement results in a useful test of the Standard Model. Many of the effects that might favour one flavour over another are independent of charge, and many of the effects that bias charge are independent of flavour. It is therefore proposed to examine this "charge-flavour" asymmetry, by comparing the rates of $e^+\mu^-$ and $e^-\mu^+$ events.

This analysis follows previous work, documented in Reference [3]. In that paper, the idea for a search such as this is introduced, and motivated using the same RPV-SUSY model that is referred to here. Detailed discussion about potential sources of bias in the measurement are described. The ATLAS implementation of the analysis was begun by another student, and is documented in their doctoral thesis [4].

The author was the 'Analysis Contact' for this search, and the leading analyser. This included optimising the final signal regions used for the ratio measurement, designing and performing studies of the SM background, performing studies of detector-based lepton charge biases, implementing the uncertainties on the measurement, and performing the full statistical analysis. Furthermore, the addition of the leptoquark model to the analysis was the author's idea, and the development and implementation of the model-dependent signal regions and production of exclusion limits was also the author's work. Other analysers drove the estimation of the fake lepton background, came up with the initial idea of the analysis and the charge-bias studies, and played a key role in, for example, optimising the variables to measure the ratio in. In addition, other analysis

team members wrote the analysis software.

This Chapter continues in Section 6.2, where a more detailed introduction to charge-flavour asymmetry is given and the new physics models to which this analysis has sensitivity are introduced. Section 6.3 describes measurements of the lepton efficiencies taken to study potential charge-flavour biases. The Monte Carlo simulation of the Standard Model and BSM signals, which are used in some parts of the analysis, is detailed in Section 6.4. The physics objects used in this search are described in Section 6.5. Definitions of the signal regions used are given in Section 6.6. Section 6.7 explains the Standard Model background estimation. Section 6.8 discusses the systematic uncertainties relevant to this search and how they are accounted for. Finally, the statistical interpretation of the data is described in Section 6.9, with the results of this presented in Section 6.10.

6.2 Charge–flavour asymmetry

In Section 6.2.1, 'charge-flavour symmetry' is defined. An explanation is given as to why the Standard Model, together with detector events, should lead to a very small excess of $e^-\mu^+$ events over $e^+\mu^-$ events — calling this the 'charge-flavour conspiracy'. This expectation is studied in SM MC in Section 6.7. This section is largely based on Reference [3], but is described here in detail as it is of significant importance to the analysis. Sections 6.2.2 and 6.2.3 introduce the R-parity-violating supersymmetric (RPV-SUSY) model and leptoquark model, respectively, which are used as benchmark models in this analysis.

6.2.1 Charge-flavour asymmetries in the Standard Model

The physics of SM charged leptons at the LHC is predominantly CP-symmetric: large differences are not expected between the decay rates of l^+ and l^- for $l \in e, \mu$, or between their production rates from neutral states. This is not to say that LHC results are expected to be charge-symmetric. For example, in ATLAS proton-proton collisions, the initial state has charge +2, leading to an excess of W^+ production over W^-; one expects to see more positively- than negatively-charged leptons. There are also other more subtle charge-bias effects such as the dominance of electrons over positrons in matter (e.g. δ-rays[1] are always negatively charged), and the possibility that sub-detectors themselves

[1] δ-rays are e^-s originating from particle interactions in silicon sensors.

could sometimes have a greater acceptance or reconstruction efficiency for one charge over the other.

Hiding amid these sources of charge and flavour bias within the LHC beam and the SM lies a surprising result. For any flavour-symmetric and suitably non-pathological event selection, almost every potentially significant bias or experimental uncertainty considered individually, preserves the following property:

$$\frac{\langle N(\mu^- e^+)\rangle}{\langle N(\mu^+ e^-)\rangle} \leq 1. \tag{6.1}$$

This is dubbed the 'strong LHC charge-flavour conspiracy'. Note that the value '1' in the above equation is the value that the ratio of expectations would take in the absence of any differences between electrons and muons. Some biases and experimental effects preserve the relationship (6.1) by leaving the ratio of expectations invariant. For example, if the reconstruction efficiency for electrons were independent of any property of the leptons in question, including their charge, then any uncertainty in the reconstruction efficiency would change the numerator and denominator by the same factor, leaving the ratio unchanged. A second class of biases preserve (6.1) by reducing the ratio of expectations. For example: were it possible for δ-rays to be detected as full tracks, which — as shown in Reference [122] — is unlikely, this would only increase the expectation in the denominator, making the ratio smaller.

Finally, a third category of bias exists that can increase the ratio, but not so much that it could take the ratio above unity. One example of this category of bias comes from the 'fake-lepton' background, which comes largely from the $W^\pm$ charge asymmetry in W + jets events. As measured in References [123, 124], there are more W^+ than W^- bosons produced at the LHC. Given that the final state considered in the analysis has a two leptons, this is only relevant if a jet which is also produced with the W boson is mis-interpreted as being a second lepton of the opposite charge to that coming from the W boson decay. Unfortunately, the 'fake-lepton' background (which was also considered in the other analyses in this thesis), while small, is not negligible. Jets can fake electrons through mis-identification, and fake muons primarily through heavy-flavour hadron decays. Technically for the muon case, the muon itself is real, but is the result of the non-prompt decay of a heavy quark hadron produced in the hard-interaction, rather than a prompt muon produced in the hard-interaction of interest. Fortunately for the survival of the conspiracy, ATLAS is good at suppressing fake muons by requiring that they are sufficiently well-isolated from other event activity. Thus, the

most probable flavour of the fake lepton is an electron. Since the charge of the W-boson is more likely to be positive, this means that the W + jets background should favour $e^-\mu^+$. In Reference [3], a more quantitative study is considered, which proves that the fake lepton background is of the third type: it could increase the ratio but not above one.

One can also consider the case where a W-boson is produced alongside an additional boson or a top quark. Here a final state can be obtained with a second, real, lepton. Given the universality of weak lepton couplings, these backgrounds are not found to be able to bias the ratio, at least to leading order.

Three exceptions to these three categories are found. First of all, one can consider lepton acceptance. ATLAS detector geometry could also induce acceptance differences depending on lepton charge. For example, the ATLAS muon system has a fixed toroidal magnetic field [125], orientated such that the trajectories of μ^+ and μ^- are bent oppositely in rapidity. No existing ATLAS studies suggest evidence for a significant charge-dependence in lepton reconstruction efficiencies, but this bending asymmetry could, in principle, lead to localised differences in acceptance or momentum resolution for differently charged muons. The effect is reversed in opposite ends of the detector, and so in a symmetric detector the bias disappears for event selections that are invariant under $\eta \leftrightarrow -\eta$. There are effects which may disrupt this symmetry, however, for example a displacement of the interaction point from the geometrical centre of the detector, or an asymmetry in the active regions of the detector, either by design or by malfunction of detector components.

The magnitude of these effects is expected to be small for a number of reasons. Event selections are typically designed such that the edges of acceptance are avoided, giving relatively uniform efficiency [62]. In the case of regions of reduced efficiency, while muons of one charge may be lost at one edge of the anomaly, the opposite charge is lost at the other edge, largely nullifying the effect on the overall ratio. A detailed study of lepton trigger and reconstruction efficiency charge-biases is made in Section 6.3, and localised muon charge biases are corrected for in the analysis.

The second exception relates to the beamspot. Considering the position of the interaction point, while the LHC beam-spot is of finite size [126], this is expected to have little effect on the asymmetry when averaging over many interactions. Displacements of the beam-spot from the centre of the detector can reach $\sim 30\,\text{mm}$ [127], but are typically small compared to the scale of the detector ($\sim 5\,\text{m}$ to the closest part of the muon

detector system). A calculation of the approximate size of the this effect on the ratio of expectations was made, and found to be $\sim 0.0001\%$.

The third exception is the phenomenon known as 'punch through'. If a high energy jet fails to be fully contained within the calorimeter, the escaping ejecta have the potential to be mis-reconstructed as muons in the muon detectors. The likelihood of such 'punch through' muons is independent of charge. They could, however, be produced at the same time as real electrons or positrons, for which the proton PDFs favour the latter. Muon punch through therefore has the potential to favour $e^+\mu^-$ events. This makes it the only source of background identified which could increase the ratio above one. It is expected that punch-through should not significantly affect this analysis since it is rare and tends to produce a collimated stream of muons. If such events did pass the baseline analysis selections, the muons produced should not be isolated enough to pass the Tight analysis requirements.

A 'weak LHC charge-flavour conspiracy' can further be defined, by demanding that (6.1) need only apply after *joint* rather than *individual* consideration of the same sources of bias and experimental uncertainty. It may be shown that the strong LHC charge-flavour conspiracy implies the weak LHC charge-flavour conspiracy, if every bias satisfies (6.1) independently of the presence (or absence) of other biases. In this analysis, the approach relies only on the weak conspiracy.

6.2.2 Charge-flavour asymmetries created by RPV Supersymmetry

The RPV-SUSY model considered introduces one non-zero RPV coupling, λ'_{231}, which couples a down quark, a top quark and a muon, where one of these is exchanged for its superpartner. For this analysis, the muon is exchanged for a left-handed smuon, allowing for its production in pp collisions. This smuon ($\tilde{\mu}$) can then decay into a muon and the lightest neutralino ($\tilde{\chi}_1^0$). A selection of masses are considered for these two sparticles, whilst all other sparticles are considered to have masses too heavy for LHC production. Theoretical motivation for this model is provided in Section 1.4.

Requiring perturbativity at the weak scale constrains $\lambda'_{231} < 3.5$. Additionally, requiring perturbativity at the GUT scale leads to $\lambda'_{231} < 1.5$[2].

When the neutralino is lighter than the top quark, the presence of a non-zero λ'_{231}

[2]Source: B.C. Allanach, private communication, 2016.

coupling allows for final states comprising a muon, a top quark and missing transverse momentum. If the neutralino were heavier than the top quark, then the neutralino could itself decay to a muon, a top quark, and an anti-down quark by the reverse of the production process. This eliminates much of the missing transverse momentum from the signature and introduces more leptons, meaning the analysis is largely insensitive.

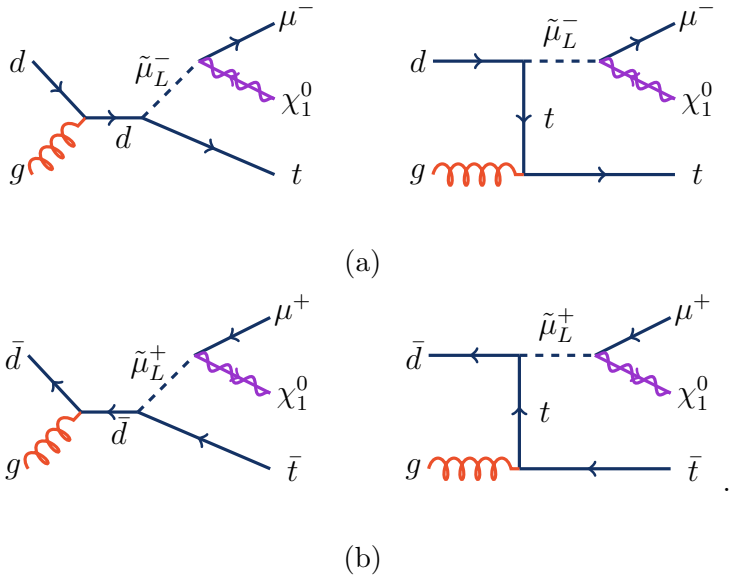

Figure 6.1: Diagrams of the RPV-SUSY model processes considered in this analysis which produce a final state containing: (a) $e^-\mu^+$ and (b) $e^+\mu^-$. Reproduced from [3].

Charge conservation ensures that the charge of the muon matches the charge of the down quark in the initial state proton. Specifically, the tree-level diagrams shown in Figure 6.1a with a down quark in the initial state only permit production of a negative muon. On the other hand, anti-muons are permitted by the diagrams shown in Figure 6.1b which each have an anti-down quark in the initial state. Since the proton's parton distribution function for the down quark is significantly larger than that for the anti-down quark, the λ'_{231} coupling is expected to produce significantly more μ^- than μ^+ events. This analysis' interest lies in the cases where the decay products of the antitop, or top, in the final state include an electron, or positron. In this case, the detector signature is an electron and a muon with opposite charge, plus missing transverse momentum. This model enhances the production of $e^+\mu^-$ relative to $e^-\mu^+$.

It is reasonable to ask what would happen in this model if selectrons were considered to have an RPV coupling switched on instead of smuons. For a process otherwise similar to that considered in Figure 6.1, i.e. initiated by a down or anti-down quark, the final

state would favour $e^-\mu^+$ over $e^+\mu^-$.

6.2.3 Charge-flavour asymmetries created by leptoquarks

A scalar leptoquark, S_1 [30], with non-zero couplings λ_{eu} and $\lambda_{\mu c}$ — permitting $S_1 \to ue^-$ and $S_1 \to c\mu^-$ respectively — can also generate an excess of LHC events containing $e^+\mu^-$ relative to $e^-\mu^+$. This is a result of proton PDF asymmetry between up and anti-up quarks. Events containing $e^+\mu^-$ in the final state are produced primarily from initial states containing up-quarks via the tree-level diagrams shown in Figure 6.2a. Note that gluon splitting is considered in preference to a charm quark initiated diagram since the gluon PDF is dominant at LHC collision energy scales. Conversely, events containing $e^-\mu^+$ in the final state are produced primarily from initial states containing anti up-quarks via the tree-level diagrams shown in Figure 6.2b. Theoretical motivation for this model is provided in Section 1.5.

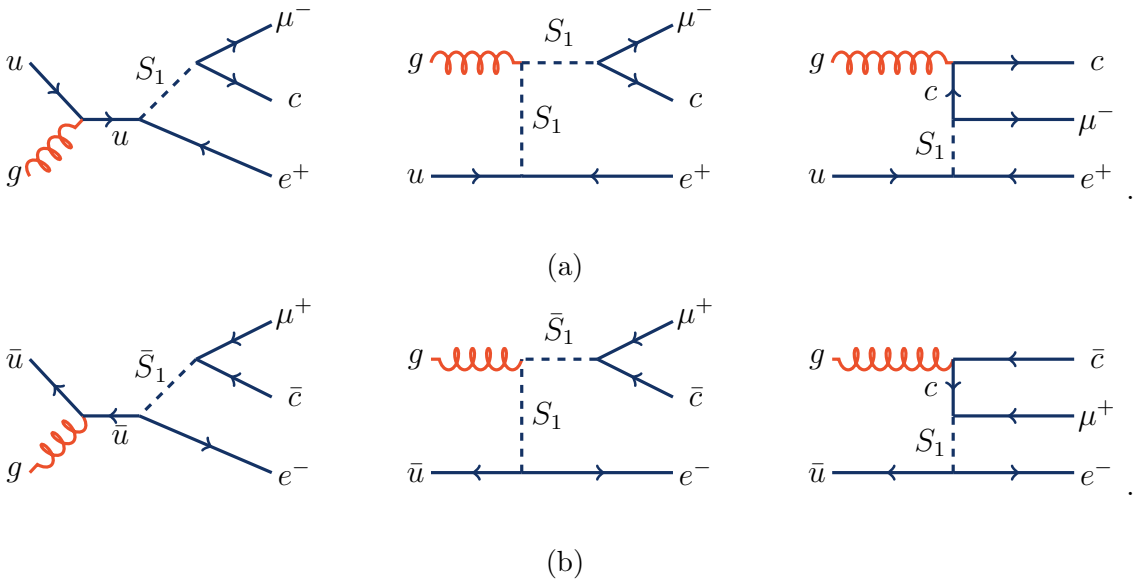

Figure 6.2: Diagrams of the leptoquark model processes considered in this analysis which produce a final state containing: (a) $e^-\mu^+$ and (b) $e^+\mu^-$. Made by another analyser.

It is important to note that gluon-gluon collisions with the same leptoquark couplings switched on could potentially generate leptoquark pairs leading to both same and different flavour final states in equal amounts. Tree-level Feynman diagrams of these processes are shown in Figure 6.3.

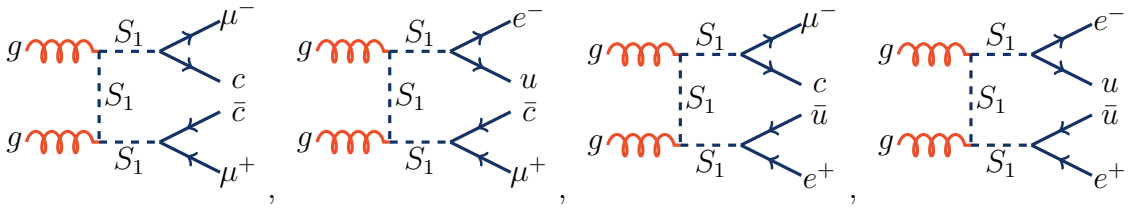

Figure 6.3: Diagrams of the pair-production leptoquark model process considered in this analysis which produce a final state containing $e\mu$. Made by another analyser.

Pair production does not lead to a charge-flavour asymmetry, but could contribute to a statistical 'washing away' of such an asymmetry generated by single production. Lowering the mass of the leptoquark (so that pair production is easier) and the reduction of the λ_{ue} coupling (so that single production is more difficult) both make this problem worse. Studies were performed looking at MC simulations of pair- and single-production modes. Significant contribution from the pair-production mode can be suppressed by vetoing events which have at least two jets, if the second hardest jet has $p_{\mathrm{T}} < 300\,\mathrm{GeV}$. This requirement is used in the regions targeting LQ-like scenarios as described in Section 6.6.

Existing constraints on leptoquarks come primarily from two sources: indirect constraints and direct searches. Most indirect constraints are derived from observables which are sensitive to an internal virtual leptoquark. The model proposed here requires two leptoquark couplings to be 'switched on'. One set of relevant constraints comes from effective four-fermion operators connecting (e, μ, u, c) such as are found in Reference [128], in the measurement of

$$\frac{BR(D^+ \to \pi^+ \bar{e}\mu)}{BR(D^0 \to \pi^- \bar{e}\nu_e)}. \tag{6.2}$$

Considering also the $D \to e\mu$ decay rate in the same paper, the leptoquark couplings are constrained to be $\lesssim 0.3$ for leptoquark masses of $\sim 1\,\mathrm{TeV}$. Results from HERA are also relevant: Reference [129] asserts that $\lambda_{eu}\lambda_{\mu c} < 0.8\ \mathrm{TeV}^{-2} m^2_{\mathrm{LQ}}$ for scalar leptoquarks. Regarding direct leptoquark searches, the ATLAS result given in Reference [130] rules out leptoquark masses below 1.25 TeV at 95% confidence.

6.3 Estimation of lepton efficiencies and biases

Electrons and muons are detected in different ways, and so have different efficiencies for detection. The efficiency at each stage from detection to reconstruction as a Signal object is quantified by experimental performance groups within ATLAS and distributed to analyses. As an example, for electrons, efficiencies are measured for the trigger, reconstruction, identification and isolation.

These efficiencies are for the most part not biased. For example, if the reconstruction efficiency for electrons and positrons were independent of charge and kinematic properties, a variation of the efficiency would affect $e^+\mu^-$ and $e^-\mu^+$ equally, and so leave the ratio of the two unchanged. This analysis is concerned, therefore, with charge-dependence of the efficiencies, which may bias the ratio. Kinematic dependence of the efficiencies may also affect the charge ratio, if coupled with a kinematic bias of the $e^+\mu^-$ and $e^-\mu^+$ events. To illustrate this, consider a situation where electrons, though produced at a rate equal to positrons, tend to have higher $|\eta|$. If the efficiency for electron reconstruction were lower here, the ratio may be biased in favour of positrons despite the absence of an explicit charge dependence.

As introduced in Section 6.2.1, some aspects of detector geometry could lead to a charge dependence in lepton efficiencies. The ATLAS muon system [125], as an example, has a toroidal magnetic field which serves to bend muons oppositely in rapidity depending on their charge. Such a deflection could mean that muons of the same pseudorapidity pass either side of an acceptance edge or through regions of differing material composition. Many such effects, while inducing a local bias, may be expected to be reversed elsewhere in the detector and so give no overall bias for a symmetrical detector. The idea of a symmetrical detector is is not met in practice, both due to practical design considerations, defects in construction, and by malfunction during use. Even in the case of a symmetrical detector, the symmetry with respect to outgoing particles may be disrupted by a displacement of the interaction point from the geometrical centre of the detector.

While concerns such as these deserve attention, there are reasons to be hopeful as to the magnitude of these biases. Event selections typically avoid areas close to the edges of acceptance, and efficiencies are typically close to uniform (or at least smooth). In the frequent case where there is no charge dependence in the "official" lepton efficiencies, it is not always clear whether this is because such a dependence has been observed to be

negligible, or has not been looked for.

6.3.1 Electrons

For the case of electrons, the solenoid magnetic field primarily deflects in the azimuthal direction. The ATLAS detector systems are largely symmetrical in ϕ so there is little reason to expect any differences in electron and positron reconstruction. In 2011, ATLAS verified in Reference [131] that any charge effect in the reconstruction is too small to measure. More recently, ATLAS colleagues confirmed that there was no bias in electron efficiencies observed, with the exception of the ECID (electron charge identification) tool [49]. The ECID tool is built using a Boosted Decision Tree (BDT), where the input variables are generally blind to the charge of the electron and thus would not introduce any bias in charge ID efficiency. However, it includes one variable which is not blind to the electron charge: $\Delta\phi_{res}$, which is defined as a the azimuthal separation between the electron's track and cluster, multiplied by the electron's charge. With the inclusion of this variable into the BDT, the resulting efficiencies and scale factors for each electron charge differ slightly at values of electron $\eta > 1.5$.

Fortunately for the general population of ATLAS, but unfortunately for this search, the biased variable is one of the most powerful variables in the BDT for background rejection. Since the observed bias is small and localised in η, its effect will be covered by recommendations for standard electron systematic uncertainties.

6.3.2 Muons

For the case of muons, the toroid magnet can lead to different muon trajectories for each charge which could cause charge based differences in reconstruction and trigger efficiencies. It has been shown in Reference [132] that for the range of $1\,\text{GeV} < p_\text{T} < 6\,\text{GeV}$ there is a measurable asymmetry in the efficiencies. For this analysis, the p_T range of interest is much higher and it was unclear to what extent this observed asymmetry is continued. One additional analysis by ATLAS in 2011, measuring $W \to \mu\nu$ charge asymmetry [121], saw no significant charged based differences in muon reconstruction or trigger efficiencies. Unfortunately this analysis was limited by its 36pb^{-1} integrated luminosity data set, which led to the efficiency measurement being the dominant uncertainty. The vastly increased amount of data now available will lead to tighter constraints in these efficiency measurements.

Muon reconstruction efficiencies

For this analysis, muon reconstruction efficiencies are measured following the tag-and-probe procedure used by ATLAS [61]. However, in order to calculate any charge based efficiency asymmetries, information about the muon charges is retained. Any asymmetry can then be corrected for by creating a weight which brings each muon reconstruction efficiency back to the averaged efficiency value of both charges. To compensate for these weights, a systematic uncertainty based on this average efficiency is also considered for the events.

The tag-and-probe method is a data driven calibration method based upon finding a region of phase space which is kinematically pure in muons, and using it as a comparison point for muons in a looser region. This analysis applies tag-and-probe to $Z \to \mu\mu$ events, since it can be expected that these contain two muons. A 'tag' muon is identified using Tight requirements (using the `Medium` muon ID working point that is used in the rest of the analysis). Since the region of phase space used is dominated by $Z \to \mu\mu$ events, it is then expected that the event contains a second muon. The second muon in the event is called the 'probe' muon.

The efficiency (ϵ(`Medium`)) is defined as the fraction of the probe muons that are correctly reconstructed. It contains contributions from each part of the detector involved in muon reconstruction: the ID tracker, muon spectrometer (MS) and calorimeter (calo). Because each of these detectors perform independently, probe muons reconstructed using ID and calo requirements allow measurement of the MS efficiency, whilst probe muons reconstructed using MS requirements allow the measurement of the ID muon reconstruction efficiency.

There are two stages to the muon efficiency calculation, defined in Equation 6.3. The first stage of the measurement looks at the efficiency of reconstructing `Medium` muons assuming an ID track is reconstructed, using a calo muon as a probe. The second stage corrects this with the efficiency of reconstructing an ID track muon, using a MS muon as a probe. There are some assumptions with this calculation. It is assumed that the ID and MS reconstructions are independent, such that $\epsilon(ID) = \epsilon(ID|MS)$. Additionally, one can assume that the choice of calorimeter or ID probe doesn't effect the probability

of `Medium` reconstruction so $\epsilon(\texttt{Medium}|\text{ID}) = \epsilon(\texttt{Medium}|\text{Calo})$.

$$\begin{aligned}\epsilon(\texttt{Medium}) &= \epsilon(\texttt{Medium}|\text{ID}) \cdot \epsilon(\text{ID}) \\ &\approx \epsilon(\texttt{Medium}|\text{Calo}) \cdot \epsilon(\text{ID}|\text{MS})\end{aligned} \tag{6.3}$$

The tag muon is identified and fires the trigger in the selection requiring the `Medium` identification working point requirements to be met. The probe muon is reconstructed in the looser regions to separately consider efficiency contributions from the three relevant detector components. For probe muons, a Z mass veto of $|m_{\mu\mu} - m_Z| < 5$ GeV for ID probes, and $< 10\,\text{GeV}$ for calo and MS probes, is made. For both cases it is required that the muon $p_\text{T} > 30\,\text{GeV}$ and $|\eta| < 2.5$, along with $|d_0(\sigma)| < 3$ and $|z_0| < 10\,\text{mm}$, and loose isolation requirements. The regions are chosen to ensure that there is a sufficiently pure muon sample. Single-lepton triggers are used to keep the tag and probe muons independent.

For a precise measurement of the efficiency, it is necessary to estimate and subtract from data any contributions from background (not $Z \to \mu\mu$) events. Contributions from $Z \to \tau\tau$ and $t\bar{t}$ backgrounds are estimated using MC simulations (N_{OC}^{MC}). To estimate the $W+$jets and multi-jets contributions, the flavour symmetric nature of these backgrounds is exploited. The oppositely charged (OC) two muon yield is estimated from data using same charge (SC) tag-and-probe pairs (N_{SC}^{Data}). This results in the following expression for the total background yield (N^{BG}):

$$N^{\text{BG}} = N_{\text{OC}}^{\text{MC}} + T \cdot (N_{\text{SC}}^{\text{Data}} - N_{\text{SC}}^{\text{MC}}), \tag{6.4}$$

where T is a global transfer factor to account for any charge asymmetry in the $W+$jets and multi-jet processes, and $N_{\text{SC}}^{\text{MC}}$ is the number of same charge events for said processes in MC. The value of T was estimated by the muon group to be $T = 1.7$, 1.1 and 1.2 for MS, ID and calo probe muons respectively. The uncertainties on these values are included in the systematic uncertainty for the muon efficiency method.

The efficiency value can then be calculated in data using:

$$\epsilon = \frac{N_{\text{R}}^{\text{Data}} - N_{\text{R}}^{\text{BG}}}{N_{\text{P}}^{\text{Data}} - N_{\text{P}}^{\text{BG}}}, \tag{6.5}$$

where N_P is the number of probe candidate muons and N_R is the number of those

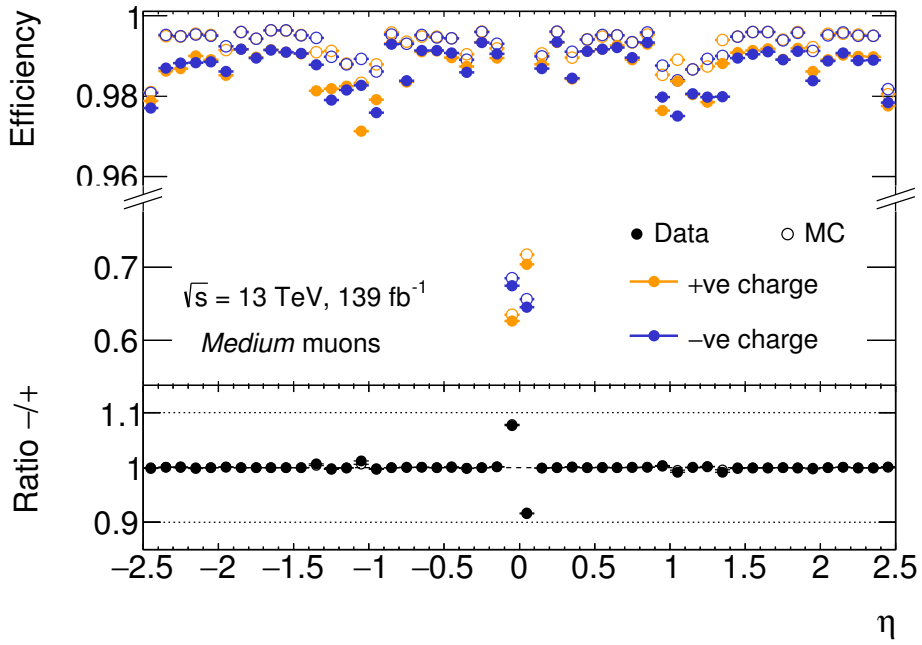

Figure 6.4: Muon reconstruction efficiency for `Medium` muons in bins of the probe muon η. The efficiency is shown separately for +ve charged muons in orange and -ve charged muons in blue.

that are successfully reconstructed as muons. The efficiency value can be compared to the ratio obtained using $Z \to \mu\mu$ MC simulations:

$$\epsilon = \frac{N_{\mathrm{R}}^{\mathrm{MC,Sig}}}{N_{\mathrm{P}}^{\mathrm{MC,Sig}}}. \tag{6.6}$$

The calculated values of muon reconstruction efficiency in bins of η can be seen in Figure 6.4. This plot shows the values separately for positively- and negatively-charged muons. The efficiencies for both charges are very similar throughout most of the η distribution. The largest charge discrepancy occurs for $-0.1 < \eta < 0.1$. This region contains 8 large sectors of no detection where cables enter the detector, so a drop in efficiency is expected. Each charge's efficiency is compared to the charge-averaged value. For $-0.1 < \eta < 0.0$ the negatively-charged muons have a relative 8% reduction in efficiency, whilst for $0.0 < \eta < 0.1$ the negatively-charged muons have a relative 8% increase in efficiency. Since positively-charged muons are deflected to large negative η by the toroid magnet's field, this trend is expected.

The angular structure of the efficiencies can be further investigated by looking at

a map in η and ϕ. In Figure 6.5a, the charge-averaged efficiency is shown and in Figure 6.5b the ratio of the per-charge efficiencies is shown. The ϕ binning reflects the muon spectrometer structure. For η, the greatest granularity occurs around ± 1.0, where the detector transitions between the barrel and end-caps. As seen already, the lowest efficiency and greatest charge dependence are found in the central region. These plots also show a reduction in efficiency at $-2.2 < \phi < -1.0$. This is caused by the feet of the detector, and affects both charges equally. Furthermore, in the transition between the barrel and end-caps at $0.95 < |\eta| < 1.05$ there is reduction in efficiency which shows asymmetries both in the muon charge and the sign of η. For both transition regions, the lower end of η shows a relative increase in the efficiency of negatively-charged muons.

This interesting behaviour can be understood by considering the structure of the ATLAS muon systems (Figure 6.6). At least two MDT hits are required for this analysis. If a negatively-charged muon, which will bend away from the (positive) z-axis, travels around $\eta \sim 1$ it is more likely to miss a second MDT hit which a positively-charged muon would not.

It is also interesting to consider the effect of the muon p_{T} on the reconstruction efficiencies. Examining Figure 6.7a, no charge bias is observed beyond 2%. Ideally the full efficiency dependence on $(\eta, \phi, p_{\mathrm{T}})$ should be studied, since higher p_{T} muons will have a larger radius of curvature in the magnetic field and so have decreased divergence between charge paths. However, since the large p_{T} bins have low statistics, dividing them further into bins of η and ϕ would not allow for any statistically significant conclusions.

The bias, defined as $\epsilon_-(p_{\mathrm{T}}, \eta, \phi)/\epsilon_+(p_{\mathrm{T}}, \eta, \phi) - 1$, is thus factorised into an angular-dependent part and a p_{T} dependent scale:

$$b(p_{\mathrm{T}}, \eta, \phi) = s(p_{\mathrm{T}}) \times b(\eta, \phi), s(p_{\mathrm{T}}) = \frac{b(p_{\mathrm{T}})}{b}. \tag{6.7}$$

Here, any parameters omitted in the argument are averaged over. The bias scale is shown in Figure 6.7b. It has the general decreasing trend expected from the reduction in divergence of the differently charged muon paths. The increase in the last bin is most likely a consequence of statistical fluctuation due to low event yields.

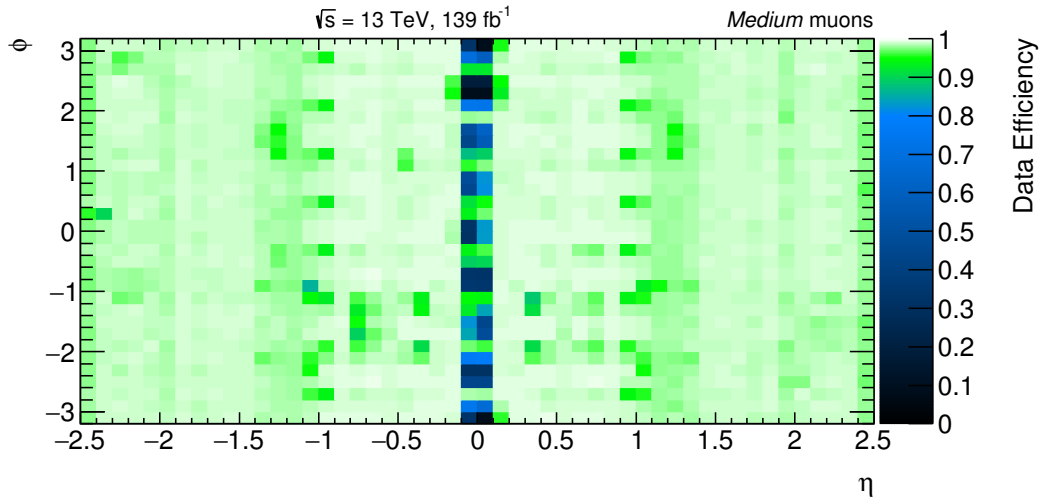

(a) Charge averaged data efficiency.

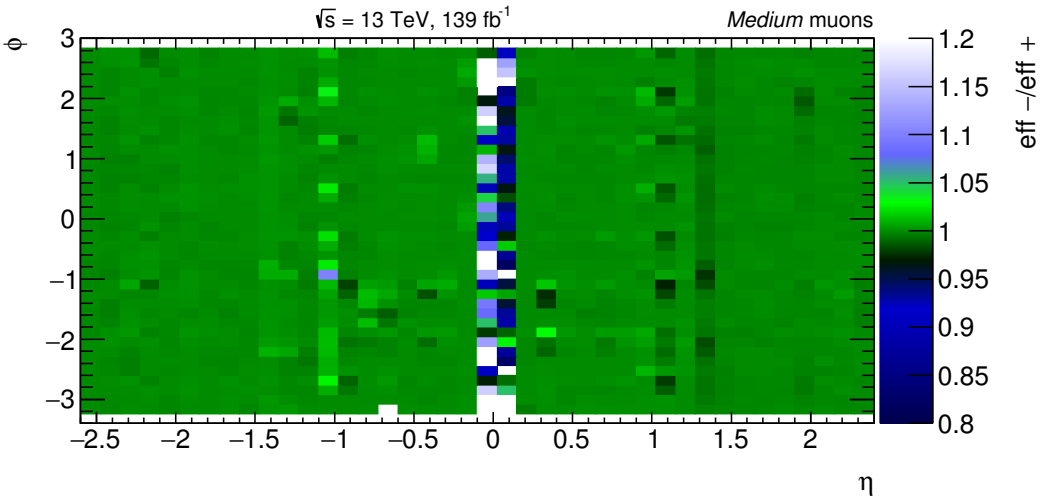

(b) Ratio of efficiencies of each charge.

Figure 6.5: Muon reconstruction efficiency for `Medium` muons in bins of the probe muon η and the probe muon ϕ.

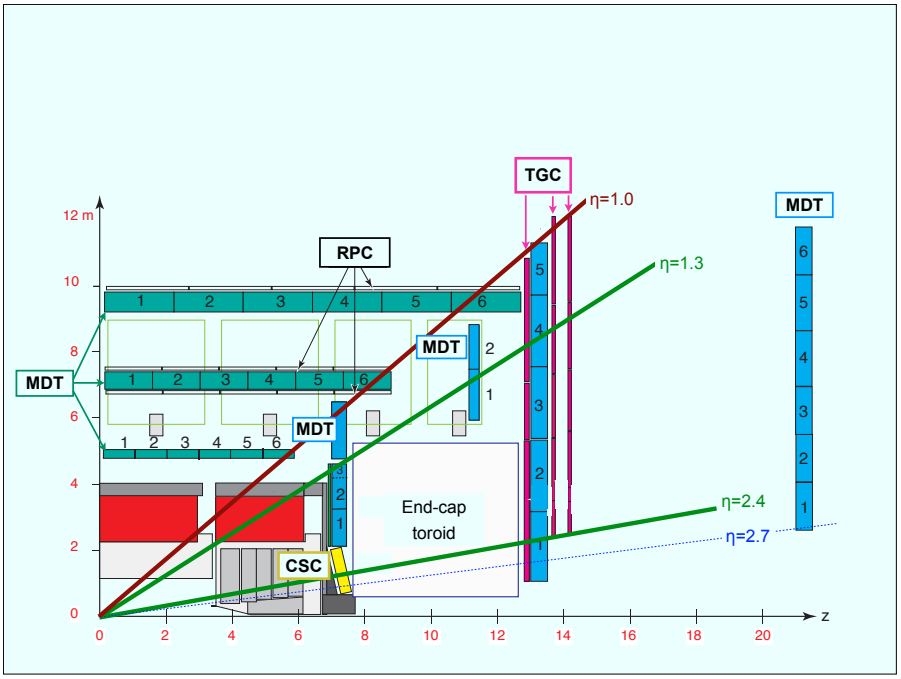

Figure 6.6: Schematic of a quarter section of the ATLAS muon system [133].

Muon trigger efficiencies

The efficiency and bias of the muon leg in $e\mu$ triggers used in the analysis can be investigated in a similar tag-and-probe method as above. A pure sample of $Z \to \mu\mu$ events is used again, following the same selections as the reconstruction efficiency case. The trigger chosen for the tag muon ensures that all events are recorded regardless of whether the probe muon would have fired a trigger.

The probe muons used for this study must satisfy similar requirements, with an additional Z mass veto of $|m_{\mu\mu} - m_Z| < 10\,\text{GeV}$. These ensure that the muon will lie within the region of the detector with triggering acceptance, be consistent with the primary vertex, and be sufficiently isolated from other event activity.

Figure 6.8 shows the calculated values of muon trigger efficiency in bins of η. This plot shows the values separately for positively- and negatively-charged muons. A similar structure to Figure 6.4 can be seen, as expected. A map of the efficiency and bias in bins of (η, ϕ) is shown in Figure 6.9, which shows the structure more clearly. A larger bias is seen around $|\eta| = 1$, where the structure of the muon spectrometer shown in Figure 6.6 can once again be considered. The triggers used for these studies require three TGC hits or > 2 RPC hits [133]. For all muons with $0.95 < |\eta| < 1.0$ TGC hits are highly unlikely,

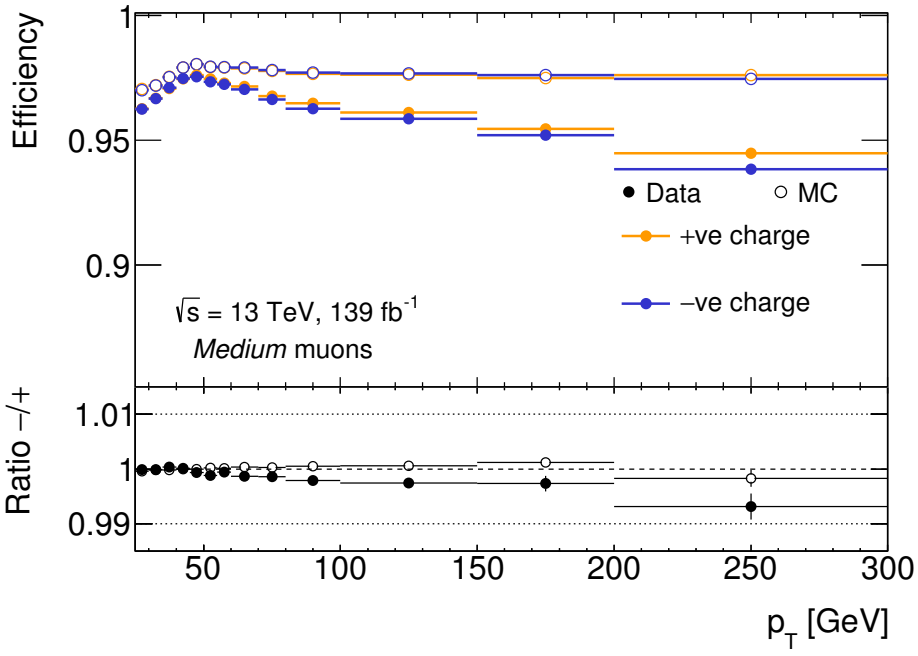

(a) p_{T} dependence of muon reconstruction efficiency for both charges.

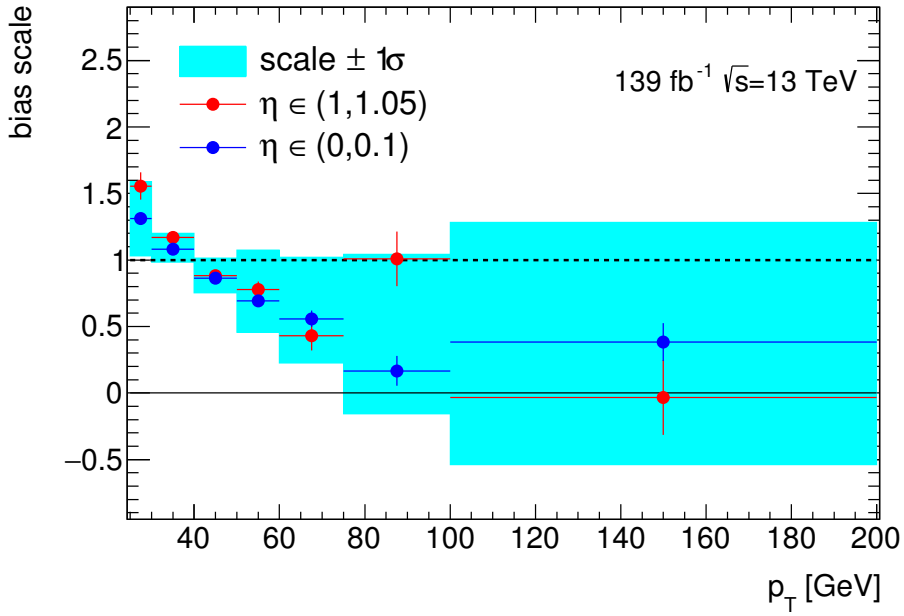

(b) Muon reconstruction efficiency bias scale $s(p_{\mathrm{T}})$. The uncertainty band shows the weighted standard deviation over the η and ϕ bins.

Figure 6.7: Muon reconstruction efficiency for `Medium` muons in bins of the probe muon p_{T}.

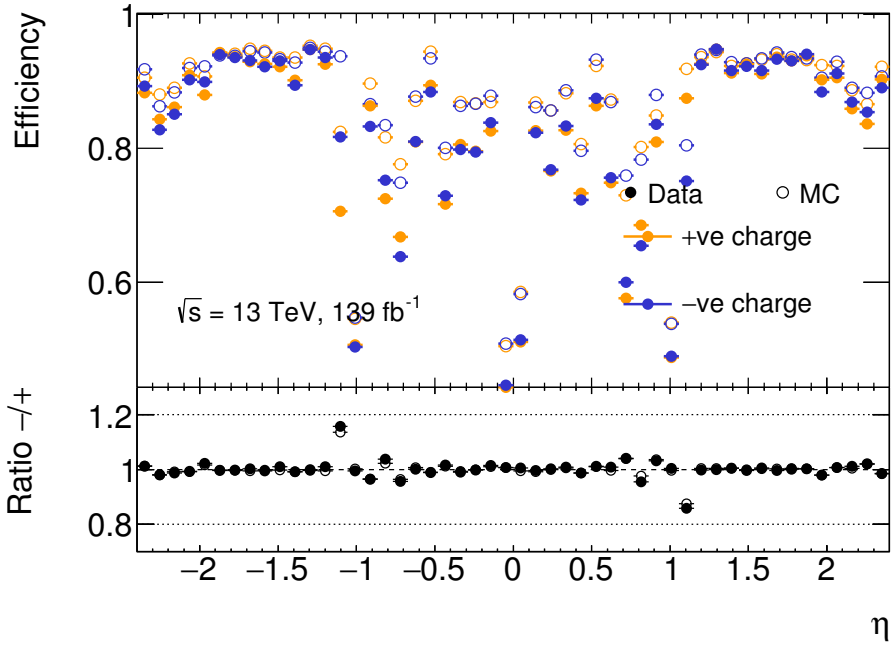

Figure 6.8: Muon trigger efficiency for `Medium` muons in bins of the probe muon η. The trigger efficiency is shown separately for +ve charged muons in orange and -ve charged muons in blue.

resulting in a low efficiency. However, since negatively-charged muons curve away from the positive z-axis they are more likely to obtain 2 RPC hits. Conversely, in the low efficiency region with $1.0 < |\eta| < 1.5$ where RPC hits are less likely, positively-charged muons will bend into the TGC layers so are more likely to obtain 3 hits.

As stated in Section 6.3.2, it is important to look at the p_{T} dependence of the efficiency. The bias defined in Equation 6.7 can also be measured for the trigger efficiencies. The p_{T} dependence and bias measurement are shown in Figure 6.10. There is a decrease in scale as muon p_{T} increases, as is expected.

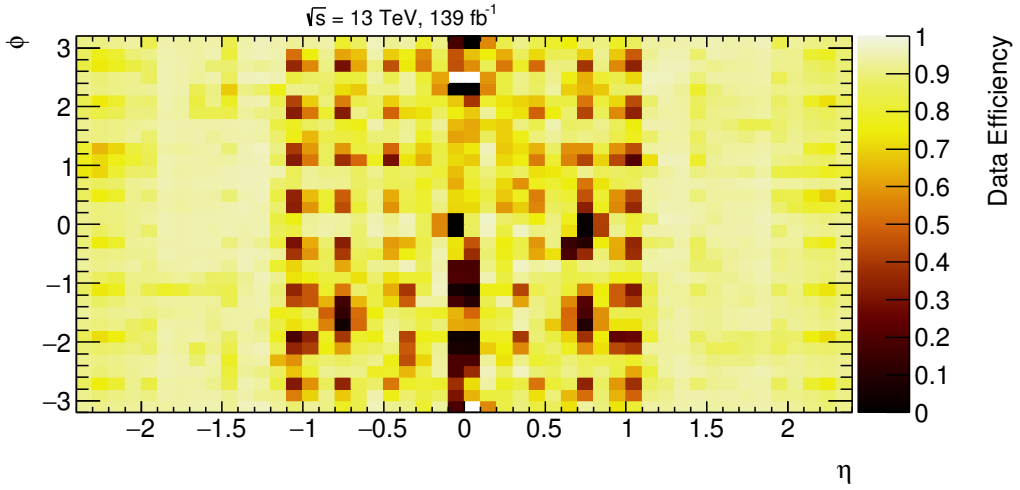

(a) Charge averaged data efficiency.

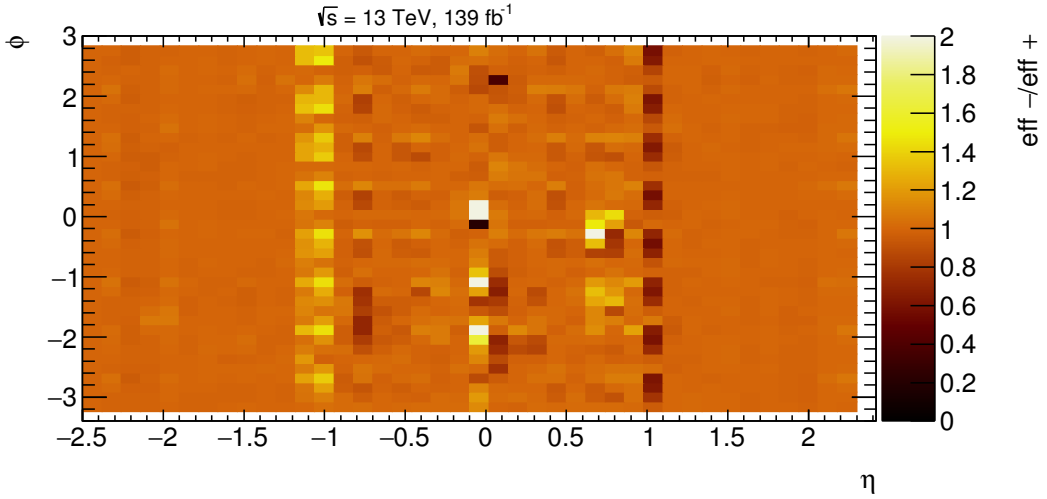

(b) Ratio of efficiencies of each charge.

Figure 6.9: Muon trigger efficiency for `Medium` muons in bins of the probe muon η and the probe muon ϕ.

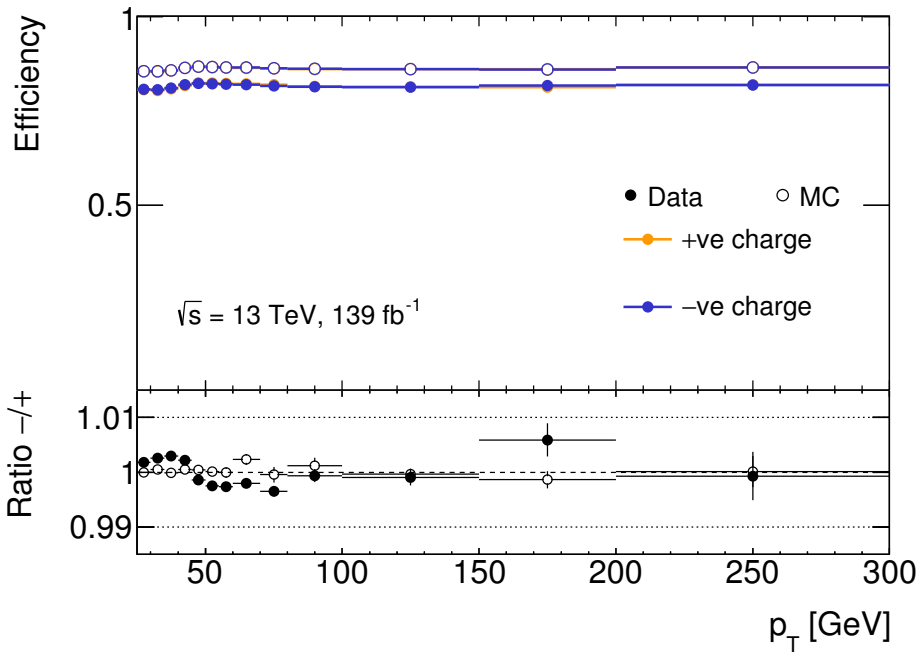

(a) p_{T} dependence of muon trigger efficiency for both charges.

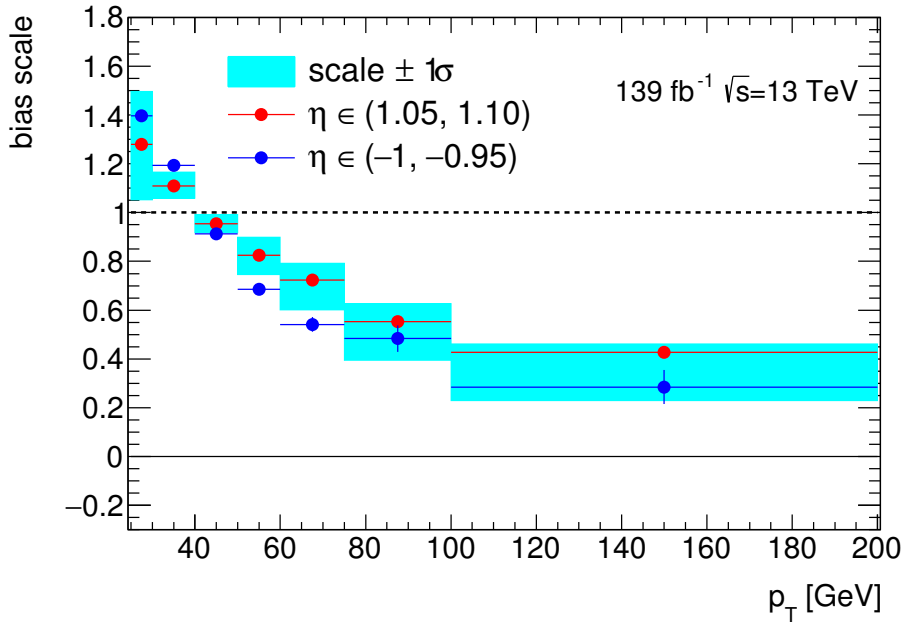

(b) Muon trigger efficiency bias scale $s(p_{\mathrm{T}})$. The uncertainty band shows the weighted standard deviation over the η and ϕ bins.

Figure 6.10: Muon trigger efficiency for `Medium` muons in bins of the probe muon p_{T}.

Correcting muon reconstruction and trigger biases

In the previous sections, the overall charge bias in efficiency measurements for $Z \to \mu\mu$ were shown to be small. However, significant differences in particular regions of η, ϕ and p_{T} — which cannot be presumed to be negligible in the main analysis events — motivate the creation of correction weights to bring efficiencies back to the charge average. These weights are calculated using the biases and scales defined in equation 6.7:

$$\frac{w_+}{w_-} = 1 + b(p_{\mathrm{T}}, \eta, \phi) = 1 + s(p_{\mathrm{T}})b(\eta, \phi) \tag{6.8}$$

The weights are also defined to obey $w_+ w_- = 1$. Thus,

$$w_+ = \sqrt{1 + s(p_{\mathrm{T}})b(\eta, \phi)} \tag{6.9}$$

$$w_- = 1/\sqrt{1 + s(p_{\mathrm{T}})b(\eta, \phi)} \tag{6.10}$$

The relevant sign weight is then applied to each $e\mu$ event selected in the main analysis, taking the weight value corresponding to the event muon's kinematic properties. The data weight distributions can be seen in Figure 6.11 for the 2015–2016 data, in Figure 6.12 for 2017 and in Figure 6.13 for 2018 data. As can be seen, the weights are generally very close to one, so will not have a particularly significant effect on the events, as expected.

The statistical uncertainty in the bias $b(\eta, \phi)$ is propagated into the weight to produce systematic uncertainties. Independently, systematic uncertainties on the p_{T} dependent scale are constructed. These are taken by propagating the statistical uncertainty, as shown by the blue band in Figures 6.7b and 6.10b, into the weight. As will be seen in Section 6.10, these uncertainties have a very small effect on the ratio measurement.

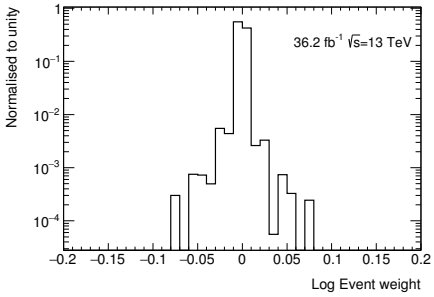

(a) Reconstruction $w+$.

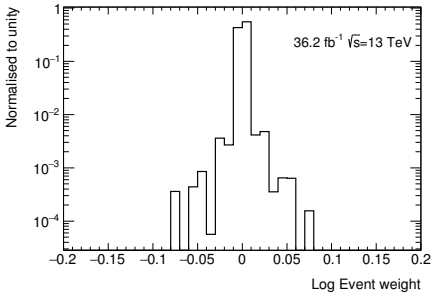

(b) Reconstruction $w-$.

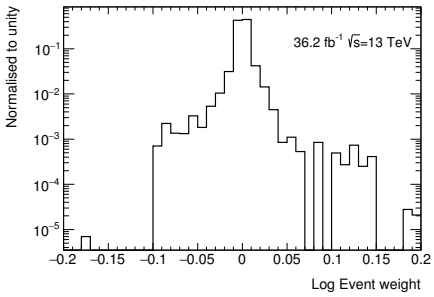

(c) Trigger $w+$.

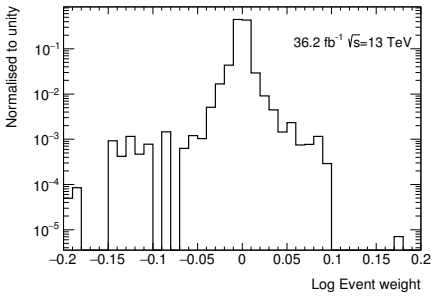

(d) Trigger $w-$.

Figure 6.11: Muon efficiency log_{10} weight distributions in data 2015–2016 analysis events.

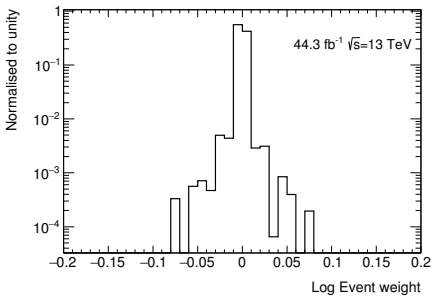

(a) Reconstruction $w+$.

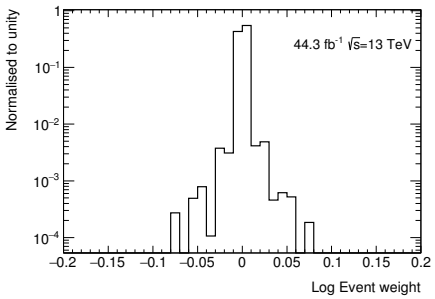

(b) Reconstruction $w-$.

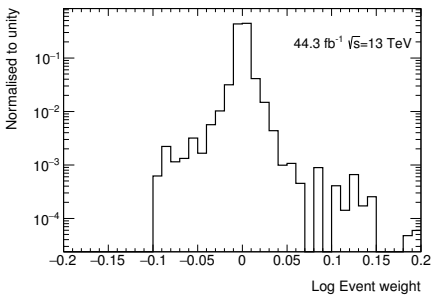

(c) Trigger $w+$.

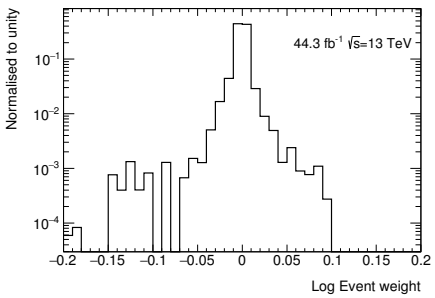

(d) Trigger $w-$.

Figure 6.12: Muon efficiency log_{10} weight distributions in data 2017 analysis events.

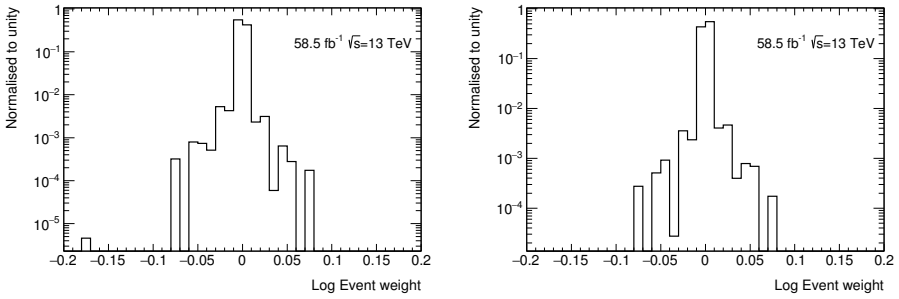

(a) Reconstruction $w+$.

(b) Reconstruction $w-$.

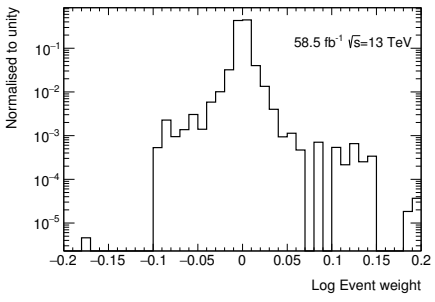

(c) Trigger $w+$.

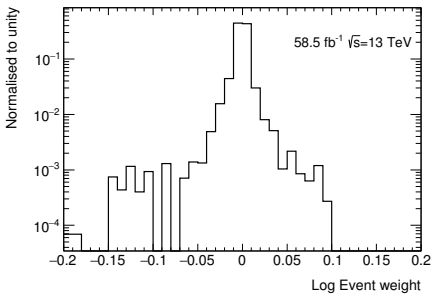

(d) Trigger $w-$.

Figure 6.13: Muon efficiency log_{10} weight distributions in data 2018 analysis events.

6.4 Data and Monte Carlo simulation

The strategy followed in the ratio measurement is (to first order) independent of simulation. In order to set exclusion limits on concrete signal models and have a good expectation of the Standard Model ratio, however, Monte Carlo simulations of these signal models and of the Standard Model background are needed. Simulations of possible signals and of the main backgrounds are also useful for optimisation of the strategy, as well as for estimation of experimental biases and systematic uncertainties.

The same data is used as detailed in Section 5.1. The dominant SM processes producing events with $e\mu$ in the final state are as follows:

- $t\bar{t}$ production, where the top quarks subsequently decay leptonically to produce e and μ,
- t production in association with a W boson, where both decay leptonically,
- and pair production of electroweak bosons ("diboson").

The configurations for all SM background MC samples used in the analysis are listed in Table 6.1. This includes the relevant parton distribution function (PDF) set, the configuration of underlying-event and hadronisation parameters, and the cross section calculation order in α_s used to normalise the sample's event yields.

Apparent $e\mu$ events can also arise from 'fake leptons', for example from a W + jets event with one jet falsely identified as a lepton, or from a multi-jet event with two jets misidentified. It is difficult to obtain an accurate estimate of such processes by Monte Carlo simulation, so they are often estimated using data-driven methods. In this analysis, the fake lepton background is calculated using a likelihood matrix method. Events from W+jets MC are not used in this analysis as the fake background estimation replaces this.

The RPV-SUSY signal events are generated at LO using MADGRAPH5_aMC@NLO version 2.61 together with the `RPV MSSM UFO` model [134]. The leptoquark signal events are also generated this way, using the `LO_LQ_S1` model. Shower evolution and hadronisation is performed by PYTHIA8 version 8.23, and the `NNPDF` 2.3 LO PDF is used.

All RPV couplings except λ'_{231} are set to zero, and λ'_{231} is set to one when generating the events. Sparticles other than the neutralino and smuon are considered to be

Physics process	Generator	Parton shower	Cross section	Tune	PDF set
$t\bar{t}$	Powheg-Box	Pythia8	NNLO+NNLL	A14	NNPDF 2.3 LO
single top	Powheg-Box	Pythia8	NNLO	A14	NNPDF 2.3 LO
fully leptonic $VV(V = W, Z)$	Sherpa 2.2.2	Sherpa 2.2.2	NLO	Sherpa default	CT10
semi-leptonic $VV(V = W, Z)$	Sherpa 2.2.1	Sherpa 2.2.1	NLO	Sherpa default	NNPDF 3.0 NNLO
loop-induced / same-charge $VV(V = W, Z)$	Sherpa 2.1.1	Sherpa 2.1.1	NLO	Sherpa default	CT10
$Z/\gamma^*(\rightarrow ll)$ + jets	Sherpa 2.2.1	Sherpa 2.2.1	NNLO	Sherpa default	NNPDF 2.3 LO
$t\bar{t} + X(X = t, WW, W, Z, t\bar{t})$	Madgraph5_aMC@NLO	Pythia8	NLO	A14	NNPDF 2.3 LO
RPV-SUSY signal	Madgraph5_aMC@NLO	Pythia8	LO	A14	NNPDF 2.3 LO
LQ signal	Madgraph5_aMC@NLO	Pythia8	LO	A14	NNPDF 2.3 LO

Table 6.1: Simulated background event samples used in this analysis with the corresponding matrix element and parton shower generators, cross section order in α_S used to normalise the event yield, underlying-event tune and PDF set.

decoupled — their masses are set to a large value. The signal samples are simulated using AtlFastII [135], a fast simulation of the ATLAS detector. Monte Carlo samples are generated for a two-dimensional grid of points, distributed in a plane of smuon and neutralino masses. The process' cross section varies with the square of the coupling, so samples for other couplings can be obtained by weighting the generated samples. Exclusion limits are calculated for a selection of different couplings but unless otherwise stated it may be assumed that in all Figures and Tables, a coupling of one is used.

All leptoquark couplings are set to zero, apart from the coupling of electrons to up quarks and muons to charm quarks, which are set to be equal to each other. The leptoquark hard processes specified include zero additional light jets in the final state. The RPV-SUSY hard processes specified include either zero or one additional light jet in the final state. This is matched to the `Pythia` parton shower using the CKKW-L [136] merging scheme. The merging scale chosen here is $Q_{\mathrm{MS}} = \frac{1}{4}(m_t + m_\chi)$, where m_χ is the mass of the neutralino.

For the leptoquark case, Monte Carlo samples are generated for a set of leptoquark masses, with a coupling of one. Given that the cross section for the single-production leptoquark process varies with the square of the coupling, samples for other couplings are obtained by weighting the generated samples. Thus, a two-dimensional grid of leptoquark mass and coupling is obtained. These points were chosen so as to be within

the potential sensitivity of the analysis.

The same considerations to correct the MC to match the observed pile-up distribution seen in data are made as described in Section 4.2.

6.5 Object selection

The electrons, muons and jets selected for this analysis are first required to satisfy 'Baseline' requirements. These Baseline objects are used for the construction of $p_{\mathrm{T}}^{\mathrm{miss}}$. After this, the Baseline objects pass through an overlap removal procedure to resolve any instances of ambiguity between close-by objects. Any objects not surviving overlap removal play no further role in the analysis.

The objects passing overlap removal are then required to pass more stringent 'Signal' requirements for use in the analysis. For jets, the same Signal selection is required throughout the analysis. For leptons, a 'Nearly-Signal' selection is first required. The objects passing this selections are used in the likelihood matrix method used to calculated the fake lepton background. Additionally they are used to define validation regions where the data-MC agreement can be checked.

Finally an even more stringent 'Signal' selection is applied to leptons. These Signal leptons and Signal jets enter the analysis signal and control regions used to produce the final results.

In addition to these requirements on specific physics objects, events are required to pass triggers, and various cleaning selections as described in Section 2.3.4. The rest of this Section will go through the definitions of the various requirements in turn.

Baseline electrons are required to have $|\eta| < 2.47$, $p_{\mathrm{T}} > 10\,\mathrm{GeV}$, and to pass the `Loose` likelihood-based identification working point defined in Reference [50]. The same p_{T} and $|\eta|$ demands are placed on baseline muons, which are also required to pass the `Medium` identification working point as defined in Reference [62].

Jets are reconstructed as described in Section 2.3.2 using the particle flow algorithm. Baseline jets are required to have $p_{\mathrm{T}} > 20\,\mathrm{GeV}$ and $|\eta| < 2.8$.

Once the baseline objects have been obtained they are used to calculate $p_{\mathrm{T}}^{\mathrm{miss}}$. Following this, they undergo the same overlap removal procedure as that described in Section 2.3.4. Next on their journey toward Signal objects, leptons (produced by MC

simulation, not real data) are required to pass a 'prompt selection' defined by the ATLAS Isolation and Fake Forum. Because the fake lepton background is so important for this analysis, as the only background that is expected to have a ratio different to one, it is preferred that the entirety of the fake lepton background is kept separate, and estimated using a more reliable data-driven approach. Here the prompt selection helps to ensure that what is taken to be the prompt, real SM background, is in fact prompt. For example, no W + jets MC events pass this prompt selection, but W + jets events are expected to be the dominant process in the data-driven fake lepton background.

As mentioned at the start of this Section, two categories of Signal lepton are defined: Nearly-Signal and Signal. Signal is a subset of Nearly-Signal. Nearly-Signal electrons are required to have $p_{\mathrm{T}} > 25\,\mathrm{GeV}$, in order to exclude the region of phase space where the triggers used have a low efficiency. They are also required to pass the ECID, which is designed to eliminate electrons whose charge has been misidentified.

The resulting Nearly-Signal electrons are then filtered even more to produce Signal electrons. Signal electrons are required to have a strong consistency with the primary vertex, through $|d_0(\sigma)| < 3$, and $|z_0 \sin(\theta)| < 0.3\,\mathrm{mm}$, where d_0 is the transverse impact parameter. They must also pass the `Tight` likelihood-based identification working point defined in Reference [50]. As motivated in Section 2.3.1, isolation requirements are placed on Signal electrons. Following Reference [50], the `Tight` isolation working point is used for electrons with $p_{\mathrm{T}} < 200\,\mathrm{GeV}$, and the `HighPtCaloOnly` isolation working point is used for electrons with $p_{\mathrm{T}} > 200\,\mathrm{GeV}$. This combination provides the highest background rejection over a wide p_{T} range.

Nearly-Signal muons have the same trigger-efficiency motivated momentum requirement as electrons. Signal Muons have the same impact parameter requirements as Signal electrons. They maintain the same `Medium` identification working point as in the Nearly-Signal and Baseline selection. For the same reasons as for electrons, isolation requirements are placed upon Signal muons. For muons with $p_{\mathrm{T}} < 200\,\mathrm{GeV}$, the `Tight` isolation working point defined in Reference [62] is used, which has a 96% efficiency at selecting prompt-muon candidates for all p_{T} and η. Muons with $p_{\mathrm{T}} > 200\,\mathrm{GeV}$ are subjected to the `FixedCutHighPtTrackOnly` isolation working point, which has a greater background rejection.

Signal jets are defined once the JVT and cleaning cuts defined in Section 2.3.2 have been applied.

6.6 Signal regions

Two different signal regions (named SR-MET and SR-JET) are used for the measurement of the charge-flavour ratio r, to obtain sensitivity to a wide class of BSM signals. A summary of these regions is contained in Figure 6.14. Both demand that events have one Signal electron and one Signal muon of opposite charge. The ratio is measured in bins of interesting kinematic variables, in order to understand its behaviour better.

In addition, a more tightly optimised region named SR-RPV is introduced for the calculation of exclusion limits for the RPV-SUSY model in the case that the ratio measurement shows no excesses. Similarly, the region named SR-LQ is introduced to calculate exclusion limits for the leptoquark model. These regions are subsets of SR-MET and SR-JET, respectively. Detailed descriptions of the motivations for the four signals region are provided in this Section.

The first signal region for the ratio measurement is SR-MET, which aims to be largely model-independent by requiring only one cut beyond the selection of exactly two oppositely-charged and different flavour Signal leptons. For example, no requirements are made about the nature of any jets present in the events. To obtain orthogonality to CR-Ratio, which will be defined in Section 6.7, a requirement of $\sum_\ell m_{\mathrm{T}}(\ell, p_{\mathrm{T}}^{\mathrm{miss}}) > 200\,\mathrm{GeV}$ is made (where $\sum_\ell m_{\mathrm{T}}(\ell, p_{\mathrm{T}}^{\mathrm{miss}})$ will be defined imminently). Six variables are used for the ratio measurement.

The example RPV-SUSY model considered predicts an $e + \mu + p_{\mathrm{T}}^{\mathrm{miss}}$ final state. More generally, the particle providing $p_{\mathrm{T}}^{\mathrm{miss}}$ could be the result of another heavy new-physics object decaying semi-invisibly to some high-p_{T} lepton. This means that variables based on picking out regions of phase space with high real $p_{\mathrm{T}}^{\mathrm{miss}}$ and high p_{T} leptons are a good place to search for new physics.

It is also expected that mass-like variables produced from the combination of the lepton p_{T} and $p_{\mathrm{T}}^{\mathrm{miss}}$ will give high values. On the other hand, the SM tends to give lower values, since the decaying SM particles are lighter. In the RPV-SUSY case, the transverse mass of the muon and $p_{\mathrm{T}}^{\mathrm{miss}}$ (as defined in Section 3.2.2) should provide an approximate lower bound on the mass of the smuon, and thus have generally higher values than for SM events and a kinematic endpoint at the mass of the smuon.

For the first variable considered, the aim is to combine these two properties of this signal topology. It is also important to avoid biasing the ratio measurement by binning it

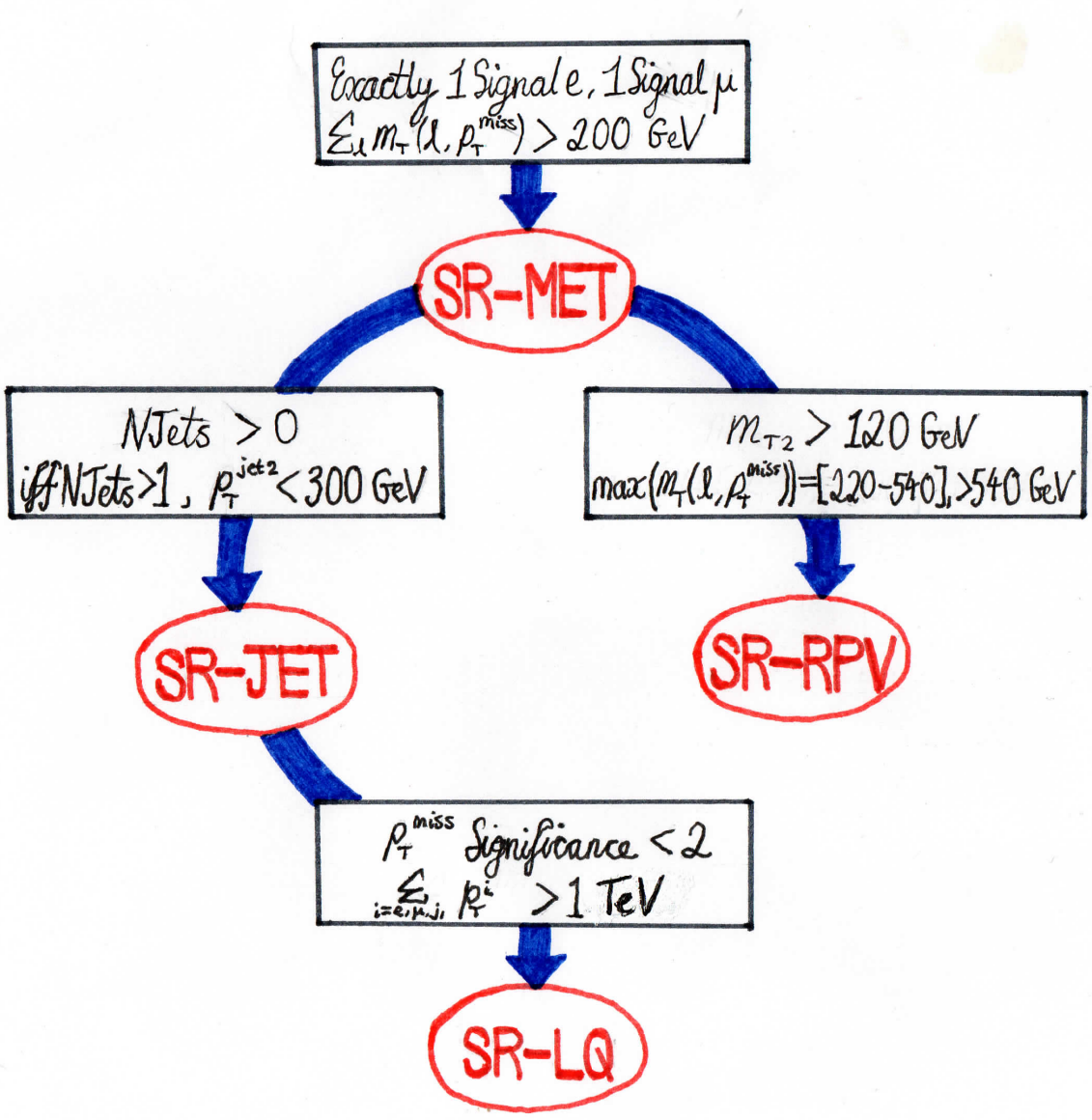

Figure 6.14: Summary of the signal regions used in the analysis. 'NJets' indicates the number of Signal jets in the event. The numbering of leptons and jets indicates their ranking when ordered in p_{T}.

in a variable with an implicit bias on the lepton flavour or charge. For example, ATLAS collides positively charged protons and on average most of the proton's longitudinal momentum is carried in valence quarks. This may lead to a bias towards positively charged leptons being produced with a lower transverse momentum. If this were to be combined with a measurement of the transverse mass of the muon, then $e^+\mu^-$ would be favoured. However, if instead the sum of the transverse masses of the two leptons

($\sum_\ell m_{\mathrm{T}}(\ell, p_{\mathrm{T}}^{\mathrm{miss}})$) was measured there would be no bias to leading order.

The remaining five variables used are similarly not implicitly charge-flavour biased, and should have higher values for BSM models like the RPV-SUSY example. In addition to taking the sum of the lepton-$p_{\mathrm{T}}^{\mathrm{miss}}$ transverse masses, the maximum of the two values can be considered as the second variable: $\max_\ell(m_{\mathrm{T}}(\ell, p_{\mathrm{T}}^{\mathrm{miss}}))$. The third variable is the $p_{\mathrm{T}}^{\mathrm{miss}}$ itself. The fourth variable is the $p_{\mathrm{T}}^{\mathrm{miss}}$ Significance (as defined in Section 3.2.2), which should again be high for the signal topology because it contains a large source of real $p_{\mathrm{T}}^{\mathrm{miss}}$. The penultimate variable is $\sum_{i=e,\mu,\mathrm{j}_1} p_{\mathrm{T}}^i$, the sum of the transverse momenta of the leptons in the event along with that of the highest p_{T} jet, should it exist. The final variable is m_{T2} (as defined in Section 3.2.2). m_{T2} is not a well-defined mass bound for the signal topology. However, the large amount of $p_{\mathrm{T}}^{\mathrm{miss}}$ and p_{T} expected allow the m_{T2} distribution to go up to a few hundred GeV, and peak at higher values than generally seen for the SM.

In summary, the six variables used for the SR-MET ratio measurement are:

- $\sum_\ell m_{\mathrm{T}}(\ell, p_{\mathrm{T}}^{\mathrm{miss}})$,
- $\max_\ell(m_{\mathrm{T}}(\ell, p_{\mathrm{T}}^{\mathrm{miss}}))$,
- $p_{\mathrm{T}}^{\mathrm{miss}}$,
- $p_{\mathrm{T}}^{\mathrm{miss}}$ Significance,
- $\sum_{i=e,\mu,\mathrm{j}_1} p_{\mathrm{T}}^i$,
- and m_{T2}.

Figure 6.15 shows the distributions of $\sum_\ell m_{\mathrm{T}}(\ell, p_{\mathrm{T}}^{\mathrm{miss}})$, $\max_\ell(m_{\mathrm{T}}(\ell, p_{\mathrm{T}}^{\mathrm{miss}}))$ and $\sum_{i=e,\mu,\mathrm{j}_1} p_{\mathrm{T}}^i$, for events of each charge combination. The three overlaid RPV-SUSY signal models shown contribute predominantly to $e^+\mu^-$ at high values of the variables, as expected. These plots include the luminosity uncertainty which is described in Section 5.4. Furthermore, Figure 6.16 shows the distributions of $p_{\mathrm{T}}^{\mathrm{miss}}$, $p_{\mathrm{T}}^{\mathrm{miss}}$ Significance and m_{T2}, for events of each charge combination, where the same behaviour is seen.

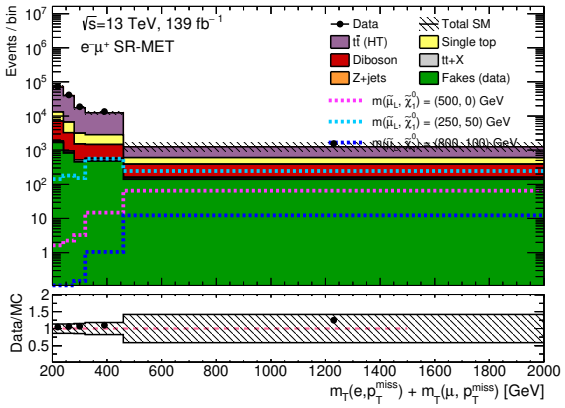

(a) $\sum_\ell m_{\mathrm{T}}(\ell, p_{\mathrm{T}}^{\mathrm{miss}})$, $e^-\mu^+$

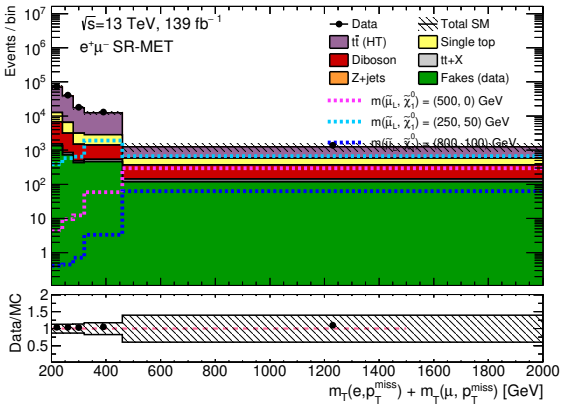

(b) $\sum_\ell m_{\mathrm{T}}(\ell, p_{\mathrm{T}}^{\mathrm{miss}})$, $e^+\mu^-$

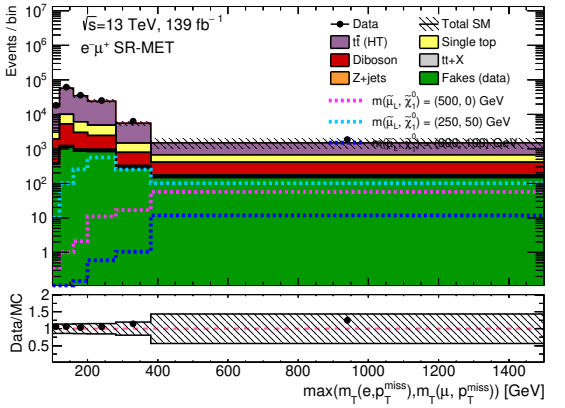

(c) $\max_\ell(m_{\mathrm{T}}(\ell, p_{\mathrm{T}}^{\mathrm{miss}}))$, $e^-\mu^+$

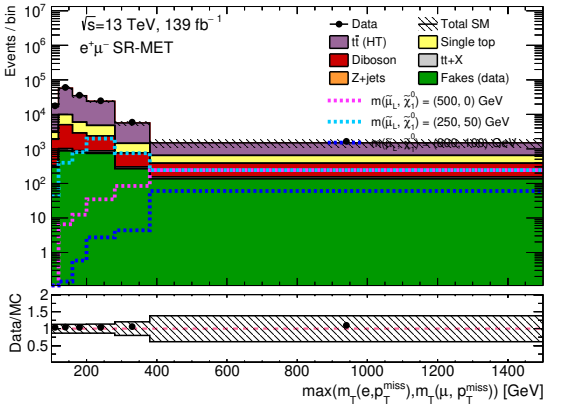

(d) $\max_\ell(m_{\mathrm{T}}(\ell, p_{\mathrm{T}}^{\mathrm{miss}}))$, $e^+\mu^-$

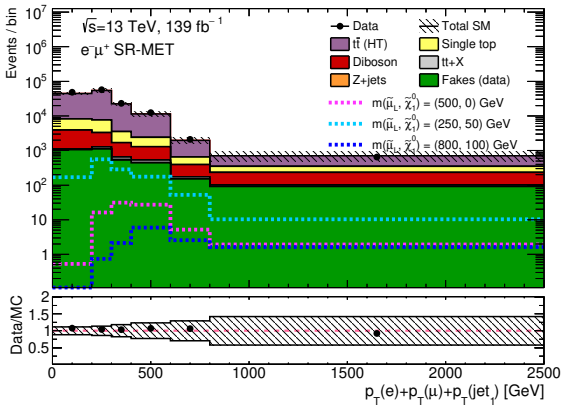

(e) $\sum_{i=e,\mu,\mathrm{j}_1} p_{\mathrm{T}}^i$, $e^-\mu^+$

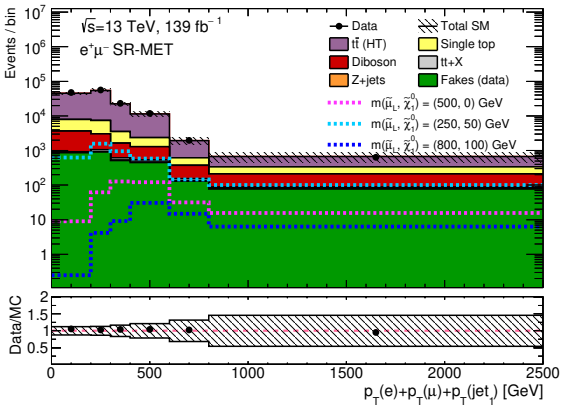

(f) $\sum_{i=e,\mu,\mathrm{j}_1} p_{\mathrm{T}}^i$, $e^+\mu^-$

Figure 6.15: Example distributions in SR-MET for $e\mu$ events of each charge combination. Distributions for three benchmark RPV-SUSY signal points are overlaid. Weights derived in Section 6.7 are applied to $t\bar{t}$ MC events. Statistical, luminosity, $t\bar{t}$ ISR and $t\bar{t}$ weight closure uncertainties are shown. The final bin includes overflow.

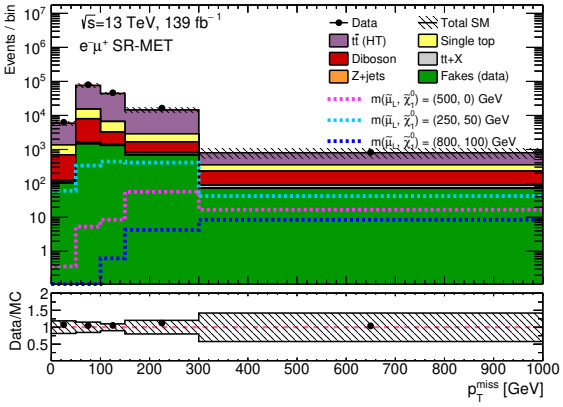

(a) $p_{\mathrm{T}}^{\mathrm{miss}}$, $e^{-}\mu^{+}$

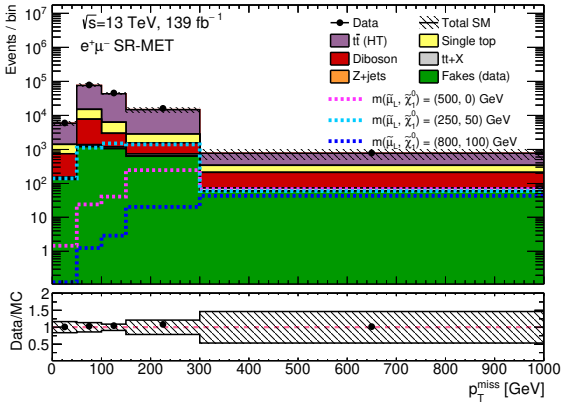

(b) $p_{\mathrm{T}}^{\mathrm{miss}}$, $e^{+}\mu^{-}$

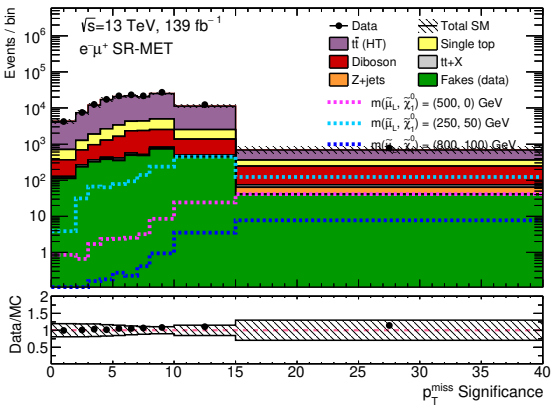

(c) $p_{\mathrm{T}}^{\mathrm{miss}}$ Significance, $e^{-}\mu^{+}$

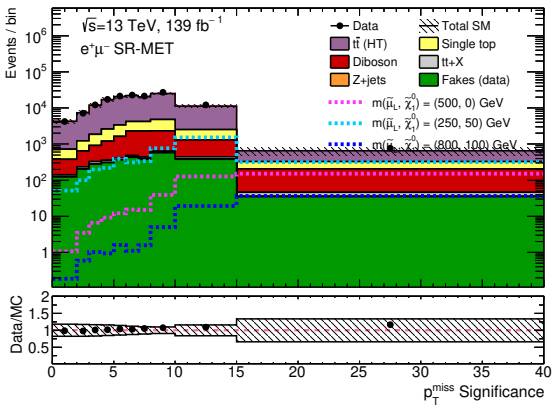

(d) $p_{\mathrm{T}}^{\mathrm{miss}}$ Significance, $e^{+}\mu^{-}$

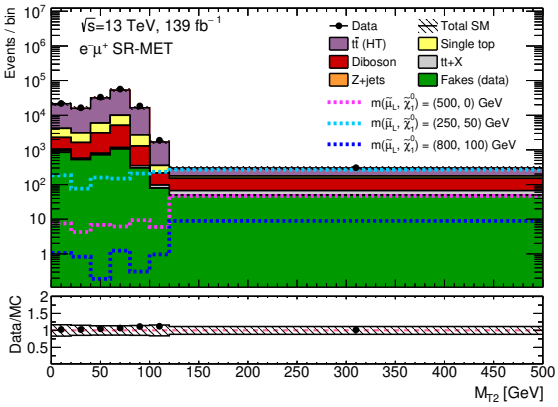

(e) m_{T2}, $e^{-}\mu^{+}$

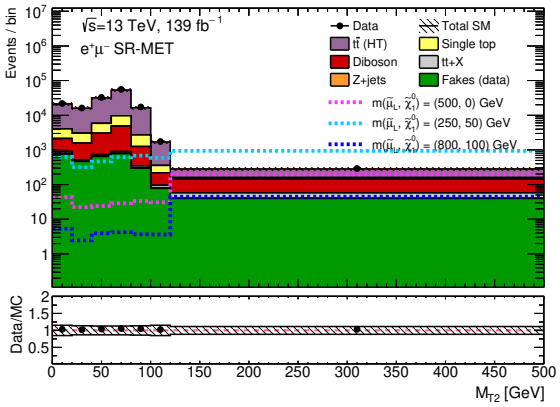

(f) m_{T2}, $e^{+}\mu^{-}$

Figure 6.16: Example distributions in SR-MET for $e\mu$ events of each charge combination. Distributions for three benchmark RPV-SUSY signal points are overlaid. Weights derived in Section 6.7 are applied to $t\bar{t}$ MC events. Statistical, luminosity, $t\bar{t}$ ISR and $t\bar{t}$ weight closure uncertainties are shown. The final bin includes overflow.

Whilst SR-MET is very generic, it does target signal models which produce $p_{\mathrm{T}}^{\mathrm{miss}}$ in the final state. What about BSM models which do not produce an invisible heavy particle in the final state, but instead a jet? In reference to an example scalar leptoquark model, events leading to final states with $e + \mu + 1$ jet can be considered. One could suppose that other BSM models may exist where a similarly hard jet–lepton pair is produced in the decay of a singly-produced heavy BSM particle. This motivates the definition of a second region for the ratio measurement: SR-JET.

To obtain orthogonality to CR-Ratio, a requirement of $\sum_{\ell} m_{\mathrm{T}}(\ell, p_{\mathrm{T}}^{\mathrm{miss}}) > 200$ GeV is made. Since the signal is expected to always produce events with at least one hard jet in the final state, a requirement on jets of NJets > 0 is made, where NJets is defined as the number of Signal jets in the event. As described in Section 6.4, BSM pair-production modes can be switched on along with the more relevant single production mode. These events will have two high p_{T} jets in the final state. It is found that these events can be effectively removed by requiring that events must either have one Signal jet, or, if at least two Signal jets exist, the second highest p_{T} jet must have $p_{\mathrm{T}} < 300\,\mathrm{GeV}$.

For SR-JET, useful variables can be constructed on the premise that the leptons and jet in the final state are generally likely to be produced with a high p_{T}, relative to SM background processes. For the leptoquark case, the invariant mass of the muon-jet pair will show a resonance peak at the mass of the leptoquark, and the transverse mass will approximately bound it. This motivates the use of mass-variables to pick out regions of phase space sensitive to new physics with this topology. For the same reasons as described regarding SR-MET, one must be careful to construct non-biased variables. As with SR-MET, all of the chosen variables should favour a BSM signal topology at higher values.

Therefore, the first two variables used to measure the ratio in SR-JET are the sum and maximum of the lepton-jet invariant masses: $\sum_{\ell} m(\ell, \mathrm{j}_1)$and $\max_{\ell}(m(\ell, j_1))$, respectively. These will both show a smeared resonance peak at the leptoquark mass. By considering the fact that a heavy decaying new particle is likely to put a higher portion of its decay products' momenta in the transverse direction than SM processes, transverse variables are also useful. The third variable used is the sum of the transverse masses of the two leptons and the highest p_{T} jet: $\sum_{\ell} m_{\mathrm{T}}(\ell, \mathrm{j}_1)$. The forth is $\sum_{i=e,\mu,\mathrm{j}_1} p_{\mathrm{T}}^{i}$. Finally, and somewhat surprisingly, m_{T2} is used. Whilst there is no real source of $p_{\mathrm{T}}^{\mathrm{miss}}$ in the example leptoquark model, the combination of fake $p_{\mathrm{T}}^{\mathrm{miss}}$ from object mis-measurement and high lepton transverse momenta allows the leptoquark m_{T2} distribution to extend (as a fairly flat distribution) beyond that of the SM.

In summary, the five variables used for the SR-JET ratio measurement are:

- $\sum_\ell m(\ell, \mathrm{j}_1)$,
- $\max_\ell(m(\ell, j_1))$,
- $\sum_\ell m_\mathrm{T}(\ell, \mathrm{j}_1)$,
- $\sum_{i=e,\mu,\mathrm{j}_1} p^i_\mathrm{T}$,
- and $m_{\mathrm{T}2}$.

Figure 6.17 shows the distributions of $\sum_\ell m(\ell, \mathrm{j}_1)$, $\max_\ell(m(\ell, j_1))$ and $\sum_\ell m_\mathrm{T}(\ell, \mathrm{j}_1)$, for events of each charge combination. The three overlaid leptoquark signal models shown contribute predominantly to $e^+\mu^-$ at high values of the variables, as expected. Furthermore, Figure 6.18 shows the distributions of $\sum_{i=e,\mu,\mathrm{j}_1} p^i_\mathrm{T}$ and $m_{\mathrm{T}2}$, for events of each charge combination, where the same behaviour is seen.

In addition to producing model-independent measurements of the ratio, one can produce limits on the two example models considered. For this goal, additional signal regions are designed to maximise sensitivity to each specific model.

To quantify the possible sensitivity of the ratio to a given model, the test statistic q can be used. q is defined as:

$$q = \frac{n_{+-} - n_{-+}}{n_{+-} + n_{-+}}, \tag{6.11}$$

where n_{+-} is the yield of $e^+\mu^-$ events and n_{-+} is the yield of $e^-\mu^+$ events. This measure should include the possible effects of uncertainty, which may alter either or both of the yields in the $e^-\mu^+$ and $e^+\mu^-$ regions. To account for this, the ns in equation 6.11 are taken to be median values of many (1000) samples from a Poisson distribution with a mean given by the observed (MC signal and SM background) yields. Justification for this test statistic approach can be found in Reference [3]. With large enough statistics for the values of n, this q corresponds to the p_0 value such that $q = 1.64$ corresponds to sensitivity at 95% confidence level.

A signal region called SR-RPV is defined, to place model-dependent limits on the RPV-SUSY model. To begin optimising SR-RPV, the same cuts as SR-MET are applied. Unsurprisingly based on the distributions in SR-MET, most of the Standard Model

background can be removed by placing a lower bound on m_{T2}. A requirement of $m_{\mathrm{T2}} > 120\,\mathrm{GeV}$ is found to be optimal.

To achieve sensitivity to different regions of smuon mass, different bins of the $\max_\ell(m_{\mathrm{T}}(\ell, p_{\mathrm{T}}^{\mathrm{miss}}))$ variable are considered. This is found to be more effective than placing requirements on any of the other variables considered in SR-MET. Sensitivity to the largest amount of mass space, without having too few events in each bin, is obtained by using two orthogonal selections: $\max_\ell(m_{\mathrm{T}}(\ell, p_{\mathrm{T}}^{\mathrm{miss}})) = [200, 540)\,\mathrm{GeV}$ and $\max_\ell(m_{\mathrm{T}}(\ell, p_{\mathrm{T}}^{\mathrm{miss}})) > 540\,\mathrm{GeV}$. Plots of the test statistic q are shown for these 2 selections in Figure 6.19. In the full exclusion fit, these regions are combined into one simultaneous profile likelihood fit.

The $\max_\ell(m_{\mathrm{T}}(\ell, p_{\mathrm{T}}^{\mathrm{miss}}))$ distributions in the two bins of SR-RPV with benchmark RPV-SUSY signals overlaid, are shown for both charge-flavour combinations in Figure 6.20.

The fourth and final signal region designed is SR-LQ, introduced in order to produce model-dependent limits on the leptoquark model. Here SR-JET is taken as a starting point.

The leptoquark signal is expected to have no 'real' $p_{\mathrm{T}}^{\mathrm{miss}}$, since it has no neutrinos or stable new physics particles in the final state. However it is possible that through mismeasurement of jets, pile-up effects, and so on, non-zero values of $p_{\mathrm{T}}^{\mathrm{miss}}$ (fake $p_{\mathrm{T}}^{\mathrm{miss}}$) can be obtained. Fake $p_{\mathrm{T}}^{\mathrm{miss}}$ can also arise in all SM backgrounds. In order to significantly reduce the SM background, rejecting events with a lot of 'real' $p_{\mathrm{T}}^{\mathrm{miss}}$ is desirable. To achieve this, placing a requirement of $p_{\mathrm{T}}^{\mathrm{miss}}$ Significance < 2 is shown to be optimal. It is worth noting that placing this requirement on $p_{\mathrm{T}}^{\mathrm{miss}}$ Significance implicitly results in all SM events with $p_{\mathrm{T}}^{\mathrm{miss}} > 200\,\mathrm{GeV}$ being removed, whereas some signal events at high $p_{\mathrm{T}}^{\mathrm{miss}}$ remain. As a result, this requirement is more effective than placing a requirement on $p_{\mathrm{T}}^{\mathrm{miss}}$ itself would have been.

After studying the variables found to be useful in SR-JET, optimal sensitivity across the leptoquark signal grid is obtained with a requirement that $\sum_{i=e,\mu,\mathrm{j}_1} p_{\mathrm{T}}^i$ is greater than 1 TeV. The sensitivity obtained using q in SR-LQ is shown in Figure 6.21. The $\sum_{i=e,\mu,\mathrm{j}_1} p_{\mathrm{T}}^i$ distribution in SR-LQ with benchmark leptoquark signals overlaid, is shown for both charge-flavour combinations in Figure 6.22.

The nominal expected yields of each SM background and that of benchmark RPV-SUSY signals in SR-MET and the total of both SR-RPV bins are shown in Table **??**.

Analogous values with benchmark leptoquark signals in SR-JET and SR-LQ are shown in Table 6.3. Both of these show that the dominant background is $t\bar{t}$, except in SR-RPV, where VV processes dominate. For the ratio measurement regions the fake lepton background is only the fourth largest background, indicating that its biased nature won't have a huge impact on the ratio.

	SR-MET		SR-RPV	
	$e^+\mu^-$	$e^-\mu^+$	$e^+\mu^-$	$e^-\mu^+$
$M(\tilde{\chi}_1^0, \tilde{\mu}) = (0, 500)$ GeV	380.8 ± 7.1	87.4 ± 3.3	195.4 ± 5.1	46.8 ± 2.5
$M(\tilde{\chi}_1^0, \tilde{\mu}) = (50, 250)$ GeV	4224.2 ± 84.9	1282.9 ± 46.7	714.3 ± 34.6	239.9 ± 20.3
$M(\tilde{\chi}_1^0, \tilde{\mu}) = (100, 800)$ GeV	68.1 ± 1.3	13.5 ± 0.6	44.7 ± 1.0	8.8 ± 0.5
Data	146626.7	148920.2	186.0	215.6
Total SM	140602.3 ± 127.8	140777.9 ± 131.4	188.9 ± 6.6	200.8 ± 6.8
Fakes	3064.2 ± 84.5	3587.9 ± 86.0	30.1 ± 5.6	39.1 ± 5.6
Z + jets	51.5 ± 18.7	100.6 ± 31.9	0.2 ± 0.1	-0.2 ± 0.7
ttX	404.4 ± 2.5	396.5 ± 2.5	14.9 ± 0.5	14.0 ± 0.5
diboson	9676.3 ± 30.1	9698.2 ± 30.7	74.0 ± 2.7	70.9 ± 2.7
single Top	12595.4 ± 56.3	12570.3 ± 56.2	11.7 ± 1.7	16.6 ± 2.0
$t\bar{t}$	114810.5 ± 69.1	114424.4 ± 69.0	58.1 ± 1.5	60.5 ± 1.5

Table 6.2: Expected yields for each of the backgrounds and benchmark RPV-SUSY signal points in SR-MET and the total of both SR-RPV bins. Weights derived in Section 6.7 are applied to $t\bar{t}$ MC events. Note the data yields can be non-integer since the muon bias weighting is applied.

	SR-JET		SR-LQ	
	$e^+\mu^-$	$e^-\mu^+$	$e^+\mu^-$	$e^-\mu^+$
$m(S_1) = 1000.0\,\text{GeV}$, $\lambda = 0.5$	222.9 ± 2.2	17.8 ± 0.6	101.3 ± 1.5	6.5 ± 0.4
$m(S_1) = 1250.0\,\text{GeV}$, $\lambda = 1.0$	287.0 ± 2.8	18.5 ± 0.7	156.2 ± 2.0	10.8 ± 0.5
$m(S_1) = 1750.0\,\text{GeV}$, $\lambda = 1.0$	40.9 ± 0.4	2.0 ± 0.1	26.1 ± 0.3	1.3 ± 0.1
Data	140991.9	143193.1	10.0	11.9
Total SM	135639.9 ± 123.3	135800.4 ± 126.9	15.5 ± 1.4	18.0 ± 2.1
Fakes	2906.9 ± 82.7	3341.0 ± 84.1	1.7 ± 1.0	4.3 ± 1.9
Z + jets	37.6 ± 8.5	71.4 ± 27.36	0.0 ± 0.0	0.1 ± 0.0
ttX	396.5 ± 2.5	389.4 ± 2.47	0.2 ± 0.1	0.2 ± 0.1
diboson	6795.7 ± 23.5	6894.3 ± 23.8	4.5 ± 0.4	4.6 ± 0.4
single Top	11958.9 ± 54.8	11941.9 ± 54.7	2.9 ± 0.8	2.4 ± 0.8
$t\bar{t}$	113544.4 ± 68.8	113162.5 ± 68.6	6.2 ± 0.24	6.4 ± 0.3

Table 6.3: Expected yields for each of the backgrounds and benchmark leptoquark signal points in SR-JET and SR-LQ. Weights derived in Section 6.7 are applied to $t\bar{t}$ MC events. Note the data yields can be non-integer since the muon bias weighting is applied.

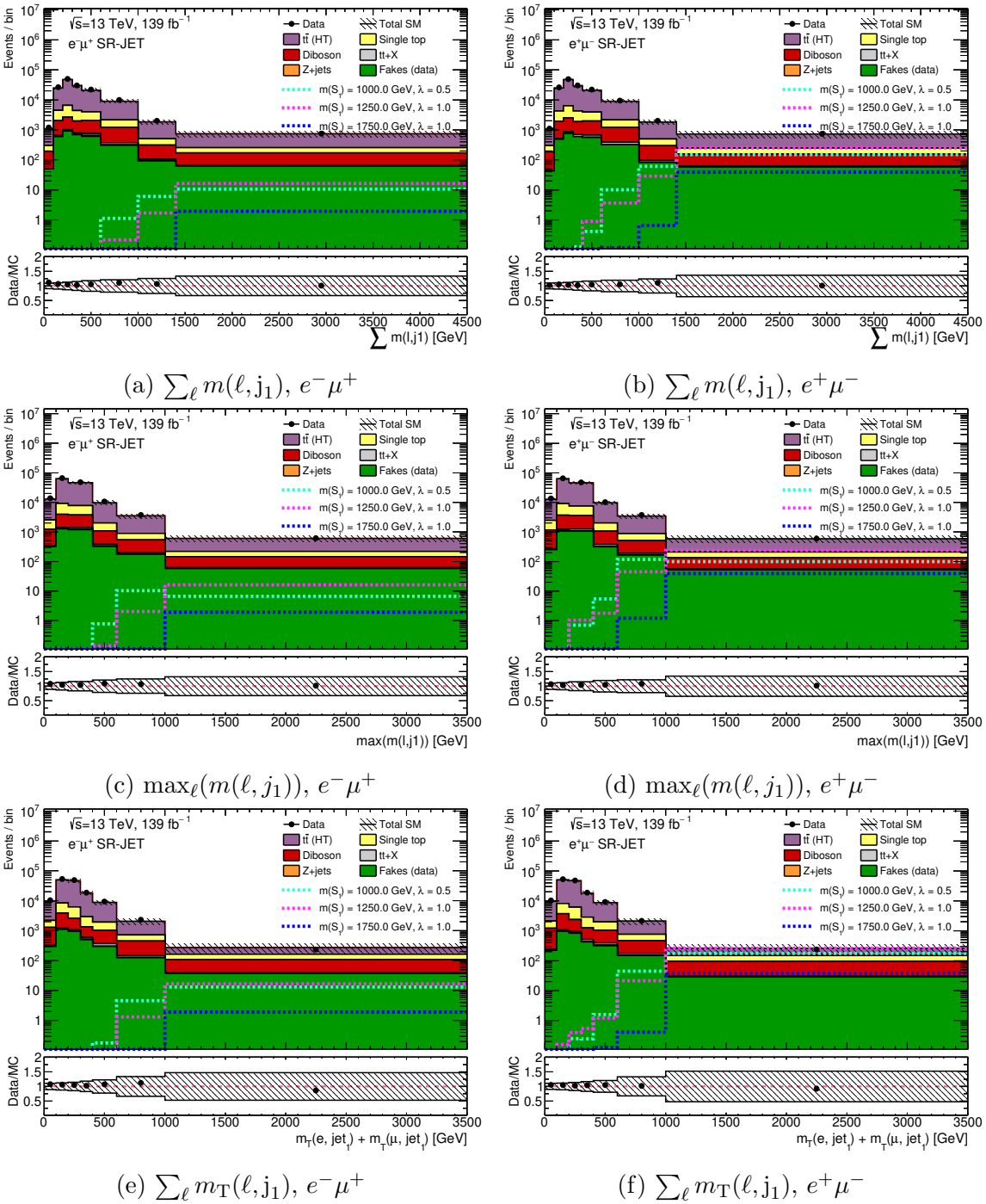

(a) $\sum_\ell m(\ell, \mathrm{j}_1)$, $e^-\mu^+$

(b) $\sum_\ell m(\ell, \mathrm{j}_1)$, $e^+\mu^-$

(c) $\max_\ell(m(\ell, j_1))$, $e^-\mu^+$

(d) $\max_\ell(m(\ell, j_1))$, $e^+\mu^-$

(e) $\sum_\ell m_\mathrm{T}(\ell, \mathrm{j}_1)$, $e^-\mu^+$

(f) $\sum_\ell m_\mathrm{T}(\ell, \mathrm{j}_1)$, $e^+\mu^-$

Figure 6.17: Example distributions in SR-JET for $e\mu$ events of each charge combination. Distributions for three benchmark leptoquark signal points are overlaid. Weights derived in Section 6.7 are applied to $t\bar{t}$ MC events. Statistical, luminosity, $t\bar{t}$ ISR and $t\bar{t}$ weight closure uncertainties are shown. The final bin includes overflow.

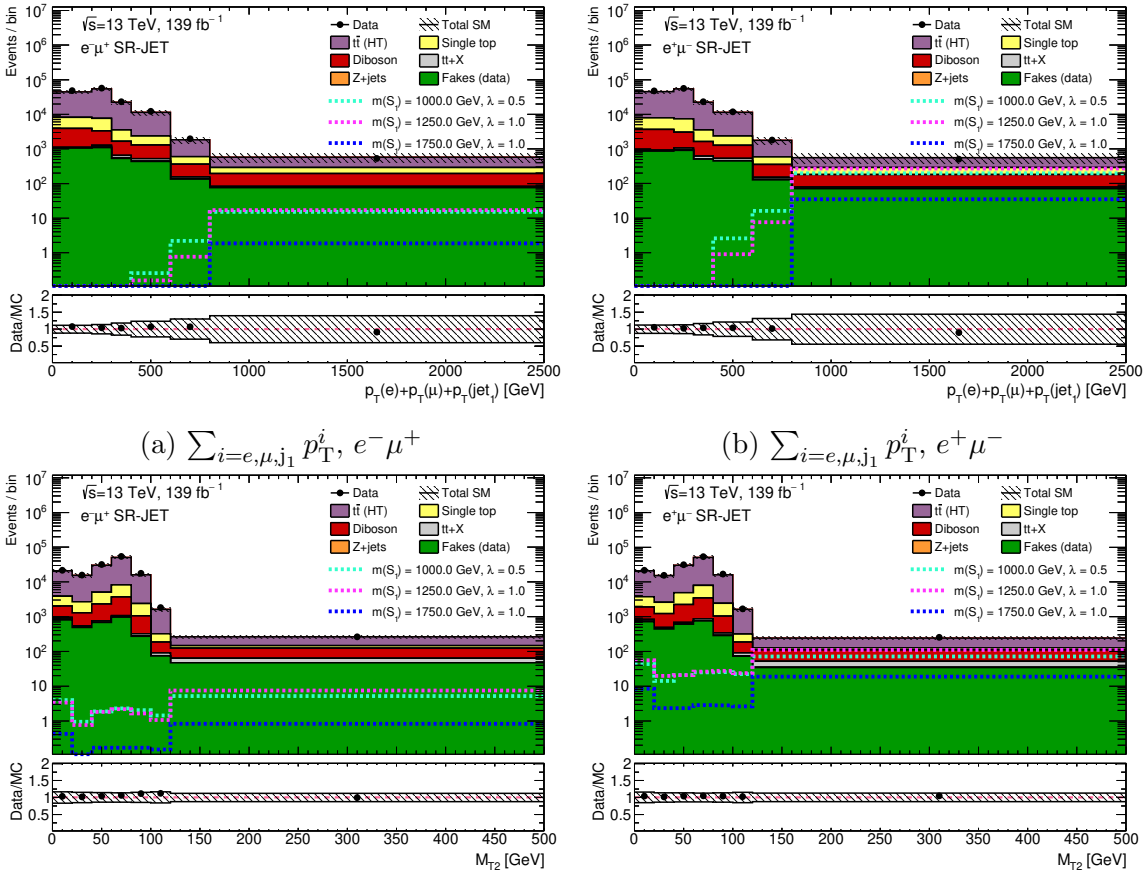

(a) $\sum_{i=e,\mu,\mathrm{j}_1} p_{\mathrm{T}}^i$, $e^-\mu^+$

(b) $\sum_{i=e,\mu,\mathrm{j}_1} p_{\mathrm{T}}^i$, $e^+\mu^-$

(c) m_{T2}, $e^-\mu^+$

(d) m_{T2}, $e^+\mu^-$

Figure 6.18: Example distributions in SR-JET for $e\mu$ events of each charge combination. Distributions for three benchmark leptoquark signal points are overlaid. Weights derived in Section 6.7 are applied to $t\bar{t}$ MC events. Statistical, luminosity, $t\bar{t}$ ISR and $t\bar{t}$ weight closure uncertainties are shown. The final bin includes overflow.

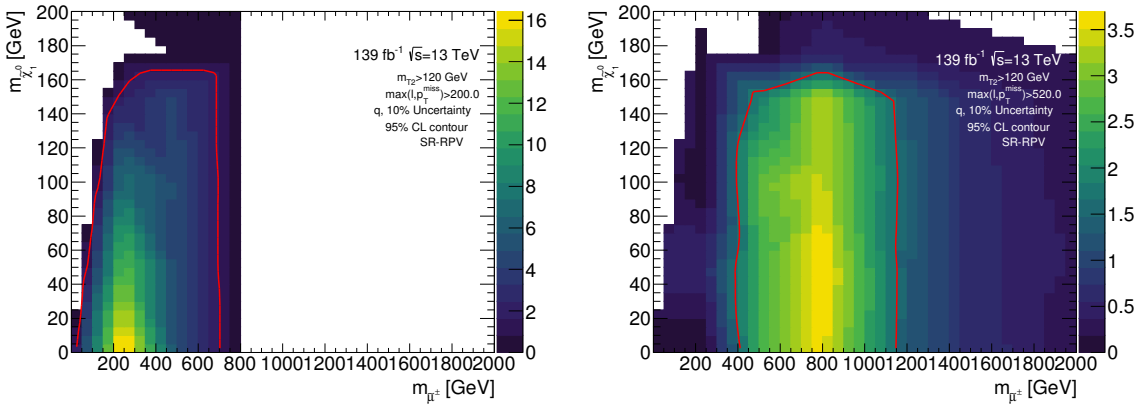

(a) $\max_\ell(m_{\mathrm{T}}(\ell, p_{\mathrm{T}}^{\mathrm{miss}}))[200, 540]$ GeV (b) $\max_\ell(m_{\mathrm{T}}(\ell, p_{\mathrm{T}}^{\mathrm{miss}}))> 540$ GeV

Figure 6.19: Expected sensitivity q for RPV-SUSY models obtained by using SR-RPV restricted to the $\max_\ell(m_{\mathrm{T}}(\ell, p_{\mathrm{T}}^{\mathrm{miss}}))$ ranges given in the captions. Weights derived in Section 6.7 are applied to $t\bar{t}$ MC events.

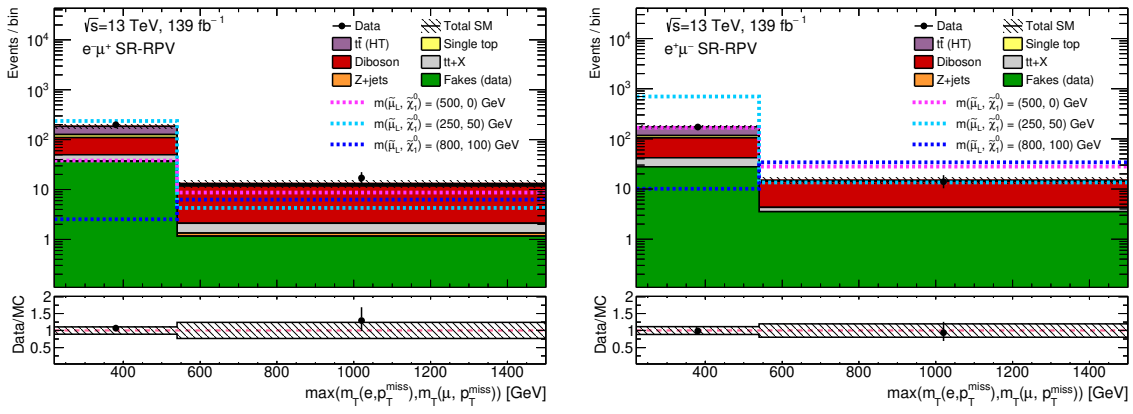

(a) $e^-\mu^+$ (b) $e^+\mu^-$

Figure 6.20: $\max_\ell(m_{\mathrm{T}}(\ell, p_{\mathrm{T}}^{\mathrm{miss}}))$ distributions in SR-RPV for $e\mu$ events of each charge combination. Distributions for three benchmark RPV-SUSY signal points are overlaid. Weights derived in Section 6.7 are applied to $t\bar{t}$ MC events. Statistical, luminosity, $t\bar{t}$ ISR and $t\bar{t}$ weight closure uncertainties are shown. The final bin includes overflow.

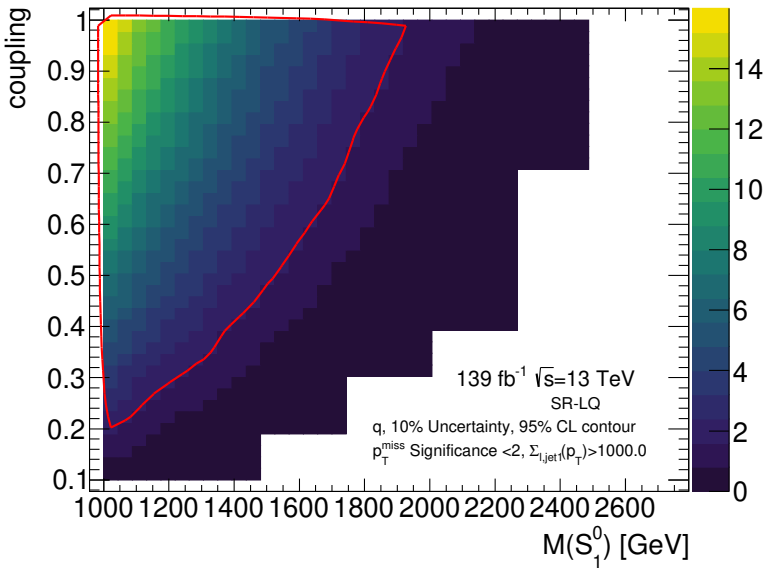

Figure 6.21: Expected sensitivity q for leptoquark models obtained by using SR-LQ. Weights derived in Section 6.7 are applied to $t\bar{t}$ MC events.

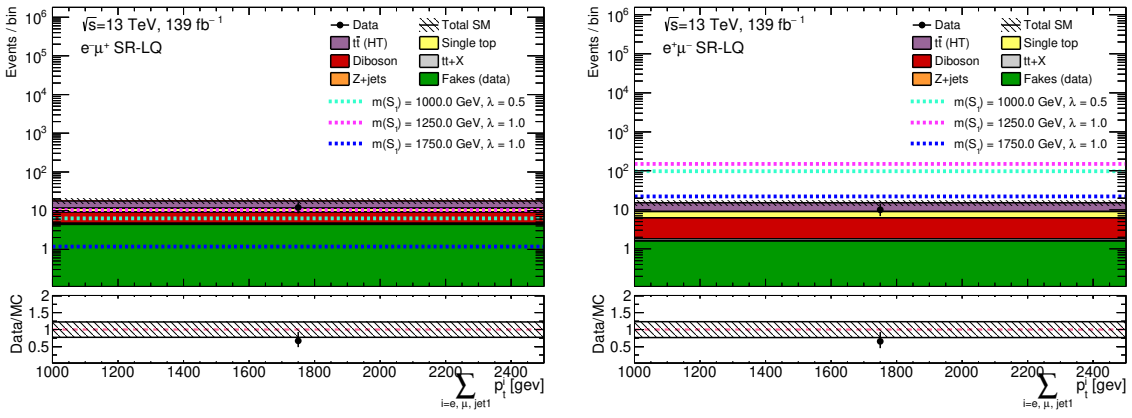

(a) $e^-\mu^+$ (b) $e^+\mu^-$

Figure 6.22: Distributions of $\sum_{i=e,\mu,\mathrm{j}_1} p_{\mathrm{T}}^i$ in SR-LQ for $e\mu$ events of each charge combination. Distributions for three benchmark leptoquark signal points are overlaid. Weights derived in Section 6.7 are applied to $t\bar{t}$ MC events. Statistical, luminosity, $t\bar{t}$ ISR and $t\bar{t}$ weight closure uncertainties are shown. The final bin includes overflow.

6.7 Background estimation

Whilst Section 6.2 provides theoretical justification for the expectation that the ratio in the Standard Model should not exceed one, it is instructive to see if this is in fact the case. A control region (CR-Ratio) which is dominated by SM processes is defined to allow such a check to be made. In this region, the ratio can be measured in both data and SM MC, in bins of some kinematic variables.

For the calculation of model-dependent exclusion limits of the two BSM models considered, a robust estimation of the SM background is required. This is based on MC simulation of the SM background processes. However mis-modelling of the $t\bar{t}$ background is observed and corrected for by weighting the $t\bar{t}$ MC events to obtain a better data–MC agreement in CR-Ratio and VR-MET. VR-MET is defined in the same way at SR-MET, but requires that the leptons are Nearly-Signal, rather than Signal. As such, SR-MET is a subset of VR-MET.

For all of the measurements in the analysis, it is also important to have an estimation of the potentially biasing fake lepton background. This estimate was produced by another analyser, using the likelihood matrix method. This method is a variant on the matrix method used in the other analyses in this thesis, and is based on comparing event yields in regions with 'loose' and 'tight' leptons. In this analysis, these loose and tight leptons are taken to be Nearly-Signal and Signal, respectively. Details of the likelihood matrix method can be found in References [137] and [138]. This method is chosen instead of the standard matrix method as it is more stable in the phase space used in this analysis, and incapable of providing a negative estimate. The estimate produced favours $e^-\mu^+$ over $e^+\mu^-$ events, as predicted. It also gives a very small contribution to the overall background in SR-MET and SR-JET, of around 2%. Uncertainties on the fake lepton background are measured and included in the statistical analysis. These are calculated by considering the statistical uncertainty on the data on the Nearly-Signal and Signal lepton yields, in addition to propagating the statistical uncertainty on the data through the calculation of the elements of the eponymous matrix.

In the remainder of this Section, the CR-Ratio study and the $t\bar{t}$ weighting procedure will be described in more detail.

The control region designed to study the SM ratio is defined to be orthogonal to the signal regions, kinematically similar to them, and low in expected contamination of any BSM signal. The benchmark models considered are used as a guide of the level of

contamination of any kind of BSM model the analysis is sensitive to. CR-Ratio is made orthogonal to the signal regions by requiring that $\sum_\ell m_{\mathrm{T}}(\ell, p_{\mathrm{T}}^{\mathrm{miss}})$ is below 200 GeV. If a requirement that the leading lepton p_{T} is less than 400 GeV is made, then the region is also low in expected RPV-SUSY and leptoquark signal events. One Signal electron and one Signal muon are required, and no further requirements are made.

The expected yields of each background and that of benchmark RPV-SUSY and leptoquark signals in CR-Ratio are shown in Table 6.4. In comparison to the composition of the signal regions, $t\bar{t}$ remains the dominant background, whilst the fake lepton background contribution remains small.

	CR-Ratio	
	$e^+\mu^-$	$e^-\mu^+$
$M(\tilde{\chi}_1^0, \tilde{\mu}) = (0, 500)$ GeV	10.8 ± 1.2	1.0 ± 0.4
$M(\tilde{\chi}_1^0, \tilde{\mu}) = (50, 250)$ GeV	690.1 ± 34.4	126.7 ± 14.6
$M(\tilde{\chi}_1^0, \tilde{\mu}) = (100, 800)$ GeV	0.7 ± 0.1	0.1 ± 0.1
$m(S_1) = 1000.0$ GeV, $\lambda = 0.5$	40.8 ± 0.9	3.7 ± 0.3
$m(S_1) = 1250.0$ GeV, $\lambda = 1.0$	21.4 ± 0.8	2.5 ± 0.3
$m(S_1) = 1750.0$ GeV, $\lambda = 1.0$	1.0 ± 0.1	0.1 ± 0.0
Data	338246.0	337562.5
Total SM	328544.2 ± 663.9	328852.5 ± 670.5
Fakes	11929.8 ± 108.0	13211.9 ± 111.3
Z + jets	35900.9 ± 640.1	37074.5 ± 646.5
ttX	566.7 ± 3.1	562.8 ± 3.1
diboson	33170.0 ± 63.5	33622.9 ± 64.2
single Top	21829.5 ± 73.9	21756.1 ± 73.8
$t\bar{t}$	225147.3 ± 99.4	222624.1 ± 98.3

Table 6.4: Expected yields for each of the backgrounds and benchmark RPV-SUSY and leptoquark signal points in CR-Ratio. Weights derived in Section 6.7 are applied to $t\bar{t}$ MC events.

Distributions of the leading lepton p_{T} and $p_{\mathrm{T}}^{\mathrm{miss}}$ in CR-Ratio are shown in Figure 6.23. Data and MC are largely consistent, which is expected as the $t\bar{t}$ weighting procedure described later in this Section has been applied.

Using the profile likelihood fit described in Section 6.9, the ratio for MC and data

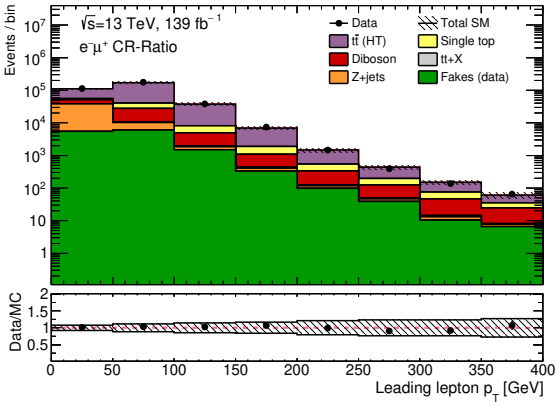

(a) Leading lepton p_{T}, $e^{-}\mu^{+}$

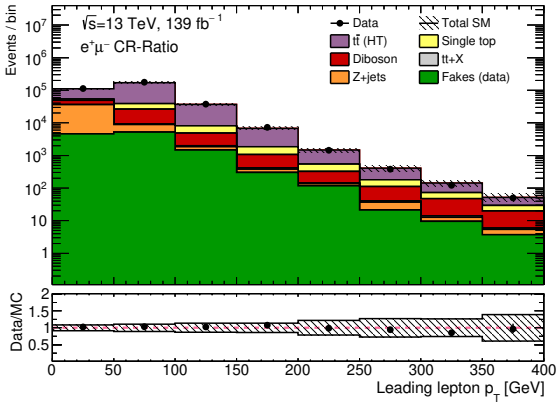

(b) Leading lepton p_{T}, $e^{+}\mu^{-}$

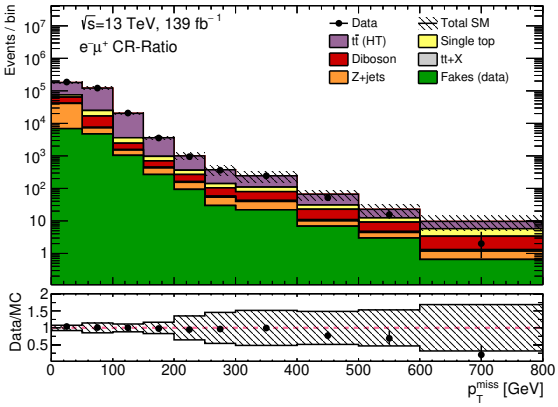

(c) $p_{\mathrm{T}}^{\mathrm{miss}}$, $e^{-}\mu^{+}$

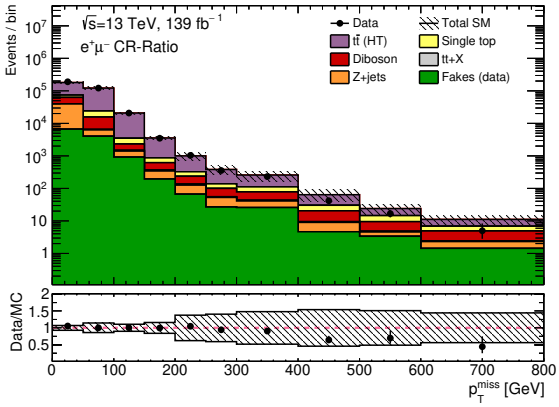

(d) $p_{\mathrm{T}}^{\mathrm{miss}}$, $e^{+}\mu^{-}$

Figure 6.23: Distributions of leading lepton p_{T} and $p_{\mathrm{T}}^{\mathrm{miss}}$ in CR-Ratio, for each charge combination. Weights derived in Section 6.7 are applied to $t\bar{t}$ MC events. Statistical, luminosity, $t\bar{t}$ ISR and $t\bar{t}$ weight closure uncertainties are shown. The final bin includes overflow.

is calculated. Some examples of the ratio are shown for MC and data in Figure 6.24. For data, these ratios include the muon bias correction and its uncertainties, along with the relevant detector uncertainties described in Section 6.8. For MC, they also included detector, theory and $t\bar{t}$ weighting uncertainties. No significant deviations from one are observed for either MC and Data. The ratio measurement is also performed in VR-METfor validation, as shown in Appendix B.

The discussion now turns to the $t\bar{t}$ mis-modelling weight procedure. As is illustrated in Figure 6.25, p_{T} dependent disagreement between data and MC is observed in CR-Ratio, which is believed to stem from mis-modelling of the main $t\bar{t}$ background MC. Similar behaviour is found in VR-MET. To correct for the mis-modelling, a set of weights

are derived that are applied to the $t\bar{t}$ MC, binned in leading lepton p_{T} and $p_{\mathrm{T}}^{\mathrm{miss}}$. Separate weights are calculated for each charge-flavour combination. These are derived in CR-Ratio, and validated to produce a closure uncertainty in VR-MET. These weights are applied to all regions. Interpolation between the weights for the central leading lepton p_{T} and $p_{\mathrm{T}}^{\mathrm{miss}}$ values of each bin is used to calculate the weight to apply to each event to avoid discontinuities in the resulting distributions.

Weights can be calculated in a given bin i of leading lepton p_{T} and given bin j of $p_{\mathrm{T}}^{\mathrm{miss}}$ as:

$$w_{ij} = \frac{N_{ij}^{\mathrm{data}} - N_{ij}^{\text{other bgs}}}{N_{ij}^{t\bar{t}\ \mathrm{raw}}}, \tag{6.12}$$

where 'other bgs' includes single-top production, $Z+\mathrm{jets}$, VV, ttX, and the fake lepton background.

The weights produced are shown in Figure 6.26. Bins of leading lepton p_{T} and $p_{\mathrm{T}}^{\mathrm{miss}}$ are chosen to avoid regions of too low statistics, but to be fine enough to capture the shape of the distribution and mis-modelling.

The effectiveness of the weights is quantified in VR-MET. An uncertainty on the weighting in each bin can be derived by considering the closure. This closure is defined to be how well the weighted $t\bar{t}$ background plus the other MC backgrounds and fake lepton background agree with the data in this validation region. The uncertainty in a bin can be calculated as:

$$u_{ij}(w_{ij}) = \frac{N_{ij}^{\mathrm{data}} - (N_{ij}^{\text{other bgs}} + w_{ij}N_{ij}^{t\bar{t}\ \mathrm{raw}})}{N_{ij}^{\text{other bgs}} + w_{ij}N_{ij}^{t\bar{t}\ \mathrm{raw}}} \tag{6.13}$$

In Figures 6.23 and 6.27, distributions of leading lepton p_{T} and $p_{\mathrm{T}}^{\mathrm{miss}}$ are shown in CR-Ratio and VR-MET with the weighting applied. The uncertainties included in these distributions are: statistical, the $t\bar{t}$ weight closure uncertainty, and the dominant systematic uncertainty — that on $t\bar{t}$ initial state radiation modelling. The weights and uncertainties cover the MC–data disagreement for the majority of bins. Similar levels of agreement are also found in other kinematic variable distributions.

It is also useful to see what effect this $t\bar{t}$ weighting has on the ratio measurement. Figure 6.28 shows the ratio calculated in CR-Ratio in MC, with or without the $t\bar{t}$ weighting applied. The results remain consistent with each other within statistical and $t\bar{t}$ weight

closure uncertainties.

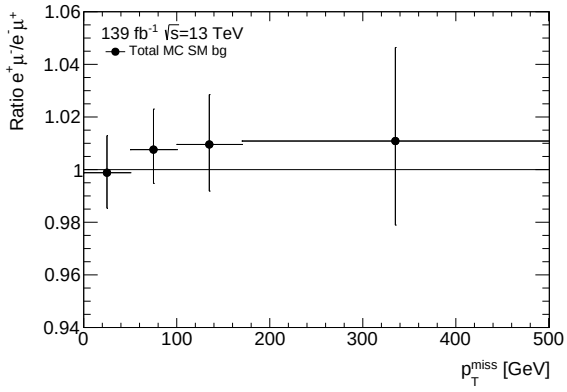

(a) Total MC $p_{\mathrm{T}}^{\mathrm{miss}}$

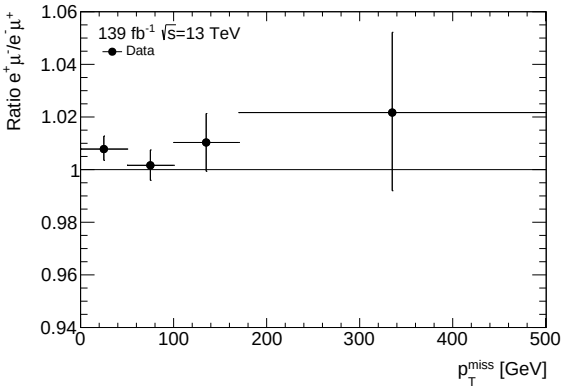

(b) Data $p_{\mathrm{T}}^{\mathrm{miss}}$

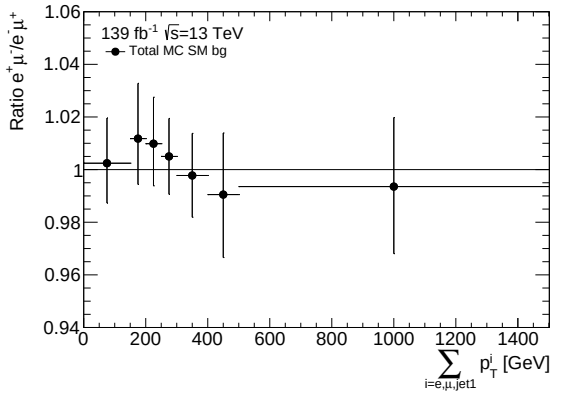

(c) Total MC $\sum_{i=e,\mu,\mathrm{j}_1} p_{\mathrm{T}}^i$

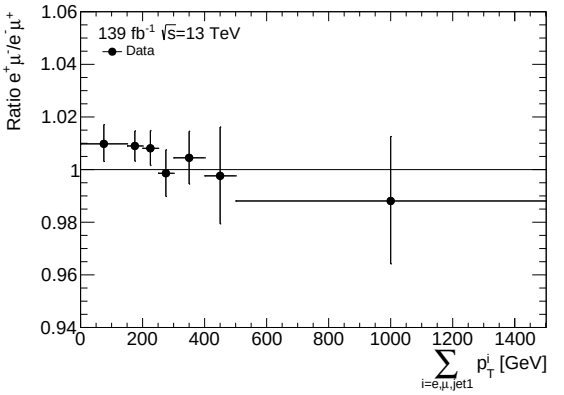

(d) Data $\sum_{i=e,\mu,\mathrm{j}_1} p_{\mathrm{T}}^i$

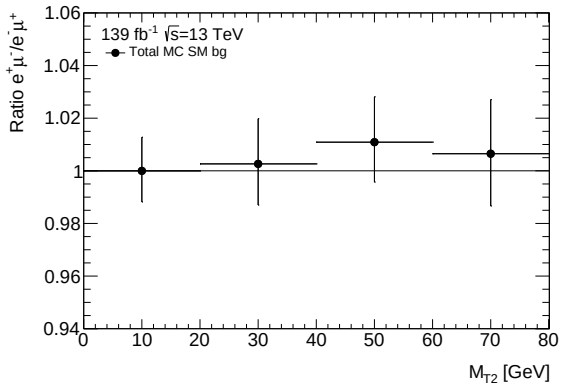

(e) Total MC m_{T2}

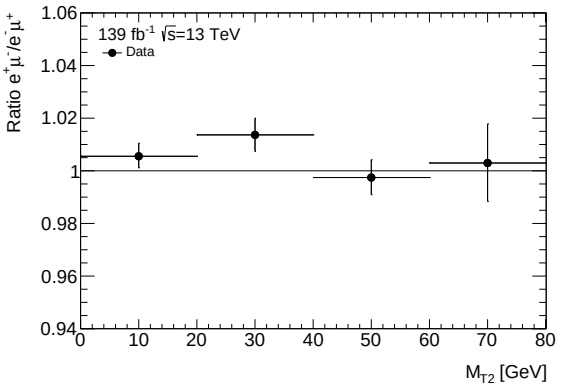

(f) Data m_{T2}

Figure 6.24: The ratio calculated in CR-Ratio for data or MC, in bins of different kinematic variables. Weights derived in Section 6.7 are applied to $t\bar{t}$ MC events. For MC and data, all relevant uncertainties described in Section 6.8 are included.

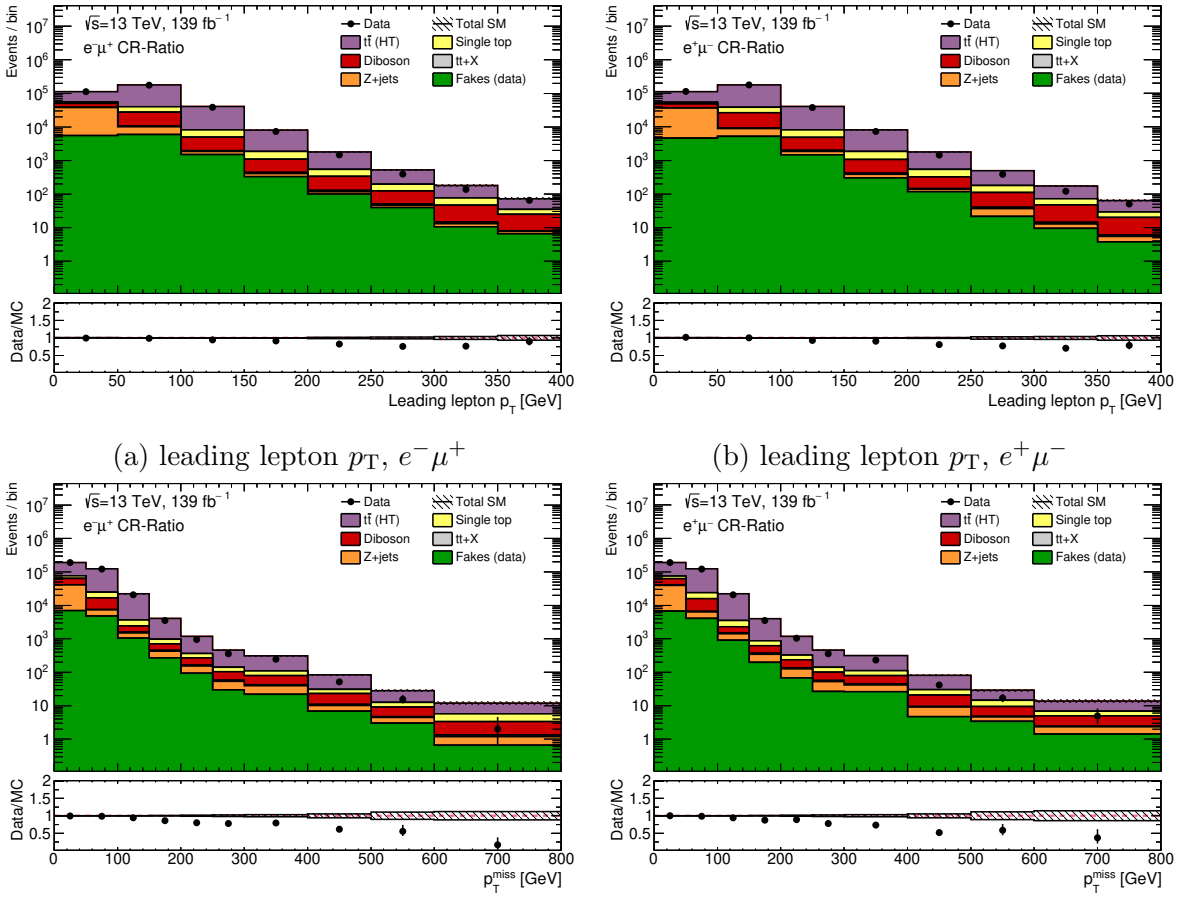

(a) leading lepton p_{T}, $e^{-}\mu^{+}$

(b) leading lepton p_{T}, $e^{+}\mu^{-}$

(c) $p_{\mathrm{T}}^{\mathrm{miss}}$, $e^{-}\mu^{+}$

(d) $p_{\mathrm{T}}^{\mathrm{miss}}$, $e^{+}\mu^{-}$

Figure 6.25: Data and MC distributions of leading lepton p_{T} and $p_{\mathrm{T}}^{\mathrm{miss}}$ in CR-Ratio, for each charge combinations and without any correction to the $t\bar{t}$ mis-modelling applied. Only statistical and luminosity uncertainties are shown. The slope visible in the data–MC is the $t\bar{t}$ modelling which the re-weighting procedure in this section hopes to address. The final bin includes overflow.

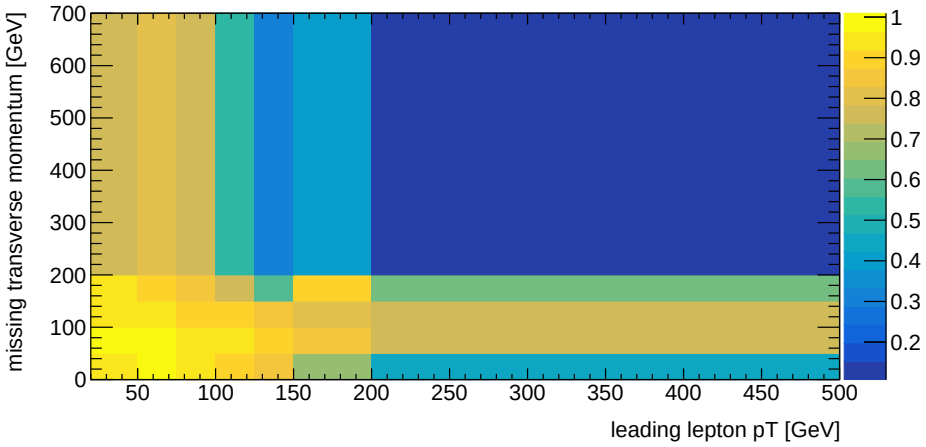

(a) $e^{-}\mu^{+}$ weights

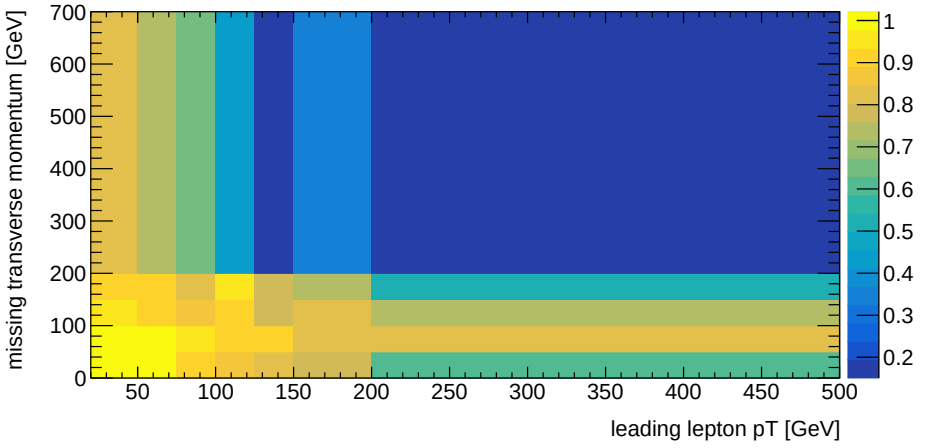

(b) $e^{+}\mu^{-}$ weights

Figure 6.26: Values of the weights derived in CR-Ratio using $e^{+}\mu^{-}$ or $e^{-}\mu^{+}$ to correct for $t\bar{t}$ MC mis-modelling.

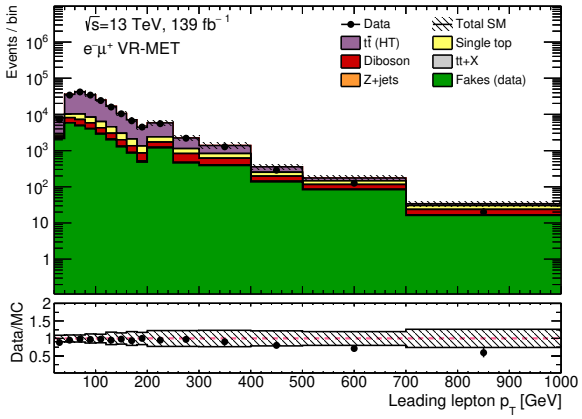

(a) leading lepton p_{T}, $e^{-}\mu^{+}$

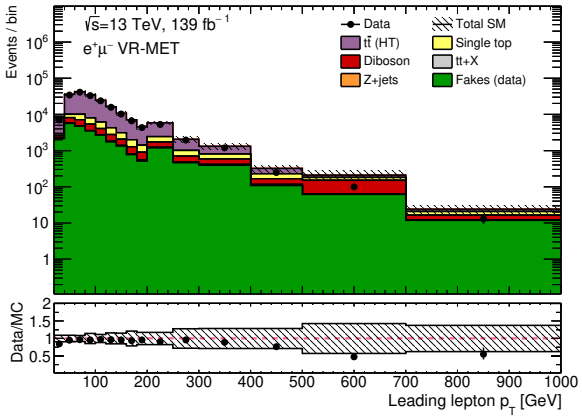

(b) leading lepton p_{T}, $e^{+}\mu^{-}$

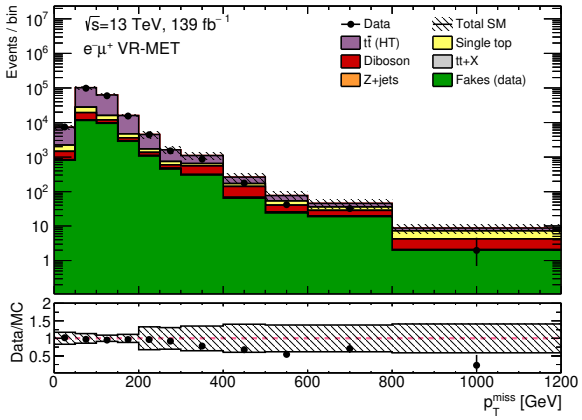

(c) $p_{\mathrm{T}}^{\mathrm{miss}}$, $e^{-}\mu^{+}$

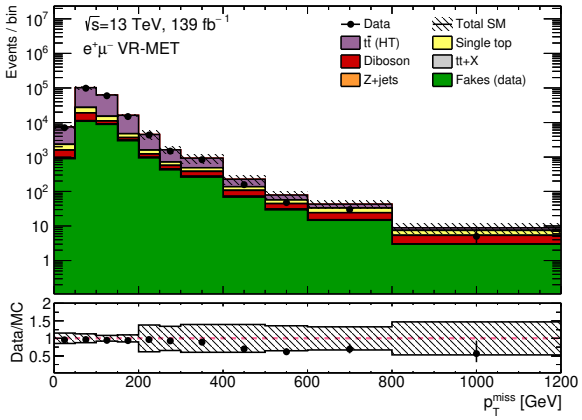

(d) $p_{\mathrm{T}}^{\mathrm{miss}}$, $e^{+}\mu^{-}$

Figure 6.27: Data and MC distributions of leading lepton p_{T} and $p_{\mathrm{T}}^{\mathrm{miss}}$ in VR-MET, with the $t\bar{t}$ weighting applied. Statistical, luminosity, $t\bar{t}$ ISR and $t\bar{t}$ weight closure uncertainties are shown. The final bin includes overflow.

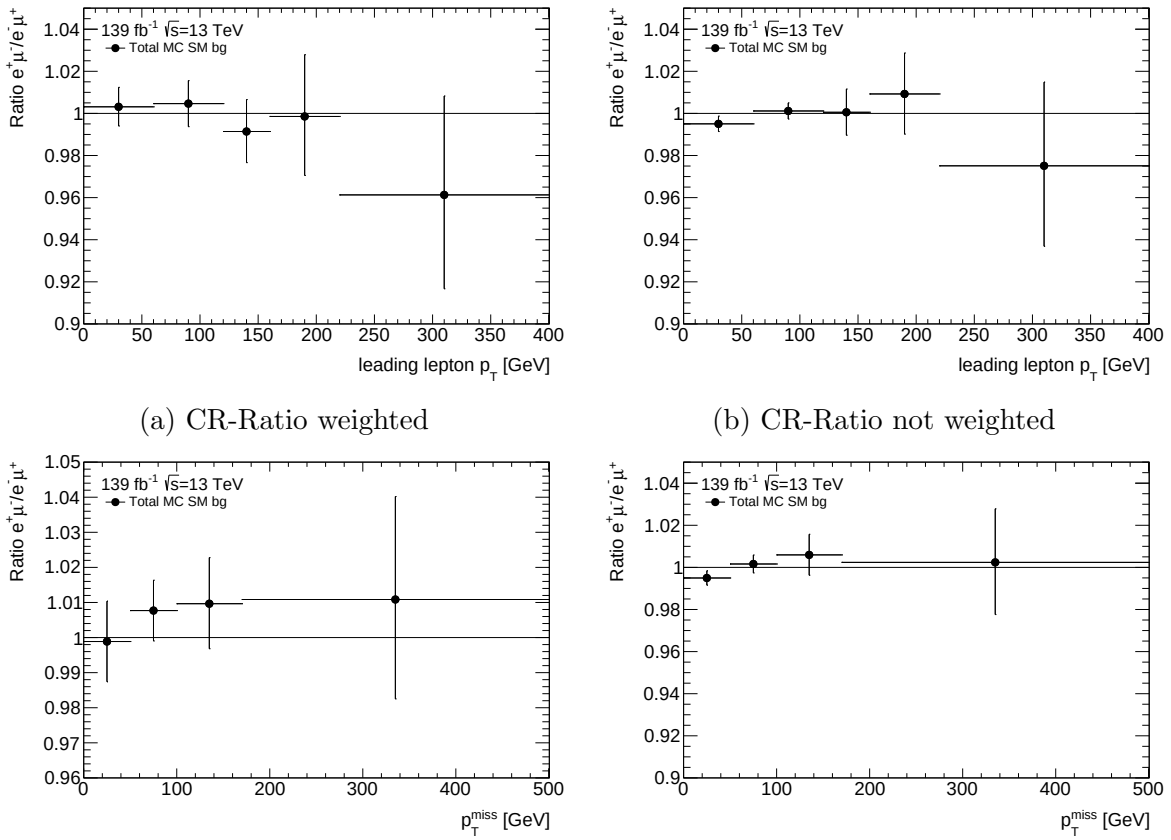

(a) CR-Ratio weighted

(b) CR-Ratio not weighted

(c) CR-Ratio weighted

(d) CR-Ratio not weighted

Figure 6.28: The ratio, with or without $t\bar{t}$ weighting applied, calculated in CR-Ratio in MC, in bins of leading lepton p_{T} and $p_{\mathrm{T}}^{\mathrm{miss}}$. Statistical and $t\bar{t}$ weight closure uncertainties (if applicable) are shown.

6.8 Systematic uncertainties

The model-dependent exclusion fits in this analysis include all relevant sources of systematic uncertainty, in addition to statistical uncertainties. Uncertainties on the muon bias weights and fake lepton background estimate are also included, along with the closure uncertainty on the $t\bar{t}$ mis-modelling weights. The systematic uncertainties are also included when considering the expected ratio measurement in MC — which is used for optimisation but not to calculate any final results. For the case of the ratio measurement performed with data, the only uncertainties included are the muon bias weight uncertainties, and a subset of the systematic uncertainties that directly affect the data — rather than being uncertainties on the MC modelling.

	$e^+\mu^-$	$e^-\mu^+$
Total	8%	8%
Electron scale/resolution	0.02%	0.02%
Electron charge ID	0.0008%	0.009%
Electron efficiency	1%	1%
Jet energy scale	0.05%	0.05%
Jet energy resolution	0.2%	0.2%
$p_{\mathrm{T}}^{\mathrm{miss}}$	0.3%	0.3%
Muon efficiency	2%	2%
Muon MS/scale/ID	0.06%	0.09%
Muon sagitta	1%	1%
Pile-up reweighting	0.6%	0.6%
Muon reconstruction bias	0.04%	0.04%
Muon trigger bias	0.2%	0.1%
Theory	7%	7%
$t\bar{t}$ weight closure	1%	2%

Table 6.5: Summary of the uncertainties on the expected yields in CR-Ratio, relative to the total expected background MC. The individual uncertainties of each type are added in quadrature to give an estimate of the total impact of that type; though it should be noted that as they may be correlated this may not reflect the final uncertainty values after a profile likelihood fit. The total uncertainty shown is calculated by summing the uncertainties in quadrature.

The systematic uncertainties considered relevant for the ratio fit in MC are those related to electrons, muons, jets, $p_{\mathrm{T}}^{\mathrm{miss}}$, and the modelling of the top MC backgrounds. The dominant uncertainties (in terms of their impact on the ratio measurement) are those on the $t\bar{t}$ background modelling, in particular the uncertainty on ISR. As the ISR uncertainty should be charge-flavour symmetric, it is likely that this is the result of MC fluctuation. This, and the $t\bar{t}$ parton shower uncertainty, are calculated following the approach described in Section 4.6. In addition, the uncertainty on the hard scatter process is calculated by comparing Powheg+Pythia8 to aMC@NLO+Pythia8. Finally, the $t\bar{t}$ PDF uncertainty is calculated by comparing Powheg+Pythia8 with internal re-weighting for PDF variations in the PDF4LHC15 PDF error set [139]. PDF uncertainties on the second largest background — single top production — are calculated in the same way.

	$e^+\mu^-$	$e^-\mu^+$
Total	9%	9%
Electron scale/resolution	0.4%	0.4%
Electron charge ID	0.007%	0.005%
Electron efficiency	1%	1%
Jet energy scale	0.09%	0.1%
Jet energy resolution	0.4%	0.4%
$p_{\mathrm{T}}^{\mathrm{miss}}$	0.6%	0.6%
Muon efficiency	2%	2%
Muon MS/scale/ID	0.3%	0.3%
Muon sagitta	0.4%	0.3%
Pile-up reweighting	0.3%	0.3%
Muon reconstruction bias	0.03%	0.03%
Muon trigger bias	0.1%	0.1%
Theory	8%	8%
$t\bar{t}$ weight closure	1%	2%

Table 6.6: Summary of the uncertainties on the expected yields in SR-MET, relative to the total expected background MC. The individual uncertainties of each type are added in quadrature to give an estimate of the total impact of that type; though it should be noted that as they may be correlated this may not reflect the final uncertainty values after a profile likelihood fit. The total uncertainty shown is calculated by summing the uncertainties in quadrature.

	$e^+\mu^-$	$e^-\mu^+$
Total	9%	9%
Electron scale/resolution	0.4%	0.4%
Electron charge ID	0.008%	0.005%
Electron efficiency	1%	1%
Jet energy scale	0.3%	0.3%
Jet energy resolution	0.4%	0.4%
$p_{\mathrm{T}}^{\mathrm{miss}}$	0.6%	0.6%
Muon efficiency	2%	2%
Muon MS/scale/ID	0.3%	0.3%
Muon sagitta	0.5%	0.2%
Pile-up reweighting	0.3%	0.3%
Muon reconstruction bias	0.03%	0.03%
Muon trigger bias	0.1%	0.1%
Theory	8%	8%
$t\bar{t}$ weight closure	1%	2%

Table 6.7: Summary of the uncertainties on the expected yields in SR-JET, relative to the total expected background MC. The individual uncertainties of each type are added in quadrature to give an estimate of the total impact of that type; though it should be noted that as they may be correlated this may not reflect the final uncertainty values after a profile likelihood fit. The total uncertainty shown is calculated by summing the uncertainties in quadrature.

The next largest uncertainty is generally the closure uncertainty on the $t\bar{t}$ mis-modelling weights. The jet and $p_{\mathrm{T}}^{\mathrm{miss}}$ uncertainties included are the same as those described in Section 4.6. Uncertainties on the electron energy scale and resolution, selection efficiencies, and ECID tool are included but generally small. Similarly, uncertainties on the muon energy scale and resolution, ID and MS tracks, sagitta bias, and selection efficiencies are included, and found to be small. Finally, uncertainties on pile-up re-weighting are considered, as described in Section 4.6. Uncertainties on the luminosity measurement are not included in the fit since they will be identical for both channels in the ratio and cancel out.

Sizes of the systematic uncertainties in each signal and control region, using MC, are displayed in Tables 6.5–6.9. For SR-MET and SR-JET, these do not show a huge

amount of disparity between $e^+\mu^-$ and $e^-\mu^+$ selections in uncertainties which aren't very small, which means a high amount of cancellation can be expected leading to a small impact on the ratio measurement. The electron charge ID uncertainties do show a large difference, though as discussed in Section 6.3.1 this is where charge bias is observed and the systematic is implemented in such a way as to correctly account for it. For SR-RPV and SR-LQ the lepton and jet uncertainties become more important, whilst the muon bias uncertainties remain the smallest.

	$e^+\mu^-$	$e^-\mu^+$
Total	9%	10%
Electron scale/resolution	2%	2%
Electron charge ID	0.01%	0.09%
Electron efficiency	1%	1%
Jet energy scale	2%	2%
Jet energy resolution	4%	4%
$p_{\mathrm{T}}^{\mathrm{miss}}$	4%	4%
Muon efficiency	2%	2%
Muon MS/scale/ID	1%	0.8%
Muon sagitta	0.8%	1%
Pile-up reweighting	0.4%	0.2%
Muon reconstruction bias	0.02%	0.02%
Muon trigger bias	0.07%	0.07%
Theory	6%	7%
$t\bar{t}$ weight closure	1%	1%

Table 6.8: Summary of the uncertainties on the expected yields in SR-RPV, relative to the total expected background MC. The individual uncertainties of each type are added in quadrature to give an estimate of the total impact of that type; though it should be noted that as they may be correlated this may not reflect the final uncertainty values after a profile likelihood fit. The total uncertainty shown is calculated by summing the uncertainties in quadrature.

When performing the ratio measurement on the data, the systematic uncertainties considered include those on the JES and JER, $p_{\mathrm{T}}^{\mathrm{miss}}$, electron energy scale and resolution, muon energy scale and resolution, muon ID and MS tracks, and muon sagitta bias. The sizes of these uncertainties in the two ratio measurement signal regions are shown in

	$e^+\mu^-$	$e^-\mu^+$
Total	13%	15%
Electron scale/resolution	3%	2%
Electron charge ID	0.3%	0.3%
Electron efficiency	3%	4%
Jet energy scale	5%	2%
Jet energy resolution	1%	7%
$p_{\mathrm{T}}^{\mathrm{miss}}$	2%	0.5%
Muon efficiency	2%	2%
Muon MS/scale/ID	2%	1%
Muon sagitta	3%	4%
Pile-up reweighting	0.6%	0.9%
Muon reconstruction bias	0.1%	0.02%
Muon trigger bias	0.05%	0.05%
Theory	10%	12%
$t\bar{t}$ weight closure	0.5%	1%

Table 6.9: Summary of the uncertainties on the expected yields in SR-LQ, relative to the total expected background MC. The individual uncertainties of each type are added in quadrature to give an estimate of the total impact of that type; though it should be noted that as they may be correlated this may not reflect the final uncertainty values after a profile likelihood fit. The total uncertainty shown is calculated by summing the uncertainties in quadrature.

Tables 6.10 and 6.11. The dominant uncertainty in this case comes from the muon bias correction, followed by the JES. The lepton detector uncertainties are negligible.

	$e^+\mu^-$	$e^-\mu^+$
Total	2%	2%
Electron scale/resolution	0.000002%	0.000003%
Jet energy scale	0.2%	0.09%
Jet energy resolution	0.00001%	0.000008%
$p_{\mathrm{T}}^{\mathrm{miss}}$	0.000008%	0.000008%
Muon MS/scale/ID	0.00001%	0.00001%
Muon sagitta	0.00001%	0.00001%
Muon reconstruction bias	1%	1%
Muon trigger bias	1%	1%

Table 6.10: Summary of the uncertainties in SR-MET, relative to the total observed data. The individual uncertainties of each type are added in quadrature to give an estimate of the total impact of that type; though it should be noted that as they may be correlated this may not reflect the final uncertainty values after a profile likelihood fit. The total uncertainty shown is calculated by summing the uncertainties in quadrature.

	$e^+\mu^-$	$e^-\mu^+$
Total	2%	2%
Electron scale/resolution	0.000002%	0.000002%
Jet energy scale	0.4%	0.5%
Jet energy resolution	0.000008%	0.000002%
$p_{\mathrm{T}}^{\mathrm{miss}}$	0.000009%	0.000006%
Muon scale	0.00002%	0.000008%
Muon sagitta	0.00002%	0.000006%
Muon reconstruction bias	1%	1%
Muon trigger bias	1%	1%

Table 6.11: Summary of the uncertainties in SR-JET, relative to the total observed data. The individual uncertainties of each type are added in quadrature to give an estimate of the total impact of that type; though it should be noted that as they may be correlated this may not reflect the final uncertainty values after a profile likelihood fit. The total uncertainty shown is calculated by summing the uncertainties in quadrature.

6.9 Statistical methodology

The statistical methods used in this analysis are implemented using RooStats [140] and TRooFit[3]. The ratio measurement is based on minimising the profile log likelihood ratio, as introduced in Section 3.3. In the absence of an excess, exclusion limits are set on the RPV-SUSY and leptoquark model hypotheses, following the CL_s prescription laid out in the same Section.

Regarding the ratio measurement, the primary question is how to define the likelihood of obtaining the dataset given some hypothesised value of the ratio of $e^+\mu^-$ to $e^-\mu^+$: r. This free parameter r can then be taken as the parameter of interest in a profile log likelihood fit to data yields, to extract the value most consistent with the data.

The observed yield for each of $e^+\mu^-$ and $e^-\mu^+$ is assumed to follow a Poisson distribution in each bin of the distribution in question (such as $\sum_\ell m_{\mathrm{T}}(\ell, p_{\mathrm{T}}^{\mathrm{miss}})$ in SR-MET). The systematic uncertainties (as detailed in Section 6.8) are represented by nuisance parameters θ (with nominal value $\tilde{\theta}$), and are assigned a Gaussian constraint.

The likelihood may be written as

$$\begin{aligned}\mathcal{L} = \prod_{i\in\text{bins}} \Bigg[&\mathrm{Pois}(N_i^{-+}, w_i^{-+}(\theta)N_{i,exp} + F_i^{-+}) \times \mathrm{Pois}(N_i^{+-}, r_i w_i^{+-}(\theta)N_{i,exp} + F_i^{+-}) \\ &\times \mathrm{Gamma}\left(F_i^{+-}, \frac{(\tilde{F}_i^{+-})^2}{\sigma^2(F_i^{+-})} + 1, \frac{\sigma^2(F_i^{+-})}{\tilde{F}_i^{+-}}, 0\right) \times \mathrm{Gamma}\left(F_i^{-+}, \frac{(\tilde{F}_i^{-+})^2}{\sigma^2(F_i^{-+})} + 1, \frac{\sigma^2(F_i^{-+})}{\tilde{F}_i^{-+}}, 0\right)\Bigg] \\ &\times \prod_{j\in\text{systs}} \mathrm{Gaus}(0, \theta_j, 1),\end{aligned}$$

where the Gamma distributions are defined following:

$$\mathrm{Gamma}(x, \gamma, \beta, \mu) = \frac{(x-\mu)^{\gamma-1}e^{-(x-\mu)/\beta}}{\Gamma(\gamma)\beta^\gamma}, \tag{6.14}$$

and Gaussian distributions follows the formalism $\mathrm{Gauss}(x, \mu, \sigma)$, with mean μ and standard deviation σ.

Here each bin has a $(e^+\mu^-)/(e^-\mu^+)$ ratio r_i and an expected yield $N_{i,exp}$, once the charge-flavour biased fake lepton yield in the bin (F_i^{+-} or F_i^{-+}) has been subtracted. This subtraction leaves only the SM backgrounds that are charge-flavour symmetric to

[3]Available here: `gitlab.cern.ch/will/TRooFit`

leading order, and potentially BSM signal. The events in $N_{i,exp}$ also have the muon bias correction (described in Section 6.3) applied. Thus, in the case of no BSM signal contribution, one expects $r_i = 1$, or slightly below.

The expected yield $N_{i,exp}$ is initially set as the total $e^-\mu^+$ data yield in the bin, with the $e^-\mu^+$ fake lepton background yield in the bin subtracted. This is considered as a nuisance parameter which is set to float between 0.01 and 5 times its initial value. The fake lepton background yield nuisance parameter $F_i^{+-/-+}$ is initialised to the likelihood matrix method yield in the corresponding bin $\tilde{F}_i^{+-/-+}$. It can float between 0.01 and 5 times its initial value. It is given a Gamma distributed prior, which has parameters set to take into account the error on the likelihood matrix method yield, and have this nominal likelihood matrix method value as its maximum. A Gamma distribution is chosen rather than a Poisson because the yield is continuous, not discrete.

The ratio r_i in each bin is the fit's parameter of interest, which is set to be equal to one for the background-only hypothesis in order to match the SM prediction of a ratio equal to one (assuming any of the biases which could make the ratio decrease below one are small). The ratio can float between 0.01 and 5.0.

The function $w_i^{-+/+-}(\theta)$ is the response function in each bin which encapsulates how the relevant uncertainties affect the expected yield in the $e^-\mu^+$ or $e^+\mu^-$ channel. This is done by creating a smooth function describing how each uncertainty's $\pm 1\sigma$ variations change the acceptance of the region in which the yield is calculated. It is worth emphasising that the response functions are calculated independently for the $e^-\mu^+$ and $e^+\mu^-$ channels, such that any uncertainty that is not completely uncorrelated in both $e\mu$ regions has any correlations or anti-correlations taken into account. Each systematic uncertainty considered is validly represented by using one nuisance parameter for both channels. With this procedure, the correct normalisation for the Gaussian constraints on the systematic uncertainty nuisance parameters, is to set the mean to 0 and the standard deviation to 1. θ_j itself can float between -5.0 and 5.0.

The likelihood fit to constrain the nuisance parameters in all the bins is done simultaneously. When the fit is unblinded, data yields are used for both the observed values and to calculate the nominal value of the expected yield. MC is not used anywhere in the measurement in this case, excepting for its role in the likelihood matrix method yield, which is used to initialise the $F_i^{+-/-+}$ nuisance parameter, and is subtracted from the data yield to obtain the nominal value of the expected yield. The only Gaussian systematic uncertainties considered are those related to the muon bias estimate, since

this weighting is applied to data, and relevant detector uncertainties mentioned in Section 6.8. If the fit is blinded, MC is used everywhere instead. In this case, all of the detector systematics, $t\bar{t}$ modelling uncertainties, $t\bar{t}$ weight closure uncertainty and muon bias uncertainties are considered.

In turning instead to the model-dependent exclusion fit, the main point of discussion is again the definition of the likelihood from which the profile log likelihood ratio is built. The likelihood constructed here is similar to that used for the ratio measurement. The parameter of interest is now μ_{sig}, which denotes the signal strength and is the same parameter in every bin. For the nominal models, $\mu_{sig} = 1$ and for a background-only hypothesis with no BSM physics $\mu_{sig} = 0$.

The likelihood may be written as

$$
\begin{aligned}
\mathcal{L} = \prod_{i \in \text{bins}} \Bigg[& \text{Pois}(N_i^{-+}, w_i^{-+}(\theta) N_{i,bg}^{-+} + \mu_{sig} N_{i,sig}^{-+} + F_i^{-+}) \\
& \times \text{Pois}(N_i^{+-}, w_i^{+-}(\theta) N_{i,bg}^{+-} + \mu_{sig} N_{i,sig}^{+-} + F_i^{+-}) \\
& \times \text{Gamma}\left(N_{i,bg}^{+-}, \frac{(\tilde{N}_{i,bg}^{+-})^2}{\sigma^2(N_{i,bg}^{+-})} + 1, \frac{\sigma^2(N_{i,bg}^{+-})}{\tilde{N}_{i,bg}^{+-}}, 0\right) \times \text{Gamma}\left(N_{i,bg}^{-+}, \frac{(\tilde{N}_{i,bg}^{-+})^2}{\sigma^2(N_{i,bg}^{-+})} + 1, \frac{\sigma^2(N_{i,bg}^{-+})}{\tilde{N}_{i,bg}^{-+}}, 0\right) \\
& \times \text{Gamma}\left(N_{i,sig}^{+-}, \frac{(\tilde{N}_{i,sig}^{+-})^2}{\sigma^2(N_{i,sig}^{+-})} + 1, \frac{\sigma^2(N_{i,sig}^{+-})}{\tilde{N}_{i,sig}^{+-}}, 0\right) \times \text{Gamma}\left(N_{i,sig}^{-+}, \frac{(\tilde{N}_{i,sig}^{-+})^2}{\sigma^2(N_{i,sig}^{-+})} + 1, \frac{\sigma^2(N_{i,sig}^{-+})}{\tilde{N}_{i,sig}^{-+}}, 0\right) \\
& \times \text{Gamma}\left(F_i^{+-}, \frac{(\tilde{F}_i^{+-})^2}{\sigma^2(F_i^{+-})} + 1, \frac{\sigma^2(F_i^{+-})}{\tilde{F}_i^{+-}}, 0\right) \times \text{Gamma}\left(F_i^{-+}, \frac{(\tilde{F}_i^{-+})^2}{\sigma^2(F_i^{-+})} + 1, \frac{\sigma^2(F_i^{-+})}{\tilde{F}_i^{-+}}, 0\right) \Bigg] \\
& \times \prod_{j \in \text{systs}} \text{Gaus}(0, \theta_j, 1).
\end{aligned}
$$

Here $N_{i,bg}^{-+}$, $N_{i,sig}^{-+}$, $N_{i,bg}^{+-}$ and $N_{i,sig}^{+-}$ are expected yield nuisance parameters with nominal values set from the MC SM background (not including the fake lepton background) or the MC signal for a given point in one of the signal grids. They are all given Gamma distributed constraints, which incorporate the MC statistical error on the nominal yield values and have a maximum at the nominal value. The expected yield nuisance parameters can float between 0.01 and 5 times their nominal value. As before, the fake lepton yield is included as its own Gamma constrained nuisance parameter. In the case that the signal yield in a given bin is zero, the expected yield is considered as a constant at zero instead of a constrained but free to move parameter. In this case, the signal does not help to constrain the μ_{sig} parameter but allows the other nuisance parameters and

background to be constrained.

A simultaneous fit of all of the bins is performed, and the CL_s values are calculated for the signal+background hypothesis where $\mu_{sig} = 1$. The CL_s values are calculated using the same asymptotic approximation described above. Expected CL_s values (and a $\pm 1\sigma$ error band) are calculated by using the Asimov dataset as the observed dataset (as introduced in Section 3.3). In the case of a blinded fit, the observed CL_s values are calculated by using the SM MC background as the observed dataset. In the case of an unblinded fit, real data is used as the observed dataset instead. Consideration of which systematic uncertainties enter the bias expression is the same as in the previous fit.

Since both of the models considered have two free parameters (either the two sparticle masses or the leptoquark mass and coupling), the results of the exclusion fit can be presented as a standard exclusion contour on a 2D plot. These contours are defined as the point where the CL_s values imply an exclusion at 95% confidence. The exclusion plots will show both the observed and expected contours, with a $\pm 1\sigma$ band on the expected limit.

6.10 Results

In this Section, the ratio measurement and model-dependent exclusion limits are shown. Firstly, expected values of the ratio in the SM, and with the addition of benchmark RPV-SUSY scenarios, are shown for the six variables considered in SR-MET in Figure 6.29. All of the systematic uncertainties described in Section 6.8 are included in the measurement. The black markers show the expected ratio for just the SM, which is consistent with one everywhere. As expected, the addition of various benchmark signal models causes the expected ratio to increase above one in the higher bins. Similar plots showing the expected ratio of the five variables considered in SR-JET are shown in Figure 6.30. Here, the same behaviour can be seen.

One question to ask is what uncertainties dominate the ratio measurement in MC. Whilst Section 6.8 considered which uncertainties were largest in the signal regions, the uncertainties which have the greatest impact on the ratio measurement should be those where there is a large difference for the two charge-flavour combinations. In cases where the uncertainty is a similar size for both $e^+\mu^-$ and $e^-\mu^+$, a large amount of cancellation should be expected. The breakdown of how much each type of uncertainty contributes

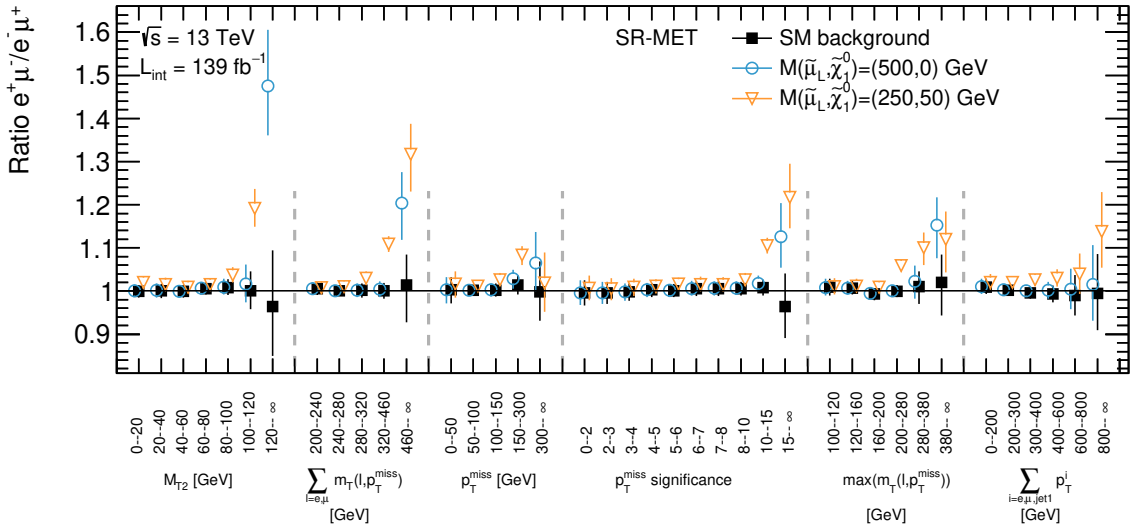

Figure 6.29: Measurement of the ratio $\frac{e^+\mu^-}{e^-\mu^+}$ in SR-MET using full Run 2 MC. Three measurements for scenarios where benchmark RPV-SUSY signal models are added to the SM MC background are overlaid. All uncertainties described in Section 6.8 are included. Weights derived in Section 6.7 are applied to $t\bar{t}$ MC events. The final bin includes overflow.

to the total uncertainty on the ratio in each bin of the eleven variables considered, were evaluated. One example of these is shown in Table 6.12, which shows that the dominant uncertainties impacting the MC ratio are theory uncertainties and $t\bar{t}$ weight closure uncertainties — neither of which are relevant for the data measurement. The statistical uncertainty becomes dominant in the higher bins where event yields are lower. Similar trends are found in the other variables.

The measurement of the ratio in data for the six variables considered in SR-MET are shown in Figure 6.31. Here, there is unfortunately no sign of the ratio increasing above one. The ratio is generally consistent with one, and in some cases slightly below. The deviation below one is most significant at high values of transverse mass. Given that good data-MC agreement is seen individually for the numerator and denominator in these variables, it is likely that where the ratio is below one, it is so as a result of detector biases rather than some alternative BSM model. One of the biases considered in Section 6.2.1, which have been assumed to be small but were not required to be properly quantified or corrected for, could be responsible for the trend — in particular if they had a larger effect for higher values of transverse mass in accordance with the observed trend. The measurement of the ratio in data for the five variables considered in SR-JET

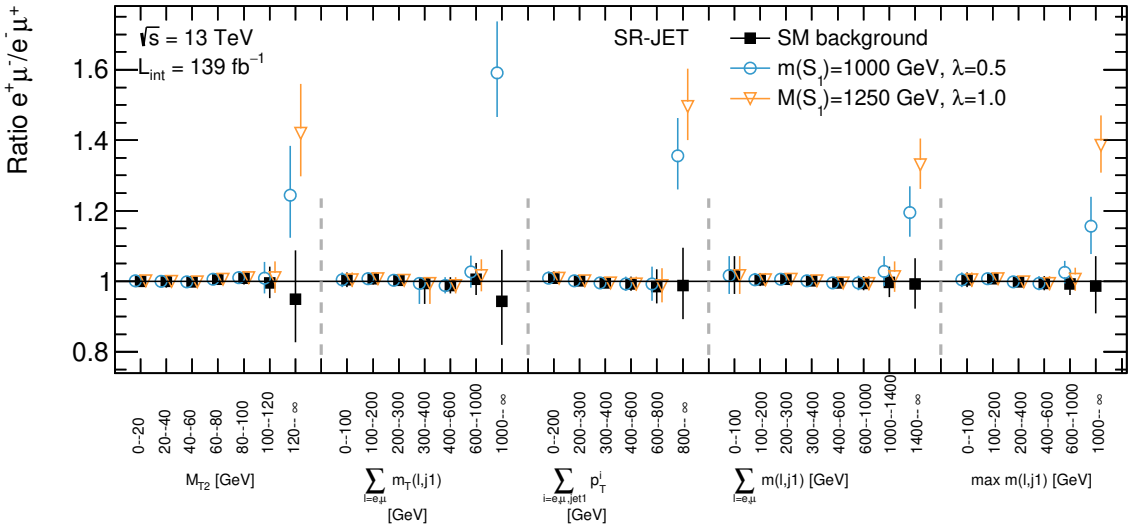

Figure 6.30: Measurement of the ratio $\frac{e^+\mu^-}{e^-\mu^+}$ in SR-JET using full Run 2 MC. Three measurements for scenarios where benchmark leptoquark signal models are added to the SM MC background are overlaid. All uncertainties described in Section 6.8 are included. Weights derived in Section 6.7 are applied to $t\bar{t}$ MC events. The final bin includes overflow.

are shown in Figure 6.32, where the same conclusions can be drawn.

Whilst the scope of this analysis is focused on answering the question of whether the ratio is larger than one, the observed trends seen in data are very interesting, and warrant further investigation in future work. To properly assess the cause of the deviation below one, a more complete quantitative estimation of the biases that could lower the ratio would be required, in order to produce a more robust Standard Model estimate. One could also consider alternative BSM models that also favour a ratio below one, for example, a scalar leptoquark model where instead of $e-u$ and $\mu-c$ couplings being switched on, $e-c$ and $\mu-u$ couplings are. Another example model would be the RPV-SUSY model considered already, but with selectrons instead of smuons being produced and the λ'_{131} coupling switched on instead of λ'_{231}.

The breakdown of how different categories of uncertainty affect the ratio measurement in data can be found in Table 6.13. This is shown for one example, but the conclusions drawn are similar for the other ten variables used. Most of the uncertainty on the ratio is statistical, with a significant portion also coming from the muon bias correction uncertainties. In the higher bins, the JES also becomes an important uncertainty.

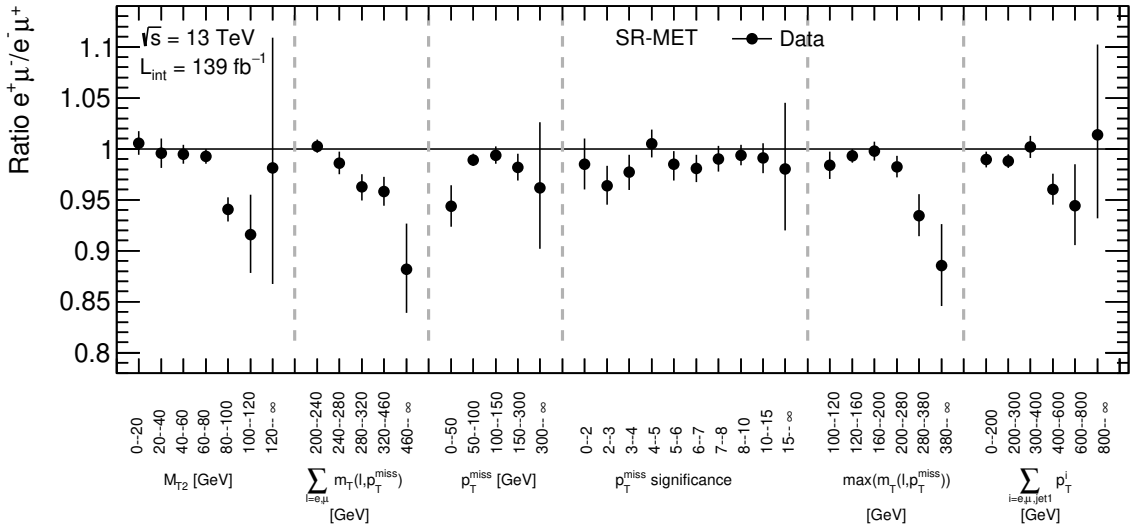

Figure 6.31: Measurement of the ratio $\frac{e^+\mu^-}{e^-\mu^+}$ in SR-MET using full Run 2 Data. Muon bias uncertainties are included. The final bin includes overflow.

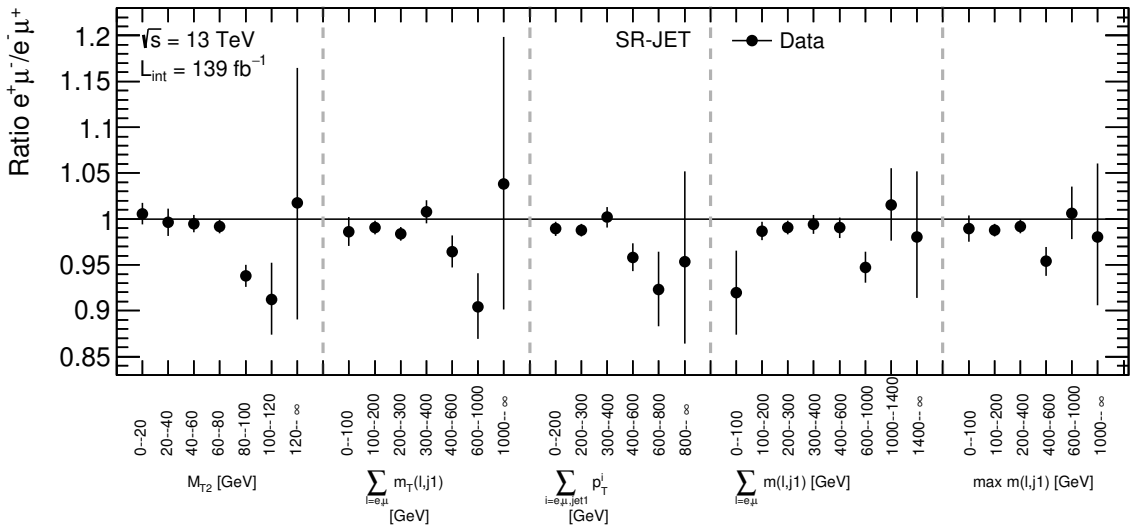

Figure 6.32: Measurement of the ratio $\frac{e^+\mu^-}{e^-\mu^+}$ in SR-JET using full Run 2 data. Muon bias uncertainties are included. The final bin includes overflow.

The overall value of the ratio in data in the two signal regions (as opposed to binned in a given variable) is also interesting to consider. In SR-MET, the ratio is found to be 0.988 ± 0.005. In SR-JET, the ratio is calculated as 0.987 ± 0.005. In both cases, the ratio is thus slightly below one, agreeing with the Standard Model hypothesis.

$\sum_{i=e,\mu,j_1} p_T^i$ [GeV]	[0, 200)		[200, 300)		[300, 400)		[400, 600)		[600, 800)		> 800	
Ratio	1.010		1.002		0.995		0.992		0.977		0.972	
Total	0.019	-0.017	0.012	-0.012	0.013	-0.014	0.018	-0.023	0.043	-0.044	0.098	-0.094
$t\bar{t}$ weight closure	0.009	-0.010	0.006	-0.006	0.003	-0.003	0.003	-0.003	0.006	-0.006	0.003	-0.003
Electron Charge ID	0.000	-0.001	0.000	-0.000	0.000	-0.000	0.000	-0.000	0.000	-0.000	0.000	-0.002
Electron efficiencies	0.000	-0.000	0.000	-0.000	0.000	-0.000	0.001	-0.000	0.002	-0.004	0.004	-0.004
Electron scale/resolution	0.000	-0.000	0.000	-0.000	0.000	-0.000	0.000	-0.000	0.001	-0.000	0.002	-0.003
p_T^{miss}	0.000	-0.000	0.000	-0.001	0.000	-0.000	0.000	-0.001	0.002	-0.003	0.007	-0.000
JER	0.001	-0.001	0.000	-0.000	0.001	-0.001	0.000	-0.001	0.003	-0.001	0.005	-0.003
JES	0.000	-0.000	0.001	-0.000	0.000	-0.000	0.000	-0.000	0.000	-0.000	0.007	-0.002
MC statistical error	0.005	-0.005	0.005	-0.005	0.007	-0.010	0.011	-0.018	0.029	-0.031	0.057	-0.067
Muon efficiencies.	0.000	-0.000	0.000	-0.001	0.000	-0.000	0.000	-0.000	0.000	-0.000	0.004	-0.002
Muon MS/Scale/ID	0.000	-0.000	0.000	-0.000	0.000	-0.001	0.000	-0.002	0.001	-0.002	0.002	-0.001
Muon sagitta	0.000	-0.000	0.000	-0.000	0.000	-0.000	0.000	-0.000	0.000	-0.000	0.000	-0.000
Muon reconstruction bias	0.001	-0.001	0.001	-0.001	0.001	-0.000	0.001	-0.000	0.001	-0.004	0.001	-0.002
Muon trigger bias	0.003	-0.004	0.002	-0.002	0.002	-0.002	0.002	-0.002	0.002	-0.000	0.002	-0.000
Pile-up re-weighting	0.000	-0.000	0.000	-0.000	0.000	-0.001	0.000	-0.000	0.003	-0.002	0.004	-0.002
Theory	0.015	-0.011	0.008	-0.007	0.007	-0.006	0.011	-0.009	0.019	-0.018	0.062	-0.046

Table 6.12: Contribution to the error on the ratio measured in MC, coming from each type of uncertainty, for the case of $\sum_{i=e,\mu,j_1} p_T^i$ in SR-JET.

$\sum_{i=e,\mu,\mathrm{j}_1} p_{\mathrm{T}}^{i}$ [GeV]	$[0, 200)$		$[200, 300)$		$[300, 400)$		$[400, 600)$		$[600, 800)$		> 800	
Ratio	0.989		0.988		1.002		0.958		0.923		0.953	
Total	0.008	-0.007	0.007	-0.006	0.010	-0.010	0.014	-0.014	0.036	-0.035	0.081	-0.075
$t\bar{t}$ weight closure	0.000	-0.000	0.000	-0.000	0.000	-0.000	0.000	-0.000	0.000	-0.000	0.000	-0.000
Electron scale/resolution	0.000	-0.000	0.000	-0.000	0.000	-0.000	0.000	-0.000	0.000	-0.000	0.000	-0.000
$p_{\mathrm{T}}^{\mathrm{miss}}$	0.000	-0.000	0.000	-0.000	0.000	-0.000	0.000	-0.000	0.000	-0.000	0.000	-0.000
JER	0.000	-0.000	0.000	-0.000	0.000	-0.000	0.000	-0.000	0.000	-0.000	0.001	-0.001
JES	0.002	-0.002	0.000	-0.000	0.002	-0.002	0.003	-0.003	0.009	-0.009	0.018	-0.016
MC statistical error	0.005	-0.005	0.004	-0.004	0.007	-0.007	0.010	-0.010	0.026	-0.024	0.060	-0.054
Muon MS/Scale/ID	0.000	-0.000	0.000	-0.000	0.000	-0.000	0.000	-0.000	0.000	-0.000	0.000	-0.000
Muon sagitta	0.000	-0.000	0.000	-0.000	0.000	-0.000	0.000	-0.000	0.000	-0.000	0.000	-0.000
Muon reconstruction bias	0.001	-0.001	0.001	-0.001	0.001	-0.001	0.001	-0.001	0.001	-0.001	0.001	-0.002
Muon trigger bias	0.003	-0.003	0.002	-0.002	0.002	-0.002	0.001	-0.001	0.001	-0.001	0.001	-0.002

Table 6.13: Contribution to the error on the ratio measured in data, coming from each type of uncertainty, for the case of $\sum_{i=e,\mu,\mathrm{j}_1} p_{\mathrm{T}}^{i}$ in SR-JET.

In the absence of any statistically significant deviations above one in the ratio in SR-MET, exclusion limits can be set for the RPV-SUSY model in the plane of smuon mass versus chargino mass. Figure 6.34 shows the exclusion limit at 95% confidence level. These results include all the uncertainties described in Section 6.8.

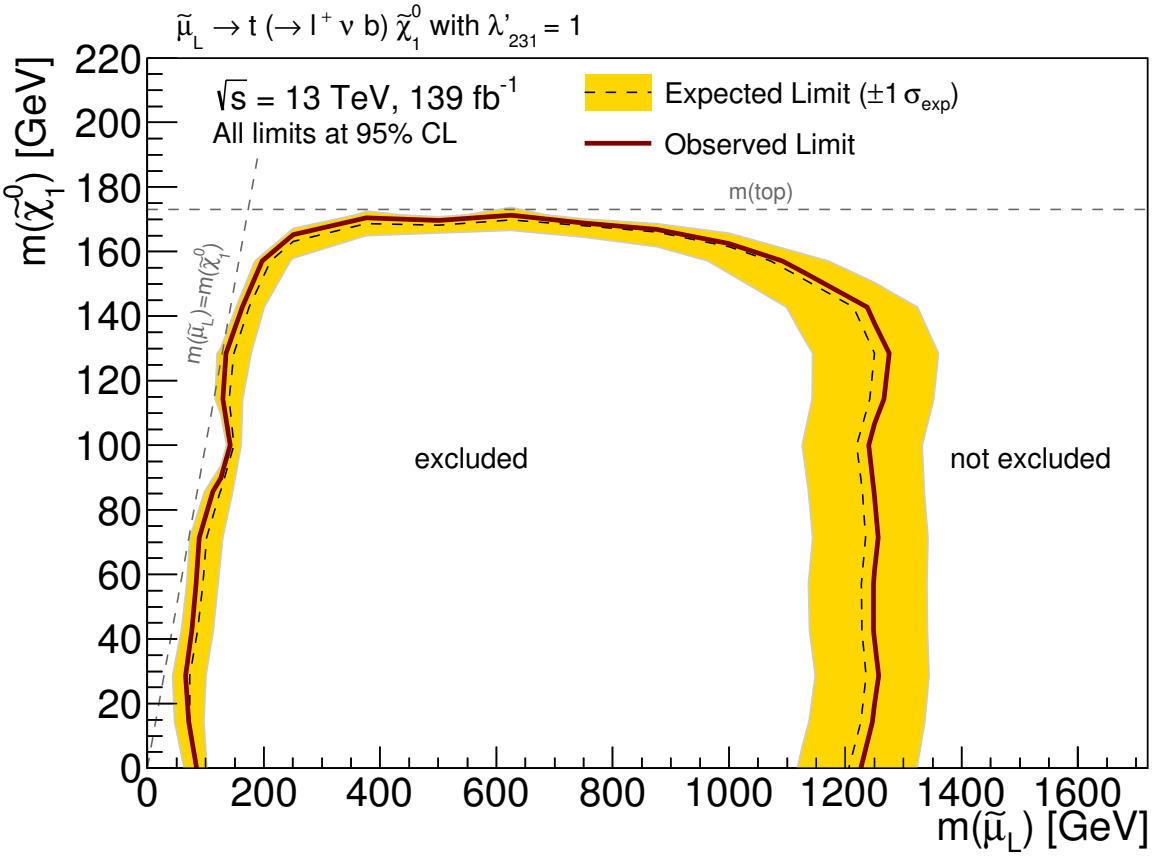

Figure 6.33: Expected and observed exclusion limits on RPV-SUSY models for smuon-single production decaying via a λ'_{231} coupling to a muon and top quark. The observed (solid thick line) and expected (thin dashed line) exclusion contours are computed at 95% confidence level. The shaded band corresponds to the $\pm 1\sigma$ variations in the expected limit, including all uncertainties described in Section 6.8. Lines are added to indicate the mass of the top quark, above which the neutralino is no longer stable on detector scales, and the kinematic limit where the smuon and neutralino masses coincide. Weights derived in Section 6.7 are applied to $t\bar{t}$ MC events.

It is also interesting to consider how the exclusion limit changes if the strength of the λ'_{231} coupling is adjusted. Here the $\tilde{\mu}_L$ limit found in the previous Chapter (and shown in Figure 5.10b) is appropriate to overlay, since it can be considered as a limit on these sparticles when the coupling is zero and only the simplified SUSY model considered in Chapter 5 remains. As expected, weakening the coupling reduces the sensitivity of the

search.

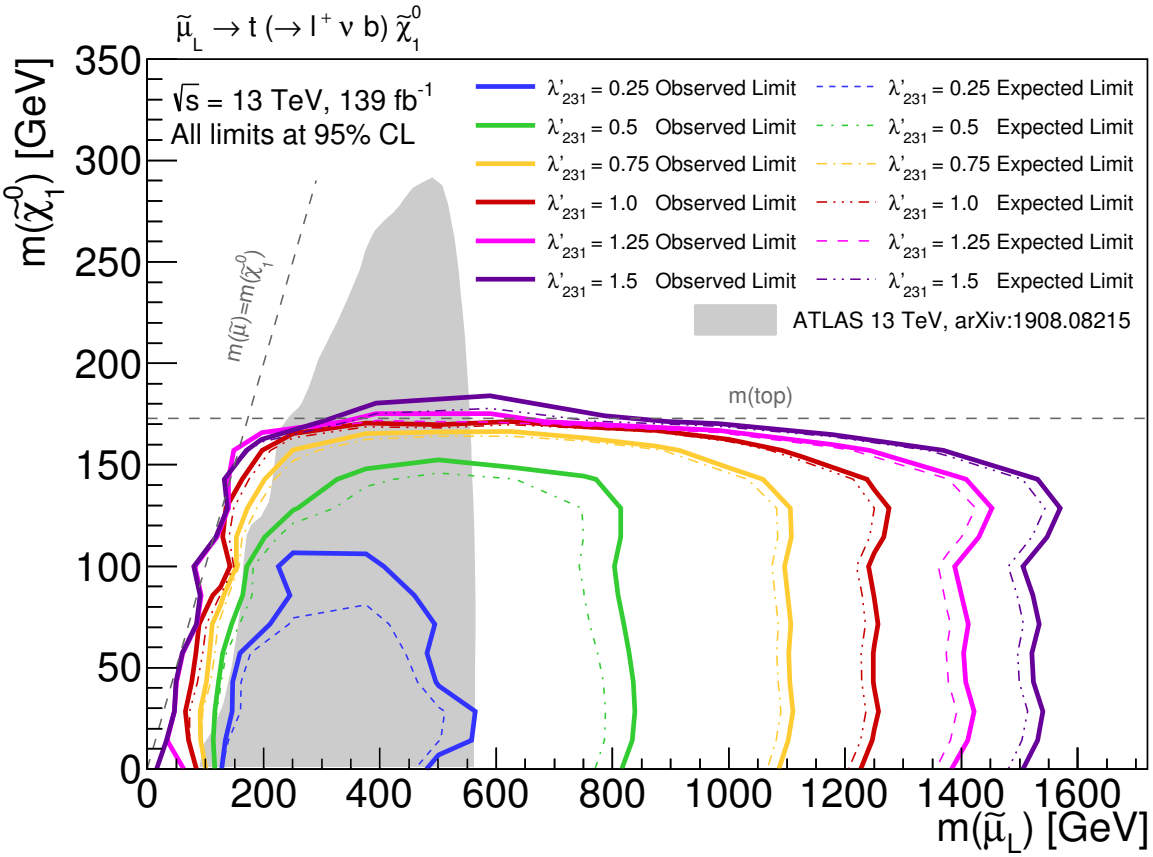

Figure 6.34: Expected and observed exclusion limits on RPV-SUSY models for smuon-single production decaying via a $\lambda'_{[}231]$ coupling to a muon and top quark. The observed (solid thick line) and expected (thin dashed line) exclusion contours are computed at 95% confidence level, including all uncertainties described in Section 6.8. Lines are added to indicate the mass of the top quark, above which the neutralino is no longer stable on detector scales, and the kinematic limit where the smuon and neutralino masses coincide. Weights derived in Section 6.7 are applied to $t\bar{t}$ MC events. The observed limit for left-handed smuon production obtained in Chapter 5 is overlaid. This figure was produced in collaboration with another analyser.

Similarly, in the absence of any statistically significant deviations above one in the ratio in SR-JET, exclusion limits can be set for the leptoquark model in the plane of leptoquark mass versus leptoquark coupling. Figure 6.35 shows the exclusion limit at 95% confidence level, with all of the uncertainties described in Section 6.8 included in the fit.

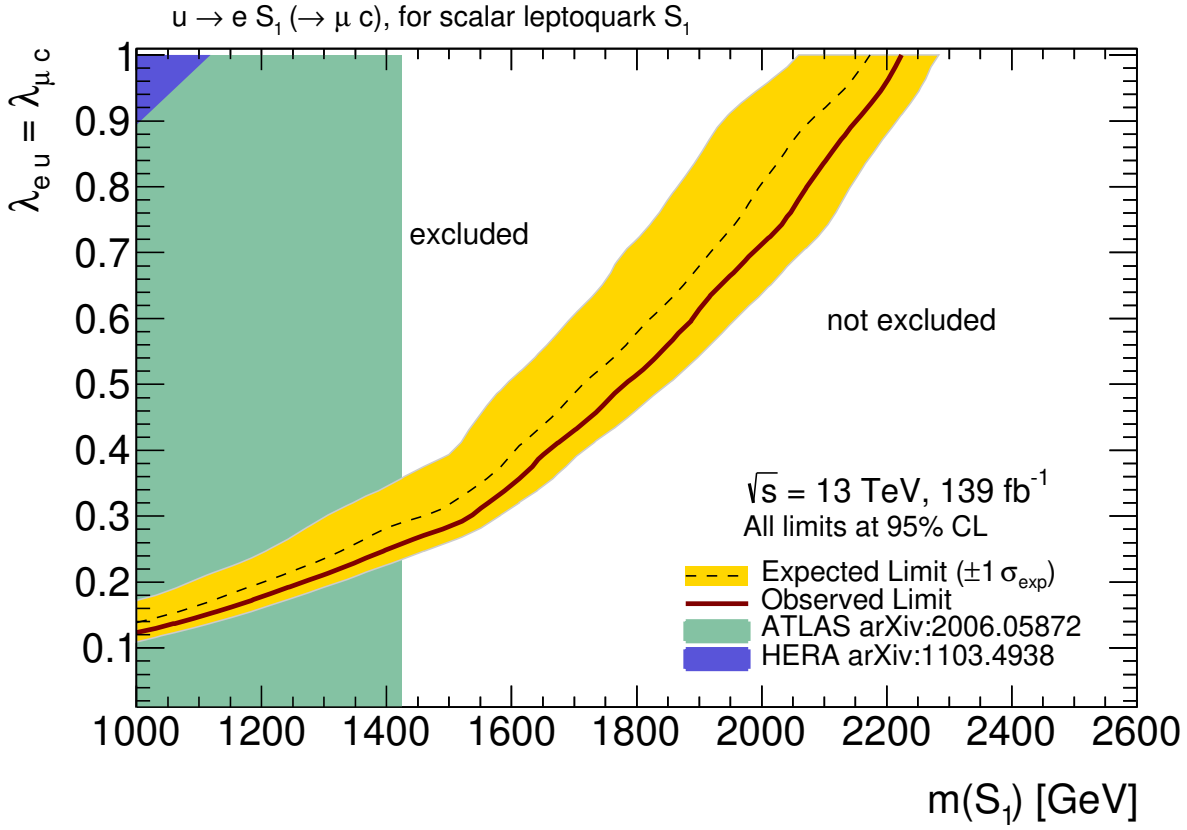

Figure 6.35: Expected and observed exclusion limits on scalar leptoquark models for single leptoquark production decaying to a muon and charm quark. The observed (solid thick line) and expected (thin dashed line) exclusion contours are computed at 95% confidence level. The upper shaded band corresponds to the $\pm 1\sigma$ variations in the expected limit, including all uncertainties described in Section 6.8. Weights derived in Section 6.7 are applied to $t\bar{t}$ MC events. The observed limits obtained from ATLAS in a relevant leptoquark pair-production search are shown in teal [130]. The observed limits on scalar leptoquarks obtained from HERA are shown in grey [129].

6.11 Conclusion

To conclude, the ratio of $e^+\mu^-$ to $e^-\mu^+$ events was measured in the full Run 2 ATLAS dataset. This was the first measurement of such a quantity at ATLAS. Whilst the ratio is expected to be less than or equal to one within the SM in proton-proton collisions at the ATLAS detector, some BSM models could allow the ratio to increase above one. In particular two example models were considered: RPV-SUSY with a single smuon production mode, and a scalar leptoquark model with a singly-produced leptoquark coupled equally to the first two generations of charged fermions. No signs of the ratio

being above one were found. This both allows for the production of exclusion limits on the two example models consisted, and can be reinterpreted in the future in the context of any other relevant BSM model.

Model-dependent exclusion limits for the RPV-SUSY model are the first LHC limits for this process, and exclude left-handed smuons up to a mass of 1.2 TeV, for neutralino masses up to 173 GeV. Exclusion limits on the leptoquark model are also the first direct constraints on the specific process considered, and for a coupling of 1, exclude leptoquark masses up to 2.2 TeV.

One appealing avenue for extending this measurement in the future would be to allow for sensitivity to signal models which predict a ratio less than one. This would require a robust estimate of all of the possible biases mentioned throughout this Chapter which could lower the ratio below one, in order to distinguish between signs of new physics and detector bias. A study of this nature would allow a proper explanation to be found of why the ratio is observed to be less than one in some areas of phase space. An alternative could be to consider the ratio using electrons or muons and taus, to provide sensitivity to a different set of BSM models.

Chapter 7

Concluding remarks

This thesis described three novel attempts to discover physics beyond the Standard Model, which is well-motivated to exist. Though it did not discover evidence for the models considered, all three searches vastly extended constraints on new physics at the LHC. Being able to narrow down what form BSM physics might take is a very valuable exercise.

Chapter 4 discussed the first ATLAS Run 2 supersymmetry search for chargino pair production decaying via W-bosons. This search was designed by the author and led to exclusion of charginos with mass up to 420 GeV for a massless neutralino, using the 2015–2017 dataset, which vastly improved on the corresponding Run 1 limit. The author was the main analyser for the extension of this search, described in Chapter 5, which added in the 2018 dataset. Exploiting this increased dataset led to the world's strongest limits on this process, raising the exclusion limit to 420 GeV for massless neutralinos. In addition, the results were re-interpreted for direct slepton production, excluding sleptons with masses up to 700 GeV for a massless neutralino, and for chargino production decaying via sleptons or sneutrinos, excluding chargino masses up to 1 TeV, again the world's strongest constraint on these models.

Chapter 6 presented preliminary results for the first ATLAS measurement of the ratio of $e^+\mu^-$ to $e^-\mu^+$ events in data, in an innovative and largely model-independent search for lepton charge-flavour violation. The author was also the leading analyser for this search within ATLAS. This search found that the ratio was consistent with the Standard Model hypothesis of not exceeding one, and was found to be less than one in some areas of phase space. The results were interpreted for two example models.

Firstly, single smuon production under an RPV-SUSY model with the λ'_{231} coupling switched on was considered. For couplings up to one and neutralino masses up to the top quark mass, smuons up to a mass of 1.2 TeV were excluded. The author added a second interpretation in a scalar leptoquark model with λ_{eu} and $\lambda_{\mu c}$ couplings set to be non-zero and equal to each other. For couplings up to one, scalar leptoquarks of mass up to 2.2 TeV were excluded.

There are many ways in which these searches can be extended in the future, for example using machine learning to optimise signal regions in more challenging areas of SUSY parameter space, or considering ratios involving taus. A tantalising area of further study would also be a thorough investigation of the cause of the deviation below one seen in some areas of phase space in the ratio measurement. However, in the light of no signs of new physics in Run 2 data, it is perhaps time to reconsider the approaches taken to more conventional model-dependent searches. Perhaps new physics particles are too heavy to be directly produced at the LHC, and so its indirect effects should be focused on; or simply, the right model hasn't been tested. Regardless of how sure physicists are that there is new physics of some kind beyond the Standard Model, it can appear in a vast number of different guises; perhaps the focus for future searches should be of the more model-agnostic type considered in Chapter 6. This search really sets a new direction for BSM searches at the LHC, both in its model-independence, but also in its power to exploit a dataset without reliance on Monte Carlo.

In conclusion, it is not time to give up on new physics appearing at the LHC. Rather than becoming disheartened at the lack of discoveries, one should instead be excited at the prospect of new and more interesting theories being proposed which fit the current BSM constraints, and relish the challenge of designing better ways to search for them.

Appendix A

Background only fit results for full Run 2 electroweak supersymmetry search

This appendix includes tables showing the result of the background only fit performed in Section 5.5.

Region	CR-WW	CR-VZ	CR-top
Observed events	962	811	321
Fitted backgrounds	962 ± 31	811 ± 28	321 ± 18
Fitted WW	670 ± 60	19.1 ± 1.9	5.5 ± 2.7
Fitted WZ	11.8 ± 0.7	188 ± 7	0.32 ± 0.15
Fitted ZZ	0.29 ± 0.06	577 ± 23	–
Fitted $t\bar{t}$	170 ± 50	1.8 ± 1.3	270 ± 16
Fitted single top	88 ± 8	0.65 ± 0.35	38.6 ± 2.6
FNP leptons	21 ± 8	5^{+6}_{-5}	4.2 ± 2.2
Other backgrounds	0.17 ± 0.06	19 ± 7	2.21 ± 0.20
Simulated WW	528	15.1	4.3
Simulated WZ	9.9	158	0.27
Simulated ZZ	0.24	487	–
Simulated $t\bar{t}$	210	2.2	327
Simulated single top	107	0.8	46.7

Table A.1: Observed event yields and predicted background yields from the fit in the CRs. For backgrounds with a normalisation extracted from the fit, the yield expected from the simulation before the fit is also shown. 'Other backgrounds' include the non-dominant background sources, i.e. Z+jets, $t\bar{t}$+V, Higgs boson and Drell–Yan events. A '–' symbol indicates that the background contribution is negligible.

Regions	VR-WW-0J	VR-WW-1J	VR-VZ	VR-top-low	VR-top-high	VR-top-WW
Observed events	2742	2671	464	190	50	953
Fitted backgrounds	2760 ± 120	2840 ± 250	420 ± 40	185 ± 17	53 ± 7	850 ± 80
Fitted WW	1550 ± 150	990 ± 120	17.6 ± 2.2	2.1 ± 0.7	2.6 ± 1.4	16.1 ± 2.5
Fitted WZ	34.2 ± 2.0	27.0 ± 2.3	99 ± 9	$0.05^{+0.17}_{-0.05}$	$0.2^{+0.6}_{-0.2}$	0.53 ± 0.13
Fitted ZZ	0.50 ± 0.06	0.39 ± 0.07	268 ± 25	–	–	$0.01^{+0.03}_{-0.01}$
Fitted $t\bar{t}$	790 ± 110	1400 ± 270	10.5 ± 3.2	157 ± 15	40 ± 7	650 ± 70
Fitted single top	336 ± 32	380 ± 40	2.2 ± 1.4	24.3 ± 2.6	4.6 ± 1.4	182 ± 15
FNP leptons	44 ± 23	38 ± 21	$0.2^{+2.1}_{-0.2}$	2.3 ± 1.4	1.8 ± 0.5	–
Other backgrounds	0.92 ± 0.30	2.1 ± 0.5	21^{+27}_{-21}	0.28 ± 0.06	3.20 ± 0.20	0.39 ± 0.11
Simulated WW	1230	790	14.0	1.6	2.0	12.8
Simulated WZ	28.8	22.8	84	0.04	0.1	0.45
Simulated ZZ	0.42	0.33	226	–	–	0.01
Simulated $t\bar{t}$	960	1700	13	190	49	790
Simulated single top	406	462	2.6	29.4	5.6	220

Table A.2: Observed event yields and predicted background yields in the VRs. For backgrounds with a normalisation extracted from the fit in the CRs, the yield expected from the simulation before the fit is also shown. 'Other backgrounds' include the non-dominant background sources, i.e. Z+jets, $t\bar{t}$+V, Higgs boson and Drell–Yan events. A '–' symbol indicates that the background contribution is negligible.

Table A.3: Observed event yields and predicted background yields from the fit for the binned DF SRs with $n_{\text{non-}b\text{-tagged jets}} = 0$. For backgrounds whose normalisation is extracted from the fit in the CRs, the yield expected from the simulation before the fit is also shown. 'Other backgrounds' include the non-dominant background sources, i.e. Z+jets, $t\bar{t}+V$, Higgs boson and Drell–Yan events. A '–' symbol indicates that the background contribution is negligible.

m_{T2}	[100, 105]	[105, 110]	[110, 120]	[120, 140]	[140, 160]	[160, 180]	[180, 220]	[220, 260]	> 260
Observed events	14	14	19	16	11	8	9	0	4
Fitted backgrounds	14 ± 4	11.3 ± 2.9	20 ± 4	21.7 ± 3.0	11.0 ± 2.0	6.3 ± 0.9	6.5 ± 1.2	3.2 ± 0.6	2.9 ± 0.5
Fitted WW	6.7 ± 1.8	7.9 ± 1.9	14.0 ± 1.7	18.4 ± 2.3	10.5 ± 1.9	6.2 ± 0.8	6.3 ± 1.1	3.0 ± 0.6	2.8 ± 0.5
Fitted WZ	0.12 ± 0.05	0.21 ± 0.07	0.33 ± 0.11	0.29 ± 0.04	0.18 ± 0.04	0.10 ± 0.03	0.13 ± 0.04	0.07 ± 0.02	0.10 ± 0.03
Fitted ZZ	$0.05^{+0.18}_{-0.05}$	$0.00^{+0.01}_{-0.00}$	$0.01^{+0.04}_{-0.01}$	< 0.04	< 0.04	< 0.04	$0.07^{+0.24}_{-0.07}$	< 0.04	$0.00^{+0.07}_{-0.00}$
Fitted $t\bar{t}$	4.3 ± 2.5	3.0 ± 1.7	4.1 ± 2.1	1.9 ± 1.1	0.24 ± 0.19	–	–	–	–
Fitted single top	1.6 ± 1.0	$0.2^{+0.4}_{-0.2}$	1.5 ± 0.8	0.42 ± 0.25	–	–	–	–	–
FNP leptons	1.37 ± 0.18	< 0.23	0.30 ± 0.15	0.59 ± 0.11	< 0.19	$0.00^{+0.02}_{-0.00}$	< 0.05	0.17 ± 0.02	–
Other backgrounds	0.02 ± 0.01	$0.00^{+0.01}_{-0.00}$	0.06 ± 0.02	0.06 ± 0.04	$0.03^{+0.03}_{-0.03}$	0.04 ± 0.01	0.02 ± 0.01	–	–
Simulated WW	5.3	6.2	11.01	14.6	8.3	4.9	5.0	2.4	2.2
Simulated WZ	0.10	0.18	0.27	0.24	0.15	0.09	0.11	0.06	0.08
Simulated ZZ	0.04	< 0.04	0.01	< 0.04	< 0.04	< 0.04	$0.06^{+0.21}_{-0.06}$	< 0.04	< 0.04
Simulated $t\bar{t}$	5.2	3.7	4.9	2.3	0.29	–	–	–	–
Simulated single top	2.0	0.3	1.8	0.51	–	–	–	–	–

Table A.4: Observed event yields and predicted background yields from the fit for the binned DF SRs with $n_{\text{non-}b\text{-tagged jets}} = 1$. For backgrounds whose normalisation is extracted from the fit in the CRs, the yield expected from the simulation before the fit is also reported. 'Other backgrounds' include the non-dominant background sources, i.e. Z+jets, $t\bar{t}$+V, Higgs boson and Drell–Yan events. A '–' symbol indicates that the background contribution is negligible.

m_{T2}	$[100, 105]$	$[105, 110]$	$[110, 120]$	$[120, 140]$	$[140, 160]$	$[160, 180]$	$[180, 220]$	$[220, 260]$	> 260
Observed events	12	12	14	15	7	4	5	3	3
Fitted backgrounds	14.7 ± 2.9	9.9 ± 2.0	14.3 ± 2.4	14.8 ± 2.2	6.5 ± 1.0	4.4 ± 0.9	5.6 ± 1.0	2.4 ± 0.7	2.7 ± 0.8
Fitted WW	5.7 ± 1.3	4.3 ± 0.9	7.7 ± 1.3	11.2 ± 2.1	5.9 ± 1.1	4.0 ± 0.9	5.2 ± 0.9	2.3 ± 0.6	2.0 ± 0.6
Fitted WZ	$0.1^{+0.5}_{-0.1}$	$0.09^{+0.10}_{-0.09}$	$0.2^{+0.7}_{-0.2}$	0.39 ± 0.08	0.20 ± 0.09	0.26 ± 0.09	0.14 ± 0.04	$0.04^{+0.14}_{-0.04}$	0.08 ± 0.03
Fitted ZZ	< 0.04	< 0.04	< 0.04	$0.00^{+0.01}_{-0.00}$	< 0.04	< 0.04	< 0.04	< 0.04	$0.07^{+0.24}_{-0.07}$
Fitted $t\bar{t}$	7.4 ± 2.7	4.6 ± 1.7	5.2 ± 1.8	2.2 ± 0.8	0.28 ± 0.17	0.09 ± 0.04	–	–	–
Fitted single top	0.9 ± 0.7	0.7 ± 0.5	1.0 ± 0.6	0.21 ± 0.13	–	–	–	–	–
FNP leptons	0.47 ± 0.07	0.24 ± 0.12	0.15 ± 0.11	0.54 ± 0.12	0.05 ± 0.04	< 0.03	0.24 ± 0.07	0.10 ± 0.03	0.45 ± 0.09
Other backgrounds	0.05 ± 0.05	0.06 ± 0.04	0.08 ± 0.05	0.23 ± 0.03	0.13 ± 0.02	0.10 ± 0.03	0.09 ± 0.02	$0.02^{+0.02}_{-0.02}$	0.04 ± 0.02
Simulated WW	4.5	3.4	6.1	8.9	4.6	3.1	4.1	1.8	1.6
Simulated WZ	0.1	0.08	0.2	0.33	0.17	0.22	0.12	0.03	0.07
Simulated ZZ	< 0.04	< 0.04	< 0.04	< 0.04	< 0.04	< 0.04	< 0.04	< 0.04	0.06
Simulated $t\bar{t}$	9.0	5.5	6.3	2.6	0.34	0.10	–	–	–
Simulated single top	1.1	0.8	1.2	0.25	–	–	–	–	–

Table A.5: Observed event yields and predicted background yields from the fit for the binned SF SRs with $n_{\text{non-}b\text{-tagged jets}} = 0$. For backgrounds whose normalisation is extracted from the fit in the CRs, the yield expected from the simulation before the fit is also shown. 'Other backgrounds' include the non-dominant background sources, i.e. Z+jets, $t\bar{t}+V$, Higgs boson and Drell–Yan events. A '–' symbol indicates that the background contribution is negligible.

m_{T2}	[100, 105]	[105, 110]	[110, 120]	[120, 140]	[140, 160]	[160, 180]	[180, 220]	[220, 260]	> 260
Observed events	14	15	24	37	20	12	12	5	8
Fitted backgrounds	15.8 ± 2.3	13.9 ± 1.9	26.9 ± 3.2	33.3 ± 3.4	17.4 ± 2.4	10.4 ± 1.2	13.4 ± 1.6	6.7 ± 1.1	6.8 ± 1.0
Fitted WW	6.9 ± 1.0	6.2 ± 0.8	14.5 ± 1.7	17.4 ± 2.3	9.6 ± 1.6	5.7 ± 0.8	6.3 ± 0.9	2.8 ± 0.5	3.3 ± 0.6
Fitted WZ	0.74 ± 0.11	0.82 ± 0.13	1.98 ± 0.20	2.75 ± 0.30	1.42 ± 0.24	1.04 ± 0.16	0.96 ± 0.14	0.50 ± 0.10	0.58 ± 0.11
Fitted ZZ	2.26 ± 0.35	2.9 ± 0.5	5.9 ± 0.6	8.0 ± 0.8	5.7 ± 0.8	3.5 ± 0.4	5.1 ± 0.6	2.4 ± 0.4	2.8 ± 0.4
Fitted $t\bar{t}$	4.0 ± 1.4	3.0 ± 1.2	3.6 ± 1.4	1.7 ± 0.6	$0.20^{+0.29}_{-0.20}$	–	–	–	–
Fitted single top	1.0 ± 0.7	0.8 ± 0.5	0.4 ± 0.4	0.12 ± 0.06	$0.04^{+0.05}_{-0.04}$	–	–	–	–
FNP leptons	0.84 ± 0.22	< 0.25	0.49 ± 0.25	1.8 ± 0.4	0.24 ± 0.13	0.17 ± 0.09	0.98 ± 0.14	1.02 ± 0.18	0.06 ± 0.05
Other backgrounds	$0.05^{+0.05}_{-0.05}$	0.11 ± 0.10	$0.1^{+1.5}_{-0.1}$	1.50 ± 0.31	0.27 ± 0.05	$0.00^{+0.03}_{-0.00}$	0.09 ± 0.03	$0.01^{+0.04}_{-0.01}$	$0.00^{+0.30}_{-0.00}$
Simulated WW	5.4	4.9	11.5	13.8	7.6	4.5	5.0	2.2	2.6
Simulated WZ	0.63	0.69	1.67	2.32	1.20	0.87	0.81	0.42	0.49
Simulated ZZ	1.90	2.5	5.0	6.8	4.8	2.9	4.3	2.0	2.4
Simulated $t\bar{t}$	4.9	3.6	4.3	2.1	0.24	–	–	–	–
Simulated single top	1.2	1.0	0.4	0.14	0.04	–	–	–	–

Table A.6: Observed event yields and predicted background yields from the fit for the binned SF SRs with $n_{\text{non-}b\text{-tagged jets}} = 1$. For backgrounds whose normalisation is extracted from the fit in the CRs, the yield expected from the simulation before the fit is also shown. 'Other backgrounds' include the non-dominant background sources, i.e. Z+jets, $t\bar{t}+V$, Higgs boson and Drell–Yan events. A '–' symbol indicates that the background contribution is negligible.

m_{T2}	[100, 105]	[105, 110]	[110, 120]	[120, 140]	[140, 160]	[160, 180]	[180, 220]	[220, 260]	> 260
Observed events	12	13	30	21	15	11	8	5	5
Fitted backgrounds	17 ± 4	13.7 ± 2.5	17 ± 4	23.3 ± 2.8	17.0 ± 2.3	9.4 ± 1.9	12.3 ± 1.6	6.5 ± 1.4	8.0 ± 2.7
Fitted WW	5.5 ± 1.1	4.9 ± 0.9	7.7 ± 1.3	9.9 ± 1.5	6.0 ± 1.1	4.6 ± 1.1	5.2 ± 0.8	2.0 ± 0.5	2.3 ± 0.6
Fitted WZ	0.85 ± 0.21	1.05 ± 0.26	1.71 ± 0.27	2.9 ± 0.4	1.79 ± 0.26	1.44 ± 0.32	1.83 ± 0.27	0.87 ± 0.21	1.03 ± 0.23
Fitted ZZ	1.13 ± 0.26	1.3 ± 0.4	2.4 ± 0.4	4.0 ± 0.6	4.3 ± 0.6	2.4 ± 0.6	3.6 ± 0.5	1.5 ± 0.4	1.7 ± 0.4
Fitted $t\bar{t}$	6.7 ± 3.3	3.6 ± 1.8	3.9 ± 2.1	1.5 ± 0.8	$0.06^{+0.06}_{-0.06}$	$0.07^{+0.10}_{-0.07}$	–	–	–
Fitted single top	1.1 ± 0.7	0.9 ± 0.6	0.6 ± 0.5	0.6 ± 0.4	$0.13^{+0.24}_{-0.13}$	–	–	–	–
FNP leptons	1.31 ± 0.18	1.39 ± 0.21	0.41 ± 0.25	1.92 ± 0.32	3.4 ± 0.5	0.93 ± 0.16	0.64 ± 0.17	0.13 ± 0.04	0.10 ± 0.05
Other backgrounds	0.7 ± 0.5	0.47 ± 0.32	$0.5^{+2.4}_{-0.5}$	2.5 ± 0.7	1.3 ± 1.0	$0.00^{+0.11}_{-0.00}$	1.0 ± 0.8	2.0 ± 0.8	2.9 ± 2.0
Simulated WW	4.4	3.9	6.1	7.9	4.8	3.7	4.1	1.6	1.8
Simulated WZ	0.72	0.89	1.44	2.4	1.51	1.22	1.55	0.73	0.87
Simulated ZZ	0.95 ± 0.21	1.1	2.0	3.4	3.6	2.0	3.0	1.3	1.4
Simulated $t\bar{t}$	8.1	4.4	4.8	1.8	0.07	0.08	–	–	–
Simulated single top	1.3	1.1	0.8	0.7	0.15	–	–	–	–

Appendix B

Ratio measurement in validation region for charge-flavour asymmetry search

Further to the ratio measurement in the control region, the ratio in VR-MET can be measured to look at a region of phase space closer to the signal regions. It is assumed that the validation region is loose enough to have relatively low signal contamination. The ratio in VR-MET is shown in Figure B.1 for data and in Figure B.2 for MC with the ttbar weights applied and all uncertainties, for the same variables and binning used for SR-MET. Overall in VR-MET the ratio evaluates to 0.987 ± 0.005 In the MC, some deviation below one is seen for high values of variables; a trend followed by the data. The deviation from one is less significant than that observed in the signal regions.

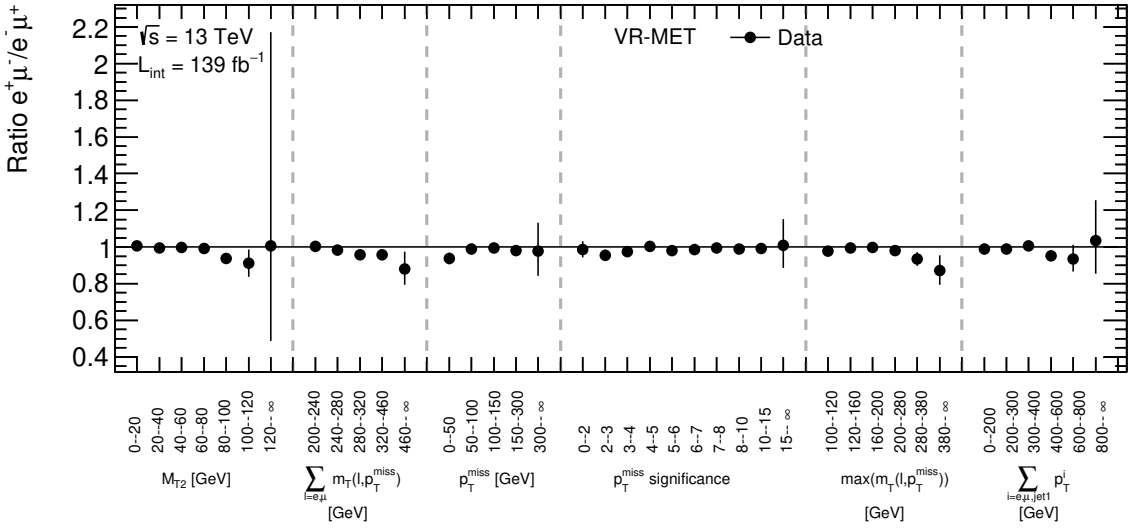

Figure B.1: The ratio calculated in VR-MET for data, in bins of different kinematic variables. Weights derived in Section 6.7 are applied to $t\bar{t}$ MC events. All relevant uncertainties described in Section 6.8 are included.

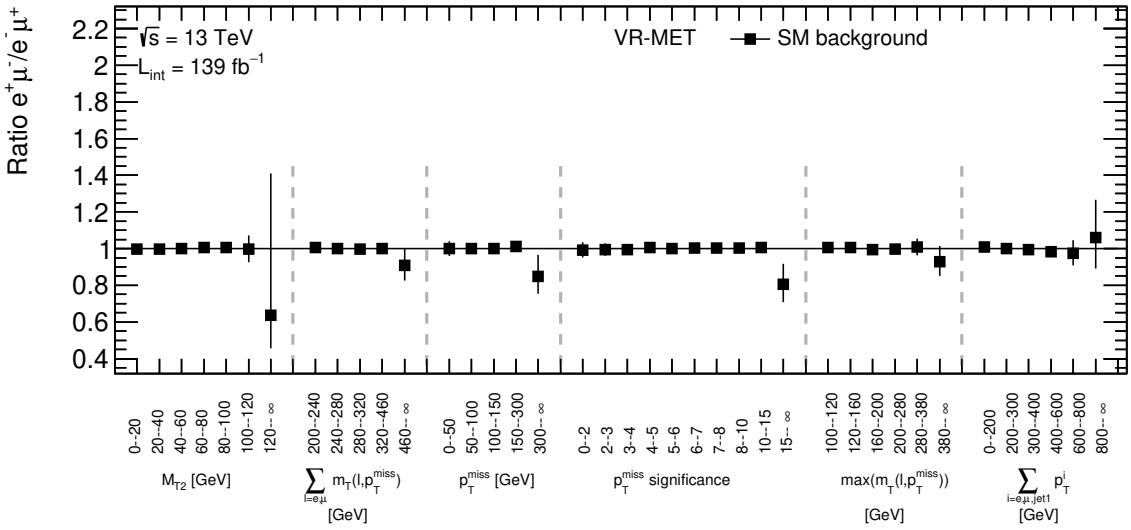

Figure B.2: The ratio calculated in VR-MET for MC, in bins of different kinematic variables. Weights derived in Section 6.7 are applied to $t\bar{t}$ MC events. All relevant uncertainties described in Section 6.8 are included.

Colophon

This thesis was made in LaTeX 2_ε using the "hepthesis" class [141].

Bibliography

[1] ATLAS collaboration. Search for direct chargino pair production with W-boson mediated decays in events with two leptons and missing transverse momentum at $\sqrt{s} = 13\,\text{TeV}$ with the ATLAS detector. ATLAS-CONF-2018-042, 2018.

[2] ATLAS collaboration. Search for electroweak production of charginos and sleptons decaying into final states with two leptons and missing transverse momentum in $\sqrt{s}$=13 TeV pp collisions using the ATLAS detector. *Eur. Phys. J. C*, 80:123, 2019, 1908.08215.

[3] C. G. Lester and B. H. Brunt. Difference between two species of emu hides a test for lepton flavour violation. *JHEP*, 03:149, 2017, 1612.02697.

[4] B. Brunt. *Searches for new physics with the ATLAS experiment.* PhD thesis, University of Cambridge, 2017. unpulished thesis.

[5] E. Noether. Invariante variationsprobleme. *Nachrichten von der Gesellschaft der Wissenschaften zu Göttingen, Mathematisch-Physikalische Klasse*, 1918:235–257, 1918.

[6] N. Cabibbo. Unitary Symmetry and Leptonic Decays. *Phys.Rev.Lett.*, 10:531–533, 1963.

[7] M. Kobayashi and T. Maskawa. CP Violation in the Renormalizable Theory of Weak Interaction. *Prog.Theor.Phys.*, 49:652–657, 1973.

[8] R.N. Mohapatra et al. Theory of neutrinos: A White paper. *Rept. Prog. Phys.*, 70:1757–1867, 2007, hep-ph/0510213.

[9] Ziro Maki, Masami Nakagawa, and Shoichi Sakata. Remarks on the unified model of elementary particles. *Prog. Theor. Phys.*, 28:870–880, 1962.

[10] I. J. R. Aitchison. Supersymmetry and the MSSM: An Elementary Introduction, 2004, 0505105v1.

[11] ATLAS collaboration. Observation of a new particle in the search for the Standard Model Higgs boson with the ATLAS detector at the LHC. *Phys. Lett. B*, 716:1–29, 2012, 1207.7214.

[12] CMS Collaboration. Observation of a new boson at a mass of 125 GeV with the CMS experiment at the LHC. *Phys. Lett. B*, 716:30–61, 2012, 1207.7235.

[13] S. P. Martin. *A Supersymmetry primer*, volume 21, pages 1–153. 2010, hep-ph/9709356.

[14] S. P. Martin and D. G. Robertson. Standard Model parameters in the tadpole-free pure $\overline{MS}$ scheme. *Phys.Rev.D.*, 100:073004, 2019.

[15] H. Goldberg. Constraint on the Photino Mass from Cosmology. *Phys. Rev. Lett.*, 50:1419, 1983. [Erratum: Phys. Rev. Lett.103,099905(2009)].

[16] J. R. Ellis, J. S. Hagelin, D. V. Nanopoulos, K. A. Olive, and M. Srednicki. Supersymmetric Relics from the Big Bang. *Nucl. Phys. B*, 238:453–476, 1984.

[17] N. Sakai. Naturalness in Supersymmetric Guts. *Zeit. Phys. C*, 11:153, 1981.

[18] S. Dimopoulos, S. Raby, and F. Wilczek. Supersymmetry and the Scale of Unification. *Phys. Rev.*, D24:1681–1683, 1981.

[19] L. E. Ibanez and G. G. Ross. Low-Energy Predictions in Supersymmetric Grand Unified Theories. *Phys. Lett. B*, 105:439, 1981.

[20] S. Dimopoulos and H. Georgi. Softly Broken Supersymmetry and SU(5). *Nucl. Phys. B*, 193:150, 1981.

[21] Y. A. Golfand and E. P. Likhtman. Extension of the Algebra of Poincare Group Generators and Violation of p Invariance. *JETP Lett.*, 13:323–326, 1971. [Pisma Zh.Eksp.Teor.Fiz.13:452-455,1971].

[22] D. V. Volkov and V. P. Akulov. Is the Neutrino a Goldstone Particle? *Phys. Lett. B*, 46:109–110, 1973.

[23] J. Wess and B. Zumino. Supergauge Transformations in Four-Dimensions. *Nucl. Phys. B*, 70:39–50, 1974.

[24] J. Wess and B. Zumino. Supergauge Invariant Extension of Quantum Electrodynamics. *Nucl. Phys. B*, 78:1, 1974.

[25] S. Ferrara and B. Zumino. Supergauge Invariant Yang-Mills Theories. *Nucl. Phys. B*, 79:413, 1974.

[26] A. Salam and J. A. Strathdee. Supersymmetry and Nonabelian Gauges. *Phys. Lett. B*, 51:353–355, 1974.

[27] B. Allanach. Beyond the Standard Model, 2016, 1609.02015v1.

[28] R. Barbieri and G.F. Giudice. Upper Bounds on Supersymmetric Particle Masses. *Nucl. Phys. B*, 306:63, 1988.

[29] G. R. Farrar and P. Fayet. Phenomenology of the Production, Decay, and Detection of New Hadronic States Associated with Supersymmetry. *Phys. Lett. B*, 76:575–579, 1978.

[30] W. Buchmüller, R. Rückl, and D. Wyler. Leptoquarks in lepton-quark collisions. *Physics Letters B*, 191(4):442–448, 1987.

[31] R. Aaij et al. Test of lepton universality with $B^0 \to K^{*0}\ell^+\ell^-$ decays. *JHEP*, 08:055, 2017, 1705.05802.

[32] L. Calibbi, A. Crivellin, and T. Li. Model of vector leptoquarks in view of the B-physics anomalies. *Phys.Rev.D*, 98:11, 2018, 1709.00692.

[33] I. Bigaran, J. Gargalionis, and Raymond R. Volkas. A near-minimal leptoquark model for reconciling flavour anomalies and generating radiative neutrino masses. *JHEP*, 1910:106, 2019, 1906.01870.

[34] ALICE Collaboration. The ALICE experiment at the CERN LHC. *JINST*, 3:S08002, 2008.

[35] CMS Collaboration. The CMS experiment at the CERN LHC. *JINST*, 3:S08004, 2008.

[36] LHCb Collaboration. The LHCb Detector at the LHC. *JINST*, 3:S08005, 2008.

[37] M. Brice. Aerial View of the CERN taken in 2008., July 2008.

[38] CERN TE-EPC group. Cern accelerator complex diagram. `https://cds.cern.ch/record/2684277`, 2019.

[39] ATLAS collaboration. Luminosity determination in pp collisions at $\sqrt{s} = 13\,\text{TeV}$ using the ATLAS detector at the LHC. ATLAS-CONF-2019-021, 2019.

[40] ATLAS collaboration. ATLAS luminosity public results Run 2, 2019.

[41] ATLAS collaboration. The atlas experiment at the cern large hadron collider. *JINST*, 3(08):S08003, 2008.

[42] G. Avoni et al. The new lucid-2 detector for luminosity measurement and monitoring in atlas. *JINST*, 13(07):P07017, 2018.

[43] ATLAS Collaboration.

[44] Karolos Potamianos. The upgraded Pixel detector and the commissioning of the Inner Detector tracking of the ATLAS experiment for Run-2 at the Large Hadron Collider. *PoS*, EPS-HEP2015:261, 2015, 1608.07850.

[45] ATLAS Collaboration. ATLAS Pixel IBL: Stave Quality Assurance. ATL-INDET-PUB-2014-006, 2014.

[46] ATLAS collaboration. *ATLAS Liquid Argon Calorimeter: Technical Design Report*. Technical Design Report ATLAS. CERN, Geneva, 1996.

[47] ATLAS Collaboration. Performance of the ATLAS detector using first collision data. *JHEP*, 09:056, 2010, 1005.5254.

[48] ATLAS Collaboration. Performance of the ATLAS Trigger System in 2015. *Eur. Phys. J. C*, 77:317, 2017, 1611.09661.

[49] ATLAS Collaboration. Electron and photon performance measurements with the ATLAS detector using the 2015–2017 LHC proton-proton collision data. *JINST*, 14(12):P12006, 2019, 1908.00005.

[50] ATLAS Collaboration. Electron and photon performance measurements with the ATLAS detector using the 2015-2017 LHC proton-proton collision data. *JINST*, 14:P12006, 2018.

[51] ATLAS Collaboration. Jet reconstruction and performance using particle flow with the ATLAS Detector. *Eur. Phys. J. C*, 77(7):466, 2017, 1703.10485.

[52] W. Lampl, S. Laplace, D. Lelas, P. Loch, H. Ma, S. Menke, S. Rajagopalan, D. Rousseau, S. Snyder, and G. Unal. Calorimeter clustering algorithms: Description and performance. *ATL-LARG-PUB-2008-002*, 2008.

[53] M. Cacciari, G. P. Salam, and G. Soyez. The Anti-k(t) jet clustering algorithm. *JHEP*, 0804:063, 2008, 0802.1189.

[54] ATLAS collaboration. Jet energy scale measurements and their systematic uncertainties in proton–proton collisions at $\sqrt{s} = 13\,\text{TeV}$ with the ATLAS detector. *Phys. Rev. D*, 96:072002, 2017, 1703.09665.

[55] ATLAS Collaboration. Performance of b-jet identification in the ATLAS experiment. *JINST*, 11:P04008, 2016, 1512.01094.

[56] ATLAS Collaboration. Optimisation and performance studies of the ATLAS b-tagging algorithms for the 2017-18 LHC run. ATL-PHYS-PUB-2017-013, 2017.

[57] ATLAS Collaboration. Tagging and suppression of pileup jets with the ATLAS detector. ATLAS-CONF-2014-018, 2014.

[58] ATLAS Collaboration. Identification and rejection of pile-up jets at high pseudorapidity with the ATLAS detector. *Eur. Phys. J. C*, 77(9):580, 2017, 1705.02211. [Erratum: Eur.Phys.J.C 77, 712 (2017)].

[59] ATLAS Collaboration. Selection of jets produced in 13 TeV proton–proton collisions with the ATLAS detector. ATLAS-CONF-2015-029, 2015.

[60] ATLAS Collaboration. Performance of pile-up mitigation techniques for jets in *pp* collisions at $\sqrt{s} = 8\,\text{TeV}$ using the ATLAS detector. *Eur. Phys. J. C*, 76:581, 2016, 1510.03823.

[61] ATLAS Collaboration. Muon reconstruction performance of the ATLAS detector in proton–proton collision data at $\sqrt{s} = 13\,\text{TeV}$. *Eur. Phys. J. C*, 76:292, 2016, 1603.05598.

[62] ATLAS collaboration. Muon reconstruction performance of the ATLAS detector in proton-proton collision data at $\sqrt{s} = 13\,\text{TeV}$. *Eur. Phys. J. C*, 76(5):292, 2016, 1603.05598.

[63] ATLAS collaboration. Performance of missing transvserve momentum reconstruction with the ATLAS detector using proton-proton collisions at $\sqrt{s} = 13\,\text{TeV}$. *Eur. Phys. J. C*, 78:903, 2018, 1802.08168.

[64] ATLAS Collaboration. Performance of algorithms that reconstruct missing transverse momentum in $\sqrt{s} = 8\,\text{TeV}$ proton–proton collisions in the ATLAS detector. *Eur. Phys. J. C*, 77:241, 2017, 1609.09324.

[65] ATLAS collaboration. $E_{\text{T}}^{\text{miss}}$ performance in the ATLAS detector using 2015–2016 LHC *pp* collisions. ATLAS-CONF-2018-023, 2016.

[66] ATLAS Collaboration. The ATLAS Simulation Infrastructure. *Eur. Phys. J. C*, 70:823, 2010, 1005.4568.

[67] S. Agostinelli et al. GEANT4: A Simulation toolkit. *Nucl.Instrum.Meth. A*, 506:250–303, 2003.

[68] C.G. Lester and D.J. Summers. Measuring masses of semi-invisibly decaying particles pair produced at hadron colliders. *Phys. Lett. B*, 463:99–103, 1999, hep-ph/9906349.

[69] A. Barr, C. G. Lester, and P. Stephens. m(T2): The Truth behind the glamour. *J. Phys. G*, 29:2343–2363, 2003, hep-ph/0304226.

[70] C. G. Lester and B. Nachman. Bisection-based asymmetric M_{T2} computation: a higher precision calculator than existing symmetric methods. *JHEP*, 03:100, 2015, 1411.4312.

[71] ATLAS collaboration. Object based missing transverse momentum significance in the ATLAS detector. ATLAS-CONF-2018-038, 2018.

[72] G. Cowan. *Statistical Data Analysis.* Oxford University Press, Oxford, 1998.

[73] J. Neyman and E. S. Pearson. On the problem of the most efficient tests of statistical hypotheses. *Philosophical Transactions of the Royal Society of London. Series A, Containing Papers of a Mathematical or Physical Character*, 231:pp. 289–337, 1933.

[74] L. Moneta, K. Belasco, K. S. Cranmer, S. Kreiss, A. Lazzaro, et al. The RooStats Project. *PoS*, ACAT2010:057, 2010, 1009.1003.

[75] G. Cowan, K. Cranmer, E. Gross, and O. Vitells. Asymptotic formulae for likelihood-based tests of new physics. *Eur. Phys. J. C.*, 71:1554, 2011, 1007.1727.

[76] A. L. Read. Presentation of search results: the cl_s technique. *journal of Physics G: Nuclear and Particle Physics*, 28(10):2693, 2002.

[77] ATLAS collaboration. Search for squarks and gluinos in final states with jets and missing transverse momentum using 36 fb^{-1} of $\sqrt{s} = 13\,\text{TeV}$ pp collision data with the ATLAS detector. *Phys. Rev. D*, 97:112001, 2018, 1712.02332.

[78] J. Alwall, P. Schuster, and N. Toro. Simplified Models for a First Characterization of New Physics at the LHC. *Phys. Rev. D*, 79:075020, 2009, 0810.3921.

[79] ATLAS collaboration. Search for direct production of charginos, neutralinos and sleptons in final states with two leptons and missing transverse momentum in pp collisions at $\sqrt{s} = 8\,\text{TeV}$ with the ATLAS detector. *JHEP*, 05:071, 2014, 1403.5294.

[80] CMS collaboration. Searches for pair production of charginos and top squarks in final states with two oppositely charged leptons in proton–proton collisions at $\sqrt{s} = 13\,\text{TeV}$. *JHEP*, 11:079, 2018, 1807.07799.

[81] L. Lönnblad and S. Prestel. Merging Multi-leg NLO Matrix Elements with Parton Showers. *JHEP*, 03:166, 2013, 1211.7278.

[82] W. Beenakker, R. Hopker, M. Spira, and P. Zerwas. Squark and gluino production at hadron colliders. *Nucl. Phys. B.*, 492:51–103, 1997, hep-ph/9610490.

[83] A. Kulesza and L. Motyka. Threshold resummation for squark-antisquark and gluino-pair production at the LHC. *Phys. Rev. Lett.*, 102:111802, 2009, 0807.2405.

[84] A. Kulesza and L. Motyka. Soft gluon resummation for the production of gluino-gluino and squark-antisquark pairs at the LHC. *Phys. Rev. D*, 80:095004, 2009, 0905.4749.

[85] W. Beenakker, S. Brensing, M. Kramer, A. Kulesza, E. Laenen, et al. Soft-gluon resummation for squark and gluino hadroproduction. *JHEP*, 12:041, 2009, 0909.4418.

[86] W. Beenakker, S. Brensing, M. Kramer, A. Kulesza, E. Laenen, et al. Squark and gluino hadroproduction. *Int. J. Mod. Phys. A*, 26:2637–2664, 2011, 1105.1110.

[87] C. Borschensky, M. Krämer, A. Kulesza, M. Mangano, S. Padhi, T. Plehn, and X. Portell. Squark and gluino production cross sections in pp collisions at $\sqrt{s} = 13$, 14, 33 and 100 TeV. *Eur. Phys. J. C*, 74(12):3174, 2014, 1407.5066.

[88] ATLAS collaboration. Summary of ATLAS Pythia 8 tunes. ATL-PHYS-PUB-2012-003, 2012.

[89] A. D. Martin, W. J. Stirling, R. S. Thorne, and G. Watt. Parton distributions for the LHC. *Eur.Phys.J. C*, 63:189–285, 2009, 0901.0002.

[90] S. Alioli, P. Nason, C. Oleari, and E. Re. A general framework for implementing NLO calculations in shower Monte Carlo programs: the POWHEG BOX. *JHEP*, 06:043, 2010, 1002.2581.

[91] J. M. Campbell, R. K. Ellis, P. Nason, and E. Re. Top-pair production and decay at NLO matched with parton showers. *JHEP*, 04:114, 2015, 1412.1828.

[92] T. Sjöstrand, S. Mrenna, and P. Z. Skands. A brief introduction to pythia 8.1. *Comput. Phys. Commun.*, 178:852, 2008, 0710.3820.

[93] P. Z. Skands. Tuning monte carlo generators: The perugia tunes. *Phys. Rev. D*, 82:074018, 10 2010.

[94] H.-L. Lai, M. Guzzi, J. Huston, Z. Li, P. M. Nadolsky et al. New parton distributions for collider physics. *Phys. Rev. D*, 82:074024, 2010, 1007.2241.

[95] J. Alwall et al. The automated computation of tree-level and next-to-leading order differential cross sections, and their matching to parton shower simulations. *JHEP*, 07:079, 2014, 1405.0301.

[96] ATLAS Collaboration. ATLAS Pythia 8 tunes to 7 TeV data. ATL-PHYS-PUB-2014-021, 2014.

[97] R. D. Ball et al. Parton distributions with lhc data. *Nucl. Phys. B*, 867:244, 2013, 1207.1303.

[98] T. Sjöstrand, S. Mrenna, and P. Z. Skands. PYTHIA 6.4 Physics and Manual. *JHEP*, 05:026, 2006, 0605.026.

[99] G. Gleisberg et al. Event generation with sherpa 1.1. *JHEP*, 02:007, 2009, 0811.4622.

[100] R. D. Ball et al. Parton distributions with lhc data run ii. *JHEP*, 04:040, 2015, 1410.8849.

[101] ATLAS Collaboration. Measurements of the Z/γ^* boson transverse momentum distribution in pp collisions at $\sqrt{s} = 7\,\text{TeV}$ with the ATLAS detector. *JHEP*, 09:055, 2014, 1406.3660.

[102] J. Pumplin et al. New generation of parton distributions with uncertainties from global qcd analysis. *JHEP*, 07:012, 2002, 0207.012.

[103] ATLAS Collaboration. Electron efficiency measurements with the ATLAS detector using the 2015 LHC proton–proton collision data. ATLAS-CONF-2016-024, 2016.

[104] ATLAS Collaboration. Electron reconstruction and identification in the ATLAS experiment using the 2015 and 2016 LHC proton-proton collision data at $\sqrt{s} = 13$ TeV. *Eur. Phys. J. C*, 79(8):639, 2019, 1902.04655.

[105] K. Cranmer. Statistical challenges for searches for new physics at the lhc. *Statistical Problems in Particle Physics, Astrophysics and Cosmology*, May 2006.

[106] M. Baak, G. J. Besjes, D. Cote, J. Lorenz, A. Koutsman, and D. Short. HistFitter software framework for statistical data analysis. *Eur. Phys. J. C*, 75:153, 2015, 1410.1280.

[107] ATLAS Collaboration. Measurement of the top quark-pair production cross section with ATLAS in *pp* collisions at $\sqrt{s} = 7\,\text{TeV}$. *Eur. Phys. J. C*, 71:1577, 2011, 1012.1792.

[108] ATLAS Collaboration. Jet Calibration and Systematic Uncertainties for Jets Reconstructed in the ATLAS Detector at $\sqrt{s} = 13$ TeV. ATL-PHYS-PUB-2015-015, 2015.

[109] ATLAS collaboration. Jet energy scale measurements and their systematic uncertainties in proton-proton collisions at $\sqrt{s} = 13\,\text{TeV}$ with the ATLAS detector. *Phys. Rev. D*, 96(7):072002, 2017, 1703.09665.

[110] ATLAS Collaboration. Studies on top-quark Monte Carlo modelling for Top2016. ATL-PHYS-PUB-2016-020, 2016.

[111] CMS Collaboration. Searches for pair production of charginos and top squarks in final states with two oppositely charged leptons in proton-proton collisions at $\sqrt{s} = 13$ TeV. *JHEP*, 11:079, 2018, 1807.07799.

[112] ATLAS collaboration. Search for electroweak production of charginos and sleptons decaying into final states with two leptons and missing transverse momentum in $\sqrt{s} = 13\,\text{TeV}$ pp collisions using the ATLAS detector. ATLAS-CONF-2019-008, 2019.

[113] ATLAS Collaboration. Search for electroweak production of supersymmetric particles in final states with two or three leptons at $\sqrt{s} = 13\,\text{TeV}$ with the ATLAS detector. *Eur. Phys. J. C*, 78(12):995, 2018, 1803.02762.

[114] CMS Collaboration. Searches for electroweak production of charginos, neutralinos, and sleptons decaying to leptons and W, Z, and Higgs bosons in pp collisions at 8 TeV. *Eur. Phys. J. C*, 74:3036, 2014, 1405.7570.

[115] CMS Collaboration. Searches for electroweak neutralino and chargino production in channels with Higgs, Z, and W bosons in pp collisions at 8 TeV. *Phys. Rev. D*, 90:092007, 2014, 1409.3168.

[116] CMS Collaboration. Search for electroweak production of charginos and neutralinos in multilepton final states in proton–proton collisions at $\sqrt{s} = 13\,\text{TeV}$. *JHEP*, 03:166, 2018, 1709.05406.

[117] CMS Collaboration. Combined search for electroweak production of charginos and neutralinos in proton–proton collisions at $\sqrt{s} = 13\,\text{TeV}$. *JHEP*, 03:160, 2018, 1801.03957.

[118] ATLAS collaboration. SUSY October 2019 Summary Plot Update, 2019.

[119] ATLAS collaboration. Search for new phenomena in events containing a same-flavour opposite-sign dilepton pair, jets and a large missing transverse momentum in $\sqrt{s} = 13\,\text{TeV}$ with the ATLAS detector. *Eur. Phys. J. C*, 77:144, 2017, 1611.05791.

[120] ATLAS collaboration. Search for supersymmetry in events containing a same-flavour opposite-sign dilepton pair, jets and a large missing transverse momentum in $\sqrt{s} = 8\,\text{TeV}$ pp collisions with the ATLAS detector. *Eur. Phys. J. C*, 75:318, 2015, 1503.032390.

[121] ATLAS Collaboration. Measurement of the W charge asymmetry in the $W \to \mu\nu$ decay mode in pp collisions at $\sqrt{s} = 7\,\text{TeV}$ with the ATLAS detector. *Phys. Lett. B*, 701:31, 2011, 1103.2929.

[122] ATLAS collaboration. Measurement of delta-rays in ATLAS silicon sensors. Technical Report ATLAS-CONF-2013-005, CERN, Geneva, Jan 2013.

[123] ATLAS collaboration. Measurement of the W charge asymmetry in the $W \to \mu\nu$ decay mode in pp collisions at $\sqrt{s} = 7\,\text{TeV}$ with the ATLAS detector. *Phys. Lett. B*, 701:31–49, 2011, 1103.2929.

[124] ATLAS collaboration. Measurement of the inclusive $W^{\pm}$ and Z/gamma cross sections in the electron and muon decay channels in pp collisions at $\sqrt{s} = 7\,\text{TeV}$ with the ATLAS detector. *Phys. Rev. D*, 85:072004, 2012, 1109.5141.

[125] ATLAS collaboration. ATLAS Muon Spectrometer Technical Design Report. Technical report, CERN, 1997.

[126] ATLAS collaboration. ATLAS beam spot public results. `https://twiki.cern.ch/twiki/bin/view/AtlasPublic/BeamSpotPublicResults`, 2017. Accessed: 2017-02-24.

[127] ATLAS collaboration. ATLAS Beam Spot Public Results, 2017, 2017.

[128] M. Carpentier and S. Davidson. Constraints on two-lepton, two quark operators. *Eur. Phys. J. C*, 70:1071–1090, 2010, 1008.0280.

[129] F. D. Aaron et al. Search for Lepton Flavour Violation at HERA. *Phys. Lett. B*, 701:20–30, 2011, 1103.4938.

[130] M. Aaboud et al. Searches for scalar leptoquarks and differential cross-section measurements in dilepton-dijet events in proton-proton collisions at a centre-of-mass energy of $\sqrt{s} = 13\,\text{TeV}$ with the ATLAS experiment. *Eur. Phys. J. C*, 79(9):733, 2019, 1902.00377.

[131] C. Anastopoulos, J. Alison, E. Benhar Noccioli, A. Bocci, et al. Supporting document on electron performance measurements using the 2011 LHC proton-proton collision data. Technical Report ATL-COM-PHYS-2012-1023, CERN, Geneva, 7 2012. This link is provided for reference, but is only accessible to ATLAS members.

[132] A. Cerri. ATLAS results on charmonium production in Pb-Pb and pp collision at the LHC, 2011.

[133] ATLAS Collaboration. Performance of the ATLAS muon trigger in pp collisions at $\sqrt{s} = 8\,\text{TeV}$. *Eur. Phys. J. C*, 75:120, 2015, 1408.3179.

[134] B. Fuks. Beyond the Minimal Supersymmetric Standard Model: from theory to phenomenology. *Int. J. Mod. Phys. A*, 27:1230007, 2012, 1202.4769.

[135] E. Richter-Was, D. Froidevaux, and L. Poggioli. ATLFAST 2.0 a fast simulation package for ATLAS. Technical Report ATL-PHYS-98-131, CERN, Geneva, 1998.

[136] L. Lonnblad. Correcting the color dipole cascade model with fixed order matrix elements. *JHEP*, 05:046, 2002, hep-ph/0112284.

[137] E. W. Varnes. A Poisson likelihood approach to fake lepton estimation with the matrix method, 6 2016, 1606.06817.

[138] P. Bakkera et al. Tools for estimating fake/non-prompt lepton backgrounds in ATLAS. Technical report, CERN, Geneva, 2019.

[139] J. Butterworth et al. PDF4LHC recommendations for LHC Run II. *J. Phys. G*, 43:023001, 2016, 1510.03865.

[140] L. Moneta, K. Belasco, K. S. Cranmer, S. Kreiss, A. Lazzaro, D. Piparo, G. Schott, W. Verkerke, and M. Wolf. The RooStats Project. *PoS*, ACAT2010:057, 2010, 1009.1003.

[141] A. Buckley. hepthesis- a LaTeX document class for academic theses. https://ctan.org/pkg/hepthesis.html, 2010.